Gold surface nanostructuring for separation and sensing of biomolecules

Erin Bedford

To cite this version:

Erin Bedford. Gold surface nanostructuring for separation and sensing of biomolecules. Chemical Physics [physics.chem-ph]. Université Pierre et Marie Curie - Paris VI; University of Waterloo (Canada), 2016. English. NNT : 2016PA066527 . tel-01529577

HAL Id: tel-01529577
https://theses.hal.science/tel-01529577

Submitted on 31 May 2017

HAL is a multi-disciplinary open access archive for the deposit and dissemination of scientific research documents, whether they are published or not. The documents may come from teaching and research institutions in France or abroad, or from public or private research centers.

L'archive ouverte pluridisciplinaire **HAL**, est destinée au dépôt et à la diffusion de documents scientifiques de niveau recherche, publiés ou non, émanant des établissements d'enseignement et de recherche français ou étrangers, des laboratoires publics ou privés.

Université Pierre et Marie Curie

University of Waterloo

ED 397

Laboratoire de Réactivité de Surface / Equipe de recherche

Gold surface nanostructuring for separation and sensing of biomolecules

Par Erin Bedford

Thèse de doctorat de Physique et Chimie de Matériaux (UPMC) et
de Chemical Engineering (Nanotechnology) (UW)

Dirigée par Mme Claire-Marie Pradier et M. Frank Gu

Présentée et soutenue publiquement le 15 novembre 2016

Devant un jury composé de :

M. Rabah Boukkheroub, Directeur de recherche, IEMN	**Rapporteur**
Mme Marie-Hélène Delville, Directrice de recherche, ICMCB	**Rapporteuse**
M. William Anderson, Professeur, University of Waterloo	**Examinateur**
Mme Christine Ménager, Professeur, UPMC	**Examinatrice**
Mme Souhir Boujday, Maître de Conférences, UPMC	**Directrice de thèse**
M. Frank Gu, Associate professor, University of Waterloo	**Directeur de thèse**
Mme Claire-Marie Pradier, Directrice de recherche, UPMC	**Directrice de thèse**

Except where otherwise noted, this work is licensed under
http://creativecommons.org/licenses/by-nc-nd/3.0/

Author's Declaration

This research proposal consists of material all of which I authored or co-authored: see Statement of Contributions included in the thesis. This is a true copy of the thesis, including any required final revisions, as accepted by my examiners.

I understand that my thesis may be made electronically available to the public.

Statement of Contributions

Chapter 2 is taken from a published research article: Bedford, E. E., Boujday, S., Pradier, C. M. & Gu, F. X. Nanostructured and spiky gold in biomolecule detection: improving binding efficiencies and enhancing optical signals. *RSC Adv.* **5,** 16461–16475 (2015). The chapter is my own work with valuable discussions and edits provided by Frank Gu, Claire-Marie Pradier, and Souhir Boujday.

Chapter 3 is taken from a published research article: Bedford, E. *et al.* An Experimental and Theoretical Approach to Investigate the Effect of Chain Length on Aminothiol Adsorption and Assembly on Gold. *Chemistry - A European Journal* **21,** 14555–14561 (2015). Frederik Tielens performed the DFT modeling and analysis. Christophe Méthivier performed the XPS analysis. I performed the experimental work, data analysis and wrote the article in collaboration with Souhir Boujday and with input from the other authors.

Chapter 4 is taken from a published research article: Bedford, E. E., Boujday, S., Humblot, V., Gu, F. X. & Pradier, C.-M. Effect of SAM chain length and binding functions on protein adsorption: β-lactoglobulin and apo-transferrin on gold. *Colloids and Surfaces B: Biointerfaces* **116,** 489–496 (2014). I performed the experimental work except for the XPS analysis, which was done by Vincent Humblot, and wrote the article, in collaboration with Souhir Boujday. Claire-Marie Pradier and Frank Gu provided valuable input and discussions regarding the experiments and the manuscript.

Chapter 5 includes experimental work performed by Elaine Huang and by myself. I performed all experimental planning, analyses, and writing, with valuable discussions and edits provided by Frank Gu, Claire-Marie Pradier, and Souhir Boujday.

Chapter 6 is entirely my own work, with valuable discussions and edits provided by Frank Gu, Claire-Marie Pradier, and Souhir Boujday.

Abstract

Detecting biomolecules for disease diagnosis, food and environmental safety, and biological research is challenging. After time-intensive purification steps, the biomolecule still has to be detected, often at extremely low concentrations. There is a push in the field of biomolecular detection for methods that are faster and easier to use than current methods, while still maintaining the high standard of sensitivity and selectivity required for accurate testing. Nanomaterials are on the same size scale as the biomolecules being detected, thus are interesting tools for advanced detection methods. In this work, we focus on biomolecular detection methods that use gold surfaces, as gold is biocompatible, easily functionalized, and can exhibit interesting optical properties that can be harnessed for sensitive detection. The goal is to work towards improved methods of gold surface-based biomolecular detection by studying and using different nanotools: self-assembled monolayers (SAMs) of alkanethiols and nanostructured gold shells on magnetic particles.

Gold surfaces are commonly functionalized with SAMs of alkanethiols for applications in biosensing. Highly selective biosensing often involves immobilizing biomolecules on a surface, but obtaining high detection efficiencies requires controlling their orientation, dispersion, and density. Functionalizing sensing surfaces with SAMs can offer control over biomolecule binding without dramatically affecting the proximity of the biomolecules to the surface. Despite how often SAMs are used, we still lack a complete understanding of the process of formation and how different SAMs influence biomolecule binding and recognition. We studied SAMs made from short-chain (cysteamine, CEA) and long-chain (11-mercaptoundecylamine, MUAM) amine-terminated alkanethiols using surface IR spectroscopy, x-ray photoelectron spectroscopy (XPS), and density functional theory (DFT) modeling. As expected, the longer chains formed a more ordered SAM than the shorter chains, but in addition, XPS showed that the sulfur binding environments differed for chains of different lengths. DFT modeling

further showed that surface reconstruction upon binding occurred differently for long compared with short chains. For the short chain alkanethiols, the thiol–gold interface governs the layer, as CEA binds more strongly with the mechanism being closer to single-molecule adsorption than self-assembly, whereas for long chains, the thiol-gold interface is less influential as interactions between alkyl chains drive the system to self-assembly, leading to a more ordered layer.

To study the dependence of protein binding and subsequent recognition on alkanethiol self-assembled monolayers (SAMs), we investigated adsorption of two proteins on amine-terminated SAMs with different chain lengths and different binding methods using surface IR spectroscopy and atomic force microscopy (AFM). We found that protein immobilization varies with SAM chain length and is also influenced by the presence of a cross-linker. The presence of a rigid cross-linker favours the binding of proteins on long chain SAMs, while the effect is almost nonexistent on shorter chains. In addition, the presence of the cross-linker induces a better dispersion of the proteins on the surfaces, regardless of the length of the thiols forming the SAMs.

Nanostructured gold has interesting optical properties for use in biomolecular detection. In the second part of this work, we synthesized spiky gold shells on magnetic particles for combined magnetic separation and surface enhanced Raman spectroscopy (SERS) detection of biomolecules. Magnetic particles are often used to separate particular biomolecules from a physiological sample. By coating the particles with a gold shell that can act as a SERS substrate, our goal is to enable the subsequent detection of the separated biomolecules without requiring additional binding steps.

The particle cores are made from controlled aggregates of superparamagnetic nanoparticles; the resulting particles are large enough to be quickly separated from solution, but still show superparamagnetic behavior and therefore can be easily redispersed in solution for subsequent biomolecule binding and washing steps. The cores are coated with silica to protect the magnetic cores and to facilitate subsequent

synthesis of the gold shell. The gold shell is made by binding small gold nanoparticle seeds to the silica surface, then using a chemical reduction method with cetyltrimethylammonium bromide (CTAB) as a stabilizer and structure-directing agent to grow the seeds into larger anisotropic gold/silver particles that combine into a shell. We explored different silica functionalization methods (bare silica, amine groups, short-chain thiol groups and long-chain thiol groups) to determine which method resulted in the best conditions for gold seed binding and growth into gold nanostructures. The gold shells can act as SERS substrates, enhancing the signal of a model Raman probe molecule, 2-mercaptopyrimidine, by a factor on the order of 10^4. Varying the growth bath conditions (concentration of CTAB and time in growth bath) changes the morphology of the shells, as well as the degree of SERS enhancement and the stability of the particles.

As a proof-of-concept, we used the particles to detect oligonucleotide hybridization. We bound thiolated oligonucleotide probes to the gold coatings and measured the SERS signal. We were able to measure relative concentrations of oligonucleotides bound and showed that a single particle provides sufficient enhancement to detect bound oligonucleotides. We also studied the decrease in signal that occurs as the distance from the surface increases and found that at an estimated distance of ~7-10 nm from the surface, DNA bases were no longer detectable. An initial experiment comparing pre-hybridized oligonucleotides bound to the surface showed that directly detecting differences between single-stranded and double-stranded DNA would be challenging, so we used a probe designed to harness the distance dependence of the signal instead. Before hybridization, the probe is expected to be in a hairpin conformation with the Raman tag near the surface. After hybridization, the probe straightens, drawing the tag away from the surface and leading to a decreased signal intensity. We successfully demonstrated that the particles could be used to detect DNA hybridization without the use of an extrinsic label.

Résumé

La détection de molécules biologiques à des fins de diagnostic médical, de sécurité alimentaire, environnementale et de recherche biologique relève d'une grande difficulté. En effet, après des étapes de purification chronophages, la molécule biologique doit encore pouvoir être détectée, et ce à des concentration souvent extrêmement faibles. Par conséquent, la recherche pour le développement de méthodes de détection rapide, faciles à mettre en œuvre, avec une grande sélectivité et sensibilité fait l'objet d'un intérêt grandissant. Les nanomatériaux étant de la même échelle que les biomolécules à détecter sont donc des candidats idéaux à inclure dans des techniques de détection avancée.

Dans ces travaux de thèse, nous nous sommes concentrés sur des méthodes de détections biomoléculaires mettant en œuvre des surfaces en or car l'or présente les avantages d'être biocompatible, facile à fonctionnaliser et démontre des propriétés optiques pouvant être sollicitées pour de la détection sensible. L'objectif est de développer des méthodes de détection biomoléculaire basées sur des surfaces en or à travers l'étude et l'utilisation de différents outils nanométriques : des monocouches auto assemblées (self assembled monolayers (SAM) en anglais) d'alcane-thiol et des coquilles d'or nanostructurées sur des particules magnétiques.

Pour des applications en biodétection, il est commun d'utiliser des surfaces d'or fonctionnalisées avec des SAMs d'alcane-thiol. Afin que la biodétection soit hautement sélective, les biomolécules doivent généralement être immobilisées sur une surface. De plus, l'orientation, la dispersion, et la densité de ces biomolécules doivent être contrôlées pour une haute efficacité de détection. La fonctionnalisation de surfaces de détection avec des SAMs permet de maîtriser l'immobilisation des biomolécules sans modifier de manières significatives la proximité des biomolécules à la surface. Cependant, malgré de nombreuses études sur les SAMs, des interrogations subsistent concernant le mécanisme

de formation de la monocouche ainsi que l'influence du type de SAM sur l'immobilisation et sur la reconnaissance.

Nous avons étudié des SAMs à base de chaînes courtes (cysteamine, CEA) et de chaînes longues (11-mercaptoundecylamine, MUAM) des alcane-thiols avec une fonction amine terminale. Les méthodes de caractérisation utilisées dans ces études incluent la spectroscopie infrarouge de surface, la spectroscopie de photoelectrons X (X-ray photoelectron spectroscopy, XPS, en anglais) ainsi que la chimie théorique (théorie de la fonctionnelle de la densité ou density functional theory, DFT, en anglais). Comme attendu, les chaînes longues forment des SAMs plus ordonnées que celles obtenues par des chaînes courtes. De plus, l'XPS montre que l'environnement des soufres immobilisés diffère en fonction de la longueur des chaînes alcanes. La modélisation DFT montre, de plus, que la longueur de chaîne influence la reconstruction de la surface. Pour les chaînes courtes d'alcane-thiol, l'interface thiol/or influence la formation de la couche. En effet, la cysteamine s'accroche plus fortement à travers un mécanisme plus proche de l'adsorption moléculaire que d'un mécanisme d'auto-assemblage. D'autre part, pour les chaînes longues, l'interface thiol/or est moins prédominante dans la formation de la monocouche car les interactions entre les chaînes alcanes poussent le système à s'auto-assembler ce qui conduit à la formation d'une couche plus ordonnée.

Afin d'étudier l'effet des SAMs d'alcane-thiol sur l'accroche de protéines (et donc la reconnaissance qui en résulte), nous avons mené une étude sur l'adsorption de deux protéines sur des SAMs comprenant un groupe amine terminal. Les caractérisations menées comprennent la spectroscopie IR de surface ainsi que la microscopie à force atomique (atomic force microscopy, AFM, en anglais). Les résultats montrent que l'immobilisation des protéines varie en fonction de la longueur de la chaîne des SAMs et en fonction de la présence d'un réticulant. La présence d'un réticulant rigide favorise l'accroche de protéines sur des SAMs avec une chaîne longue alcane alors que l'effet est quasi-inexistant pour des SAMs de chaînes courtes. De plus, la présence d'un réticulant implique une meilleure dispersion des protéines à la surface, indépendamment de la longueur de chaînes.

L'or nanostructuré possède des propriétés optiques intéressantes pour des applications en détection biomoléculaire. Dans la seconde partie des travaux, nous avons synthétisé des coquilles d'or nanostructurées sur des particules magnétiques afin de combiner la séparation magnétique et la détection de biomolécules par la spectrométrie Raman exaltée de surface (surface enhanced Raman spectroscopy, SERS, en anglais). Les particules magnétiques sont souvent utilisées afin de séparer les biomolécules particulaires de l'échantillon physiologique. Notre objectif est ainsi de permettre la détection, sans étape d'accroche subséquent, de biomolécules séparées, en déposant une coquille d'or pouvant agir en tant que substrat SERS sur les particules.

Le coeur des particules est constitué d'agrégats contrôlés de nanoparticules superparamagnétiques; les particules résultantes sont assez larges pour être séparées rapidement de la solution, mais conservent un comportement paramagnétique et peuvent donc être facilement re-dispersées en solution pour des étapes d'immobilisation de biomolécules et de lavages. Les noyaux sont recouverts de silice afin de protéger les coeurs magnétiques et de faciliter la synthèse subséquente de la coquille d'or.

Afin de former la coquille d'or, des initiateurs d'or sont déposés sur la surface de silice. Cette étape est suivie d'une réaction de réduction chimique avec le cetyltrimethylammonium bromide (CTAB) qui joue le rôle de stabilisateur et d'agent structurant permettant de contrôler la croissance des initiateurs en particules d'or et d'argent anisotropiques qui peuvent s'assembler en coquille.

Nous avons exploré plusieurs méthodes de fonctionnalisation de silice (silice pure, groupe amine, groupe de chaîne courte de thiol et groupe de chaîne longue de thiol) afin de déterminer quelle méthode serait la plus appropriée pour l'accrochage des initiateurs d'or ainsi que pour leur croissance en nanostructure d'or. Les coquilles d'or peuvent se comporter comme des substrats SERS permettant ainsi d'augmenter le signal d'une sonde Raman, la 2-mercaptopyrimidine, par un facteur de l'ordre de 10^4. La morphologie des coquilles, le degré d'augmentation du degré de SERS ainsi que la stabilité des particules se sont montrés influencés par les conditions de croissance (la concentration de CTAB et la durée).

Afin d'établir une preuve de concept, nous avons utilisé les particules nanostructurées pour la détection de l'hybridation d'oligonucléotides. Des sondes d'oligonucléotides thiolés ont été déposées sur des dépôts d'or et le signal SERS résultant a été mesuré. Des concentrations relatives d'oligonucléotides ont pu être mesurées et il a été montré qu'une particule seule présente un signal suffisamment élevé pour une détection d'oligonucléotide. Nous avons aussi étudié l'effet de l'augmentation de la distance à la surface sur la baisse de signal. Les résultats montrent qu'à une distance de 7 – 10 nm de la surface, les bases ADN n'étaient plus détectables. Une première expérience, comparant les oligonucléotides pré-hybridés accrochés à la surface, montra que la détection directe des différences entre l'ADN simple brin et double brin était compliquée. Nous avons donc utilisé une sonde spécifique (Cy5) afin de maîtriser la dépendance du signal à la distance. Avant hybridation, nous nous attendions à ce que la sonde soit dans une conformation en épingle à cheveux quand la sonde Raman est près de la surface. Après hybridation, l'oligonucléotide se redresse, poussant la sonde loin de la surface et conduisant à une diminution de l'intensité du signal. Nous avons ainsi montré que ces particules pouvaient être utilisées pour la détection d'hybridation de l'ADN et, ce, sans l'utilisation d'une sonde extrinsèque.

Acknowledgements

I have had the enormous pleasure to have spent the last few years working in two excellent institutions: l'Université Pierre et Marie Curie (UPMC) and the University of Waterloo (UW). The opportunity to do a cosupervised/cotutelle PhD was provided by the IDS-FunMat program. I'm also grateful to my funding sources: to UPMC and UW, the Natural Science and Engineering Research Council of Canada (NSERC), the French Embassy in Canada/France-Canada Research Fund (FCRF), and the Waterloo Institute for Nanotechnology (WIN).

To my supervisors, Prof. Frank Gu, Dr. Claire-Marie Pradier, and Prof. Souhir Boujday—thank you. Thank you for helping to guide me throughout my work and for supporting me on the path to becoming an independent researcher. You guided me and provided me with your valuable expertise, but always left me with the freedom to choose my own path. This has made me not just a better researcher, but also a better person. Your encouragement in both the day-to-day work and in my future career choices has been amazing. You have my sincere gratitude.

Thank you as well to my committee members, Dr. Rabat Boukherroub, Dr. Marie-Hélène Delville, Prof. William Anderson, and Prof. Christine Ménager for agreeing to review my thesis and share their expertise.

Another thanks goes to Tornado Spectral Systems for lending us a Raman spectrometer that was used extensively in experiments and especially to Yusuf Bismilla for helping to set this up.

Many thanks to all members of the Laboratoire de Réactivité de Surface. Your help in both the lab and in navigating life in Paris was amazing—I couldn't have done it without you. You put up with my not-so-great French and helped me to reach the point where (I'm pretty sure) we could understand each other without resorting to English. A big thanks to the many members of the lab who helped me throughout my work—to

Vincent Humblot, Jean-Marc Krafft, Christophe Méthivier, Christophe Calers, and Sandra Casale for their help obtaining and analyzing data, and the indispensable discussions surrounding it. Special thanks also to Rickielle, Kim, Cédric, Jane, Maroua, Noémie, Antoine, Jessie, Colin, and Catarina for the support in the lab and the great times spent over coffee or a pint.

Many thanks as well to the Waterloo lab members. I've always considered myself ridiculously lucky to be able to turn around at my desk and ask "hey guys, do you have a second?", throw out an idea, and get amazing feedback. And thanks for the fun times as well—if the origami buckyball goes missing from the office, the first place to check should probably be my living room. Special thanks to Sandy for putting up with me staring into "space", i.e. the side of his head, to Jasper for the bike rides and jogs, to Sarah for the support and friendship (and for making it so that I wasn't surrounded by only boys), to Elaine for being an amazing co-op student, to Paul, Perry, and Jackson for making and sending me particles, and to Mohit, Tim, Stuart, and Kuba for the always helpful chats and inspiration.

I'd also like to thank those in both universities who helped me to sort out the paperwork and day-to-day administrative tasks associated with doing a PhD, especially with doing a PhD in two countries. In the LRS, special thanks to Sabine Mendes, Sabine Même, Annie Mettendorf, and Sonia M'Barek. At UW, special thanks to Judy Caron and the others in the chemical engineering and grad studies offices.

While my above thank-you's certainly include those who I consider not just co-workers but also friends, I'd also like to thank my friends outside of the lab who helped to maintain my sanity. To my Waterloo IDS-FunMat crew and friends—Edgar, Uyxing, Mylène, Dan, Cam, An, Jiang—thanks for the lunches, coffees, w(h)ine and cheeses, and general support and fun. Thanks as well to all my MEC friends—especially to Heather and Michèle for the semi-marathon training and delicious meals, to Sophie for the course notes and company, and to Guillaume for the support, encouragement, and all around great times. And thanks to my friends in Canada—to Richard for always, always being there, to Helen for the listening ear and the belaying hand, and to the Grad House gang when the best option seems to be (in celebration or otherwise) a beer.

To my family—thank you for the never-ending support. Mom and dad, I guess you've done a pretty good job of raising me to feel confident supporting me in whatever decisions I've made—thank you, from the bottom of my heart. Don, your support has also been amazing. Taylor, my little sister, thanks for being wonderful.

Table of Contents

Author's Declaration iii

Statement of Contributions iv

Abstract v

Résumé viii

Acknowledgements xii

List of Figures xviii

List of Tables xxiv

List of Abbreviations xxv

Chapter 1 : Introduction 1

1.1 Overview 1

1.2 Outline 3

Chapter 2 : Literature Review 5

2.1 Summary 5

2.2 Introduction 5

2.3 Benefits of Nanostructuring 8

2.3.1 Geometric Benefits 8

2.3.2 Enhancement of Optical Detection Methods 12

2.4 Types of Gold Nanostructuring 18

2.4.1 Planar Surface Nanostructuring 19

2.4.2 Particle Nanostructuring 24

2.5 Conclusion 33

Chapter 3 : An Experimental and Theoretical Approach to Investigate the Effect of Chain Length on Aminothiol Adsorption and Assembly on Gold 34

3.1 Summary 34

3.2 Introduction **35**

3.3 Experimental Section **36**

3.3.1 Materials 36

3.3.2 Methods 36

3.3.3 Techniques 37

3.4 Results and Discussion **39**

3.4.1 PM-IRRAS characterization of SAMs on gold surface 39

3.4.2 XPS characterization of SAMs on gold surface 40

3.4.3 DFT geometry optimizations and binding energies of the SAM systems 43

3.4.4 General discussion 47

3.5 Conclusions **48**

Chapter 4 : Effect of SAM chain length and binding functions on protein adsorption: β-lactoglobulin and apo-transferrin on gold **50**

4.1 Summary **50**

4.2 Introduction **51**

4.3 Experimental Section **53**

4.3.1 Materials 53

4.3.2 Methods 54

4.3.3 Characterization techniques 56

4.4 Results **57**

4.4.1 SAM formation and cross-linker binding 57

4.4.2 Protein immobilization 59

4.5 Discussion **64**

4.6 Conclusion **66**

Chapter 5 : Synthesis and characterization of nanostructured gold coatings on magnetic particles **67**

5.1 Summary **67**

5.2 Introduction **67**

5.3 Experimental Section **70**
5.3.1 Materials 70
5.3.2 Methods 71
5.3.3 Characterization techniques 75
5.4 Results and Discussion **77**
5.4.1 Magnetic properties 77
5.4.2 Gold shell growth: Influence of silica-iron oxide core functionalization 81
5.4.3 Gold shell growth: Influence of growth bath conditions 93
5.4.4 Particle stability over time 96
5.5 Conclusion **99**
Chapter 6 : Nanostructured gold shells on magnetic particles for oligonucleotide detection **100**
6.1 Summary **100**
6.2 Introduction **100**
6.3 Experimental Section **103**
6.3.1 Materials 103
6.3.2 Methods 103
6.4 Results and Discussion **107**
6.4.1 Oligonucleotide binding 107
6.4.2 Micro-Raman study of individual particles and small clusters 111
6.4.3 Raman study of oligonucleotide “rulers” 116
6.4.4 DNA hybridization detection 120
6.5 Conclusion **127**
Chapter 7 : Conclusions and Perspectives **128**
References **131**
Appendix A : Apo-transferrin data **146**
Appendix B : Magnetic separation calculations **148**

List of Figures

Figure 2.1: General scheme of biosensors. Targets in a biological sample bind to receptors bound to a substrate. Signal transduction indicates target binding............ 6

Figure 2.2: Proposed model of the effect of nanostructuring on DNA binding and hybridization. Nanostructured microelectrodes (NMEs) were used for electrochemical detection of DNA hybridization with and without nanotexturing. Reprinted with permission from ref[49]. Copyright 2010 American Chemical Society. [49].. 10

Figure 2.3: Proposed model of the effect of nanostructuring on protein-antibody (biotin-IgG) interactions. Feature sizes similar to the size of the binding domains of IgG result in higher recognition (B, C). Feature sizes that are too small prevent recognition (A) and those that are too large result in random orientations (D). Reprinted with permission from ref [10]. Copyright 2008 American Chemical Society. 12

Figure 2.4: Simulations of electromagnetic enhancement at a) nanogaps[72], b) sharp tips[73], and c) combined sharp tips and nanogaps (bowtie nanoantenna)[74]. 14

Figure 2.5: General scheme of nanosphere lithography... 23

Figure 2.6: SEM images of gold nanostructured surfaces formed by electrodeposition for different times: (A) 20 s, (B) 100 s, (C) 300 s, and (D) 600 s.[54]...................................... 24

Figure 2.7: Examples of anisotropic particles from literature. Labels correspond to those in Table 2.1. 31

Figure 3.1: Cysteamine (CEA) and 11-mercaptoundecylamine (MUAM) SAMs formed on gold surface (schematic representation) 37

Figure 3.2: PM-IRRAS spectra of: a) Au-CEA and b) Au-MUAM...................................... 40

Figure 3.3: High-resolution XPS S2p region for Au-MUAM (left) and Au-CEA (right) .. 42

Figure 3.4: Side views of the optimized geometry of a) CEA and b) MUAM SAMs........ 44

Figure 3.5: Top view of a) CEA SAM and b) MUAM SAM showing only the sulfur and gold atoms. The sulfur atom (red) on the Au surface (yellow: bulk atoms, green: surface Au atoms, magenta: surface extracted Au atoms).. 45

Figure 3.6: Top view of a) CEA SAM and b) MUAM SAM showing the relative displacement (arrows) of the sulfur atoms (red). The gold atoms (green) are at a distance smaller than 2.69 Å from the Sulfur atoms.. 46

Figure 4.1: Schematic drawing of protein immobilization methods on SAMs made from amine-terminated short-chain thiols (cysteamine, CEA) and long-chain thiols (11-mercaptoundecylamine, MUAM). (Top) Immobilization on surface amine groups following EDC/NHS activation of acid groups on proteins. (Bottom) Cross-linker binding and protein immobilization by reaction with amine groups on proteins... 55

Figure 4.2: PM-IRRAS spectra of Au-CEA, Au-CEA after PDITC binding, Au-MUAM and Au-MUAM after PDITC binding. 58

Figure 4.3: PM-IRRAS spectra after β-lactoglobulin (a) and antibody recognition (b) on CEA, MUAM, CEA-PDITC and MUAM-PDITC. 60

Figure 4.4: AFM images of gold-coated substrates following SAM formation and β-lactoglobulin binding. Upper images: Scan area: 10 μm x 10 μm, height scale: 40 nm. Lower images: Scan area: 1 μm x 1 μm, height scale: 10 nm. 62

Figure 5.1: Schematic diagram of spiky particle synthesis steps. Gold seeds are bound to a silica-coated magnetite particle, then grown into gold spikes using a gold salt and CTAB bath solution. 71

Figure 5.2: Silica coatings were functionalized using different groups. Silica shells were a) left bare (bare), b) amine-coated, using APTES (NH_2), c) short-chain thiol-coated,

using MPTMS (SC-SH), and d) Long-chain thiol-coated, using MUA grafted onto amine-coated particles (LC-SH). 73

Figure 5.3: Magnetization curves of silica-coated iron oxide particles before (solid) and after (dashed) gold/silver shell coating. The inset shows the small amount of hysteresis occurring at low magnetic fields 78

Figure 5.4: Measured opacity over time for water dispersions of particles at 1 mg Fe_3O_4/SiO_2 particles/ml (greater mass upon gold coating) in a 45 T/m gradient, before (solid) and after (dashed) gold shell coating. 79

Figure 5.5: Interaction potential at short distances between two silica-coated iron oxide particles (iron oxide core diameter = 224 nm, silica shell diameter = 336 nm) with a charge density of -0.9 e/nm^2 in 10 mM concentration of 1:1 electrolyte (surface potential $\Phi_0 \approx -73$ mV). (Blue) no applied magnetic field—zero magnetization, (red) remanent magnetization following removal of magnetic field, (green) applied magnetic field—saturation magnetization of 32 emu/g. 80

Figure 5.6: TEM images of particles after gold seed binding on a) bare silica, b) amine-functionalized silica, c) short-chain thiol-functionalized silica, and d) long-chain thiol-functionalized silica 83

Figure 5.7: UV-Vis spectra of particles before and after gold seed binding 83

Figure 5.8: TEM images of spiky particles, with spiky nanostructures grown on a) bare silica, b) amine-functionalized silica, c) short-chain thiol-functionalized silica, and d) long-chain thiol-functionalized silica. Insets show high magnification of spiky shells 85

Figure 5.9: UV-Vis spectra of spiky particles 86

Figure 5.10: Raman spectra of 2-mercaptopyrimidine with and without particles. Note that a concentration of 2-mercaptopyrimidine 10^3 lower is used to demonstrate

enhancement by particles (10 μM) compared with the unenhanced signal (10 mM). All samples used 50 μl of 2 mg/ml particles in 1 mM CTAB added to 3 ml of water. 89

Figure 5.11: Raman spectra of 2-mercaptopyrimidine (MPym) at different concentrations with particles featuring spiky gold shells on bare silica-coated magnetite particles. All samples used 50 μl of particles in 1 mM CTAB added to 3 ml of water. Peaks with red labels correspond to peaks that increased after adding MPym and peaks with black labels correspond to peaks seen on particles before adding MPym—likely CTAB........ 90

Figure 5.12: Change in peak height of Raman signal corresponding to the Raman reporter (MPym) at different concentrations. A fit to a Langmuir model (red line) shows saturation behavior ($R^2 = 0.98$)........ 91

Figure 5.13: Change in peak heights corresponding to CTAB at different Raman reporter (MPym) concentrations........ 92

Figure 5.14: a) TEM images showing representative particles at varying growth times and CTAB concentrations and b) corresponding UV-Vis extinction spectra for particles synthesized at different growth times using (top) 10 mM and (bottom) 100 mM CTAB........ 94

Figure 5.15: a) TEM images and b) (i-iii) corresponding Raman spectra of particles in 167μM CTAB with i) spiky shells (EB-150-a), ii) bumpy shells (EB-150-b), and iii) nanoparticle spotted (EB-150-c), and iv) Raman spectra of 0.2M CTAB in water (1200x more concentrated than particle-enhanced measurements)........ 95

Figure 5.16: a) TEM images showing representative particles over time and b) corresponding UV-Vis extinction spectra for (left) spiky particles and (right) bumpy particles over time........ 98

Figure 5.17: Raman spectra of (top) spiky and (bottom) bumpy particles in 167 μM CTAB 99

Figure 6.1: Oligonucleotides as received. TCEP is used to reduce them to thiol form... 107

Figure 6.2: SERS spectra of spiky gold-coated magnetic particles functionalized with a) i) 3-mercapto-1-propanol, and ii) oligonucleotides with sequence 5′-$C_{12}A_3$-3′-$(CH_2)_3$-S-, b) i) 6-mercapto-1-hexanol, and ii) oligonucleotides with sequence -S-$(CH_2)_6$-5′-A_3C_{12}-3′ 109

Figure 6.3: SERS spectra of oligonucleotides (5′-$C_8A_3C_4$-3′-S-) bound to particles using different binding concentrations 110

Figure 6.4: Comparison of measured Raman intensity of peak at 1029 cm^{-1} and UV-Vis intensity at 260 nm for oligonucleotides on particles using different binding concentrations 111

Figure 6.5: Micro-Raman (SERS) spectra of thiolated oligonucleotides bound to spiky gold-coated magnetic particles on silicon. Each spectrum represents a separate measurement focusing on a) individual particles and b) small groups of particles (2-4) 113

Figure 6.6: a) TEM images of particles with different gold shell morphologies: i) super spiky shells, ii) spiky shells, and iii) bumpy shells. b) Average micro-Raman (SERS) spectra of 7-10 measurements for (blue) individual particles, (solid red) small groups of particles, and (dashed red) small groups of particles normalized using the average number of particles in the measurements, which were i) 2.2, ii) 2.8, and iii) 2.4. c) Graphs highlighting average Raman spectra peak height similarity between signals from single particles and small groups of particles after adjusting for the average number of particles. No pairs of means show significant differences. Error bars indicate 95% confidence intervals........ 115

Figure 6.7: Graphs highlighting average micro-Raman (SERS) spectra peak height differences between signals from particles of different morphologies. Significant differences are indicated by asterisks: (*) indicates $p \leq 0.05$ and (***) indicates $p \leq 0.001$. Error bars indicate 95% confidence intervals. 116

Figure 6.8: SERS spectra of oligonucleotide “rulers” bound to spiky gold-coated particles. The rulers (i-vii) correspond to those listed in Table 6.2. Two spectra are shown overlaid for each oligonucleotide. 118

Figure 6.9: Normalized Raman peak intensity (I_{1338}) for oligonucleotides with different adenine group positions. The red line shows a fit to the data based on the distance dependence of the SERS signal. Error bars indicate a 95% confidence interval. 120

Figure 6.10: Scheme of hairpin probe with Raman tag, before and after hybridization to target strand 121

Figure 6.11: a) SERS spectra and b) normalized SERS spectra (using intensity at 1087 cm^{-1}) of i) oligonucleotide probes only, ii) oligonucleotide probes hybridized with complementary oligonucleotides, and iii) oligonucleotide probes hybridized with non-complementary oligonucleotides 122

Figure 6.12: a) SERS spectra and b) normalized SERS spectra (using intensity at 1023 cm^{-1}) of i) Cy5-tagged oligonucleotide probes only, ii) Cy5-tagged oligonucleotide probes hybridized with complementary oligonucleotides, and iii) Cy5-tagged oligonucleotide probes hybridized with non-complementary oligonucleotides 123

Figure 6.13: a) Normalized SERS spectra and b) average peak height of i) Cy5-tagged oligonucleotide hairpin probes, ii) hybridization with complementary oligonucleotides and iii) hybridization with non-complementary oligonucleotides. Error bars indicate 95% confidence intervals. 125

List of Tables

Table 2.1: Particles with nanostructured surfaces – method of synthesis and demonstrated application 32

Table 3.1: XPS-determined atomic percentages and S2p photopeak decompositions corrected by Scoffield factors 41

Table 4.1: Change in area of amide I and II (1660 cm^{-1} + 1550 cm^{-1}) peaks from PM-IRRAS following binding and ratio of bound antibodies to corresponding proteins adjusted for mass (errors correspond to standard deviation from measurements of two to four separate chips). 60

Table 5.1: Separation times of particles, determined based on time required to reach 5% and 1% of initial opacity (see dotted lines in Figure 5.4) 79

Table 5.2: XPS results showing elemental breakdown of particle surfaces following treatment 81

Table 5.3: XPS-determined atomic percentages following coating procedures in different conditions 96

Table 6.1: Gold shell synthesis parameters and approximate concentration of oligonucleotides bound 112

Table 6.2: Oligonucleotide sequences used as “rulers” 117

List of Abbreviations

APTES: (3-aminopropyl)triethoxysilane

AFM: atomic force microscopy

AuNPs: gold nanoparticles

CEA: cysteamine

CTAB: cetyltrimethylammonium bromide

dsDNA : double-stranded deoxyribonucleic acid

EDC: 1-ethyl-3-(3-dimethylaminopropyl)carbodiimide hydrochloride

EDTA: ethylenediaminetetraacetic acid

NHS: *N*-hydroxysuccinimide

MPym: 2-mercaptopyrimidine

MPTMS: (3-mercaptopropyl)trimethoxysilane

MUA: 11-mercaptoundecanoic acid

MUAM: 11-mercaptoundecylamine

NPs: nanoparticles

PDITC: p-phenylene diisothiocyanate

PM-IRRAS: polarization modulation infrared reflection absorption spectroscopy

SAM : self-assembled monolayer

SEM: scanning electron microscopy

SERS: surface-enhanced Raman spectroscopy

SPR: surface plasmon resonance

ssDNA : single-stranded deoxyribonucleic acid

TCEP: tris(2-carboxyethyl)phosphine

TEM: transmission electron microscopy

UV-Vis: ultraviolet-visible spectroscopy

XPS: x-ray photoelectron spectroscopy

Chapter 1: Introduction

1.1 Overview

Biomolecular detection is used in a number of fields—to detect disease, to determine if a source of water is safe to drink, and to learn more about the form and function of organisms, for example. Biomarkers of disease or contamination can include proteins, nucleic acids, and other molecules specific to a given pathogen. Current methods of detection such as ELISA, polymerase chain reaction (PCR), and DNA/RNA microarrays work, but tend to require advanced labs with experienced personnel, as well as time and money. There is a push in the field of biomolecular detection/biosensing to develop methods that are fast and easy-to-use, while still exhibiting sufficient enough sensitivities and specificities for practical use.

Controlling small things means using small tools. As our ability to work with and control the microscopic biological world grows, our need for tools that can interact with this world does as well, which is where nanomaterials are playing an increasingly important role.[1] In this work, we study several of these tools and use them to improve biomolecular detection, specifically self-assembled monolayers (SAMs) of alkanethiols on gold and nanostructured gold surfaces. Gold surfaces are commonly used in biomolecular detection methods due to their biocompatibility, easy functionalization, and interesting electromagnetic properties that result at the nanoscale. SAM functionalization and nanostructuring of gold surfaces are important tools in the quest towards biomolecular detection that is more sensitive, faster, and easier to use.

Achieving high sensitivities in biosensing often involves using a surface-bound probe molecule to specifically detect the analyte (e.g. antibody, aptamer, complementary DNA). The nature of the probe binding—including factors such as probe density, conformation, and orientation—has a large influence on target binding efficiencies. Controlling the surface chemistry and other properties is therefore crucial to biosensor function.[2] Crowding effects due to high densities can prevent target molecules from accessing binding sites on probe molecules.[3-8] Good access to binding sites also requires that the probes be bound in a suitable conformation and orientation.[3,9,10] Self-assembled monolayers of alkanethiols on gold are one tool that can be used to control probe molecule binding. In the case of proteins, for example, using surfaces functionalized with different groups changes which part of the protein is bound to the surface, thus which part of the protein is exposed and available for target binding.[11] SAMs can also act as diluting or spacing groups between probe molecules to control the density.[3] While SAMs on gold are commonly used in biosensing methods, optimization of these surfaces requires a better mechanistic understanding of SAM formation and biomolecule binding, which surface science methods can help provide.

Nanostructured gold is an increasingly common tool in biomolecular detection research because of its interesting optical properties.[12-17] Surface-enhanced Raman spectroscopy (SERS) uses nanostructured metallic surfaces (typically gold or silver) to enhance the electromagnetic signal of both the light incident to the surface and light scattered by molecules near the surface; the result is a signal intensity orders of magnitude greater than what is observed in ordinary Raman spectroscopy. SERS substrates are made in a variety of forms; commonly used substrates include planar surfaces with nanoscale metallic features, but SERS can also be done using gold or silver nanoparticles in solution. The greatest enhancements occur at hot-spots—sharp tips or nanogaps—so most current efforts involve synthesizing structures of this type that give a strong, reproducible enhancement.[14,18]

Multifunctional nanoparticles, where a single particle exhibits multiple functions (such as magnetism, fluorescence, catalytic, or optical properties), open up additional possibilities to improve biomolecular detection using nanomaterials. Here, we aim for combined separation and detection of biomolecules using magnetic cores with nanostructured gold shells that can act as SERS substrates. Biological samples are a complex mixture of biomolecules, so a first step in any attempt to work with a specific biomolecule is to separate it from the rest. With the goal of a simple biosensing method with fewer steps, an ideal method would involve detecting the presence and quantity of the analyte directly after separation. Magnetic particles are commonly used for separating and concentrating specific biomolecules.[19-23] Following magnetic separation, the analyte is bound to the surface of the particles; directly detecting its presence without any further dissociation or binding steps is possible using the concept of multifunctional particles. We use magnetic particles coated with a nanostructured gold shell that can be used to see changes in the SERS signal upon binding of the target to the nanostructured gold surface.

1.2 Outline

We begin by reviewing methods of gold surface nanostructuring for biomolecular detection in Chapter 2. This includes both planar and particle-based methods and the benefits that have been shown in the literature.

The first part of the experimental work involves studying self-assembled monolayers of alkanethiols on planar gold surfaces and their influence on protein binding and recognition (Chapter 3 and Chapter 4). Self-assembled monolayers are often used in biosensing because they can easily form a layer of functional groups on the surface that can be used for biomolecule attachment. In the case of alkanethiols, the length of the carbon chain between the thiol group and the head group influences the properties of the self-assembled monolayer that forms. In Chapter 3, we investigate this effect in amine-terminated alkanethiols using x-ray photoelectron spectroscopy (XPS) and density functional theory (DFT) modeling to compare long and short chain adsorption and assembly on gold surfaces. Long-chain alkanethiols are known to form more ordered layers than short-chain alkanethiols,[24-27] but the nature of the gold-sulfur interface is not yet completely understood. In this chapter, we propose a mechanism involving gold surface rearrangement that contributes to explaining the observed differences in SAM organization with different chain lengths due to the nature of the gold-sulfur bond.

In Chapter 4, we study protein binding and recognition on different alkanethiol surfaces. We compared the binding of two proteins of different sizes (β-lactoglobulin and apo-transferrin) to SAMs of different chain lengths, with or without a cross-linker group, using polarization modulation infrared reflection absorption spectroscopy (PM-IRRAS) and atomic force microscopy (AFM). Protein binding amount and density is influenced by the nature of the SAM; consequently, recognition of the proteins by an antibody is also affected, due in part to the nanoscale arrangement of proteins on the surface.

In the second part of this work, we developed multifunctional particles for combined separation and detection of biomolecules (Chapter 5 and Chapter 6). The particles feature a nanostructured gold coating on a magnetic core; the gold coating acts as a surface-enhanced Raman spectroscopy (SERS) substrate, enhancing the Raman signal of molecules bound to their surface and the magnetic core allows the particles to be quickly separated from solution using magnetic forces. Chapter 5 describes their synthesis and the influence of varying conditions on their use as SERS substrates. In Chapter 6, we use the particles to detect DNA binding and hybridization, as a proof-of-concept. Using a Raman tagged oligonucleotide hairpin probe we can detect oligonucleotide hybridization by harnessing the distance dependence of the SERS signal.

Chapter 7 summarizes the results and discusses them from the perspective of the broader context of the field. We look at the implications and potential future directions of the work.

This PhD work was carried out in a collaboration between two universities: Université Pierre et Marie Curie (UPMC) in the Laboratoire de Réactivité de Surface (LRS) and the University of Waterloo (UW). The joint PhD collaboration was organized as part of the International Doctoral School in Functional Materials (IDS-FunMat), an Erasmus Mundus joint doctorate program.

Chapter 2: Literature Review

2.1 Summary

Nanostructured gold can improve the ability to detect biomolecules. Whether planar nanostructured surfaces or nanostructured particles are used, similar principles governing the enhancement apply. The two main benefits of nanostructured gold are improved geometry and enhancement of optical detection methods. Nanostructuring improves the geometry by making surface-bound receptors more accessible and by increasing the surface area. Optical detection methods are enhanced due to the plasmonic properties of nanoscale gold, leading to localized surface plasmon resonance sensing (LSPR), surface-enhanced Raman spectroscopy (SERS), enhancement of conventional surface plasmon resonance sensing (SPR), surface enhanced infrared absorption spectroscopy (SEIRAS) and metal-enhanced fluorescence (MEF). Anisotropic, particularly spiky, surfaces often feature a high density of nanostructures that show an especially large enhancement due to the presence of electromagnetic hot-spots and thus are of particular interest. In this review, we discuss these benefits and describe examples of nanostructured gold on planar surfaces and particles for applications in biomolecule detection.

2.2 Introduction

From medicine to environmental monitoring to food contamination protection, detection of biomolecules helps to protect our health and our environment. Over the past two decades, biosensor research has taken off, inspired by the success of the hand-held glucose sensors used by diabetic patients, but expanding into the detection of all types of biomolecules using a variety of transduction methods.[28] No matter the method of detection, high sensitivity is one of the constant goals within the field of biosensor research. Since many methods involve concentrating biomolecules on a surface for signal transduction, a key strategy to achieve high sensitivities is to optimize the surfaces on which probes are bound so that a large number of analyte molecules can be bound and a sufficiently strong signal produced.

Affinity-based biosensors harness the specific affinity between certain biomolecules to detect the presence and quantity of a biomolecule. These make use of the same interactions that allow for currently used methods of detecting biomolecules such as immunoassays, which make use of the affinity between antigens and antibodies (ELISA, for example), and hybridization assays, which make use of the affinity between complementary nucleic acid strands (Southern and northern blot assays, for example). By using affinity interactions to specifically bind an analyte of interest—typically on a solid surface—they can be detected by various methods of signal transduction (Figure 2.1). Biomolecules are small, so harnessing their specific interactions requires tools of a comparable scale—a job that nanostructured gold fills well; gold is biocompatible, chemically stable, and can easily be functionalized.[1,12,29,30]

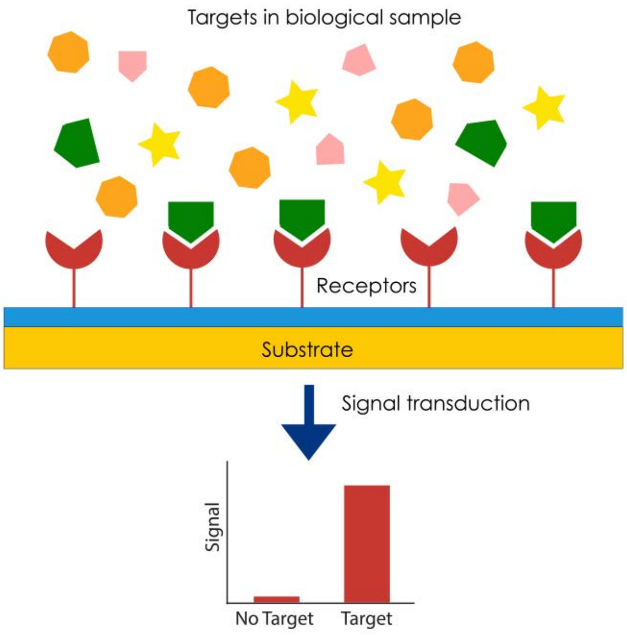

Figure 2.1: General scheme of biosensors. Targets in a biological sample bind to receptors bound to a substrate. Signal transduction indicates target binding

While electrochemical methods have traditionally been the most commercially successful biosensing methods, optical detection methods have also proved interesting by offering highly sensitive, label-free detection— a primary example being the prevalence of surface plasmon resonance (SPR) detection in R&D.[28] Optical methods of detection make use of changes in the optical signal—absorption, luminescence, fluorescence, and plasmon resonance, for example—that occur upon binding. Again, nanostructured gold stands out as an interesting material, in this case, because of its interesting optical properties. Surface plasmons can be excited in metallic nanoparticles by specific wavelengths of light due to the confinement of electrons within the small particles.[31,32] In gold nanoparticles, this surface plasmon resonance (SPR) frequency is in the visible range, leading to the characteristic red colour of gold nanospheres and other colours in gold nanoparticles of different shapes and sizes. In addition to these distinct colours, the confined surface plasmons lead to enhanced electromagnetic fields at the particle surfaces. Anisotropic shapes, such as "spiky" tips, lead to particularly strong enhancements, often referred to as electromagnetic hot-spots.[31,33-36] In localized surface plasmon resonance (LSPR) sensing, biomolecule binding leads to a shift in gold nanoparticle absorbance, which is larger when biomolecules are bound to hot-spots compared with other areas of the gold nanoparticle surface.[37-40] Other methods of optical detection, such as surface-enhanced Raman spectroscopy (SERS),[18,33,41] surface enhanced infrared absorption spectroscopy (SEIRAS),[33,42,43] and metal-enhanced fluorescence (MEF)[44] also show an enhanced signal due to this hot-spot phenomenon that can be harnessed for biosensing applications.

Extraordinarily innovative methods have been used to form spiky gold nanostructures that exhibit the above features. Methods like electron beam lithography and atomic force microscopy can make precise structures that are extremely useful in studying the above phenomena, but the practical harnessing of these phenomena in biosensing will likely require simpler methods of nanostructure formation that can be done on a larger scale or that are more accessible to non-specialized laboratories.

In this review, we first discuss the benefits of using nanostructured gold—specifically, the improved binding efficiencies and enhanced optical signals that can result—

followed by a (non-exhaustive) look at examples of methods used to nanostructure gold surfaces with a focus on chemical methods and those requiring less specialized equipment.

2.3 Benefits of Nanostructuring

Recent work has shown that there are numerous benefits to nanostructuring surfaces, including geometric benefits involving the position, orientation, and accessibility of immobilized biomolecules as well as enhancement of optical transduction methods. Our focus in this review will be on the geometric benefits and the enhancement of optical detection methods using nanostructured gold. This covers two different methods of enhancement: geometric optimization, by increasing the number of targets available for detection, and optical detection method enhancement, by increasing the sensitivity of the technique to a single recognition event.

2.3.1 Geometric Benefits

2.3.1.1 *Nucleic acids*

DNA biosensors use the specific interaction between complementary strands of DNA bound to a surface and the DNA molecules of interest to detect the presence of a particular DNA sequence. Hybridization with DNA probes bound to a surface introduces new challenges compared with standard hybridization in solution. Hybridization efficiencies are reduced by electrostatic repulsion and steric hindrance between immobilized strands, and by non-specific adsorption of oligonucleotides to the surface.[4-6,45]

The idea that working with small biomolecules requires small tools has led to much research on the differences that occur between binding oligonucleotides to nanostructured surfaces and binding to planar ones. In particular, the surface curvature influences the interactions between bound probes, and consequently, the number of probes that can be immobilized on a surface. Researchers have found that the loading density of thiolated DNA strands on sufficiently curved gold surfaces (for spherical particles, this means having a diameter less than 60 nm) can be an order of magnitude larger than on planar surfaces.[46,47] This may be due to decreased electrostatic repulsion due to increased deflection angles between strands on smaller particles.[46,47] This theory is supported by the fact that loading density also depends on salt concentration, where an increase in salt concentrations, up to a point, results in increased loadings due to its neutralizing effects on the negatively charged phosphate backbone of DNA.

While DNA loading is increased on curved surfaces, whether the highest possible DNA probe loading also results in optimal DNA hybridization is another question. While high DNA probe loadings are important in ensuring that a high number of targets are bound to a surface through hybridization, steric and electrostatic issues also become factors. On planar surfaces, optimal probe coverage for target binding involves a balance between a high number of probes for targets to be bound to and a low enough density that steric and electrostatic issues are not a problem. Several groups have shown that high probe densities reduce hybridization efficiencies.[4-6] Irving et al demonstrated that the reduction in hybridization efficiencies that results with high probe densities can be divided into regimes based on the main mechanism of hybridization suppression: an electrostatic suppression regime at lower salt concentrations and a packing suppression regime at higher salt concentrations.[5]

Do the same crowding issues occur on non-planar surfaces? We know that curved surfaces result in increased deflection angles between immobilized strands, so it would be expected that immobilization on convex surfaces at the same “footprint” densities as on planar surfaces would result in greater spacing between the accessible ends of strands, thus reduced electrostatic and steric barriers. This phenomenon has, in fact, been demonstrated experimentally. The Kelley lab has demonstrated that detection limits are decreased by several orders of magnitude when electrochemically detecting DNA hybridization on nanostructured palladium[48-50] or gold[51-53] compared with smooth metal surfaces. Their work supported the hypothesis that the enhancement is caused by favorable geometries for hybridization (Figure 2.2) by showing that the greatest enhancements occur with fine nanostructuring (20-50 nm)—a similar length scale to the immobilized oligonucleotides (5-10 nm)[50]—and by showing that higher hybridization efficiencies occurred on nanostructured surfaces even after surface area normalization.[49]

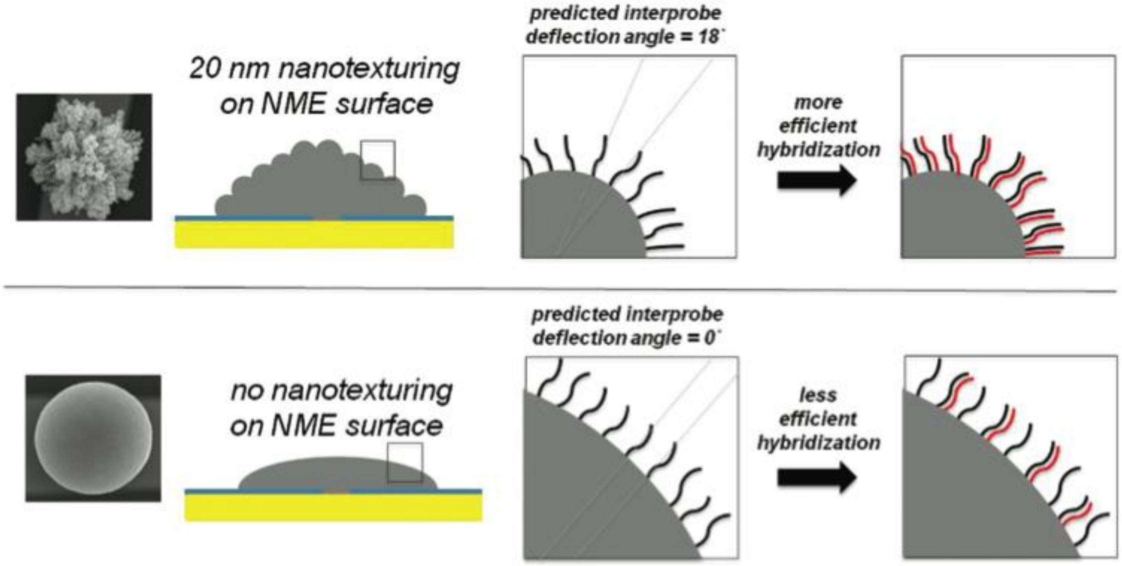

Figure 2.2: Proposed model of the effect of nanostructuring on DNA binding and hybridization. Nanostructured microelectrodes (NMEs) were used for electrochemical detection of DNA hybridization with and without nanotexturing. Reprinted with permission from ref[49]. Copyright 2010 American Chemical Society. [49]

Other researchers have also demonstrated improved surface hybridization efficiencies due to nanostructured surfaces.[1] Enhancement of electrochemical DNA hybridization sensors has been shown using dendritic gold nanostructures,[54] gold nanoflower-like structures,[55] gold-nanoparticle coated surfaces,[56] other roughened gold surfaces,[56,57] and chemical nanostructuring and sub-nanometer structuring using mixed self-assembled monolayers (SAMS).[58]

As we can see, much of the work to date involving harnessing the geometric benefits of nanostructured surfaces on DNA hybridization has involved electrochemical sensors. There is good reason to believe, though, that it would exhibit enhancements in other detection methods as well, such as optical or piezoelectric-based transduction methods, since increasing the number of species bound will increase the signal of any quantitative or semi-quantitative method.

2.3.1.2 *Proteins*

Like nucleic acids, the surface adsorption of proteins is influenced by surface nanostructuring. Unlike nucleic acids, proteins often exhibit a number of functional sites that can be bound to a surface, making control over their binding orientation both more difficult and more critical for subsequent recognition. For example, in immunosensing, involving recognition between an antibody and its corresponding antigen, it is required that the antibody be immobilized on a surface in an orientation that leaves the antigen binding site (Fab fragment) accessible.[9] It is also critical to avoid protein denaturation or conformational changes when binding proteins to a surface.[59-61] There are a number of methods that can be used to do this, as discussed already in a number of publications.[7,9,59,62] In addition to immobilization in the proper orientation, it is important to ensure that the density of bound proteins does not interfere with recognition ability. High protein densities on the surface can block the active sites of antibodies or other protein probes, preventing antigen binding.[7,8]

Surface nanostructuring can be a good way to ensure suitable binding densities and protein spacing. Work involving differently nanostructured arrays prepared by AFM nanografting of SAMs demonstrates the dependence of protein binding density and local environment on subsequent protein recognition; when arrays were designed according to the size of antibodies Fab sites, greater antibody recognition occurred[10] (proposed model in Figure 2.3). A number of methods have also successfully been used to increase recognition efficiencies, including mixed SAMs giving chemically nanostructured surfaces,[10,63,64] the use of dendrimers to create nanoscale spacing between SAMs containing active groups,[65] and nanostructured surfaces created by nanoparticle deposition.[66-68]

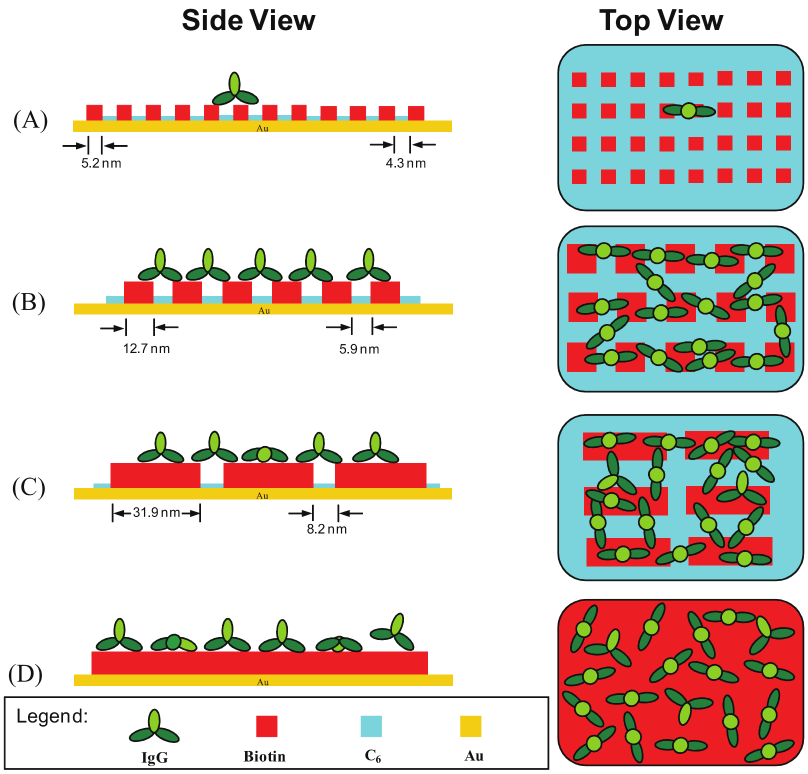

Figure 2.3: Proposed model of the effect of nanostructuring on protein-antibody (biotin-IgG) interactions. Feature sizes similar to the size of the binding domains of IgG result in higher recognition (B, C). Feature sizes that are too small prevent recognition (A) and those that are too large result in random orientations (D). Reprinted with permission from ref [10]. Copyright 2008 American Chemical Society.

Another benefit of nanostructuring is an increased surface area available for probe binding. Rusling's group claims this to be a contributing factor to the extremely low detection limits achieved in their electrochemical immunosensors featuring nanostructured surfaces using gold nanoparticles.[67,68] The effects of these two contributing mechanisms of enhancement—optimal protein density and increased surface area—can be difficult to separate, but the existing literature suggests that both play role in increasing analyte binding.

2.3.2 Enhancement of Optical Detection Methods

The plasmonic properties of gold surfaces and nanostructures have made them a major focus in current diagnostics research. Surface plasmons are electron cloud oscillations that occur at the boundary between a metal and a dielectric. Waves of surface plasmons, known as surface plasmon polaritons, can be excited by photon or electron irradiation. Surface plasmon resonance (SPR) sensing makes use of changes related to these surface plasmon waves due to analyte binding for sensing applications including food quality and safety analysis, medical diagnostics, environmental monitoring, and drug discovery.[13,69] In the case of nanosized and nanostructured materials, the surface plasmon polariton is confined to a small area, smaller than the wavelength of the incident light, resulting in a phenomenon called localized surface plasmon resonance (LSPR). The wavelength for LSPR depends, among other factors, on the size of the nanostructure; when excited, it leads to enhanced light absorption and scattering. When these types of structures are used as substrates in techniques involving light absorption and scattering, such as Raman and infrared spectroscopy and fluorescence detection, they can electromagnetically enhance the detection signal, leading to phenomena such as surface-enhanced Raman scattering (SERS), surface-enhanced infrared absorption (SEIRA), and metal-enhanced fluorescence (MEF). Another related phenomenon involves electromagnetic hot-spots created at sharp tips and in small spaces between nanostructures, nanogaps, that can enhance optical processes, further increasing the enhancements seen in SERS, SEIRA, and MEF (Figure 2.4).[33-36] While all related phenomena have been used, both independently and simultaneously in interesting biosensing methods, the focus in this work regarding enhancement of optical methods will be on methods that make use of the latter phenomena—the creation of electromagnetic hot-spots and their use in diagnostic applications.

Several other reviews cover the general topic of optical enhancement by nanomaterials for biomedical applications in more detail.[1,70,71]

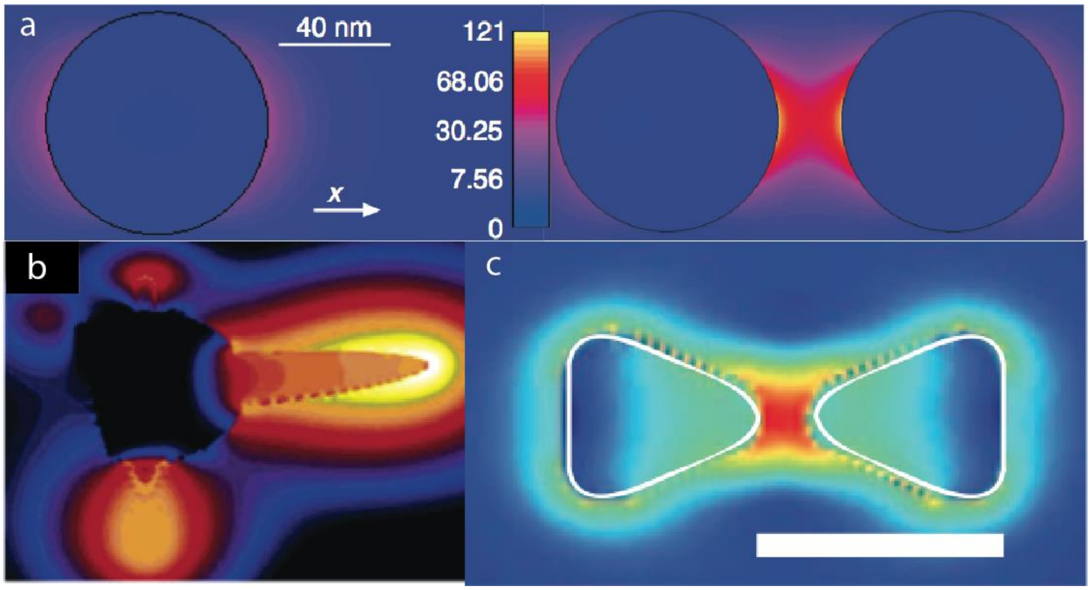

Figure 2.4: Simulations of electromagnetic enhancement at a) nanogaps[72], b) sharp tips[73], and c) combined sharp tips and nanogaps (bowtie nanoantenna)[74].

2.3.2.1 *LSPR sensors*

Localized surface plasmon resonance (LSPR) sensors offer some of the simplest set-ups in terms of optical methods making use of nanostructured surfaces. Sensing can require as little as the human eye, as is the case for colorimetric biosensing, or for more sensitive detection, a UV-visible spectrometer. LSPR sensing involves detecting changes in the refractive index, due to analyte binding, for example; a change in the refractive index causes changes in the frequencies needed for surface plasmon resonance. The greatest changes occur when binding occurs at electromagnetic hot-spots, such as nanogaps and sharp tips.[37-39]

A number of different formats have been used in LSPR sensing. Most LSPR sensors can be divided into either aggregation sensors or refractive index sensors.[34] In aggregation sensors, analyte presence induces metal nanoparticle aggregation, which results in a shift in the plasmonic peak of the particles.[75-77] In refractive index sensors, analyte presence induces a change in the refractive index of the dielectric medium at the surface of the metal, which also results in a plasmonic peak shift. A change in the refractive index at an electromagnetic hot-spot results in especially large shifts. A recent review names preferential binding to these hot-spots as the next step in LSPR research,[70] and to date, some researchers have demonstrated hot-spot enhancement by preferentially binding biomolecules to hot-spot structures. Beeram and Zamborini demonstrated this by selectively binding anti-IgG to the edges of gold nanostructures on planar surfaces; the limit of detection when anti-IgG was selectively bound to electromagnetic hot-spots was at least 500 times lower than when not bound selectively.[37] Feuz et al also demonstrated this by selectively binding proteins to the hot-spot between two nanodisks and comparing the signal with binding to single gold disks. When normalized for surface area and thus signal per molecule, the signal is greater in nanogaps than on entire disks.[38]

2.3.2.2 *SPR sensors*

Surface plasmon resonance (SPR) sensors detect changes at a metal-dielectric interface by measuring changes in the conditions required to excite surface plasmons.[69] Previous work has shown that combining planar gold surfaces with plasmonic nanostructures can result in stronger signals and higher sensitivities.[13] The enhancement is thought to be due to coupling between surface plasmon polaritons (SPP) of the planar surface and localized surface plasmon resonance (LSPR) of the nanostructures.[78,79] While the greatest improvements have been seen using gold nanostructures as labels[78,80-85] (as the presence or absence of coupling is dependent on analyte binding), modest improvements have also been observed when gold nanoparticles are incorporated into the substrate.[79,86-91] Nano- and micro-hole arrays offer another example of this coupling phenomenon.[16] Holes in gold surfaces produce localized plasmons (similar to the nanogap enhancement observed between particles) and these are coupled with surface plasmons that propagate across the sample surface.

2.3.2.3 *SERS*

Surface-enhanced Raman spectroscopy, widely known as SERS, uses electromagnetic fields in metallic nanostructures to enhance the intensity of the signal in Raman spectroscopy. SERS results in a signal enhancement of many orders of magnitude, inspiring many potential applications due to its fingerprint specificity. In the case of biosensing applications, detection could involve directly measuring the spectra of the analyte, but more often, detection involves measuring the spectra of a Raman reporter molecule combined with a metallic nanostructure; the fingerprint specificity of Raman spectroscopy allows a multiplexing approach through the use of different reporter molecules. Much of the enhancement due to metallic nanostructures is thought to be because of electromagnetic enhancements caused by SPR. To briefly discuss, incident light excites surface plasmons, creating a strong electromagnetic field on the surface. The Raman modes of molecules close to the surface are consequently enhanced. Further enhancement occurs when the Raman mode is the same as the plasmon resonance wavelength. Chemical enhancement based on the interaction between bound molecules and the metal surface is also thought contribute to the observed enhancement.[41,92]

Many different structures and set-ups have been used for SERS, ranging from the initial discovery of the phenomenon using a roughened silver electrode,[93] to spherical and anisotropic nanoparticles free in solution or deposited on surfaces, to periodic arrays of metal nanostructures.

Based on numerous experimental and theoretical studies, evidence suggests that the electromagnetic field enhancement needed for SERS is particularly prominent in two general types of nanostructures: nanogaps and sharp tips, together called hot-spots. Nanogaps as hot-spots are commonly seen when using solution-based SERS, using metallic (usually gold or silver) nanoparticles[33,94,95]. The SERS intensity varies with interparticle distance and is greatest when the particles are close together; both experimental and theoretical demonstrations of dimer plasmons show this phenomenon.[36,96-99] Nanostructures with sharp tips feature strong electromagnetic enhancement at the tip.[35,100,101] The SERS signal of molecules bound at or near the tips can be enhanced by many orders of magnitude.[17] Gold nanostars, featuring a sphere-like core and branches of various numbers and sizes, are often investigated for this purpose.[35,73,102,103]

One of the main challenges in SERS is reproducibility of the substrate. Small changes in the substrate, such as the size of or distance between nanostructures, result in large changes in signal, which makes the synthesis of reproducible substrates challenging. As this continues to be a hurdle in bringing SERS into more general use, the reproducibility issues are discussed in detail in other reviews.[41,104] While extremely high SERS enhancement has been shown—as high as 10^{14} for single molecule measurements—these enhancements can be attributed to the hot-spot phenomenon, occurring in only a small part of a measurement. When measurements are averaged over a larger area and time, enhancements tend to be on the order of 10^4 to 10^7.[41] Nanoparticle solution-based methods often suffer from low reproducibility as the presence of hot-spots requires the molecule of interest to be in a nanogap between two or more particles; well-dispersed sols therefore often show weak SERS signals.[104] A common method is to deposit the sol on a solid substrate, which results in much greater enhancements, but still suffers from reproducibility issues due to surface inhomogeneity.[41]

Using SERS substrates that make use of a sharp tip hot-spot can avoid some of these reproducibility issues resulting from the difficulty in ensuring molecules are trapped within nanogaps. Rather than immobilizing molecules in gaps between gold nanostructures, molecules can be immobilized on anisotropic surfaces. A common example of this is the use of gold nanostars for SERS. Nordlander's group modeled gold nanostars by the finite-difference time-domain method, showing that the tips generate electromagnetic field enhancements that are increased by the nanostar core, which acts like a nanoscale antenna; the resulting plasmons thus result from hybridization of the core and tip plasmons.[73] Gold nanostars show greater SERS signals than spherical gold nanoparticles due to this tip-based enhancement, without the need for particle aggregation to create nanogaps.[35,103,105,106]

2.3.2.4 *SEIRAS*

Surface enhanced infrared absorption spectroscopy (SEIRAS) is another example of nanostructured metals providing electromagnetic enhancement. The effect is similar to SERS but with enhancement occurring in the mid-infrared region and lower enhancement factors compared with SERS, on the order of 10 to 10^3.[42,43] As in SERS, nanostructured metals lead to greater enhancements, although the type of nanostructures and mechanism of enhancement differs.[107,33] Substrates that exhibit both SERS and SEIRAS—gold nanoshells, for example—can allow for the complementary use of both techniques.[33,107]

2.3.2.5 *MEF*

Fluorescent labels are the most common labels used in the life sciences for detection of biomolecules. Increasing the signal intensity of these methods would be of definite benefit. Metal enhanced fluorescence (MEF) makes use of the plasmonic properties of metal nanostructures to amplify the light emitted by fluorophore excitation. In addition to increasing the quantum yield of fluorophores, metal nanostructures can also improve the photostability of fluorophores.[44,108] As observed in other optical detection methods, fluorophore binding in electromagnetic hot-spots results in signals orders of magnitude greater than without electromagnetic enhancement.[109-111]

2.4 Types of Gold Nanostructuring

There are an extraordinary number of methods that can be used to create gold nanostructured surfaces. Nanomaterial synthesis is traditionally divided into bottom-up or top-down techniques, where bottom-up refers to building nanomaterials from smaller components and top-down refers to building nanomaterials using larger equipment to etch or deposit nanoscale features. The emphasis in this paper will be on bottom-up approaches to gold nanostructuring and hot-spot formation, which tend to take inspiration from classical chemical synthesis and less often require specialized equipment.

Different methods of biosensing will benefit from different types of surfaces. While biosensors using nanoparticles in solution have the benefit of large surface areas, planar surfaces often offer better control over signal reproducibility. In all cases, compatibility with the sensing method is the deciding factor.

2.4.1 Planar Surface Nanostructuring

2.4.1.1 *Self-assembled monolayers*

“Self-Assembled Monolayers of Thiolates on Metals as a Form of Nanotechnology”, a well-known review by Love et al of the Whitesides group,[112] excellently describes how self-assembled monolayers—SAMs—can be involved in nanostructuring surfaces. SAMs have become a necessary tool in biosensor research, with uses that include both enabling interaction of nanostructured surfaces with biomolecules and creating nanostructured domains of functional groups that can be used to selectively bind nanostructures or biomolecules directly.

Self-assembled monolayers of alkanethiols are commonly used for biomolecule attachment on sensor surfaces because they can easily be formed and their functionality can be easily controlled by choosing suitable alkanethiol head groups. By using, for example, amine or carboxylic acid head groups, proteins can be covalently bound to SAMs on gold surfaces.[11,113-117] On crystalline surfaces under controlled vacuum conditions, well-ordered SAMs form in which the molecules align due to van der Waals interactions between the hydrocarbon backbones.[112,118] On surfaces featuring deviations from perfect crystallinity—through defects or intentional nanostructuring—chains have been shown to align differently, further enhancing how a defect is “seen” by a biomolecule. Polycrystalline gold surfaces are common substrates for biosensing applications; alkanethiolate SAMs on these surfaces show areas of order and disorder, with areas of disorder often corresponding to areas of gold grain boundaries, impurities, and defects such as steps and vacancies.[112]

For certain applications, the defects can be harnessed and used to their advantage. Place exchange reactions occur more easily in these areas of disorder because of lower intermolecular interactions, allowing for chemical nanostructuring by controlling areas of order and disorder of the substrate.[112,119] Defects can also result in "cage-like" sites, meaning that a biomolecule at a defect will encounter a geometry allowing it to contact more functional groups at once.[117]

Research involving alkanethiol monolayers on gold has shown that when two or more different alkanethiols are used (different head group or alkane chain), rather than creating monolayers with an even distribution of alkanethiols, they tend to phase separate and, under certain conditions, form nanostructured domains. While precise control is difficult, the average size and number of these nanostructured domains can be controlled by changing the ratio between components in the deposition solution.[120,121]

The size of these nanostructured domains is often similar to the size of many proteins (10-50 nm^2), which makes them interesting in biosensing applications where control over biomolecule density and prevention of non-specific binding are important factors.[116,122-124] Mixed monolayers can also include diluting thiol-tagged oligonucleotides with an alkanethiol that prevents non-specific binding and increases spacing between bound DNA strands for hybridization-based sensing.[125-127]

When more precisely defined domains are desired, SAMs can be patterned using classic nanotechnology methods, such as using AFM for dip-pen nanolithography or nanografting, soft lithography methods like microcontact printing, or patterning using energetic beams.[10,64,112,119]

In addition to linking biomolecules to gold surfaces, SAMs are also used to link nanostructures synthesized separately and planar surfaces, as shown by several of the examples given in the following section.

2.4.1.2 *Nanoparticle and large molecule binding*

When nanostructures involving more than just nano-sized domains of functional groups are desired, a common method is to bind previously synthesized nanostructures to the surface. Nanostructures at similar scales to the biomolecule of interest can help control the biomolecule density. When the nanostructures are gold or another plasmonic material, they can also exhibit plasmonic enhancement effects.

Many researchers have investigated gold nanoparticles bound to gold surfaces primarily for the potential optical detection enhancement that can arise.[67,68,128,129] These surfaces have shown SPR enhancement which is the subject of a previous review.[13] The quest for reproducible SERS substrates is another application of this type of nanostructured gold surface. In this case, the goal is controlled spacing—or at least controlled average spacing—between gold nanoparticles to avoid the issues of reproducibility that plague the SERS literature. Strategies to achieve this include binding the nanoparticles to groups on a gold or other surface (often –SH or $-NH_2$).[130] The average interparticle spacing can be controlled by the nanoparticle concentration, deposition time, and other experimental factors. When averaged over a large enough laser spot size, the resulting signal can be reproducible. Very monodisperse nanoparticles will even assemble into ordered arrays with small, controlled spacing between particles that can be tuned by varying the length of stabilizing molecules.[94,131]

Other molecules on the same size scale as biomolecules can also be used to nanostructure surfaces. The primary goal in this case is for geometrical considerations—controlled spacing between biomolecules. Researchers have made nanostructured surfaces using dendrimers,[65,132] polyoxometalates,[133] TiO_2 nanoparticles,[66] and carbon nanotubes.[134]

2.4.1.3 *Nanosphere lithography*

Unlike the previously discussed approaches, nanosphere lithography is a top-down approach to nanostructuring, but one that is more easily applied in a non-specialized laboratory than traditional lithography techniques. In nanosphere lithography, a layer of near-monodisperse nanospheres is deposited on a substrate and used as a mask for further deposition or etching steps (Figure 2.5). Under the right conditions, the nanospheres will form an ordered array. The Van Duyne group first introduced this method in 1995[135] using a polystyrene nanosphere array as a mask for evaporated metal, forming nanotriangles. Later work uses the same method to prepare silver nanotriangle arrays of controlled size and spacing for LSPR[136] and SERS[137] sensing surfaces. The size and shape of the formed nanostructures can be varied by changing the size and number of layers of nanospheres used to form the mask.

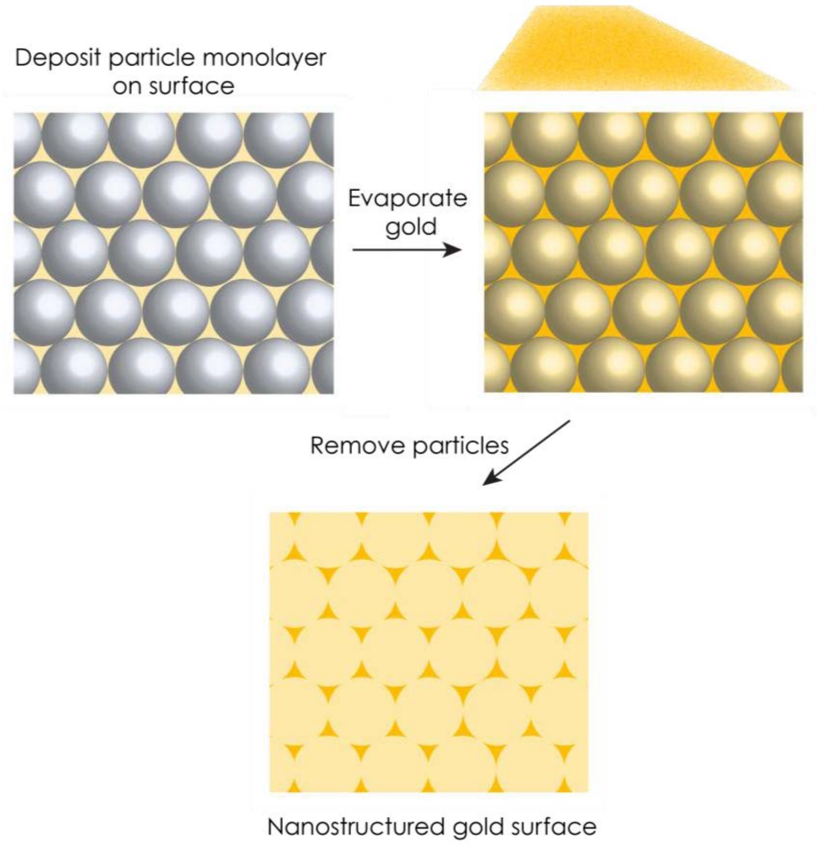

Figure 2.5: General scheme of nanosphere lithography

2.4.1.4 *Electrodeposition*

Electrochemical deposition of nanostructures on planar gold electrodes has resulted in biosensing surfaces with high sensing efficiencies.[54,57] Applying a potential to the electrode in the presence of a gold salt solution results in various morphologies of gold nanostructures (Figure 2.6). Using a similar method but with platinum instead of gold, the Kelley group was able to control the size of nanostructures on electrodes, and demonstrated that finer nanostructuring resulted in higher hybridization efficiencies of oligonucleotides.[49,50] In biosensing, this method has most often been used with electrochemical sensors where only geometrical enhancement plays a role, but in other areas, electrochemically deposited surfaces have proven to also provide optical enhancement, in their use as SERS substrates for example. Researchers synthesized dendritic gold structures[138] and nanoflowers[139] using electrochemical deposition and were able to detect rhodamine 6G at concentrations as low as 10^{-12} M. Another approach used a mask similar to that used in nanosphere lithography to synthesize organized nanoflower arrays by electrodeposition and also exhibited SERS enhancement.[140] Gold deposited in this way likely exhibits multiple hot-spots at the tips of the structures[138] as well as in nanogaps between the structures.[140] It may be of interest to further investigate the use of electrochemically synthesized gold nanostructures as templates for biomolecule detection using optical methods like SERS.

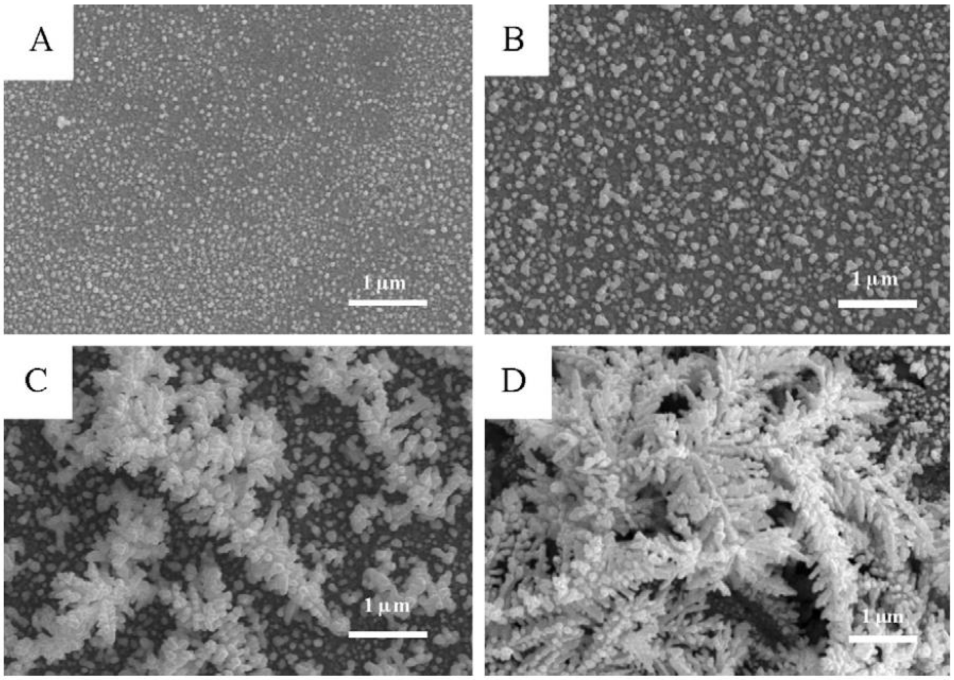

Figure 2.6: SEM images of gold nanostructured surfaces formed by electrodeposition for different times: (A) 20 s, (B) 100 s, (C) 300 s, and (D) 600 s.[54]

2.4.2 Particle Nanostructuring

2.4.2.1 *Anisotropic Gold nanoparticles*

Easily the most well known form of nanostructured gold used in biosensing applications is the gold nanoparticle. Gold sols have been used in various forms for centuries,[141] but only in the past half a century has their use in diagnostics been investigated. As the main interest lies in exploiting their size-dependent optical properties, the ability to synthesize controlled, monodisperse, stable sols is critical to their use. The most commonly used methods of synthesis involve reduction of a gold salt in the presence of a stabilizing ligand; citrate reduction of $HAuCl_4$ is useful when a loose shell of ligands is desired, and the Brust-Schiffrin method, using thiols as stabilizing ligands, is useful when more monodisperse and stable particles are needed.[142,143]

More recently, interest in nonspherical gold nanoparticles has grown, largely due to the interesting optical phenomena they exhibit. Gold nanorods, nanostars, nanocubes and other particles of different shapes and sizes (see Dreaden et al[12] for further examples) often feature multiple plasmon bands and bands that reach into NIR wavelengths. These alternative shapes, particularly those with high aspect ratio features like nanostars, can result in electromagnetic hot-spots that can enhance optical signals (as discussed in the section on electromagnetic enhancement).

The most common method used to synthesize both gold nanorods and nanostars is a seeded approach. [144-146] Gold seeds are synthesized then added to a solution containing gold salt, a reducing agent, and various shape-directing agents. Alternatively, a one-pot approach can be used in which gold nuclei form and are grown into larger structures in the same solution.[147] One common method uses an aqueous solution of ascorbic acid as reducing agent and CTAB and $AgNO_3$ as shape-directing agents. Other shape directing agents used for anisotropic gold nanoparticle synthesis include polyvinylpyrrolidone (PVP)[102,148] and 2-[4-(2-hydroxyethyl)-1-piperazinyl] ethane-sulfonic acid (HEPES) buffer.[149]

The optical properties of anisotropic gold nanoparticles, such as nanostars, have been carefully studied. Anisotropic particles often show multiple plasmon peaks, unlike single well-dispersed particles that only show a single peak,[142,150] and polarization-dependent scattering.[145,151]

In the following sections, we look at how interest has grown out of solid gold particles into particles with more complex nanostructures, featuring multiple hot-spots and multifunctionality, and their potential use in expanding our abilities to detect biomolecules.

2.4.2.2 *Gold nanoshells*

The first syntheses of gold nanoshells,[152] involving gold shells covering cores of a dielectric material, are credited to Zhou et al for their synthesis of Au_2S/Au core/shell particles[153] and later, to Oldenburg et al for their synthesis of silica/Au core/shell particles.[154] The significance of the latter synthesis was that it could be applied to particles of various sizes and compositions, thus opening up the study of the diagnostic potential of gold nanoshells. The synthesis involves binding gold seeds to a silica surface functionalized with amine groups, then adding the seeded particles to a solution containing gold salts to grow the seeds into a complete shell. By changing the core/shell ratio, the optical properties can be tuned.

In a recent work, Sauerbeck et al demonstrated that a partial shell results in greater second harmonic scattering (SHS) than a full shell, suggesting that the electromagnetic fields that lead to enhancement are greater when gold islands are present rather than a complete shell.[155] This effect may be due to the nanogaps between gold islands; as the spacing between islands decreases, the electric field in the gap increases until the gap closes and enhancement drops.

In the first cases of gold nanoshells, the core was used primarily as a template—a surface allowing for growth of a thin shell that exhibited interesting optical properties and a biocompatible surface for integration in diagnostic systems. Researchers quickly recognized, though, that using multiple materials could also be used to impart multiple functionalities. Since then, core-shell type particles with gold surfaces have been made incorporating properties such as magnetism, fluorescence, and Raman sensitivity.[156]

Multifunctional particles that include both a magnetic component and a plasmonic component have been investigated. These can be useful in situations where both particle movement and sensing are desired, such as purification and characterization of a biomolecule. Gold coating of small iron oxide particles is a common method,[157,158] since iron oxide particles less than 35 nm in diameter exhibit superparamagnetism.[159] The gold shell protects the iron oxide core and makes for simple functionalization chemistry, but more importantly, allows the particles to be used in applications that make use of the optical properties of nanogold, such as *in vivo* applications like contrast agents or applications combining magnetic separation and detection of biomolecules.

Gold shells have also been used to create nanogaps of a controlled size. Lim et al synthesized particles with a controllable interior gap by forming gold shells around gold cores using DNA to facilitate the formation of a nanogap between the core and the shell.[160] By inserting Raman dyes into the ~1 nm nanogap, the researchers achieved quantitative and controllable SERS signals.

2.4.2.3 *Anisotropic gold nanoshells*

Particles with nanostructured surfaces are a next step in gold nanoparticle and nanoshell synthesis. In this section, the focus is on anisotropic and spiky particles with cores other than single small spherical gold seeds—nanoparticles most commonly known as gold nanostars. As previously discussed, using alternative cores can infer new properties to the particles such as magnetism and fluorescence. Anisotropic shells can be formed on particles of different shapes and sizes (Figure 2.7 and Table 2.1); multifunctionality in the sense of particles with multiple size scales can also lead to interesting new properties. In general, syntheses involve growing a gold shell around a core particle using variations of methods used to synthesize anisotropic particles. These particles exhibit interesting optical properties as the anisotropic points on the particles can create electromagnetic hot-spots, as described previously.

Similar methods can be used whether the core particle is gold, iron oxide, or other. Solid gold nanostructured particles are formed by growing branched structures on gold seeds or other gold nanoparticles. Alternatively, core-shell type particles can be nanostructured by either first forming a solid gold shell around a core of another material, or by binding gold seed particles to the core particle.

The most common strategy for anisotropic, spike growth is to reduce gold salts in the presence of a structure-directing agent. One common method involves reduction of $HAuCl_4$ with ascorbic acid in the presence of CTAB and $AgNO_3$, which are involved in anisotropic structure formation. By varying the parameters, a number of different particle shapes can be formed—a similar method is in fact commonly used to form gold nanorods. Branched nanostructures are formed when the ratio of seeds to gold ions is lowered.[161]

Small iron oxide particles have been coated with gold using this method to form gold nanostars with iron oxide cores.[162-164] Synthesis typically involves forming superparamagnetic iron oxide nanoparticles, followed by either the growth of a thin gold shell or gold seeding, then growing the shell using methods similar to those used to form anisotropic gold particles. This type of synthesis was reported where the researchers formed ultrathin gold shells (<2 nm) on Fe_3O_4 nanoparticles in organic solvents, followed by anisotropic growth using a CTAB-based solution.[162,163] These anisotropic particles, with a final diameter of about 100 nm, were used for gyromagnetic imaging, which uses a rotating magnetic field gradient to vary the NIR scattering intensities; for applications such as contrast agents for biomedical imaging, this can result in images with less noise and thus better contrast.[162,163] In another example, researchers bound THPC-stabilized gold seeds to mercaptoundecanoic acid (MUA) terminated Fe_3O_4 NPs, then used the CTAB-based method to grow spiked gold nanostars with iron oxide cores.[164] The resulting particles were used as recyclable catalysts for the reduction of $K_3Fe(CN)_6$.

A CTAB-based growth method was also used to form spiky gold shells on larger particles, specifically block copolymer assemblies and polymer beads.[165,166] They first formed silver nanoparticles on the surface then used these as seeds in CTAB/Ag-solution based gold shell growth. This formed spiked shells with light adsorption reaching into the NIR range that varied with spike size. These were shown to give a single particle SERS signal with a low standard deviation compared with typical nanoparticle aggregates.

The sensitivity of the particle structure to the reagents is shown by researchers who used cetyltrimethylammonium chloride (CTAC) instead of cetyltrimethylammonium bromide (CTAB) and obtained nanoflowers with a different nanostructure than what has been seen using a CTAB-based method.[167] These gold nanoflowers were used as SERS tags in the detection of carcinoembryonic antigen (CEA) along with magnetic nanoparticles as supporting substrates.

Another procedure used to form nanostructured gold particles uses gold salts and polyvinylpyrrolidone (PVP) in DMF.[105,168-170] In this case, PVP acts as structure-directing agent and DMF is both solvent and reducing agent. The procedure has been used to grow spikes on gold nanowires,[169] gold nanorods,[105] and magnetite nanoparticles.[170] In the case of the magnetite particles, gold seeds were first grown on the surface, followed by spiked gold shell growth. All types of particles showed SERS enhancement. In the case of the gold/magnetite core-shell particles, used for protein magnetic separation, magnetically concentrating the particles led to the creation of SERS hot-spots as well.[170]

In most cases, spike growth is random and limited in the size of spikes that can be formed. Pedireddy et al demonstrated control over spike length using a PVP-based growth method on octahedral silver particles.[171] Spike length could be tuned between 10 and 130 nm by controlling the amount of gold salt and its injection rate throughout growth. Using electron energy loss spectroscopy (EELS), the researchers found that different spike lengths exhibited different optical responses.

Recent work has shown that surfactants are not necessary to form nanostructured particle surfaces. The main benefit of these methods is that the gold surface is relatively bare and can be more easily functionalized. Researchers used hydroquinone as a reducing agent to grow branches on gold seeds[172] and on gold-coated iron oxide.[173] Hydroxylamine can also act as a reducing agent in forming anisotropic particles when a shape-directing agent such as silver ions is present.[174] Another method uses triethanolamine in ethylene glycol to form clean gold nanoflowers, where the viscosity of the solution likely plays a role in directing anisotropic growth.[175]

Another approach to anisotropic particles involves controlled aggregation of small particles into larger, anisotropic clusters. One method uses HEPES buffer as a structure-directing agent.[149,176] The buffer acts as both a weak reducing agent and particle stabilizing agent, directing the growth of gold first into aggregates then into anisotropic nanoflowers. The size of the anisotropic branches can be controlled by varying the HEPES concentration. Researchers have demonstrated that the particles can act as SERS tags with signals several orders of magnitude greater than seen with spherical particles.[149] They have also been functionalized with proteins for potential use as Raman-active tags for *in vivo* applications.[176] Others have used a similar approach based on the aggregation of small particles, but used superparamagnetic iron oxide nanoparticles coated with a thin gold shell to form the nanoclusters. Hydroxylamine directs gold reduction on the surface of particles, which then cluster together into nanoroses with diameters around 30 nm.[177,178] Researchers investigated the use of these particles for potential *in vivo* applications such as imaging, photothermal therapy, and drug delivery.

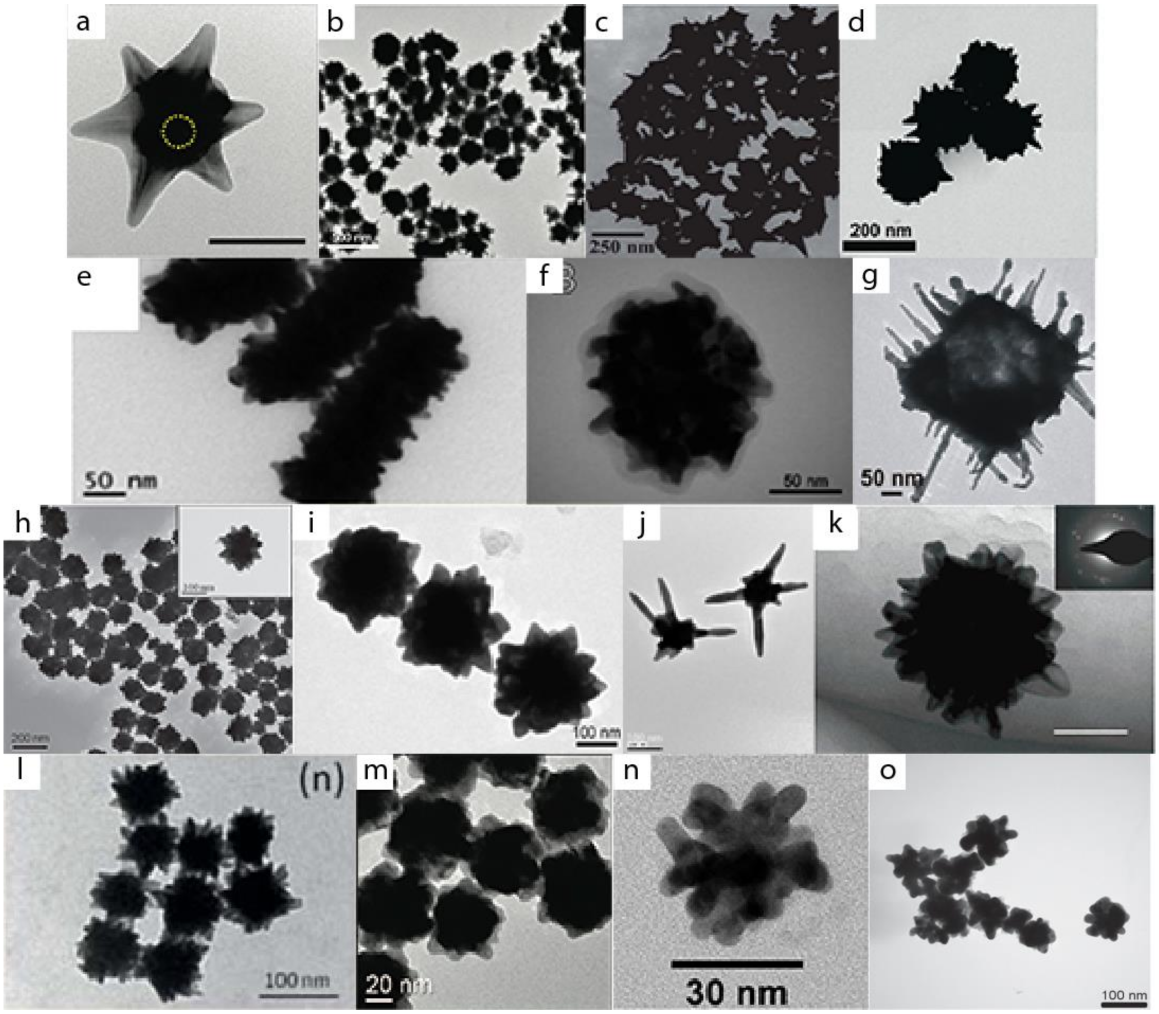

Figure 2.7: Examples of anisotropic particles from literature. Labels correspond to those in Table 2.1.

Table 2.1: Particles with nanostructured surfaces – method of synthesis and demonstrated application

	Reducing agent	Structure directing and/or stabilizing agent	Core	Demonstrated application	Reference
a, b	Ascorbic acid	CTAB and $AgNO_3$	Fe_3O_4@Au core-shell NPs	Gyromagnetic imaging	[162,163]
c			Fe_3O_4 NPs with THPC-stabilized AuNP seeds	Recyclable catalysts	[164]
d			Polystyrene beads and block copolymers with Ag seeds	SERS	[165,166]
e	DMF	PVP	AuNPs, Au nanorods, Au nanowires	SERS	[105,168,169]
f			Fe_3O_4 NPs with AuNP seeds	Magnetic separation of proteins and SERS	[170]
g	Galvanic replacement	PVP	Silver octahedral particles	Enhanced electromagnetic properties	[171]
h, i	Hydroquinone	sodium citrate	AuNPs, Fe_3O_4@Au core-shell NPs	Enhanced electromagnetic properties	[172,173]
j	Hydroxylamine	$AgNO_3$	AuNPs	Enhanced electromagnetic properties	[174]
k	Triethanolamine	Triethanolamine/ ethylene glycol	-	SERS	[175]
l	Hydroxylamine/ HEPES	HEPES	AuNPs, agglomeration based	SERS	[149]
m	HEPES	HEPES	-	non-toxic Raman tags	[176]
n, o	Dextrose/ hydroxylamine	Hydroxylamine	Fe_3O_4 NPs	Cancer cell targeting, imaging, and therapy	[177,178]

2.5 Conclusion

Nanostructured gold is a valuable tool in the detection and separation of biomolecules. Nanostructuring results in higher surface areas available for binding—a well-known fact within nanotechnology research—but biomolecules immobilized on a nanostructured surface are also recognized by a target molecule with higher efficiencies than biomolecules immobilized on flat surfaces. As gold structures decrease in size, interesting plasmonic properties also appear that enhance signals of many optical detection methods. Creating these gold nanostructures has been the subject of much creativity and effort; methods include chemical and topographical nanostructuring of planar and particle surfaces, involving nanogaps, sharp spikes, shells, and experimental and theoretical demonstrations of their use in sensing and separation of biomolecules. Despite the tremendous work in the area, challenges still remain in moving towards nanostructured gold based biosensors or particles for biomolecule separation. The reproducibility issues seen with nanostructured gold SERS substrates in particular are common to most of the quantitative detection methods presented here; good solutions use simple methods of synthesis to make nanostructures with controlled size and spacing. Nanostructured gold shells have been formed on many types of materials, including magnetic particles; in the area of biomolecule separation, nanostructured surfaces to improve analyte binding efficiencies is a potential area for future investigation. Particles that can be used as two-in-one materials for biomolecule separation and sensing are a natural extension of this idea.

Chapter 3: An Experimental and Theoretical Approach to Investigate the Effect of Chain Length on Aminothiol Adsorption and Assembly on Gold

3.1 Summary

Despite the numerous studies on the self assembled monolayers (SAMs) of alkylthiols on gold, the mechanisms involved, especially the nature and influence of the thiol-gold interface, are still under debate. In this work, the adsorption of aminothiols on Au(111) surfaces has been studied by using surface IR, X-ray photoelectron spectroscopy (XPS), as well as by density functional theory modeling (DFT). Two aminothiols were used, cysteamine (CEA) and mercaptoundecylamine (MUAM), which contain two and eleven carbon atoms, respectively. By combining experimental and theoretical methods, it was possible to draw a molecular picture of the thiol-gold interface. The long chain aminothiol produced better ordered SAMs, but interestingly, the XPS data showed different sulfur binding environments depending on the alkyl chain length; an additional peak at low binding energy was observed upon CEA adsorption, which indicates the presence of sulfur in a different environment. DFT modeling showed that the positions of the sulfur atoms in the SAMs on gold with similar unit cells [$(2\sqrt{3}\times2\sqrt{3})R30°$] depended on the length of the alkyl chain. Short chain alkylthiol SAMs were adsorbed more strongly than long chain thiol SAMs and were shown to induce surface reconstruction by extracting atoms from the surface, possibly forming adatom/vacancy combinations that lead to the additional XPS peak. In the case of short alkylthiols, the thiol-gold interface governs the layer, CEA adsorbs strongly and the mechanism is closer to single-molecule adsorption than self assembly, whereas for long chains, interactions between alkyl chains drive the system to the assembly, leading to a higher level of SAM organization and restricting the influence of the sulfur/gold interface.

3.2 Introduction

Self-assembled monolayers (SAMs) of organic molecules are molecular assemblies formed spontaneously on surfaces by adsorption and are organized into more or less large ordered domains.[112,118,179-183] SAM layers consisting of alkylthiols adsorbed on gold surfaces are widely used in applications ranging from nanostructuring[182,184] and molecular-electronics[185-187] to biosensor design[7,116,117]. In the last case, the structure and organization of a SAM layer greatly influences further biomolecule grafting and bioactivity[7,116,117], demonstrating the need to understand and master their formation. For detailed summaries of the characterization of the thiol SAM structure, we refer to references cited above and also to the works of Woodruff et al.[188,189] and a review by Vericat et al.[118] and references therein. Experimental studies showed that surface thiol species are attached to gold adatoms[190,191] and that it is the movement of these gold adatom-thiolate moieties that produce the SAM structure. Another enlightening experiment was done by Kankate et al.,[192] who proved that hydrogen was produced after aromatic thiol adsorption, providing evidence of S-H bond breaking and thiol chemisorption during SAM formation. The surface reconstruction that occurs upon gold adatom formation appears to depend on many factors including thiolate functionality and chain length. When *n*-alkanethiols, or alkanethiols terminated with small functional groups (i.e. -NH_2, -COOH, -CN) are used to form SAMs, those with longer alkyl chains consistently form more ordered layers than those formed from shorter chains.[24-27] Chains align in the same orientation due to interactions between alkyl chains; these interactions are greater between longer chains and so result in more ordered SAMs.

Despite these numerous studies, the characterization of the molecular geometry, especially at the thiol-gold interface, and the formation mechanism of alkyl thiol SAMs is far from being understood. The interface is challenging to characterize as the organic chains block access of the analyzing beam to the gold surface. A more complete strategy to characterize the gold surface at the molecular level is to combine experiments with ab intio calculations.[193-197] In the past, the effect of the tail group substitution, chain length, thiol mixtures, and surface defects were studied mainly theoretically.[193-206] To the best of our knowledge, we present herein the first molecular model of the surface reconstruction in (long and short alkyl chain) aminothiol SAM systems, in line with experimental results.

In this work, we have explored the adsorption of two amino-thiols with different chain lengths, cysteamine (CEA), with two carbon atoms, and 11-mercaptoundecylamine (MUAM), with eleven carbon atoms, on Au(111) surfaces. We combine polarisation-modulation infrared reflection-absorption spectroscopy (PM-IRRAS), X-ray photoelectron spectroscopy (XPS), and density functional theory modeling (DFT). The combined results present a new molecular picture at the molecular level of thiol-Au SAM formation highlighting the influence of chain length on the transition between simple molecule adsorption and self-assembly.

3.3 Experimental Section

3.3.1 Materials

Cysteamine (CEA) and 11-mercaptoundecylamine (MUAM) were purchased from Sigma-Aldrich (Saint-Quentin Fallavier, France). All solvents were reagent-grade. Reagents were used without any further purification. Experiments were carried out under ambient conditions. All experiments were performed on borosilicate glass substrates (11 mm × 11 mm) coated first with a 2.5 ± 1.5 nm thick layer of chromium then a 250 ± 50 nm thick layer of gold (Arrandee, Werther, Germany). These coated glass substrates were annealed in a butane flame to ensure good crystallinity of the topmost layers, then cleaned with UV-ozone and rinsed in a bath of absolute ethanol (5 mL/chip, 5 min).

3.3.2 Methods

Gold-coated sensor chips were immersed in solutions of CEA or MUAM in ethanol (1 mM, 5 mL/chip) and left covered overnight with gentle agitation. The chips were then washed once with ethanol, subjected to ultrasound for 30 seconds, and washed once again with ethanol and once with ultrapure water. The SAMs based on the two amino-terminated are shown in Figure 3.1.

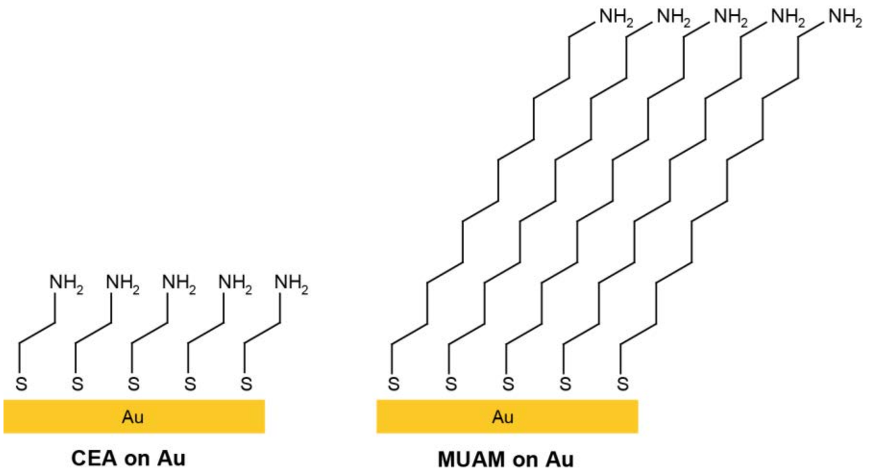

Figure 3.1: Cysteamine (CEA) and 11-mercaptoundecylamine (MUAM) SAMs formed on gold surface (schematic representation)

3.3.3 Techniques

3.3.3.1 *PM-IRRAS*

PM-IRRAS spectra were recorded on a commercial Thermo-scientific (France) Nexus spectrometer described previously.[207] The external beam was focused on the sample with a mirror, at an optimal incident angle of 85°. A ZnSe grid polarizer and a ZnSe photoelastic modulator, modulating the incident beam between *p*- and *s*-polarizations (HINDS Instruments, PEM 90, modulation frequency = 37 kHz), were placed in front of the sample. The light reflected at the sample was then focused onto a nitrogen-cooled MCT detector. The presented spectra result from the sum of 128 scans recorded with resolution of 8 cm^{-1}. The PM-IRRAS signal is given by the differential reflectivity[208,209]:

$$\Delta R/R = (R_p - R_s) / (R_p + R_s)$$

3.3.3.2 *XPS*

XPS analyses were performed using a PHOIBOS 100 X-ray photoelectron spectrometer from SPECS GmbH (Berlin, Germany) with a monochromated AlKα X-ray source (hν = 1486.6 eV) operating at P = 1×10^{-10} Torr or less. Spectra were carried out with a 50 eV pass energy for the survey scan and 10 eV pass energy for the C1s, O1s, N1s and S2p and Au4f regions. High-resolution XPS conditions have been fixed: "Fixed Analyzer Transmission" analysis mode, a 7 x 20 mm entrance slit leading to a resolution of 0.1 eV for the spectrometer, and an electron beam power of 150 W (15 kV and 10 mA). A takeoff angle of 90° from the surface was employed for each sample and binding energies were calibrated against the Au4f$_{7/2}$ binding energy at 84.0 eV. Element peak intensities were corrected by Scofield factors to calculate the atomic fractions[210]; the spectra were fitted using Casa XPS v.2.3.15 Software (Casa Software Ltd., UK) and applying a Gaussian/Lorentzian ratio G/L equal to 70/30.

3.3.3.3 *Computational details*

All geometry optimizations were performed using an ab initio plane-wave pseudopotential approach as implemented in VASP.[211,212] The Perdew-Burke-Ernzerhof (PBE) functional[213,214] was chosen to perform the periodic DFT calculations with an accuracy of the overall convergence tested elsewhere.[215-218] The valence electrons were treated explicitly and their interactions with the ionic cores were described by the Projector Augmented-Wave method (PAW)[219,220], which allows the use of a low energy cut off equal to 500 eV for the plane-wave basis. A 3 × 3 × 1 Monkhorst-Pack mesh of K-Points is used in the Brillouin-zone integration. Methfessel-Paxton order 1 smearing was used for metals. The positions of all atoms besides the two bottom layers of the gold slab in the super cell were relaxed until the total energy differences decreasd below 10^{-4} eV. The atom positions as well as the unit cell were relaxed. In a second step, the dispersion interaction energy (ΔE_{disp}) was added to the system by means of the DFT-D approach[221] as implemented in VASP, which consists of adding a semi-empirical dispersion potential to the conventional Kohn-Sham DFT energy. In particular we used the DFT-D method of Grimme[222] up to D2 corrections.

The SAMs are modeled by using a repeated slab model consisting of 4 layers representing a Au(111) surface. A (2√3×2√3)R30° unit cell is used to build the different configurations containing four thiol chains. The models count in total 100 atoms for CEA, and 208 atoms for the MUAM of which 60 atoms are gold atoms. The same unit cell has been used in the past[193,194,197] and is deduced from scanning tunneling microscopy (STM) studies. The thiols form (√3×√3)R30° and (2√3×3)rect. or c(4×2) phases. The unit cell parameter of the A (2√3×2√3)R30° unit cell used are a = 10.059 Å, b = 9.992 Å, α = 90.0°, β = 91.3°, γ = 59.6°. The Au-Au distance in the bulk structure was calculated to be 2.874 Å, which is in agreement with the experimental value of 2.88 Å.[223] These phases generally coexist in spatially-distinct domains, and switching between these phases and their relative occupation occurs rapidly through subtle changes in temperature, or perhaps even as a result of sweeping the STM tip over them (e.g. see ref. [224]). Evidently, these structural phases must have very similar energies, and switching from one to the other must involve very small energy barriers, as will be discussed below.

3.4 Results and Discussion

3.4.1 PM-IRRAS characterization of SAMs on gold surface

PM-IRRAS spectra of CEA and MUAM layers formed on gold surfaces are given in Figure 3.2. Peaks from 1650-1640 cm^{-1} can be assigned to primary amine groups in CEA and MUAM samples, specifically N-H deformation vibrations. The peak around 1550 cm^{-1} is due to the deformation vibration of protonated amine groups and a broad peak at approximately 1400 cm^{-1} can be assigned to the CH$_2$ scissor vibration.[225]

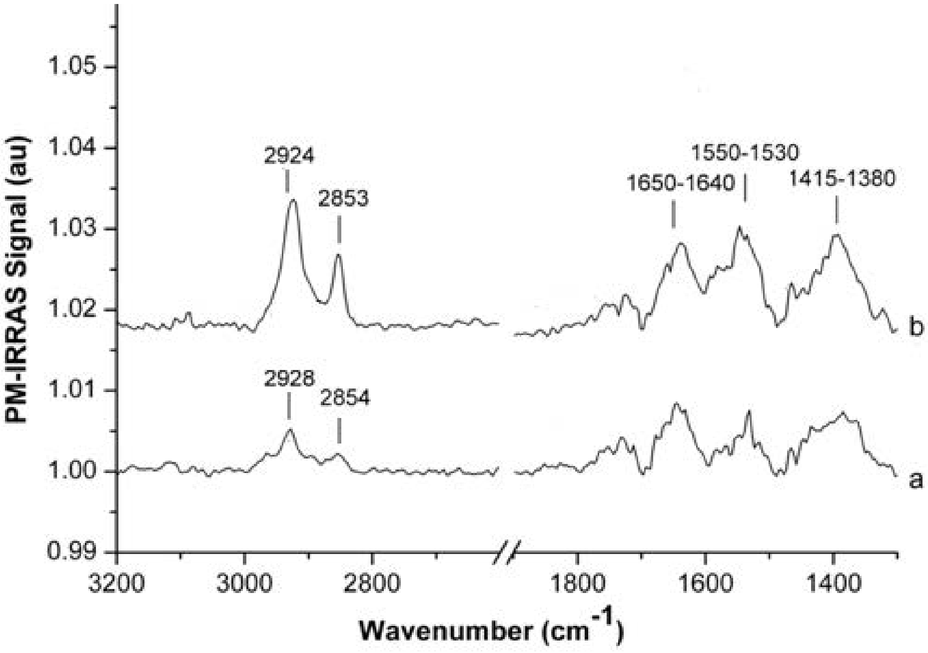

Figure 3.2: PM-IRRAS spectra of: a) Au-CEA and b) Au-MUAM

The spectra show bands in the region 2928-2854 cm^{-1} which have been assigned to the asymmetric and symmetric $\nu_{C\text{-}H}$ modes of the alkyl chains.[25,226] The intensities of the peaks of MUAM are greater than those of CEA, which correlates with the longer alkyl chains. The position of the symmetric and asymmetric CH_2 stretching bands corresponds to the order of the alkyl chains and therefore the crystallinity of a SAM, [25,226] with lower wavenumbers corresponding to a higher degree of order. As expected, the MUAM SAMs show peaks at lower wavenumbers (2924 cm^{-1} and 2853 cm^{-1}) than the CEA SAMs (2928 cm^{-1} and 2854 cm^{-1}) indicating that the long-chain layers are more ordered than the short-chain layers, which is in line with the nature of the intermolecular interactions between the alkyl chains.

3.4.2 XPS characterization of SAMs on gold surface

Both the Au-CEA and Au-MUAM systems were analyzed by XPS. In both cases the presence of gold, nitrogen, sulfur, oxygen, and carbon was observed. The presence of oxygen is probably due to contamination of the samples, which is difficult to avoid when working at a solid-liquid interface, and therefore we focused on the gold, nitrogen and sulfur components. The atomic percentages of these elements are given in Table 3.1. The Au4f signal is smaller for MUAM than for CEA due to attenuation by the longer chain. For the same reason, the N/S ratio is close to 1 for CEA, while for MUAM, the sulfur signal is attenuated by the long alkyl chain.

Table 3.1: XPS-determined atomic percentages and S2p photopeak decompositions corrected by Scoffield factors

	CEA	**MUAM**
	Atomic percentage [%]	
Au4f (%)	**52.1**	**41.5**
N1s (%)	**4.1**	**3.3**
S2p (%)	**4.0**	**1.8**
N1s/S2p	**1.02**	**1.83**
	S2p photopeak decomposition: Relative S % (absolute %)	
S-H(%)	**39.9 (1.60)**	**25.8 (0.46)**
S-Au$_{162}$ (%)	**39.4 (1.58)**	**74.2 (1.34)**
S-Au$_{161}$ (%)	**20.7 (0.83)**	——
S-Au/Au	**0.046**	**0.032**

Figure 3.3 shows the high resolution XPS spectra recorded for the S2p region for gold surfaces functionalized respectively with CEA and MUAM. For the Au-MUAM surfaces, we can observe two S2p doublets (both the $S_{3/2}$ and $S_{1/2}$ contributions) with the main signals ($S2p_{3/2}$) centered at 162.3 and 163.8 eV. The first doublet can be assigned to sulfur bound to gold surface atoms[227,228] whereas the second indicates unbound sulfur, often present despite the extensive rinsing of samples.[229,230] In the spectrum of Au-CEA, the XPS data show the same two doublets for bound and unbound sulfur atoms at 162.3 and 163.7 eV, respectively, for the $S2p_{3/2}$ contribution. In addition, a third doublet is observed at a lower binding energy of 161.4 and 162.5 eV.

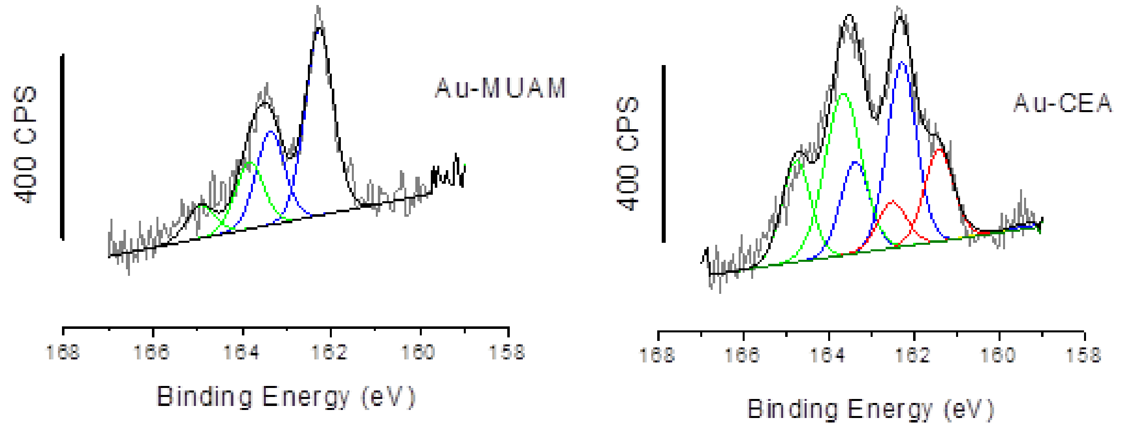

Figure 3.3: High-resolution XPS S2p region for Au-MUAM (left) and Au-CEA (right)

There is an open question in the literature regarding the assignment of this low binding energy doublet. Experimental evidence associates the peak with SAM disorder,[231-234] a claim that our results further support as the low energy doublet is only seen in the less ordered CEA SAM. Researchers have proposed that the doublet is due to a different alkanethiolate binding geometry or sulfur coordination[228,233,235-238], or atomic or oligomeric sulfur binding.[232,239,240] For CEA, this doublet has previously been assigned to multi-coordinated sulfur atoms bound to the gold surface (S-Au$_x$).[228,235] In any case, this peak corresponds to sulfur atoms with a different electronic density supporting the assumption of a different alkanethiolate binding environment (see also the theoretical results below).

The percentage of S2p components are given in Table 3.1. For CEA, the amount of physisorbed aminothiol was higher, an observation consistent with a less ordered layer. The two components at 161 and 162 eV are more informative about the SAM organization. The low binding energy contribution observed for CEA represents 34% of the total sulfur; we therefore conclude that this second environment is strongly present. We also calculated the ratio S-Au/Au, with S-Au referring to sulfur bound to gold. The S-Au/Au ratio was higher for CEA than for MUAM, which indicates that on average, more thiols in CEA are covalently adsorbed on gold than thiols in MUAM. In conclusion, a stronger and more complex S-Au surface adsorption is expected in the case of CEA.

3.4.3 DFT geometry optimizations and binding energies of the SAM systems

The DFT geometry optimization of thiol-Au SAMs systems is very sensitive due to the flat potential energy surface. The inclusion of dispersion forces improved the quality of the interaction energies, especially for the MUAM system. The final geometry for the CEA SAM was obtained from a series of geometry optimizations starting from different trial geometries. In most thiol-Au system optimizations presented so far at the DFT level, the surface geometry was treated in two different ways: 1) in many cases, the geometry was not relaxed or left unperturbed and 2) pre-incorporated reconstruction such as the inclusion of adatoms or vacancy sites in the models. It is interesting to note that in our optimization strategy we obtained a surface reconstruction without any input[196] starting from a defect free Au(111) surface. One drawback of this method is that we cannot state without any doubt that the geometry obtained is the most stable one; the calculation tools used do not allow us to scan the complete potential energy surface for every type of reconstruction, nor is it possible to include a change in the number of gold atoms in the unit cell, which may be needed to reconstruct the surface to a minimum rather than to a metastable or transition state. Nevertheless, the relaxation of the surface between two different systems, as is the case here, can be compared, and initial conclusions can be drawn and extrapolated.

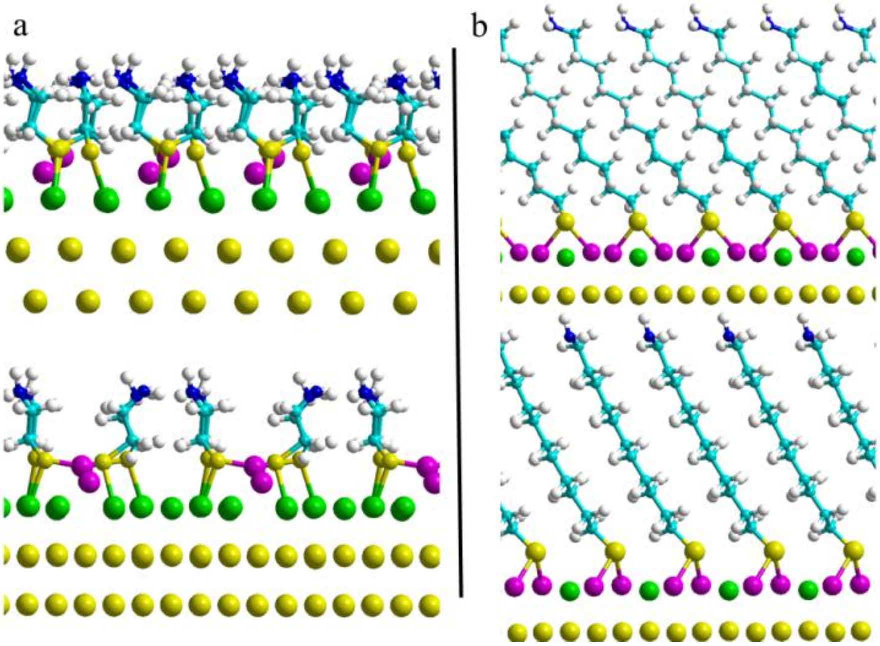

Figure 3.4: Side views of the optimized geometry of a) CEA and b) MUAM SAMs

The main result is that the two systems behave differently. The gold surface reconstructs more when CEA is adsorbed compared with MUAM. MUAM preferentially binds to a bridge site, in agreement with the literature[118], whereas CEA extracts a gold atom from the surface and resembles a precursor state of adatom adsorption. CEA interacts with one extracted gold atom, but two different orientations of the sulfur atoms are observed (See Figure 3.5). For MUAM the surface becomes wavy, as observed previously in the case of mercaptoundecanol (MUOH) SAMs.[196] Moreover, the single adsorption site corresponds to the XPS results, which indicate a single S-Au interaction.

The MUAM molecules are more ordered on the surface and show only one type of adsorption site, that resembling a bridge site (two magenta atoms), which is in agreement with earlier reports on the adsorption sites of thiol molecules on gold surfaces. In contrast, CEA molecules clearly show two different adsorption geometries (Figure 3.4a), in line with the more complex situation observed in the XP spectrum. One adatom (magenta in Figure 3.5a) accommodates two CEA molecules. The first configuration shows a CEA-Au-CEA angle (top view, Figure 3.5a) of about 180° and with the pseudo adatom less extracted from the surface and a second geometry with a

CEA-Au-CEA angle of about 60°. The coordination in the first geometry is comparable to that of the MUAM geometry, whereas the second one is different and shows a clearer adatom adsorption geometry. These two distinct adsorption geometries are seen in the XP spectra, that is, one for the MUAM SAM and two for the CEA SAM.

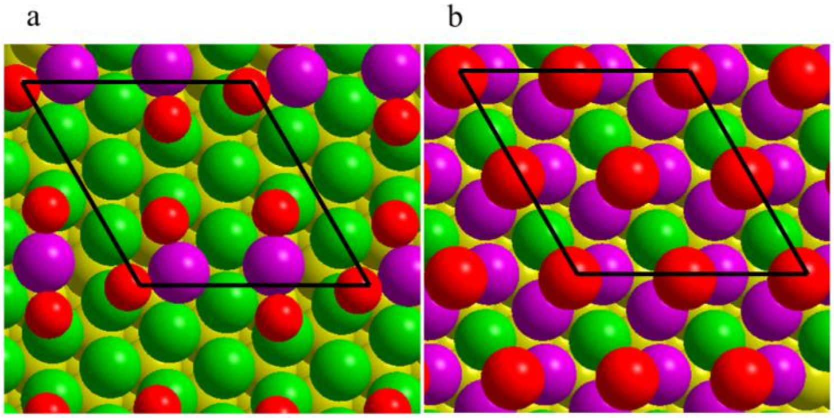

Figure 3.5: Top view of a) CEA SAM and b) MUAM SAM showing only the sulfur and gold atoms. The sulfur atom (red) on the Au surface (yellow: bulk atoms, green: surface Au atoms, magenta: surface extracted Au atoms)

As shown above, gold surface reconstruction occurs more in the formation of the CEA SAM than in the formation of the MUAM SAM. To investigate the effect on the Au-S interactions, we can visualize the gold atoms closest to the sulfur atoms. From Figure 3.6 we can see that due to the strong surface reconstruction, the sulfur atoms have been displaced more from their original position in the case of the CEA SAM. The vertical spacing between the top gold layer and the gold atom with the largest displacement from the top gold layer is 2.052 and 0.325 Å for CEA and MUAM SAMs, respectively. The second type of pseudo adatoms formed in our CEA SAM model emerges 1.294 Å out of the surface. For the MUAM SAM, with the bridge type adsorption site, the second atom raises only 0.133 Å out of the surface, which indicates a weaker interaction between the MUAM and the surface than between the CEA and the surface. This result is also reflected in the Au-S distance, which is 2.330 and 2.464 Å for CEA and MUAM, respectively. These two Au-S distances are consistent with a covalent bond distance.[241] This reorganization leads to a S/Au ratio, in which Au denotes the number of first neighbor gold atoms, that is higher for the CEA SAM than for the MUAM SAM (1.25 vs. 1, respectively), which is in agreement with the experimental XPS data (see below).

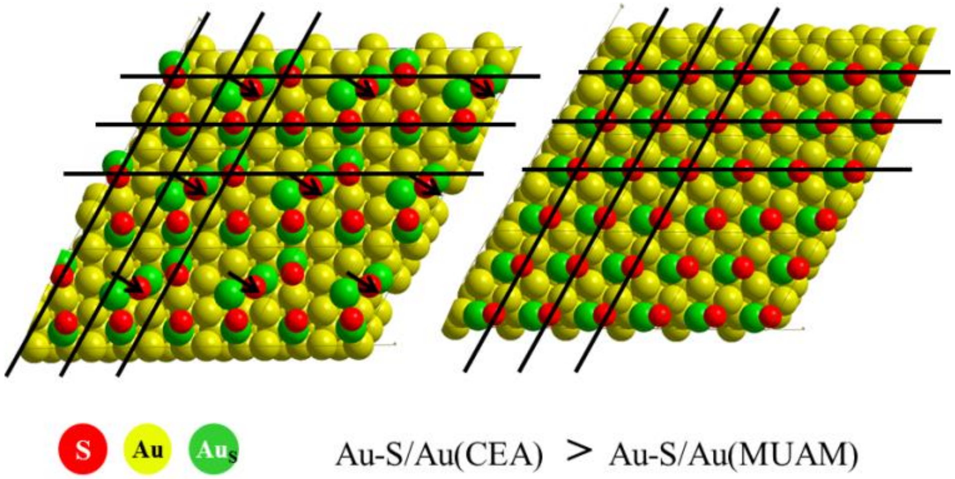

Figure 3.6: Top view of a) CEA SAM and b) MUAM SAM showing the relative displacement (arrows) of the sulfur atoms (red). The gold atoms (green) are at a distance smaller than 2.69 Å from the Sulfur atoms

Again, it should be noted that there are limitations to the reconstruction obtained with the geometry optimizations, such as the crossing of high energy barriers and the invariable number of atoms in the unit cell. It can be reasonably assumed that the reconstructions obtained after the geometry optimizations are not the final geometries, but rather intermediate ones. For example, in the case of CEA, only one gold atom of the unit cell is sufficiently extracted to alter the thiol adsorption geometry, whereas symmetrically, one can expect two, thus increasing the S/Au ratio to 1.5 for CEA.

The total interaction or binding energy ΔE_{bind} per thiol chain was calculated as follows, in which E_{SAM}, E_{thiol}, and E_{Auslab} are the electronic energies of the SAM system, the thiol radical, and the gold slab, respectively.

$$\Delta E_{bind} = (E_{SAM} - 4E_{thiol} - E_{Au_{slab}})/4$$

For CEA and MUAM, ΔE_{bind} values of -1.56 and -1.30 eV were calculated, respectively. From these data, we can conclude that the short chain CEA binds more strongly to the surface than MUAM. This result can be explained from the density of states (DOS) of alkylthiolates on gold surfaces, which was investigated in former studies.[193,242] The destabilization of the long chain thiol adsorption follows from the electron donating effect of the methylene groups through the filling of the anti-bonding orbitals of sulfur. A stronger adsorption/binding is also in line with a stronger reconstruction of the surface after binding.

3.4.4 General discussion

In agreement with the literature, the longer 11-mercaptoundecylamine molecules form more ordered self-assembled monolayers (SAMs) than the short-chain cysteamine. Previous studies have suggested that this is due to the increased interaction between the alkyl groups in the longer chains[24-27]; there is a general agreement on a minimum length of 10 carbon atoms in the alkyl chain to achieve ordered SAMs and most investigations of the chain length effect initiate at 11 carbon atoms.[26,243] In the case of the short-chain CEA SAMs, the XPS results show two environments for the binding of sulfur to gold, whereas the long chain thiol SAMs exhibit a single binding environment, that is, the well-defined bridged mode. It is interesting to note that the low binding energy doublet was also observed upon adsorbing 6-mercaptohexanoic acid on an Au(111) surface but not for the longer 11-mercaptoundecanoic acid.[27] Although several interpretations are given in the literature, we support the assignment of this peak to a different alkanethiolate binding geometry and/or sulfur coordination to gold.[228,233,235-238] In this interpretation, the S2p peak observed for both short and long alkanethiols is due to a S-Au interaction that "extracts" a gold atom from the surface thereby inducing ordered SAMs, whereas in the second mode of coordination, the sulfur atom would be surrounded by two different types of gold surface atoms (i.e. one strongly extracted and one weakly extracted), and be pulled closer to the surface.[196]

This result is supported by theoretical calculations, and is explained by the difference in intermolecular interaction forces, mainly dispersion (London) interactions, and also by the electron donating character of the alkyl chain, which destabilizes the Au-S bond. The total interaction energy can be subdivided into intermolecular interactions and binding energy. The intermolecular interactions are stronger between the long alkyl chain MUAM molecules than between the short alkyl chain CEA molecules. As a consequence, the long chains are less free or flexible and thus more ordered than the short chains, which has been observed experimentally.[118] The short chain SAMs arrange in more complex conformations and change more easily between conformations than the long chain SAMs. The long chain SAMs are thus more constrained and less able to find a conformation suited to an optimal S-Au interaction.

In contrast, because of the weak intermolecular interactions, the short chains interact more strongly with the surface. This strong interaction with the surface is observed by greater surface atom displacement, which leads to a possibly drastic reconstruction.

The presence of two different sulfur-gold interfaces for short- and long-chain molecules may be interpreted as being a result of SAM organization and intermolecular interactions. All the same, SAM organization can be driven by the sulfur-gold interface, at least for short alkyl chain thiols in which the influence of intermolecular interactions is reduced: in the adsorption of short thiols, the mechanism is closer to single molecule adsorption than self assembly, inducing a strong surface reconstruction and less-organized layers, whereas for long chains, interactions between alkyl chains restrict the influence of sulfur-gold interface and drive the system to self-assembly, which leads to a higher level of SAM organization.

3.5 Conclusions

The adsorption on Au(111) of cysteamine (CEA) and 11-mercaptoundecylamine (MUAM), aminothiols with two and eleven carbon atoms in the alkyl chain, respectively, has been studied using PM-IRRAS, XPS, and DFT methods. By combining these techniques, we propose a molecular picture of the thiol-gold surface interface. The PM-IRRAS data confirmed that long chain MUAM produces a better ordered SAM than the short chain CEA. The S2p XP spectrum shows that the coordination of sulfur is different in the two cases; although the usual thiolate-Au peak is present at 162 eV in both cases, the CEA adsorption shows an additional peak at a lower binding energy due to a second binding environment of the sulfur atoms. Adatom formation is proposed in the case of short alkyl chain thiols, but the presence of pairs of adatoms and/or vacancy sites cannot be excluded. The total adsorption energy reveals stronger adsorption of short chains (CEA) than long chains (MUAM). We have here experimental proof of the surface reconstruction of short chain SAMs and a hypothesis for the formation of the surface reconstruction based on a theoretical description. We also highlight, experimentally and theoretically, the difference between single molecule adsorption for short chains and self-assembly when the chains are enough long to drive the adsorption mechanism to self-assembly. For short chains, the resulting layers are very different from an organized SAM and this may impact the properties of the envisioned functional material.

Chapter 4: Effect of SAM chain length and binding functions on protein adsorption: β-lactoglobulin and apo-transferrin on gold

4.1 Summary

Controlled immobilization of proteins is crucial in many applications, including biosensors. Allergen biosensing, for example, requires molecular recognition of suitably immobilized proteins by specific antibodies and sensitive measurement of this interaction.

Self-assembled monolayers (SAMs), terminated by active functions, and are of great interest for the immobilization of biomolecules. The efficiency of further biorecognition involving molecules immobilized on these surfaces demonstrates an interesting dependence on the chain length and terminal function of the SAM. This motivated us to investigate adsorption of two proteins both known as milk allergens–β-lactoglobulin and apo-transferrin–on amine-terminated SAMs. We varied the chain length by using either short or long chain amine-terminated thiols (cysteamine, CEA, and 11-mercaptoundecylamine, MUAM). We also investigated the influence of the addition of a rigid cross-linker, p-phenylene diisothiocyanate (PDITC), to these amine layers prior to protein adsorption. Protein binding was studied using polarization modulation-infrared reflection absorption spectroscopy (PM-IRRAS) and atomic force microscopy (AFM) to characterize their amount and dispersion. We found that protein immobilization varies with SAM chain length and is also influenced by the presence of a cross-linker. The presence of a rigid cross-linker favours the binding of proteins on long chain SAMs, while the effect is almost nonexistent on shorter chains. In addition, the presence of the cross-linker induces a better dispersion of the proteins on the surfaces, regardless of the length of the thiols forming the SAMs. The effects of chain length and chemistry of protein binding are discussed.

4.2 Introduction

Sensitive biosensors require the sensing surface to be optimized for the binding of the bioreceptor. Alkanethiols and their derivatives form Self-Assembled Monolayers (SAMs) on a number of metals and are well-suited for this purpose due to their ease of formation, their versatile surface properties through functionalization and patterning, and their compatibility with a number of characterization techniques (including PM-IRRAS, QCM, SPR, XPS and AFM).[112,113,207,244] Thiolates on gold have been particularly valuable systems as they are simple to use, compatible with biomolecules and often already well characterized. The structure and properties of a SAM are dependent on the type (or types) of thiolate molecules used in its formation. Researchers have developed techniques to alter the functionalization of thiolate SAMs and to permit various types of interactions with biomolecules, including both resistance to and optimized control over protein adsorption,[113,124,245,246] the latter being the subject of this paper.

In addition to their tail functionality, thiolate chain length is an important factor in determining the properties of the SAM. When n-alkanethiols or alkanethiols terminated with small functional groups (i.e. -NH2, -COOH, -CN) are used to form SAMs, those with longer alkyl chains consistently form more ordered layers than those formed from shorter chains.[24] Long chains tend to align and form dense, crystalline-like arrangements, thanks to interactions between alkyl chains.

Recently, it has been shown that SAMs of thiols containing aromatic rings permits high intermolecular interactions, along with higher rigidity of the SAMs compared to alkyl-based SAMs. Though aliphatic thiols gave rise to the majority of the studies of SAM structure, more recent investigations demonstrated that aromatic chains within the ring may both increase the ordering and stability of the layer—via pi-pi interactions and cross-linking—and change the electron properties and wettability of the whole layer. [247-250]

The amount and orientation of proteins bound to a SAM depends strongly on the nature of the SAM[11,116]. The orientation of proteins on a surface determines which of their sites are accessible for binding. Control over orientation and thus subsequent accessibility is a key factor in understanding biomolecular recognition and in improving biosensor sensitivity and selectivity. This principle is most commonly employed when immobilizing antibodies, for which the F(ab')2 fragment must be accessible for binding, leaving the Fc fragment to ideally be bound to the surface[7,9]. The amount of proteins adsorbed can also influence the subsequent biorecognition reactions. Specifically, high protein binding reduces the efficiency of biorecognition reactions likely due to steric hindrance – referred to here as "crowding effects".[7,9,115,116,251]

A better understanding of these parameters when using alkylthiol SAMs to immobilize proteins, is the goal of the present work, where two proteins of different sizes, β-lactoglobulin and apotransferrin, were chosen to evaluate the influence of the SAM structure upon the recognition efficiency. β-lactoglobulin is a globular protein found in milk that has been identified as an allergen. It has a mass of 18 kDa but at physiological pH levels it is typically found in its dimerized form which measures 3.5 nm x 1.8 nm. β-lactoglobulin is an acid protein with an isoelectric point of 5.1.[252] Apo-transferrin is a glycoprotein found in blood plasma that binds to iron and controls iron levels in the body; it has also been identified as a potential allergen in milk. It is an ellipsoid protein weighing approximately 80 kDa with a size of 6.2 nm x 2.5 nm and having an isoelectric point of 5.9.[253] Besides the interest of immobilizing two proteins of different sizes, studying the recognition of their corresponding IgEs is the first step towards the development of biosensors that can be used to identify a potential milk allergy.

In this work, we immobilized β-lactoglobulin and apo-transferrin on organic thiol SAMs of different alkyl chain lengths using two different immobilization methods, *Cf.* Figure 1. SAMs of cysteamine (CEA) or 11-mercaptoundecylamine (MUAM) were formed on gold surfaces. To these surfaces, we covalently bound proteins to the terminal amine groups either directly, through activation of the acid groups on the proteins, or by attaching a rigid cross-linking group to the thiol chains that can bind the amine groups of the proteins. Protein binding was studied using Polarization Modulation-Infrared Reflection Absorption Spectroscopy (PM-IRRAS) and Atomic Force Microscopy (AFM) to characterize their amount and dispersion. We then examined protein accessibility through biorecognition by a corresponding IgG. Finally, we correlated the initial surface characteristics with protein binding and biorecognition results to better understand how SAMs of different chain lengths affect protein adsorption.

4.3 Experimental Section

4.3.1 Materials

Cysteamine (CEA), 11-mercaptoundecylamine (MUAM), p-phenylene diisothiocyanate (PDITC), *N*-hydroxysuccinimide (NHS), *N*-1-(3-dimethylaminopropyl)-*N'*-ethylcarbodiimide hydrochloride (EDC), Tween 20, β-lactoglobulin from bovine milk, bovine apo-transferrin, anti-transferrin antibody produced in chicken, phosphate buffered saline (PBS) and bovine serum albumin (BSA) were purchased from Sigma-Aldrich (Saint-Quentin Fallavier, France). Rabbit serum containing specific IgG against β-lactoglobulin (633 mg/L), was provided by the allergy research team at ESPCI/ParisTech LECA, UMR 7195. All solvents were reagent-grade. Reagents were used without any further purification. Experiments were carried out under ambient conditions.

All experiments were performed on borosilicate glass substrates (11 mm × 11 mm) coated first with a 2.5 ± 1.5 nm thick layer of chromium then a 250 ± 50 nm thick layer of gold (Arrandee, Werther, Germany). They were annealed in a butane flame to ensure good crystallinity of the topmost layers, then cleaned with UV-ozone and rinsed in a bath of absolute ethanol (5mL/chip, 5 minutes).

4.3.2 Methods

4.3.2.1 *SAMs formation and activation*

Gold-coated sensor chips were immersed in solutions of CEA or MUAM in ethanol (1 mM, 5 mL/chip) and left covered overnight with gentle agitation. The chips were then washed once with ethanol, ultrasonicated for 30 seconds in order to remove all thiol molecules not covalently bounded to the gold surfaces, then washed once again with ethanol and once with water.

For sensor chips incorporating a PDITC cross-linking group, the chips were immersed in a solution of PDITC in a 9:1 mixture of dimethylformamide (DMF) and pyridine (0.2 %w/v). After 2 hours, the chips were removed and washed once in DMF/pyridine 9:1, twice in ethanol, and once in water with gentle agitation.

4.3.2.2 *Protein immobilization*

β-lactoglobulin and apo-transferrin solutions of 50 mg/L (2.78 μM and 0.625 μM respectively) were prepared in PBS. Two different immobilization methods were used, which are shown in Figure 4.1.

Amine terminated surfaces: Immobilization by acid groups

Either β-lactoglobulin or apo-transferrin was directly immobilized on the SAMs modified surface following activation of the protein carboxylic acid groups through treatment with a solution of NHS and EDC (each at 1.2 equivalents by mass) for 2.5 hours. The proteins were then immobilized by placing a 150 μL drop on the chip surfaces and left for 1 hour. The chips were then washed twice in PBS with 0.1% Tween 20 and once in water (5 mL/chip, 5 minutes) with gentle agitation.

Cross-linker terminated surfaces: Immobilization by amine groups

For samples using surfaces incorporating PDITC, a 150 μL drop was placed on each sensor chip and left for 1 hour. The chips were then washed twice in PBS with 0.1 % Tween 20 and once in water (5 mL/chip, 5 min) with gentle agitation.

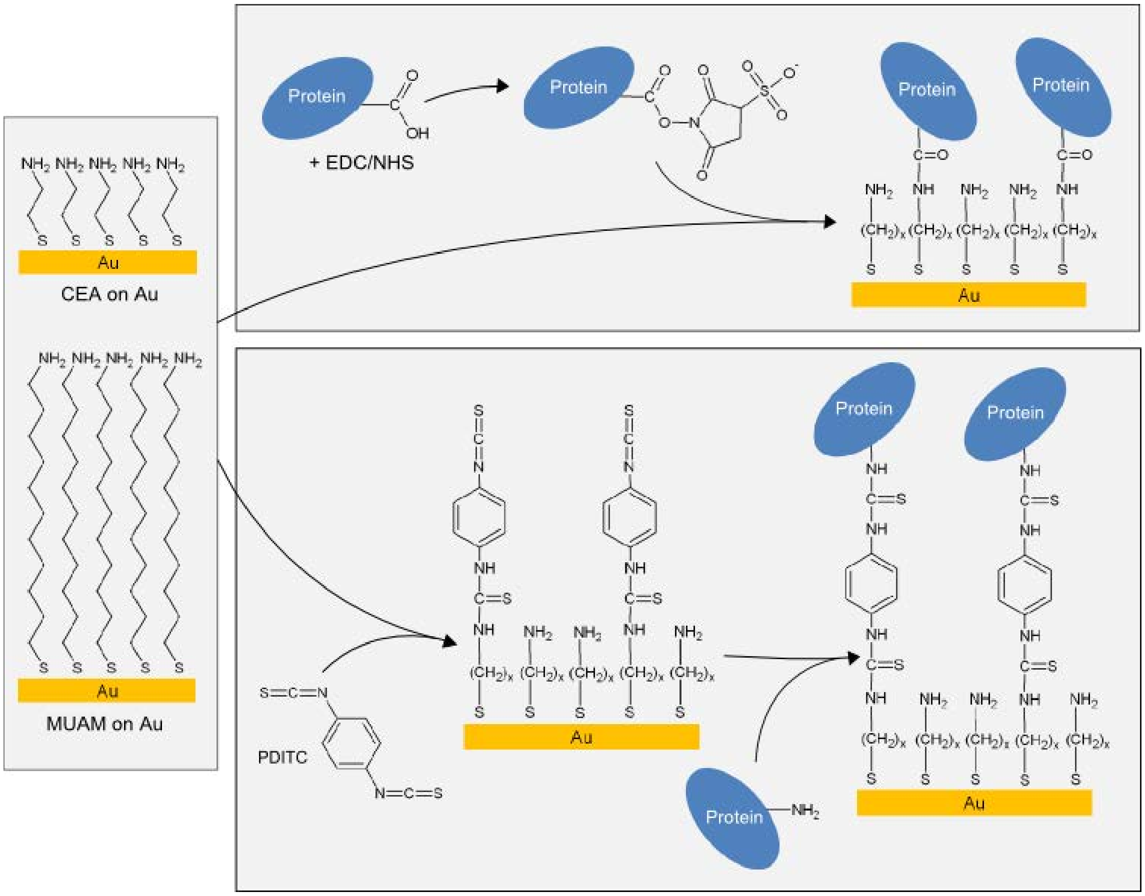

Figure 4.1: Schematic drawing of protein immobilization methods on SAMs made from amine-terminated short-chain thiols (cysteamine, CEA) and long-chain thiols (11-mercaptoundecylamine, MUAM). (Top) Immobilization on surface amine groups following EDC/NHS activation of acid groups on proteins. (Bottom) Cross-linker binding and protein immobilization by reaction with amine groups on proteins.

4.3.2.3 *Bioaffinity recognition by antibodies*

Antibody solutions were prepared at 1/50 dilutions in PBS, resulting in a concentration of 12.7 mg/L (133 nM) and 20 mg/L (84 nM) for β-lactoglobulin and apo-transferrin antibodies respectively. A 150 μL drop was placed on each sensor chip and left for 1 hour. The chips were then washed twice in PBS with 0.1% Tween 20 and once in water (5 mL/chip, 5 minutes) with gentle agitation.

4.3.3 Characterization techniques

4.3.3.1 *PM-IRRAS*

Polarization Modulation-Infrared Reflection Absorption Spectroscopy (PM-IRRAS) spectra were recorded using a commercial THERMO Nexus 5700 spectrometer. The external beam was focused on the sample with a mirror at an optimal incident angle of 85°. A ZnSe grid polarizer and a ZnSe photoelastic modulator, modulating the incident beam between p- and s-polarizations (HINDS Instruments, PEM 90, modulation frequency = 37 kHz) were placed prior to the sample. The light reflected at the sample was then focused onto a nitrogen cooled MCT detector. The presented spectra result from the sum of 256 scans recorded with 8 cm^{-1} resolution. The PM-IRRAS signal is given by the differential reflectivity,

$$\frac{\Delta R}{R} = \frac{R_p - R_s}{R_p + R_s}$$

Results given represent an average of two to four measurements and error values are given as the standard deviation to give an idea of variability between measurements.

4.3.3.2 *AFM analysis*

AFM images were recorded using a commercial AFM (NanoScope 8 MultiMode AFM, Bruker Nano Inc., Nano Surfaces Division, Santa Barbara, CA) equipped with a 150 × 150 × 5 µm scanner (J-scanner). The substrates were fixed on a steel sample puck using a small piece of adhesive tape. Images were recorded in peak force tapping mode in air at room temperature (22-24 °C) using oxide-sharpened microfabricated Si_3N_4 cantilevers (Bruker Nano Inc., Nano Surfaces Division, Santa Barbara, CA). The spring constants of the cantilevers were measured using the thermal noise method, yielding values ranging from 0.4 to 0.5 N/m. The curvature radius of silicon nitride tips was about 10 nm (manufacturer specifications). All images shown in this paper are flattened data using a third-order polynomial built-in the Nanoscope Analyse software v. 1.30 also provided by Bruker Nano Inc..

4.4 Results

4.4.1 SAM formation and cross-linker binding

Self-Assembled Monolayers (SAMs) based on two types of amine-terminated alkanethiols with different chain lengths, cysteamine (CEA) and 11-mercaptoundecylamine (MUAM), were formed on gold surfaces. For samples on which proteins were to be immobilized by their amine groups, a cross-linking group was bound to the amine-terminated thiols (Figure 4.1). The surfaces were characterized by PM-IRRAS.

4.4.1.1 *PM-IRRAS characterization*

The PM-IRRAS spectra of layers of CEA or MUAM formed on gold surfaces are given in Figure 4.2. The spectra show several bands in the 2928-2854 cm^{-1} region, assigned to the asymmetric and symmetric νC-H modes of the alkyl chains.[25,225] The peak intensity for the MUAM samples is greater than that of CEA, which correlates with the longer chain length. Others have shown that the position of the symmetric and asymmetric CH_2 stretching bands is indicative of the order and therefore crystallinity of a SAM,[24,25,250] with lower wavenumbers corresponding to a higher degree of order. As expected, MUAM SAMs show peaks at slightly lower wavenumbers (2924 cm^{-1} and 2853 cm^{-1}) than CEA SAMs (2928 cm^{-1} and 2854 cm^{-1}) confirming that the long chain layers are better ordered than the short chain layers.

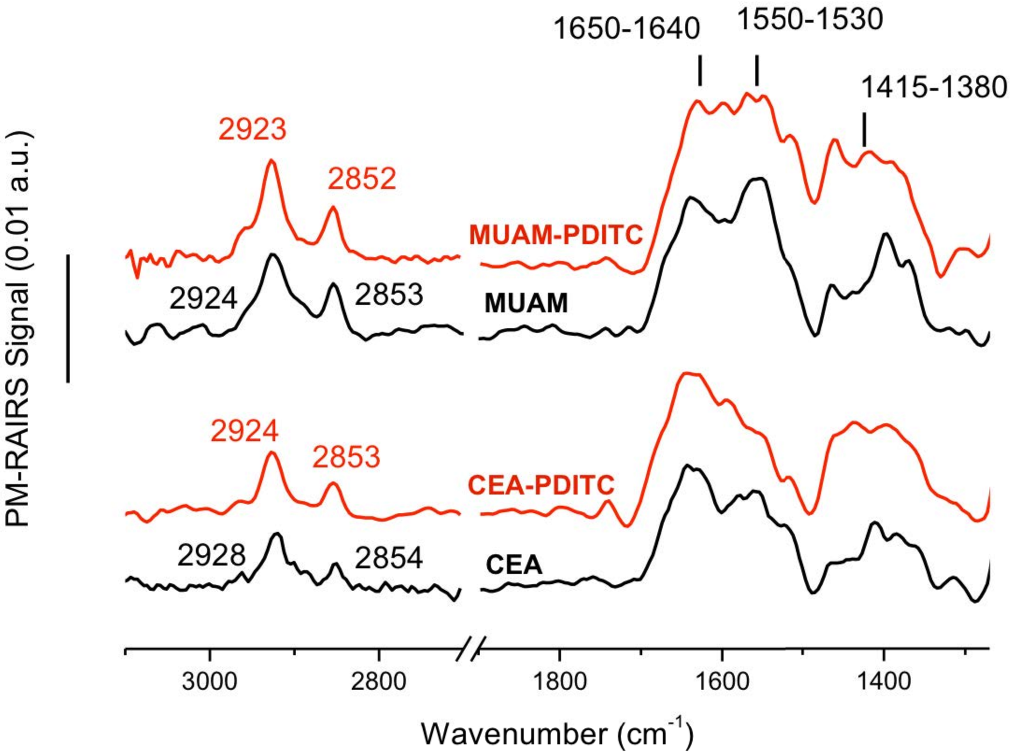

Figure 4.2: PM-IRRAS spectra of Au-CEA, Au-CEA after PDITC binding, Au-MUAM and Au-MUAM after PDITC binding.

Upon PDITC binding, a slight shift of the symmetric and asymmetric CH_2 stretching bands to lower wavenumbers appears on both long and short chain surfaces indicating an increase in chain order. This effect is more pronounced for the CEA layer where, after PDITC binding, the C-H asymmetric stretch band shifts from 2928 cm^{-1} to 2924 cm^{-1}. The orientation of PDITC on the surface may allow intermolecular interaction via pi orbitals and/or potentially add rigidity to the structures leading to improved ordering.[250,254,255]

On CEA and MUAM spectra, bands in the lower wavenumber region at 1650-1640 cm^{-1} can be attributed to the N-H deformation vibration, thus confirming the presence of primary amine groups. The peak around 1550 cm^{-1} may be due to the deformation vibration of protonated amine groups. A peak at about 1460 cm^{-1}, more present on the MUAM spectra than on the CEA spectra, can be assigned to the CH_2 scissor vibrations.[225]

Following PDITC addition, the peak intensities in this region slightly increase; in particular, the band at 1650 cm^{-1} increases, which may be due to the imine C=N stretch of the unreacted isothiocyanate of PDITC, or to remaining primary amine groups due to incomplete cross-linker binding. The intensity increase in the 1380-1450 cm^{-1} region may be due to –N-C=S groups of PDITC.[225,256]

4.4.2 Protein immobilization

Apo-transferrin and β-lactoglobulin binding was then studied by PM-IRRAS and AFM. For covalent binding on amine-terminated surfaces (CEA or MUAM without cross-linker), the acid groups on the proteins were activated in an EDC/NHS solution, then allowed to bind to the surfaces, while on surfaces bearing the PDITC cross-linker, proteins in a buffered solution were dropped on the surfaces for reaction by their amine groups (Figure 4.1). After protein binding and characterization, biorecognition of the corresponding rIgG antibodies was monitored by PM-IRRAS.

4.4.2.1 *PM-IRRAS characterization of the protein layer*

Protein binding was evidenced by the presence of intense bands at 1660 cm^{-1} and 1550 cm^{-1}, attributed to amide I and amide II vibrations respectively; see all spectra labeled (a) on Figure 4.3 for β-lactoglobulin binding (spectra following apo-transferrin binding are in Appendix A). Comparing band areas provides semi-quantitative information on the amount of bound proteins on the different surfaces.[7] The changes in peak areas are given in Table 4.1.

The amount of bound β-lactoglobulin varied with chain length. Binding was 60% less on MUAM compared with CEA. However, when a cross-linker was added, binding on MUA increased leading to an amide band area about 60% larger on long than on short chains. On CEA, adding a cross-linker led to a slight decrease in the amide band area, while on MUAM, the same treatment resulted in a signal about two times greater.

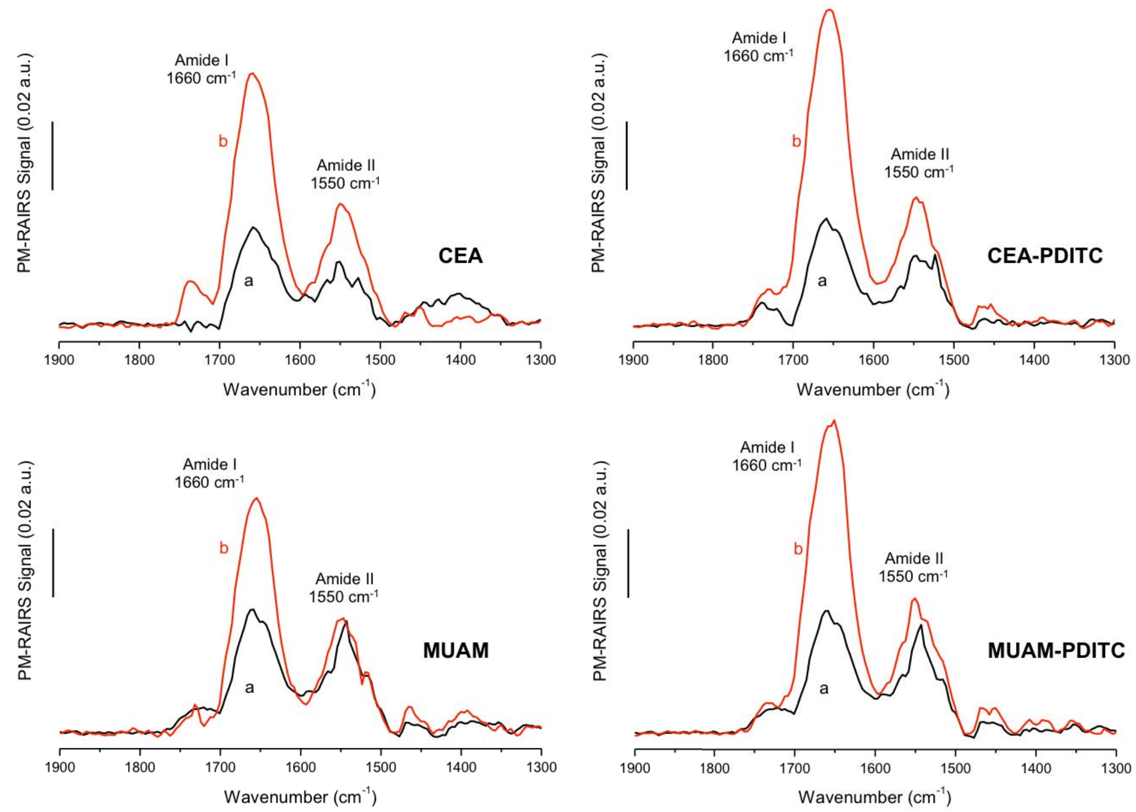

Figure 4.3: PM-IRRAS spectra after β-lactoglobulin (a) and antibody recognition (b) on CEA, MUAM, CEA-PDITC and MUAM-PDITC.

Table 4.1: Change in area of amide I and II (1660 cm^{-1} + 1550 cm^{-1}) peaks from PM-IRRAS following binding and ratio of bound antibodies to corresponding proteins adjusted for mass (errors correspond to standard deviation from measurements of two to four separate chips).

	Surfaces without cross-linker		**Cross-linker terminated surfaces**	
	CEA	MUAM	CEA	MUAM
β-lactoglobulin binding	2.5 ± 0.1	0.9 ± 0.2	2.3 ± 0.2	3.5 ± 0.3
Anti-β-lactoglobulin binding	4.6 ± 0.2	5.2 ± 0.2	4.9 ± 0.2	7.5 ± 0.3
Ab/Pr (adjusted for mass)	0.22	0.70	0.26	0.26
Apo-transferrin binding	2.8 ± 0.2	1.7 ± 0.2	2.7 ± 0.2	4.7 ± 0.4
Anti-transferrin binding	0.7 ± 0.1	1.4 ± 0.1	1.1 ± 0.1	1.9 ± 0.1
Ab/Pr (adjusted for mass)	0.12	0.50	0.20	0.22

Similar trends occurred upon transferrin binding—see Figure S1 and Table 4.1. The amide band area following transferrin immobilization was 40% lower on MUAM compared to CEA without cross-linker, but adding a cross-linker led to an increase in protein binding on long chains, the amide band area being multiplied by a factor of three, while the signal hardly changed on short chains (only a 7% decrease) following cross-linker addition.

4.4.2.2 *AFM characterization of the protein layer*

The dispersion of proteins on the different surfaces was investigated by AFM.

Figure 4.4 shows β-lactoglobulin immobilized on the four different surfaces, each at two different length scales (10 μm x 10 μm and 1 μm x 1 μm). On both short and long chain amine-terminated thiol surfaces, β-lactoglobulin was found to preferentially bind to the edges of terraces forming thick lines. The smaller scale images (lower inserts of Figure 4.4) show that some binding occurs on the terrace surfaces, but without forming a homogeneous layer. On the cross-linker terminated surfaces, for both CEA and MUAM layers, the dispersion was improved and protein binding preferentially occurred on the terrace surfaces. The dispersion on cross-linker terminated long chains appeared more homogeneous than on cross-linker terminated short chains. At the larger scale, agglomerates on the order of several hundred nanometers can be observed on the CEA-coated surfaces with or without using a cross-linker.

AFM data of apo-transferrin on the various surfaces (shown in the supplementary material section, Fig S2) present the same tendencies as β-lactoglobulin. On amine-terminated surfaces, apo-transferrin preferentially binds at the edges of the gold terraces, particularly on long chain-coated surfaces where clear protein lines appear along terrace edges. When using a cross-linker to bind apo-transferrin, binding preferentially occurs on the terraces, thus leading to a more homogeneous protein layer.

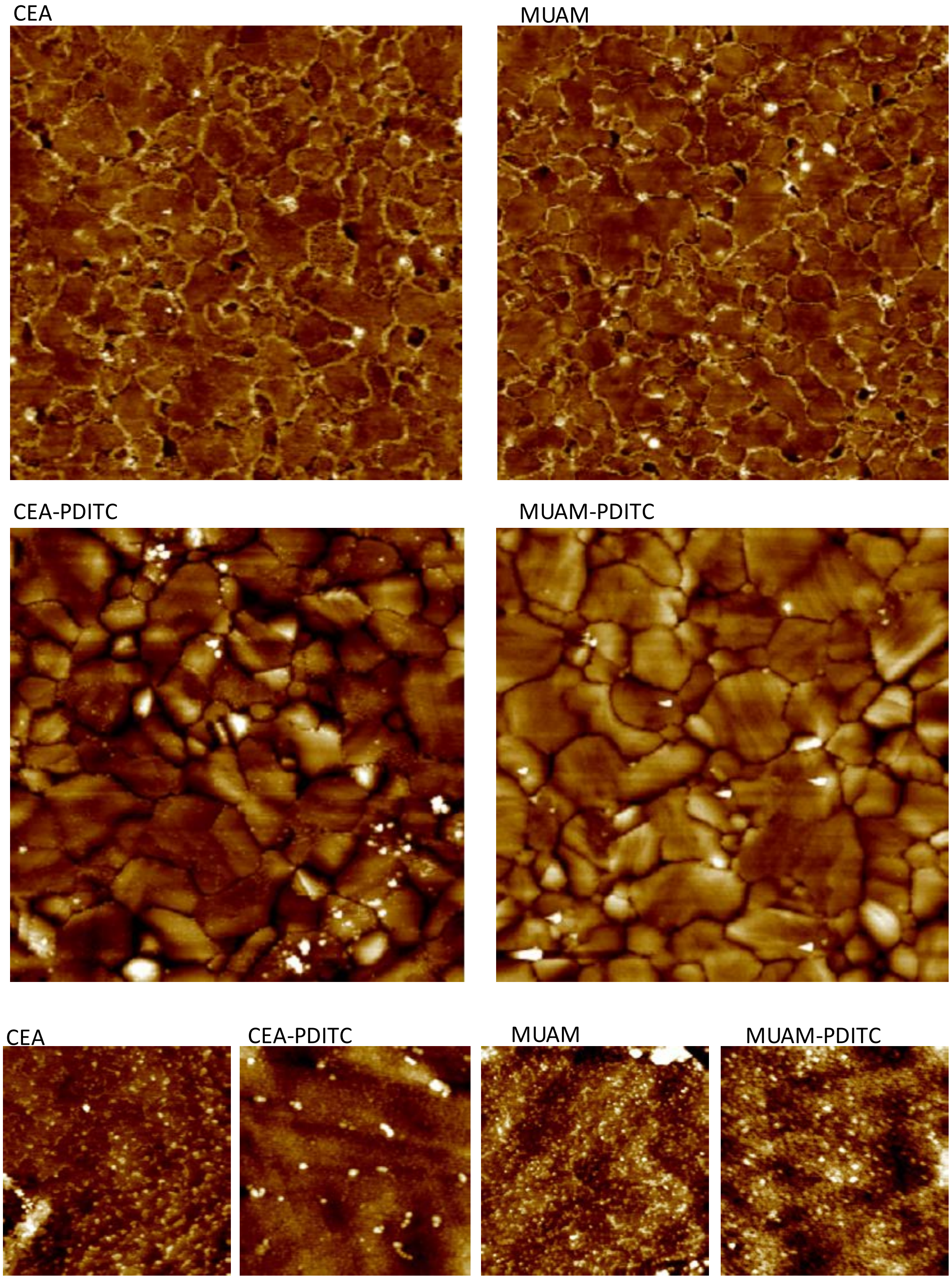

Figure 4.4: AFM images of gold-coated substrates following SAM formation and β-lactoglobulin binding. Upper images: Scan area: 10 μm x 10 μm, height scale: 40 nm. Lower images: Scan area: 1 μm x 1 μm, height scale: 10 nm.

When comparing the CEA-PDITC and MUAM-PDITC layers, one observes some agglomerates on the short chain layer while very few appear on the long chain layer.

Irrelevant of protein type, a better dispersed layer results on SAMs incorporating a PDITC cross-linker than on amine-terminated SAMs.

4.4.2.3 *Biorecognition by specific antibodies*

Antibody recognition of the proteins was monitored by measuring the changes in the amide I and II bands. Results are shown in Figure 4.3. A useful metric to compare biorecognition on different surfaces is the ratio between IR areas after antibody and protein binding, adjusted for the appropriate molecular masses (see last line of Table 1).

The amide band areas suggest that anti-β-lactoglobulin and anti-transferrin binding was higher on MUAM than on CEA, without cross-linker. The values observed on MUAM without cross-linker are very high, but likely due to non-specific physisorption of antibodies because of abnormally low protein coverage. In all other cases, the Ab/β-lactoglobulin ratio appears to be almost constant, ≈ 0.2, no matter the length and terminal function of the SAM; a slight enhancement is observed on CEA when adding the cross-linker.

Upon anti-transferrin binding on amine-terminated surfaces (without cross-linker), the amide band area was higher on long than on short chains and also higher in the presence of a cross-linker. The difference due to chain length was lower when a cross-linker was added. Note again that the difference in binding efficiency with a cross-linker was small—only 20% lower on long chains compared with short chains.

To summarize, recognition efficiency between anti-transferrin and transferrin, or anti-β-lactoglobulin and β-lactoglobulin, followed similar trends. On long chains, binding efficiency values were three times greater than on short chains without cross-linker, but this is likely due to non-specific physisorption; once a cross-linker was added, we observed almost no change (about 5%). Again, it is remarkable to observe an almost constant protein-antibody ratio on most SAM layers and for the two proteins.

4.5 Discussion

In this study, we investigated the adsorption of two proteins–β-lactoglobulin and apo-transferrin, mainly differing by their sizes—on two amine-terminated SAMs built from short chain cysteamine (CEA) and long chain 11-mercaptoundecylamine (MUAM) amine-terminated thiols. Two immobilization methods were used to attach proteins to the surfaces: a direct binding to the terminal amine functions, after activating the acid groups of protein in solution, and a binding through the addition of a rigid cross-linker (PDITC), that reacts with the amine groups of proteins. Although the studied proteins were very different in size, the same trends were observed. The influence of the chain length on the amount of adsorbed proteins was very dependent on the method of immobilization.

When proteins were bound via their acid groups directly to the SAMs, through activation in solution of their acid groups, the adsorption on CEA short chains was favoured for both β-lactoglobulin and apo-transferrin. Interestingly, AFM images showed that a non-negligible part of adsorbed proteins were located in the defects on the gold grain boundaries. We previously observed preferential adsorption of β-lactoglobulin in these cracks suggesting that the presence of multiple amine groups around the protein favours its grafting through acid functions.[257] Indeed, Love et al. showed that these defects display many functional groups, which can constitute a kind of "cage" (Figure 7 in ref 1). These groups may thus offer the protein multipoint binding to the surfaces explaining the high density in proteins around these defects. Moreover, as the long chains are more ordered than the short ones (see IR data), proteins are preferentially adsorbed on planar gold terraces rather than in the defects on the gold grain boundaries. Thus, fewer multipoint binding sites would be available for protein grafting. This difference may explain the lowest amount of protein adsorbed on long chain MUAM compared to the short CEA.

When proteins were bound via their amine groups through the addition of a rigid cross-linker, PDITC, adsorption on long MUAM SAMs was favoured for both proteins. In this case, the terminal groups of proteins involved in the binding are amine rather than the acid ones reacting in the previous case. The AFM investigation of protein adsorption showed another interesting difference—the absence of proteins in the defects on the gold grains boundaries. Similar trends were observed previously upon studying β-lactoglobulin grafting via its amine groups on mercaptoundecanoic acid SAM (see figure 2 in Thébault et al[257]). We may thus assume that proteins linked through their amine functions do not react with these cage-shaped binding sites, but more likely with sites consisting of planar terminal reactive functions. Furthermore, this planar geometry for protein amine groups' binding sites is consistent with the higher adsorption on long and better-ordered MUAM SAMs.

Studying the molecular recognition of immobilized proteins by specific antibodies was not very informative when proteins were bound via their acid groups on amine terminated SAMs; the results were affected by the low protein coverage. When the proteins were immobilized on the cross-linker- terminated surfaces, the protein-antibody ratio for β-lactoglobulin was remarkably close for both proteins, and almost constant on the two chain length thiols. This low variability suggests similar orientations of proteins on short CEA and long MUAM chains. In conclusion, the SAM length seems to affect the amount of adsorbed proteins, offering a higher density of binding sites on short chains when proteins are immobilized through their acid groups, while a higher density is observed on long chains when protein immobilization is carried out through their amine groups. Regarding the orientation and accessibility of protein layers, no impact of SAM length was observed; the nature of the chemical groups involved in the interaction rather governs the recognition. One interesting perspective to this work would be the investigation of grafted protein orientation using ToF-SIMS. This technique has already been used to determine the orientation of physically adsorbed β-lactoglobulin on amine and alkyl terminated SAMs.[11] This work suggests that, in the case of β-lactoglobulin adsorption on amine-terminated surfaces, binding may occur between the surface amine groups and activated glutamic acid groups found in the Glu-Asn-Gly-Glu sequences of the protein. Future work would involve further analysis of the orientation of grafted proteins and correlation to molecular recognition by specific antibodies.

4.6 Conclusion

We investigated the adsorption of two proteins both known as milk allergens—β-lactoglobulin and apo-transferrin—on amine-terminated SAMs. Two different SAMs were built by using either short or long chain amine-terminated thiols (cysteamine, CEA, and 11-mercaptoundecylamine, MUAM). Two binding modes were explored for each of these SAMs: amide binding through the activation of protein acid groups, and reaction with the amine groups of protein upon addition of a cross-linker, p-phenylene diisothiocyanate (PDITC). The same tendencies were observed for both proteins: protein immobilization varied with SAM chain length and with the presence or absence of a cross-linker. When proteins were bound via their acid groups, adsorption was favoured on CEA short chains in cage-like binding sites. Conversely, when proteins were bound via their amine groups, adsorption was favoured on long MUAM SAMs and the binding sites seemed to consist of planar terminal reactive functions. We assessed the molecular recognition of immobilized proteins by specific antibodies and observed no influence of SAM length on the orientation and accessibility of proteins; rather, the nature of the chemical groups involved in the interaction played a larger role in their recognition.

Chapter 5: Synthesis and characterization of nanostructured gold coatings on magnetic particles

5.1 Summary

Multifunctional micro- and nanoparticles have potential uses in advanced detection methods, such as combined separation and detection of biomolecules. Magnetic separation is commonly used to separate biomolecule analytes from complex environments. Combining this with the ability to detect the presence and/or nature of the analyte has potential applications in simplifying analyses. In this work, we synthesized nanostructured gold shells on magnetic particle cores and demonstrated the use of them in surface-enhanced Raman scattering (SERS). Nanostructured gold has interesting optical properties that can be harnessed to enhance optical detection methods. To grow the gold shells, gold seeds were bound to silica-coated iron oxide aggregate particles with different functional groups on the surface; an aqueous cetyltrimethylammonium bromide (CTAB) based method was then used to grow the seeds into spikes. We demonstrated that the particles showed SERS enhancement in the detection of a model Raman probe molecule, 2-mercaptopyrimidine, on the order of 10^4. We compared different types of gold shells, including spiky and bumpy shell morphologies, to determine what characteristics of the shell leads to the highest SERS enhancements. We found that while spiky shells lead to greater enhancements, their high aspect ratio structures are less stable and morphological changes occur more quickly than observed with bumpy shells.

5.2 Introduction

Micro- and nanoparticles are becoming key components in advanced detection methods, including applications in disease diagnosis, environmental monitoring, and as tools in research labs.[258,259] Their small size offers a large surface area for interaction with the molecule or biomolecule of interest—a clear advantage when it comes to detecting small concentrations. Multifunctionality is a key concept in many of these pursuits; when a single particle can perform multiple tasks, we can better tailor particles to a specific application. Particles used for detection enable an observable signal when a molecule is at or near the particle surface. Optical transduction methods that make use of size-specific properties of micro- and nanoparticles are commonly used; examples include measuring the interaction between light, particles, and adsorbed molecules (SERS, SEIRAS), measuring refractive index changes that occur in the presence of molecules (SPR and LSPR), and making use of fluorescent markers. Much of the time, the analyte of interest is in a complex physiological or environmental fluid and separating them out is advantageous or necessary for signal transduction. Magnetic particles can be used to separate out an analyte by specifically binding it to their surface. Drawing on the concept of multifunctionality leads to the idea of combining magnetic separability with optical transduction to design particles for combined separation and sensing.

Magnetic particles for separation of biomolecules and other molecules have benefits in laboratory and clinical diagnostics including a simple and inexpensive set-up (typically requiring only the particles themselves and a magnet), no extensive technical training, and result in highly sensitive and selective separation.[260] Superparamagnetic particles are considered optimal since they only exhibit magnetic properties while under the influence of a magnetic field. They will remain dispersed when added to a sample, allowing the analyte to freely bind to the surface, but will be separated when a magnet is used.[261,262] Superparamagnetic properties are typically exhibited in small nanoparticles, i.e. Fe_3O_4 particles must be less than 30 nm to be superparamagnetic,[263,264] but separation of these small particles, especially once coated, can be prohibitively slow.[265,266] Our approach to magnetically separable particles, outlined in previous work,[267] uses controlled aggregates (150-300 nm) of superparamagnetic nanoparticles (~20 nm) to increases the total magnetic moment while still maintaining the superparamagnetic properties of the particles. Since the end result of magnetic separation is that the analyte of interest is specifically bound to the particle surface, a surface-sensitive detection method partners well with magnetic particles.

Optical surface-sensitive characterization methods take advantage of certain metal structures—nanostructures, in particular[1,17,141]—to alter optical signals upon biomolecule binding through electromagnetic enhancement or plasmonic effects; these include surface enhanced Raman scattering (SERS),[18,41] surface plasmon resonance (SPR), [13,69,268] surface enhanced infrared absorption spectroscopy (SEIRAS),[42,43] and metal enhanced fluorescence (MEF).[44,108] SERS has been heavily investigated due to the fingerprint specificity of Raman spectroscopy and the extremely large enhancements seen on certain substrates (on the order of 10^4-10^7).[41]

When magnetic cores are combined with gold shells, there is a limitation in the degree of enhancement that can be encountered using a simple spherical magnetic core/plasmonic shell particle structure.[269,270] The greatest SERS enhancements are observed at specific electromagnetic hot-spots[18,94]—sharp tips[271] and nanogaps[99,272]—neither of which are present on individual solid shells.[155] Anisotropic particles can provide a larger SERS signal,[35,103,105,106] since anisotropic nanostructures can result in greater electromagnetic enhancement on a single particle, rather than depending on the intermittent nanogaps[33] that arise when particles are drifting free in solution. This brings us to our current work—developing anisotropic, or spiky, gold shells on magnetic particle cores for combined separation and sensing.

Nanostructured gold is commonly used for SERS and other surface sensitive optical detection methods.[14,94] In addition to providing electromagnetic enhancement, leading to the surface sensitive signals, nanostructured surfaces also offer geometric benefits—surface-bound probes are more accessible to target biomolecules and nanostructuring leads to greater surface areas.[14] Various gold nanoparticle structures can be used, including spherical and anisotropic gold nanoparticles, as well as core-shell nanoparticles where a gold shell is combined with a core material that allows for additional applications.

Several other researchers have investigated forming spiky gold shells on various core particles. Gold nanostars with small iron oxide cores (gold nanostars: ~100 nm, iron oxide cores: <30 nm) have been synthesized for use in gyromagnetic imaging,[162,163] as recyclable catalysts,[164] for protein separation and SERS detection,[170] and for enhanced electromagnetic properties.[172,173] Others have formed spiky shells on cores of various materials including polymer beads,[165,166] block copolymer assemblies,[165] gold nanowires,[169] gold nanorods,[105], and other metallic particles.[168,171,174] Various methods have been used to synthesize the anisotropic gold shells; typically, they involve reduction of a gold salt in the presence of a structure-directing agent, such as cetyltrimethylammonium bromide (CTAB)[162-164,166,273] or polyvinylpyrrolidone (PVP).[105,168-171]

In this work, we synthesized spiky gold-coated superparamagnetic particles exhibiting fast magnetic separation and demonstrated their use as SERS substrates. A silica coating between the magnetite cluster core and gold shell provides protection to the core from oxidation to less magnetic forms of iron oxide and a suitable surface for spiky gold shell formation. Spiky gold shell growth was compared on differently functionalized silica surfaces, including bare surfaces, amine-functionalized surfaces, and thiol-functionalized surfaces, and using different growth conditions to determine the optimal shell properties for SERS detection of molecules at the gold surface.

5.3 Experimental Section

5.3.1 Materials

Gold(III) chloride hydrate ($HAuCl_4 \cdot xH_2O$), cetyl trimethylammonium bromide (CTAB), sodium borohydride ($NaBH_4$), silver nitrate ($AgNO_3$), and ascorbic acid, were purchased from Sigma Aldrich. Millipore water and reagent grade ethanol were used.

Silica-coated iron oxide particles were synthesized previously at the University of Waterloo[267].

5.3.2 Methods

Particle synthesis was done in several steps: magnetite sphere synthesis, silica coating and functionalization, gold seed binding, then growth of the gold seeds into spikes (Figure 5.1).

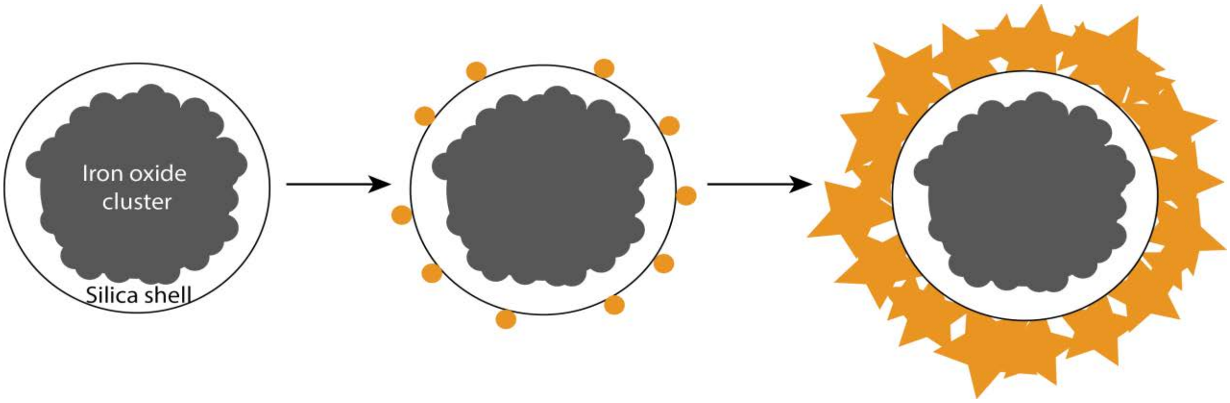

Figure 5.1: Schematic diagram of spiky particle synthesis steps. Gold seeds are bound to a silica-coated magnetite particle, then grown into gold spikes using a gold salt and CTAB bath solution.

5.3.2.1 *Synthesis of magnetite spheres and silica coating*

Magnetite spheres were synthesized using a previously developed hydrothermal synthesis[267,274,275]. In brief, sodium citrate dihydrate, polyacrylamide (PAM), and $FeCl_3 \cdot 6H_2O$ were mixed and dissolved in Millipore water. A small amount of ammonium hydroxide was then added to the solution under vigorous stirring. This mixture was poured into a 125 mL PTFE-lined stainless steel pressure vessel (Parr Instrument Company) and heated at 200°C for 12 h. The product was recovered magnetically and washed with deionized water and ethanol by magnetic decantation, then dried under nitrogen.

Silica coating was done in a second step[267]. In brief, the magnetite particle powder was dispersed into a solution of EtOH and Millipore deionized water by probe sonication. Ammonium hydroxide was then added to the dispersion, followed by the slow dropwise addition of TEOS in EtOH solution over 1 h under vigorous mechanical stirring. This mixture was then stirred at room temperature for 18 h, after which the product was recovered magnetically and washed with EtOH by magnetic decantation, then dried under nitrogen.

Magnetic separation of samples in all steps was performed using either a small neodymium magnet or a rare earth homogenous magnetic separator (Sepmag Lab 2142, inner bore diameter 31 mm, radial magnetic field gradient 45 T/m). The samples were placed in or near the magnet and left to separate for 1-2 minutes. The supernatant was then gently removed using a pipette.

5.3.2.2 *Functionalizing silica surfaces*

Three different types of functionalization were performed on the silica surfaces of the particles: amine functionalization, and two different methods of thiol functionalization (Figure 5.2). These surfaces were chosen because gold is known to form bonds with amine and thiol groups.

Amine functionalization

Silica-coated magnetite spheres were dispersed in 2:1 ethanol:Millipore water for a final concentration of 5 mg/ml by bath sonication. Separately, a 20% v/v solution of (3-aminopropyl)triethoxysilane (APTES) in Millipore water was prepared. While mechanically stirring the particles in a 50°C water bath, APTES solution was quickly added so that the final APTES concentration was 2% v/v. After 24 hours of stirring at 50°C, the particles in solution were magnetically separated and decanted, then washed three times in Millipore water by magnetic separation and dried under a stream of nitrogen.

Short-chain thiol functionalization

Silica-coated magnetite spheres were dispersed in 1:1 toluene:ethanol for a final concentration of 5 mg/ml by bath sonication. After heating the solution to 50°C, (3-

mercaptopropyl)trimethoxysilane (MPTMS) was added to a final concentration of 2.5% v/v. The particles in solution were sealed well in a vial and kept at 50°C with gentle mixing. After 24 hours, the particles in solution were magnetically separated and decanted, then washed once in toluene:ethanol and twice in ethanol by magnetic separation and dried under a stream of nitrogen.

Long-chain thiol functionalization

Amine-functionalized silica-coated magnetite spheres were functionalized with MUA to add thiol groups to the surface. To bind the MUA to the amine groups, the carboxylic acid groups were activated by adding 12 mM of NHS and 12 mM of EDC to 10 mM MUA in ethanol and left for 15 minutes. The particles were dispersed in the activated MUA solution and mechanically mixed for 90 minutes. The particles were then magnetically decanted and washed three times in ethanol by magnetic separation.

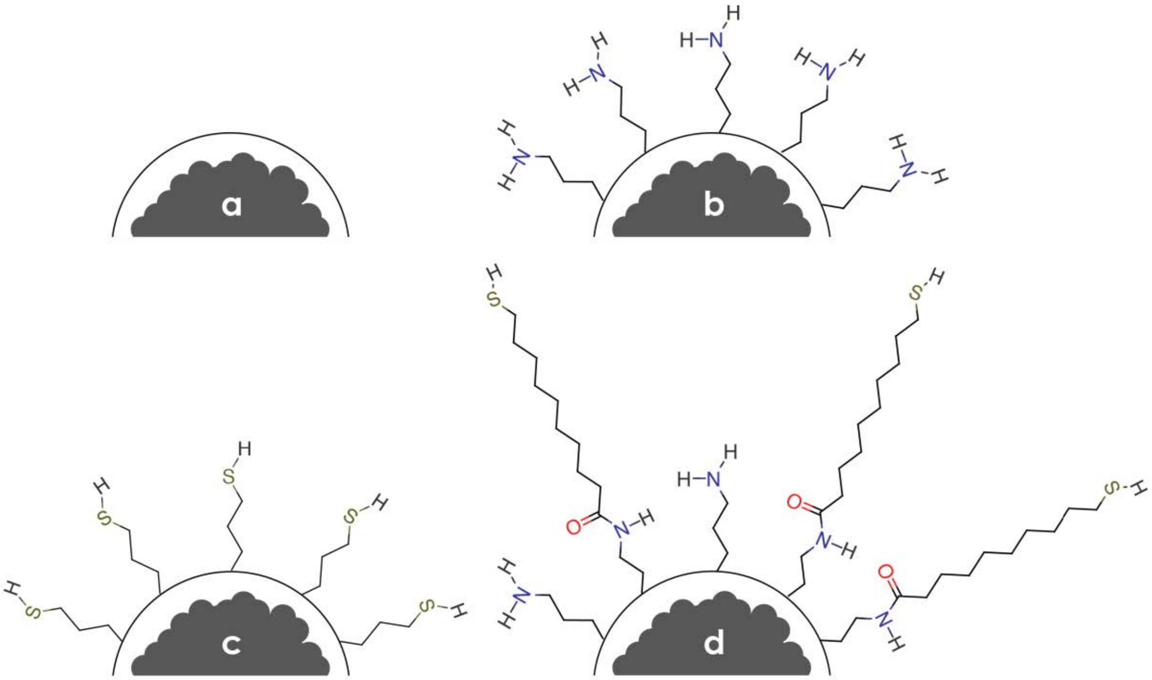

Figure 5.2: Silica coatings were functionalized using different groups. Silica shells were a) left bare (bare), b) amine-coated, using APTES (NH_2), c) short-chain thiol-coated, using MPTMS (SC-SH), and d) Long-chain thiol-coated, using MUA grafted onto amine-coated particles (LC-SH).

5.3.2.3 *Binding gold seeds*

Silica-coated magnetite spheres were dispersed in ethanol at 2 mg/ml using a sonic bath for 20 minutes. Gold seeds were prepared by warming 5 ml of 0.2 M CTAB in Millipore water in a glass vial to 30°C using a water bath, then by adding 0.125 ml of 0.01 M $HAuCl_4{\cdot}xH_2O$ to the vial while magnetically stirring. The bright yellowish-orange solution was stirred for 5 minutes. While still under magnetic stirring in the water bath, 0.3 ml of 0.01 M $NaBH_4$ in Millipore water was added. The light brown solution was stirred for 10 minutes.

The silica-coated magnetite spheres, dispersed in ethanol, were combined with equal parts Millipore water and gold seeds (1 ml of each) and mixed by gentle shaking. The mixture was placed on a gentle rotating mixer for 1 hour. The particles were then magnetically decanted, washed three times using magnetic separation in 1 mM CTAB, and redispersed in the same volume of 1 mM CTAB as the ethanol that was first used to disperse particles at 2 mg/ml.

5.3.2.4 *Growing gold spikes*

Growth solution was prepared by adding 0.5 ml of 0.01 M $HAuCl_4{\cdot}xH_2O$ and 0.1 ml of 0.01 M $AgNO_3$ to 10 mM or 100 mM CTAB, then partially reducing the metal salts using 0.08 ml of 0.1 M ascorbic acid (final concentration of 0.5 mM $HAuCl_4$, 0.1 mM $AgNO_3$, and 0.8 mM ascorbic acid). When multiple samples were being synthesized, growth solution volume was scaled up accordingly. The solution was warmed to 30°C using a water bath and magnetically stirred for 10 minutes. Following this, seeded particles were added to 10 ml of growth solution and mixed by inversion. For the first set of experiments, 100 μl of seeded particles were added to 10 ml of growth solution, and for the second set, 400 μl of seeded particles were added to 20 ml of growth solution. The mixture was kept at 30°C using either a water bath (without magnetic stirrer) or oven for 30 minutes. If growth occurred, the bath changed from a light brown to light grey (bound gold nanoparticles), dark blue (free gold nanoparticles), or a colour in between.

The particles in the bath were magnetically decanted, washed three times using magnetic separation in 1 mM CTAB, and redispersed in a volume of 1 mM CTAB equal to the volume of seeded particles used for storage.

5.3.3 Characterization techniques

5.3.3.1 *Magnetic property characterization*

Magnetization curves were acquired by a superconducting quantum interference device (SQUID) magnetometer at 300K using particles dried in air.

Magnetic separation times were acquired using the Sepmag. An x mL vial containing x ml of 1 mg/ml particles dispersed in water was placed in the centre of the magnetic separator. A green LED was placed above the vial and a spectrometer was placed under the vial to measure the light transmitted through the solution as the particles magnetically separated. The light transmitted at 510 nm was recorded every 0.125s until the solution was clear and the light measured no longer changed. The resulting curve of time versus transmitted light was smoothed using a percentile filter (50%) and normalized for opacity.

5.3.3.2 *Particle characterization*

UV/Vis spectroscopy (UV-Vis, BioTek Epoch Microplate Spectrophotometer) and transmission electron microscopy (TEM, Philips CM10) were used to characterize the optical absorption, size, and structure of the particles. Samples for all methods were prepared by diluting 25 μl of particles at the final listed concentrations with 1 ml of Millipore water. Average gold nanoparticle sizes were measured using TEM and ImageJ software and average spiky particle sizes were measured using TEM and DLS. The presence and amount of functional groups on the surfaces following silica modification and gold coating was characterized using XPS. XPS analyses were performed using a PHOIBOS 100 X-ray photoelectron spectrometer from SPECS GmbH (Berlin, Germany) with a monochromated AlKα X-ray source ($h\nu = 1486.6$ eV) operating at $P = 1\times10^{-10}$ Torr or less. Spectra were carried out with a 50 eV pass energy for the survey scan and 10 eV pass energy for the Si2p, O1s, C1s, N1s and S2s regions. High-resolution XPS conditions have been fixed: "Fixed Analyzer Transmission" analysis mode, a 7 x 20 mm entrance slit leading to a resolution of 0.1 eV for the spectrometer, and an electron beam power of 150 W (15 kV and 10 mA). A takeoff angle of 90° from the surface was employed for each sample and binding energies were calibrated against the $Au4f_{7/2}$ binding energy at 84.0 eV. Element peak intensities were corrected by Scofield factors to calculate the atomic fractions[210]; the spectra were fitted using Casa XPS v.2.3.15 Software (Casa Software Ltd., UK) and applying a Gaussian/Lorentzian ratio G/L equal to 70/30.

5.3.3.3 *Surface-enhanced Raman scattering (SERS)*

First set: influence of silicon-iron oxide core functionalization

In the first set of experiments, we compared the SERS signal from the gold-coated particles prepared using differently functionalized cores, since this led to different types of gold coatings. Samples for surface-enhanced Raman scattering (SERS) were prepared by adding 50 µl of 2 mg/ml particles dispersed in CTAB to 3 ml of Millipore water; this amount was chosen because it was the minimum amount required for signal saturation, as determined by an initial test. Particles were initially dispersed in 1 mM CTAB (final CTAB concentration of 16.7 µM) and varying amounts of the Raman probe, 2-mercaptopyrimidine (MPym), were added.

Second set: influence of bath conditions

In the second set of experiments, we compared the SERS signal from the gold-coated particles prepared using different gold growth bath conditions, which also led to different types of gold coatings. Samples were also prepared by adding 50 µl of particles dispersed in CTAB to 3 ml of Millipore water, but particles were initially dispersed in 10 mM CTAB (final CTAB concentration of 167 µM), which resulted in a signal large enough to be compared without the use of an additional Raman probe.

Raman measurements

Spectra were recorded in the 500–3400 cm^{-1} range on a modular Raman spectrometer (Model HL5R of Kaiser Optical Systems, Inc.) equipped with a high-powered near-IR laser diode working at 785 nm. Before spectra acquisition, an optical microscope was used to focus the laser beam into the PymSH solution containing particles. The laser output power was 100 mW. For each spectrum, 10 acquisitions of 30 s were recorded to improve the signal-to-noise ratio.

5.4 Results and Discussion

5.4.1 Magnetic properties

The idea behind using a magnetic core is that particles can be easily separated from a solution using a magnetic field. Use of the particles in practical applications, such as the separation of biomolecules, requires fast separation times and the ability to be redispersed (no aggregation) before and after separation. The magnetic properties of the particles were studied before and after gold coating to determine whether or not the particles fit these requirements.

A SQUID magnetometer was used to obtain magnetization curves of the particles before and after gold coating (Figure 5.3). The saturation magnetization (M_s) of the amine-functionalized silica-coated iron oxide particles was 32 emu/g and after long-chain thiol functionalization and gold shell coating, it was 9 emu/g. It is important to note that the values are adjusted according to the overall mass of the particles, including both magnetic and non-magnetic materials, so what looks to be a large decrease in saturation magnetization upon coating is in fact expected and does not in itself imply that the coating leads to reduced magnetization. With this said, non-magnetic coatings can reduce the magnetization of particles;[276,277] the silica-iron oxide core of the particles makes up 40-50% of the weight of the particles giving an adjusted saturation magnetization of 18-23 emu/g, which when compared with the measured 32 emu/g before gold shell coating suggests that some reduction in magnetization occurs upon coating.

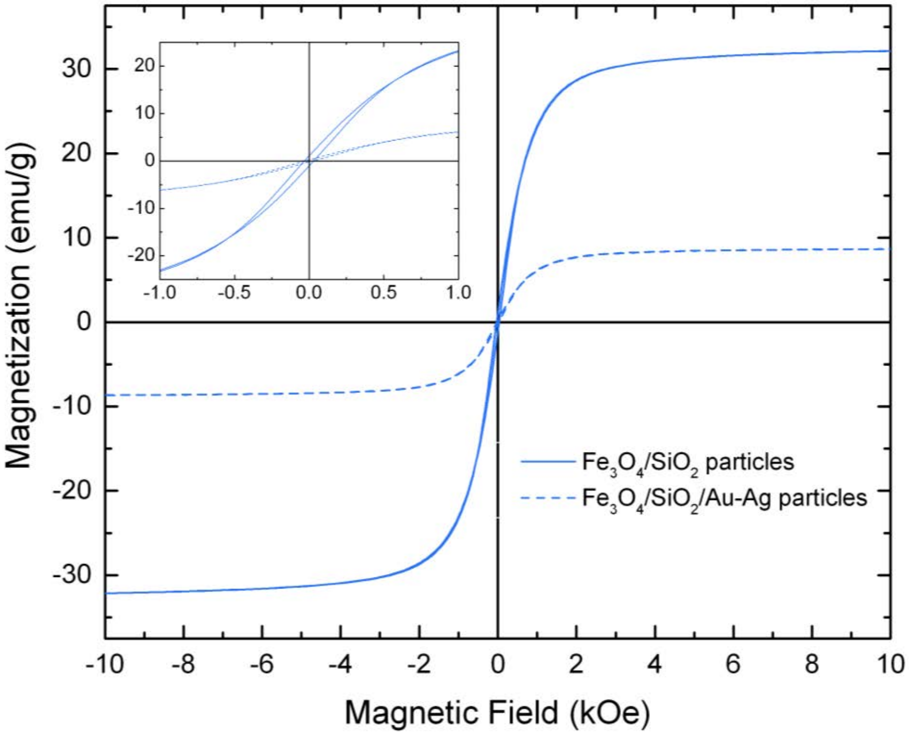

Figure 5.3: Magnetization curves of silica-coated iron oxide particles before (solid) and after (dashed) gold/silver shell coating. The inset shows the small amount of hysteresis occurring at low magnetic fields

We see further evidence of the reduction by examining the magnetic separation curves (Figure 5.4) and times (Table 2.1). While a simple fridge magnet provides a sufficient magnetic field for separation, in these experiments we used a magnet that provides a constant magnetic field gradient for controlled separation (Sepmag). The gold-coated particles took longer to separate than the particles without a gold shell. Separation time (t_{sep}) decreases with increased saturation magnetization, possibly according to an inverse power relationship ($t_{sep} \propto 1/M_s^{2\alpha/3}$, where α depends on the experimental parameters),[261] so it is likely that the magnetization is reduced upon gold shell formation. Despite this, both types of particles separated quickly, with opacities reaching below 1% in less than two minutes.

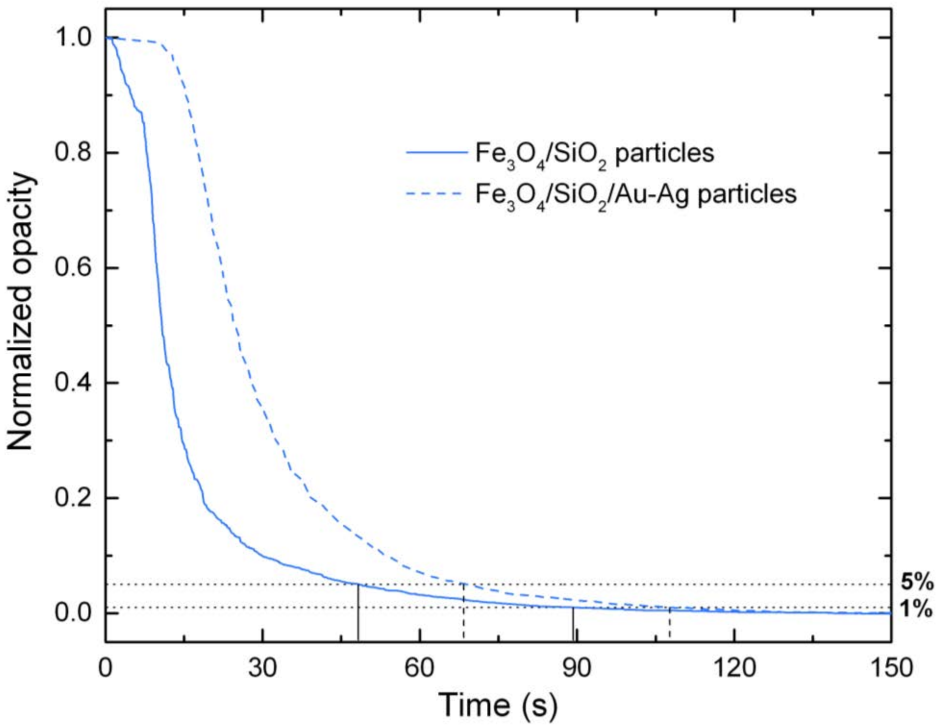

Figure 5.4: Measured opacity over time for water dispersions of particles at 1 mg Fe_3O_4/SiO_2 particles/ml (greater mass upon gold coating) in a 45 T/m gradient, before (solid) and after (dashed) gold shell coating.

Table 5.1: Separation times of particles, determined based on time required to reach 5% and 1% of initial opacity (see dotted lines in Figure 5.4)

	Separation time (seconds)	
	5% opacity	*1% opacity*
Fe_3O_4/SiO_2	48	89
Fe_3O_4/SiO_2/Au-Ag	68	108

The magnetization curve (Figure 5.3) also shows that particles have low remanent magnetization; for the silica-coated iron-oxide particles, the remanent magnetization is 1 emu/g and for the gold-coated particles, the value is 0.25 emu/g. A remanent magnetization suggests that the particles do not meet the formal definition of superparamagnetism, but with such a low value, do they exhibit superparamagnetic behavior in practical applications? Experimental observations suggest that they do; neither visible aggregation nor a size change according to DLS occurs after applying and removing a magnetic field. Furthermore, theoretical calculations show that a 1 emu/g magnetization has a negligible effect on the interaction potential between particles (Figure 5.5). The calculation uses an extended DLVO theory[278] to study the interaction potential between particles, incorporating the potential due to the attractive van der Waals force (V_{VdW}), the repulsive electric double layer force (V_{DL}), and the attractive magnetic force (V_{mag}). The values used match those of typical silica-coated particles used in the experiments, with a diameter of 336 nm (iron oxide core diameter of 224 nm) and a surface potential of -73 meV in 10 mM NaCl. Details regarding the calculations can be found in Appendix A. The curve representing the case where there is a remanent magnetization following the removal of a magnetic field (1 emu/g) nearly overlaps the curve for the case where there is no magnetic field and no magnetic force between particles (0 emu/g). In both cases, the interaction potential is repulsive for all separations until the drop following the high-energy barrier at very small distances. It can also be noted that in all cases, the high-energy barrier prevents non-reversible particle aggregation; while the magnetic force leads to particle attraction at larger distances, non-reversible aggregation will not occur—a result confirmed by experimental observations.

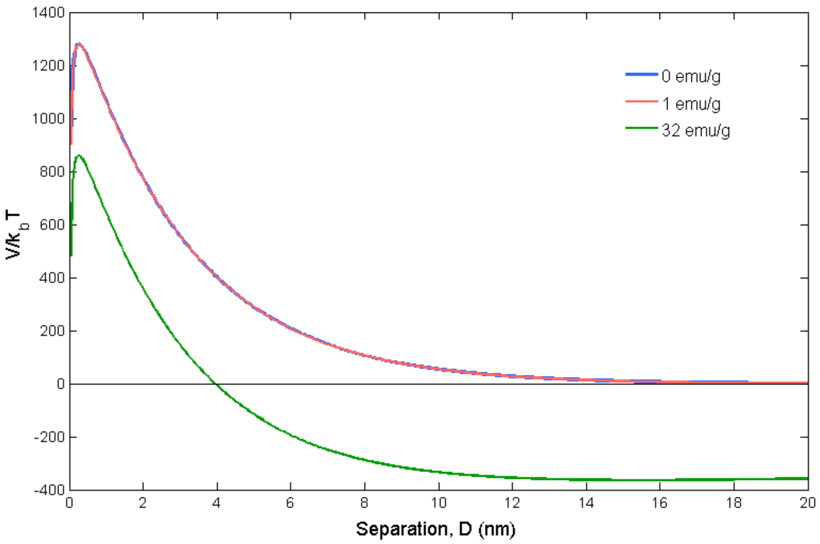

Figure 5.5: Interaction potential at short distances between two silica-coated iron oxide particles (iron oxide core diameter = 224 nm, silica shell diameter = 336 nm) with a charge density of −0.9 e/nm² in 10 mM concentration of 1:1 electrolyte (surface potential $\Phi_0 \approx -73$ mV). (Blue) no applied magnetic field—zero magnetization, (red) remanent magnetization following removal of magnetic field, (green) applied magnetic field—saturation magnetization of 32 emu/g.

The particles have a quick separation time and negligible remanent magnetization, confirming that they would be suitable for practical applications such as biomolecule separation based on their magnetic properties.

5.4.2 Gold shell growth: Influence of silica-iron oxide core functionalization

We grew gold spikes on silica-coated iron oxide spheres using a two-step method; first, CTAB-stabilized gold nanoparticle seeds were bound to the silica surface, then the seeds were grown into spiky particles using an aqueous, CTAB-based growth solution (Figure 5.1).

5.4.2.1 *Silica-iron oxide core functionalization*

We looked at growth on four differently functionalized silica surfaces (Figure 5.2) to determine how the interaction between the surface and gold nanoparticles affects spiky shell growth. The particles were analyzed with XPS to confirm successful functionalization. All expected groups are present on the particles. APTES functionalized particles show nitrogen groups on their surfaces at a significantly larger concentration than the trace nitrogen signal on bare particles, which is likely from ammonium hydroxide used in synthesis. Both short chain and long chain thiol-coated particles show thiol groups on the surface. In the case of the long-chain thiol-coated particles, MUA is estimated to be bound to at least 13% of the amine groups (ratio of S/N), which results in a thiol density comparable to that on the short-chain thiol-coated particles.

Table 5.2: XPS results showing elemental breakdown of particle surfaces following treatment

	Si 2p	**O 1s**	**C 1s**	**N 1s**	**S 2s**
Bare silica (bare)	33.8	56.6	9.0	0.6	-
MPTMS (SC-SH)	33.6	55.4	10.7	-	0.3
APTES (NH_2)	30.1	46.0	21.3	2.6	-
APTES-MUA (LC-SH)	27.5	44.4	25.1	2.6	0.3

5.4.2.2 *Gold shell synthesis*

After binding gold seeds to particles with differently functionalized silica surfaces, TEM (Figure 5.6) and UV-Vis (Figure 5.7) showed that the size and number of gold seeds varied with type of surface functionalization. Larger gold nanoparticles (3.5-5 nm) were seen on bare (Figure 5.6a) and short-chain thiol functionalized (Figure 5.6c) silica surfaces and smaller gold nanoparticles (<1 nm) were seen on long-chain thiol functionalized (Figure 5.6d) silica surfaces. Few gold nanoparticles were seen on amine-functionalized (Figure 5.6b) silica surfaces.

UV-Vis spectra (Figure 5.7) support the TEM results. After gold seed binding, the spectra show a shift towards longer wavelengths—towards the plasmon peak of gold nanoparticles retrieved after binding. In confirmation with the lack of gold nanoparticles bound seen in TEM, the spectrum of amine particles following seeding showed very little shift compared with the other types of particles. Gold nanoparticle size shows some correlation with the wavelength of the plasmon peak, where smaller particles exhibit plasmon peaks at lower wavelengths[279,280]. While attempts to determine the size of bound gold nanoparticles from the UV-Vis spectra are hindered by confounding of adsorptions from different parts of the particles, we can see that for the long-chain thiol functionalized particles, the peak is relatively higher at lower wavelengths compared with bare and short-chain thiol functionalized particles.

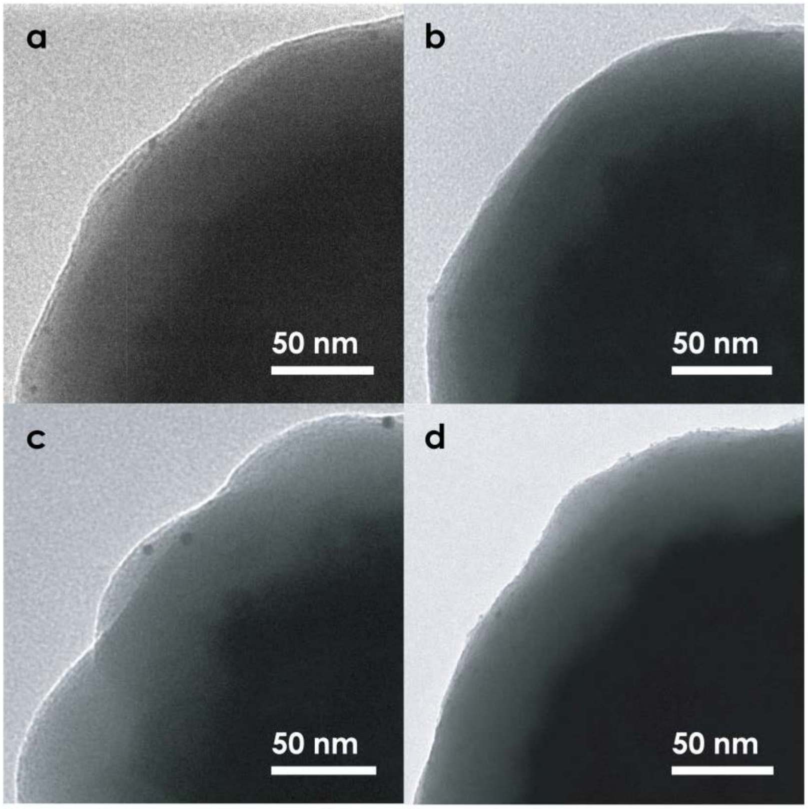

Figure 5.6: TEM images of particles after gold seed binding on a) bare silica, b) amine-functionalized silica, c) short-chain thiol-functionalized silica, and d) long-chain thiol-functionalized silica

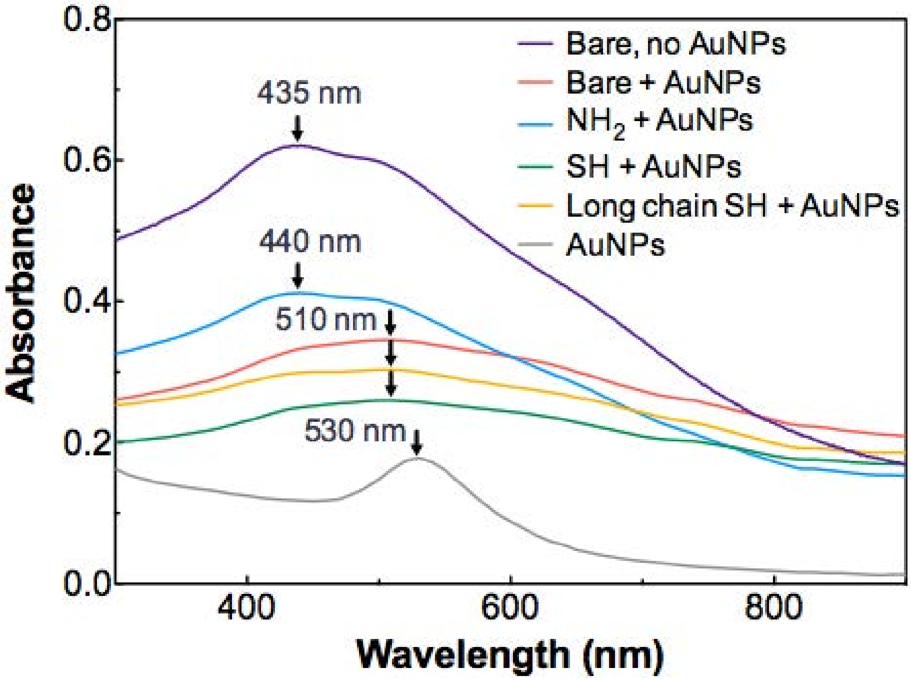

Figure 5.7: UV-Vis spectra of particles before and after gold seed binding

Figure 5.8 shows TEM images of the particles after spiky shell growth and Figure 5.9 shows their UV-Vis spectra. Based on TEM and UV-Vis results, spiky gold shells grew on all silica surfaces except on the amine-coated surface (Figure 5.8a), where only gold stars can be seen on the surface of the particles—a result that is consistent with those noted above regarding gold seed binding. Shell coverage was greatest on the long-chain thiol functionalized particles surface (Figure 5.8d) and was at an intermediate amount on the bare (Figure 5.8a) and short-chain thiol (Figure 5.8c) functionalized particles. As would be expected based on the method of synthesis, shell growth results from the individual growth of gold seeds into anisotropic gold shapes (nanostars, bipyramids, etc), which eventually coalesce into full shells surrounding the particles. UV-Vis results correlate well with TEM. Several researchers have studied the optical response of gold shells and have shown that as individual gold nanoparticles (seeds) begin to grow and coalesce, intercoupling between the plasmon modes of the gold particles leads, first, to a broadening of the plasmon peak and shift to longer wavelengths, then, to a shift to shorter wavelengths as the shell approaches full coverage[154,155]. Our results show that plasmon peak broadening and increased optical absorption at longer wavelengths occurs after gold growth on particles that came closer to approaching full shell growth, i.e. bare silica or thiol functionalized surfaces, while very little shift occurred on particles after gold growth on particles where shells were not formed, i.e. amine-functionalized surfaces. In addition, on long-chain thiol functionalized surfaces, we see the appearance of a peak at around 630 nm along with the increase of a broad peak reaching into the NIR range. Based on the experimental results and simulations from previous work[154,155], this may be due to the shift to shorter wavelengths that can occur upon complete shell formation.

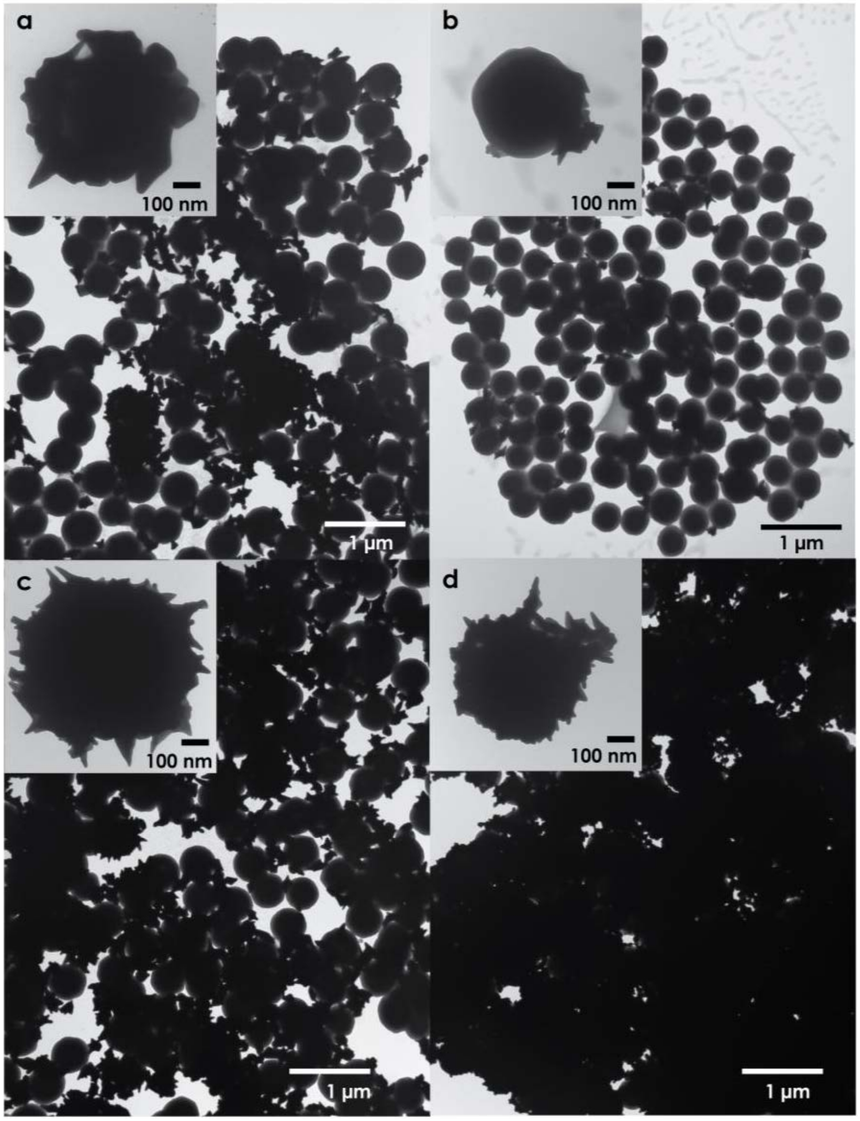

Figure 5.8: TEM images of spiky particles, with spiky nanostructures grown on a) bare silica, b) amine-functionalized silica, c) short-chain thiol-functionalized silica, and d) long-chain thiol-functionalized silica. Insets show high magnification of spiky shells

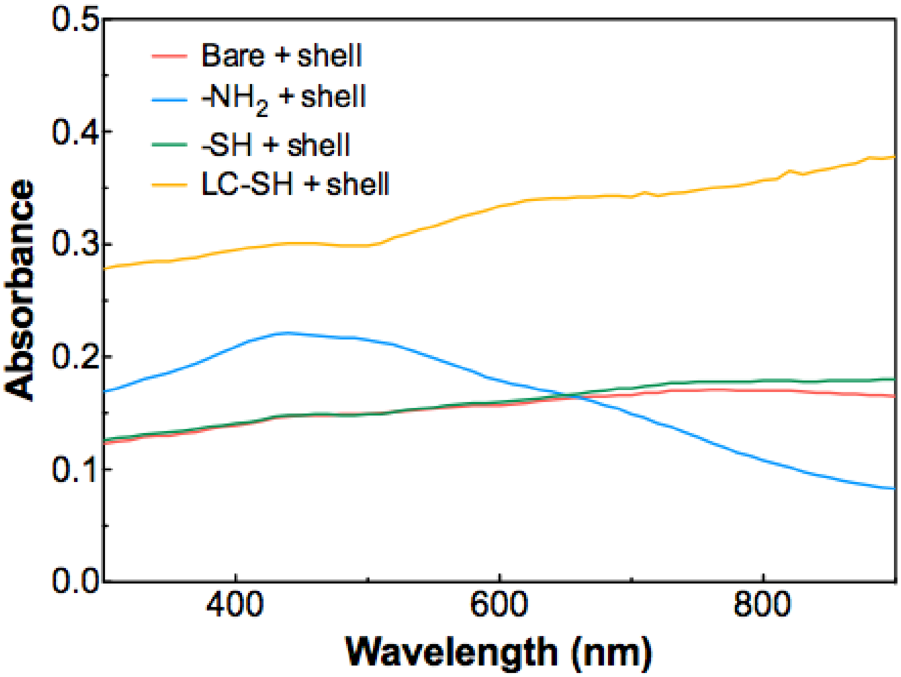

Figure 5.9: UV-Vis spectra of spiky particles

Why shell growth depends on surface functionalization likely involves interactions between surface functional groups and gold nanoparticles and their stabilizing groups. A first step is to explain why there is a difference in size and number of gold seeds bound to different surfaces. The gold nanoparticles are formed in a CTAB solution and growth occurs in CTAB. When $HAuCl_4$ is in CTAB, $AuCl_4^-$ and $AuCl_2^-$ ions form complexes with the cetyl trimethylammonium cations (CTA^+)[281,282]. Before the gold salt-CTAB solution is added to the particles dispersed in ethanol (gold seed binding step), there is no plasmon peak, which suggests that $NaBH_4$ addition does not immediately reduce the gold salt to the nanoparticles observed on the silica-coated magnetic particle surfaces. When water is used instead of ethanol to disperse the silica-coated particles, gold nanoparticles large enough to exhibit a colour change take several days to form. When the gold salt-CTAB solution is added to ethanol, additional experiments have shown that gold nanoparticles form with a plasmon peak that varies in position depending on the proportion of ethanol added. This suggests that adding ethanol destabilizes the $AuCl_x^-$ CTA^+ complexes, resulting in gold salt reduction into gold nanoparticles.

The differently functionalized silica surfaces have different electrostatic charges and will therefore interact differently with the complexes and CTAB-stabilized gold nanoparticles. In the case of the amine-functionalized surfaces, the particles will have a positive charge under the experimental conditions used, so likely, electrostatic repulsion between CTA^+ and the positively-charged surfaces prevent gold nanoparticles from forming and binding to the surface. On the bare silica and short-chain thiol-functionalized surfaces, reduction at the surface is more favorable because of the attraction between CTA^+ and the more negatively charged surfaces.

Differences in spiky shell growth can be seen as a direct result of the differences in gold seed binding to the surface. More gold seeds bind to the thiol-functionalized surfaces than to the bare or amine-functionalized surfaces because of electrostatic repulsion or attraction as well as the strong gold-thiol bond that may form. Few gold seeds bind to the amine-functionalized surface because of electrostatic repulsion and little seed growth occurs on those that do because growth also involves CTAB as a structure-directing/stabilizing group. Some gold nanostructures are still seen attached to the amine particles possibly because of the strong gold-amine bond that forms, despite electrostatic repulsion between the surface and stabilizing groups.

5.4.2.3 *Surface-enhanced Raman scattering (SERS)*

To study whether or not the particles demonstrated Raman scattering enhancement, we used 2-mercaptopyrimidine (MPym) as a Raman reporter molecule because of its high Raman activity and ability to strongly interact with the gold surface through the thiol group.

The SERS analytical enhancement factor (AEF), given below, is often used to describe the degree of SERS enhancement from a given system by comparing the unenhanced Raman signal, I_{RS}, from a molecule at a concentration c_{RS}, with the SERS enhanced signal, I_{SERS}, from the same molecule at a concentration c_{SERS}.[283]

$$AEF = \frac{I_{SERS}/c_{SERS}}{I_{RS}/c_{RS}}$$

Particles with spiky gold shells demonstrated a SERS analytical enhancement factor on the order of 10^4, a value comparable with those seen in comparable literature when the SERS signal involves averaging.[41] Measurements using only the seeded particles—gold nanoparticles bound to silica-coated magnetite particles—in combination with 10 μM PymSH showed no signal.

Particles with gold shells on differently functionalized silica surfaces produced different signal intensities (Figure 5.10). The largest intensity was seen using particles with gold shells formed on bare silica-coated magnetite cores, while the other particles showed lower intensities. The reason for the differences is thought to be due to an optimal amount of gold coverage; too little gold and the gold surface that leads to SERS enhancement is small, but too much gold and the particle suspension becomes unstable, leading to particle aggregation. Aggregation was observed in the case of long-chain thiol functionalized particles, and to a more limited extent, short-chain thiol functionalized particles. Amine functionalized particles showed less gold coverage than the other particles (Figure 5.8 and Figure 5.9). Another possibility that could explain the differences is that an incomplete nanoshell shows greater enhancement than a complete one[155], possibly due to an optimal size and number of nanogaps between surface-bound gold nanostructures.

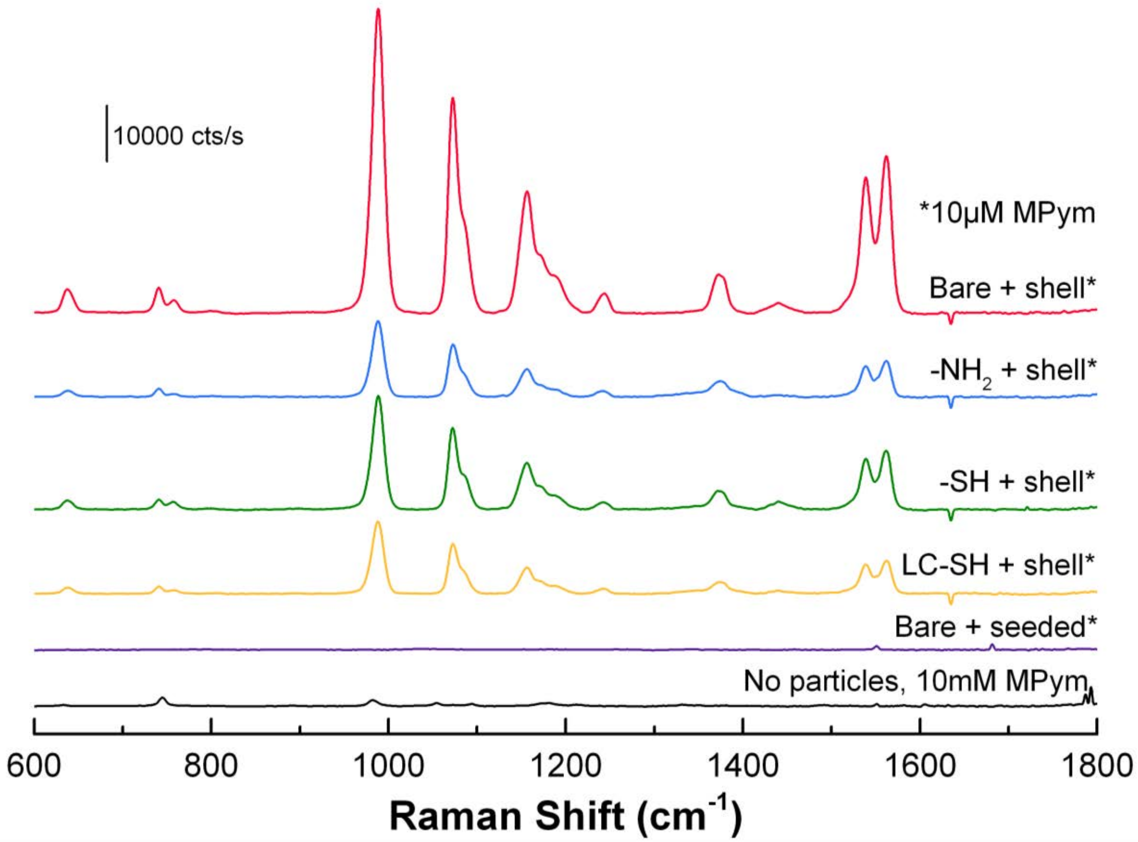

Figure 5.10: Raman spectra of 2-mercaptopyrimidine with and without particles. Note that a concentration of 2-mercaptopyrimidine 10^3 lower is used to demonstrate enhancement by particles (10 μM) compared with the unenhanced signal (10 mM). All samples used 50 μl of 2 mg/ml particles in 1 mM CTAB added to 3 ml of water.

How does the measurement vary with Raman reporter concentration? Particles with spiky gold shells on bare silica-coated magnetite cores, before optimization, were used to enhance the Raman signal of MPym at different concentrations (Figure 5.11). The signal from peaks corresponding to MPym increased with increasing concentrations. The peak at 1073 cm^{-1}, corresponding to the pyrimidine group of MPym, was used to study this trend since the largest peak at 990 cm^{-1} overlapped with a peak from CTAB. The lowest concentration clearly detectable was less than 100 nM.

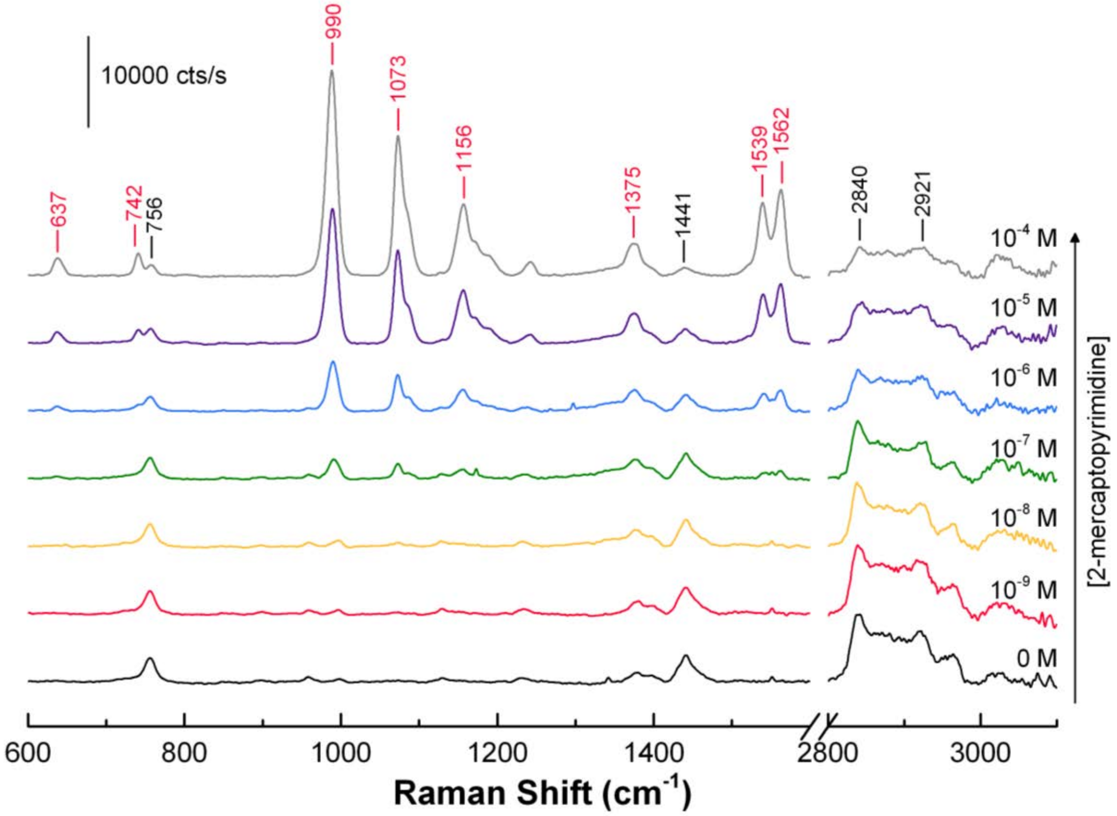

Figure 5.11: Raman spectra of 2-mercaptopyrimidine (MPym) at different concentrations with particles featuring spiky gold shells on bare silica-coated magnetite particles. All samples used 50 µl of particles in 1 mM CTAB added to 3 ml of water. Peaks with red labels correspond to peaks that increased after adding MPym and peaks with black labels correspond to peaks seen on particles before adding MPym—likely CTAB

As would be expected from a surface sensitive method, the signal increased with increased concentration of MPym, but also showed saturation behavior, as demonstrated by the dashed line in Figure 5.12, which is a fit to an extended Langmuir model. Note that the data do not fit the criteria for a Langmuir model (the surface is rough and the stabilizing CTAB molecules must be displaced for MPym molecules to bind), so the fit is shown only as a guide to the eye to demonstrate saturation.

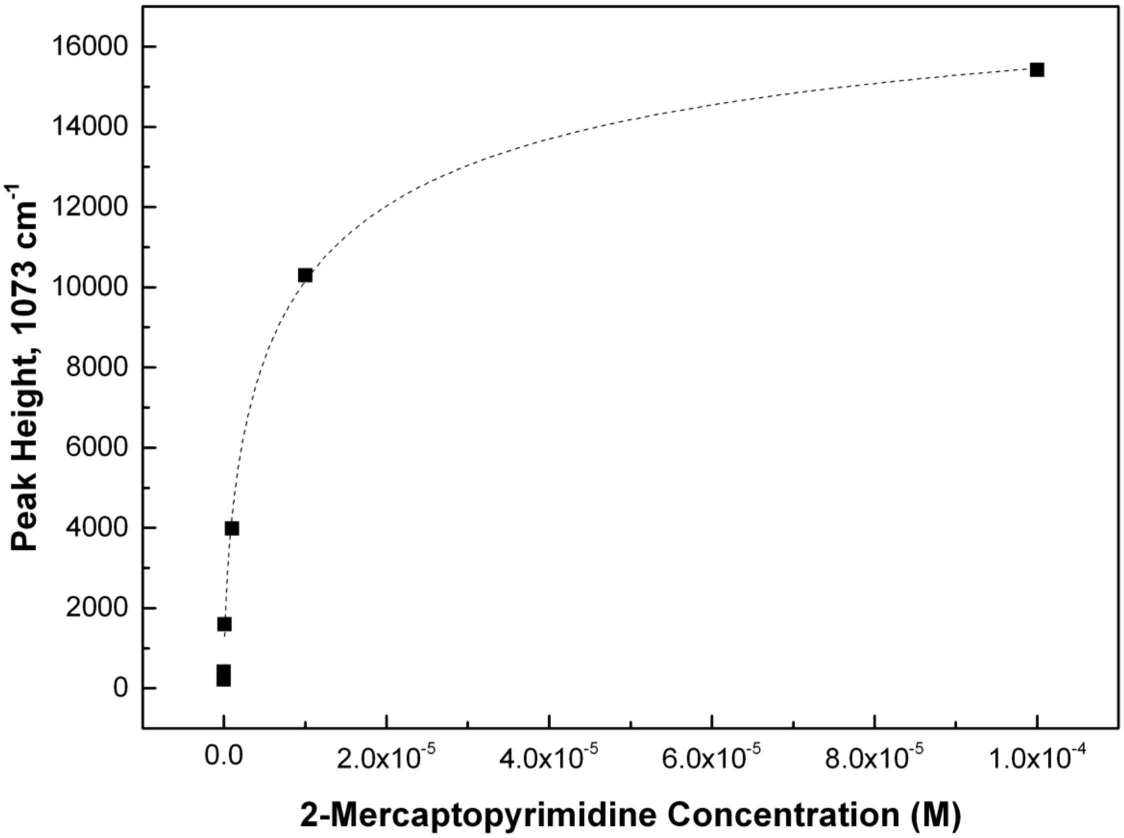

Figure 5.12: Change in peak height of Raman signal corresponding to the Raman reporter (MPym) at different concentrations. A fit to a Langmuir model (red line) shows saturation behavior (R^2 = 0.98)

Another interesting observation was that the signal due to CTAB decreased as the MPym concentration increased. The particles also provided enhancement of the signal from CTAB, which acted as a stabilizing group on the particles. Looking at three peaks, 2840 cm^{-1}, corresponding to the C-H stretching vibrations that are greater on CTAB than PymSH, 1441 cm^{-1}, corresponding to the CH_2 scissor modes and to the amine-bound C-H symmetrical deformation, and 756 cm^{-1}, corresponding to the symmetric stretch of the trimethylammonium head group,[225,284] shows that there is a decrease in CTAB at the surface of the particles when the Raman reporter concentration increases (Figure 5.13). This result suggests that the Raman reporter can successfully replace CTAB groups at the surface. It is important to note, though, that with CTAB groups still present on the surface, the observed limit of detection of MPym is likely hindered by the presence of these groups. Future applications will require ensuring that the stabilizing groups do not interfere with detection limits.

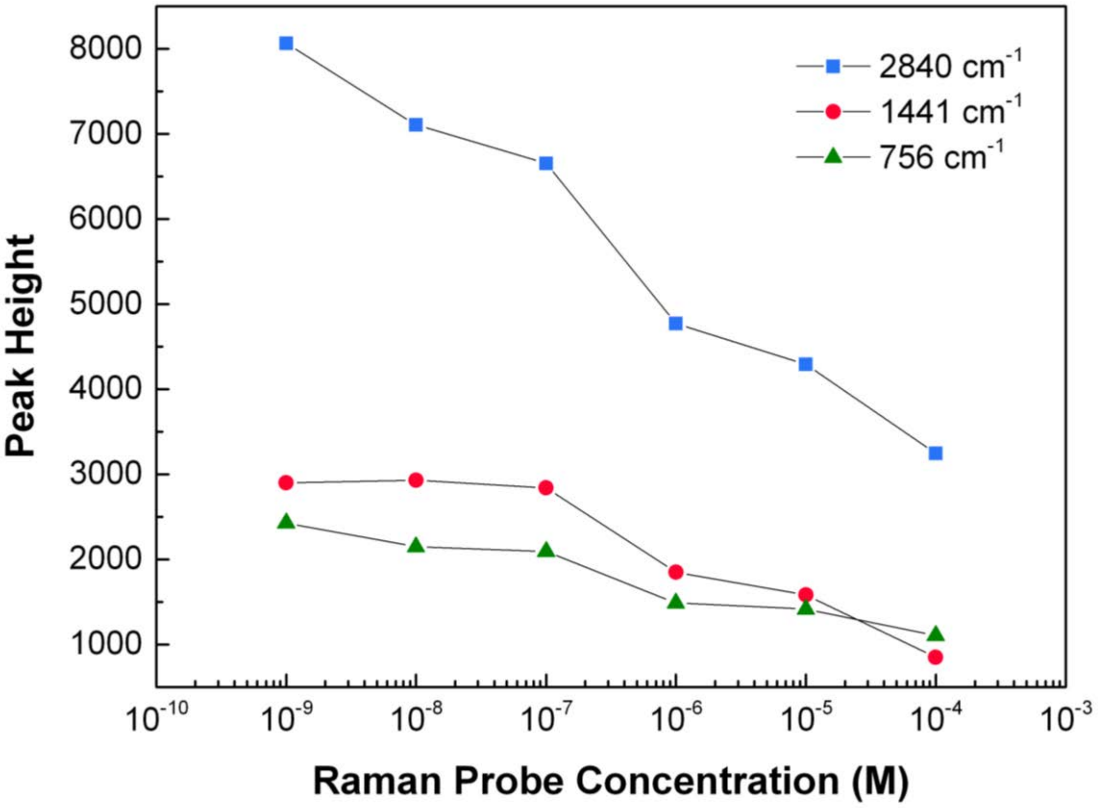

Figure 5.13: Change in peak heights corresponding to CTAB at different Raman reporter (MPym) concentrations.

5.4.2.4 *A comment on particle stability*

As previously noted, the long-chain thiol-coated particles aggregated, which likely led to a lower SERS signal. Despite this, the long-chain thiol-coated particles resulted in the most gold coverage and the least amount of gold nanoparticles observed free in the supernatant; based on these observations, we concluded that these particles had the greatest potential for reproducible measurements and longer-term stability. All following experiments were therefore performed using long-chain thiol-coated particles, but using 10 mM CTAB instead of 1 mM CTAB for the washing steps. This minor modification prevented aggregation and resulted in stable particles with sufficiently high SERS signals.

5.4.3 Gold shell growth: Influence of growth bath conditions

We wanted to investigate growing shells of different morphologies to study how this would affect SERS enhancement. Many parameters can affect gold growth in CTAB-based syntheses,[145] including growth time,[164,285] reagent concentrations,[161,273,285-288] and the presence of other halide ions.[273,285,288] Here, we investigated two important ones: the influence of growth time and CTAB concentration on shell growth. We then selected several different shell morphologies to investigate the influence of shell morphology on SERS enhancement.

5.4.3.1 *Varying growth time and CTAB concentration*

As expected, increasing the time that seeded particles spent in the growth bath increased the amount of gold bound to the surface. As well, increasing the concentration of CTAB in the growth bath decreased the amount of gold bound to the surface at a given time (Figure 5.14). The amount of CTAB used also changed the morphology of particles: spiky particles were made using a higher CTAB concentration (100 mM), but using a lower CTAB concentration (10 mM) resulted in shells with lower aspect ratio protrusions—called from here on bumpy particles. Using an even lower CTAB concentration (1 mM) resulted in $HAuCl_4$ reduction to Au_0 by ascorbic acid, as evidenced by the colour change of the bath solution before seeded particles were added. Others have proposed that CTAB forms a complex with the gold chloride ions; the critical micelle concentration (CMC) of CTAB is approximately 1 mM, so a possible interpretation of the data is that gold chloride ions in the bath solution are stabilized by micelles as long as the concentration of CTAB is above the CMC[289]. Since ascorbic acid is a weak reducing agent, gold seeds are required as nucleation sites for complete reduction of the gold salt to occur. As would be expected, growth also occurred more quickly when a lower CTAB concentration was used.

For both bumpy (10 mM CTAB) and spiky (100 mM CTAB) particles, the UV-Vis absorbance increased in the NIR region with increased growth time. This result fits with previous research showing that hybridization between the resonances of the individual gold nanostructures on the particle surface leads to a broad NIR absorption band that red shifts with increased coverage.[155,273]

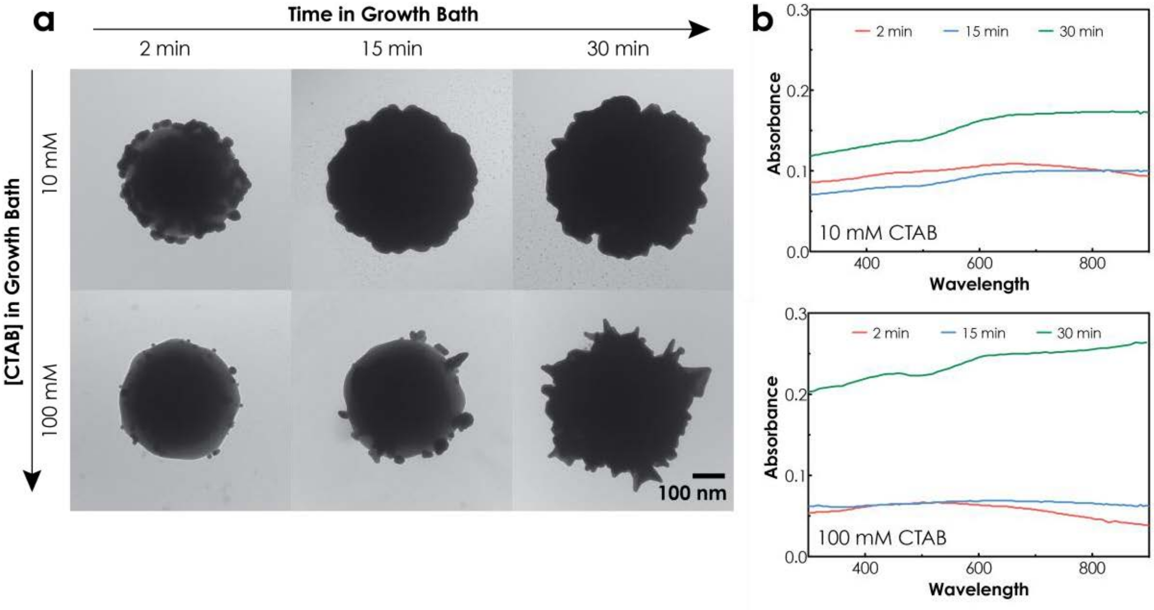

Figure 5.14: a) TEM images showing representative particles at varying growth times and CTAB concentrations and b) corresponding UV-Vis extinction spectra for particles synthesized at different growth times using (top) 10 mM and (bottom) 100 mM CTAB

5.4.3.2 *Different shell morphologies: XPS and SERS*

Several different gold shell syntheses were chosen to investigate how SERS enhancement varied across different morphologies. The morphologies investigated were spiky shells, bumpy shells, and particles with small gold nanoparticles (<20 nm) attached to their surfaces (AuNP spotted particles). TEM images of the particles and the Raman spectra taken of the particles in a solution of 167 μM CTAB along with the Raman spectra of unenhanced 0.2 M CTAB (for comparison) are given in Figure 5.15.

We found that the spiky particles led to greater SERS enhancement than the bumpy particles, and that both of these led to more enhancement than the spotted particles, for which the SERS signal of CTAB was practically negligible. Using the height of the peak at 763 cm^{-1} (corresponding to the trimethylammonium headgroup[225,284]) to compare the enhancement shows that the enhancement due to the spiky particles was somewhat greater (approximately 1.5x) than that due to the bumpy particles. Comparing the signal to the CTAB signal has some practical issues—namely that the SERS selection rules for the modes observed and their relative strengths are different than for Raman in bulk solution—but the analytical enhancement factor (AEF) appears to be on the order of 10^4 for both types of nanostructured particles.

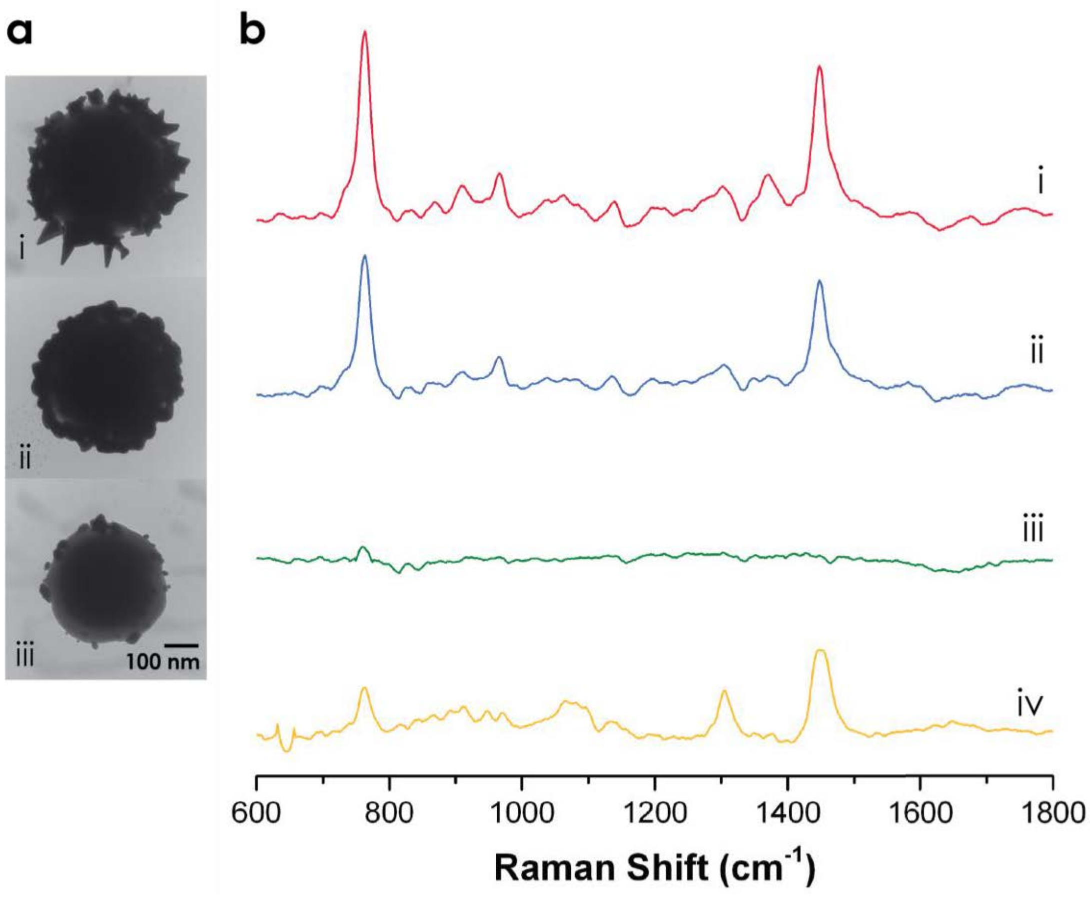

Figure 5.15: a) TEM images and b) (i-iii) corresponding Raman spectra of particles in 167μM CTAB with i) spiky shells (EB-150-a), ii) bumpy shells (EB-150-b), and iii) nanoparticle spotted (EB-150-c), and iv) Raman spectra of 0.2M CTAB in water (1200x more concentrated than particle-enhanced measurements).

We then asked whether the differences in enhancement were caused by the amount of gold and silver bound to the surfaces, or whether the morphology did in fact play a role. XPS spectra were taken of the different particles to compare the amount of gold and silver on the surface (Table 5.3). We used the Si 2p, Au 4f, and Ag 3d signals to represent the particle surfaces and used their sum as a normalizing factor. Since both adsorbed and unbound CTAB are present in the sample, the elements corresponding to CTAB were not useful in the analysis. The amount of enhancement was not directly dependent on the relative amounts of gold and silver detected by XPS; the spiky shells, which showed greater SERS enhancement than the bumpy shells, showed a lower relative amount of gold and silver. We therefore posit that the enhancement is related to the morphology. There are then two factors that could lead to the greater enhancement: greater surface area available for CTAB adsorption and therefore signal enhancement, or greater electromagnetic enhancement due to the sharp tips on the particles. The XPS and TEM results suggest that the spiky particles have a less complete shell (more silica is exposed) than the bumpy particles, but can they provide information on the available gold surface area? In general, the shell is thicker than the penetration depth of XPS, but often, the gold features (spikes) are smaller than the penetration depth, so the surface area may be underestimated if it is assumed to directly correspond with the ratios based on the XPS atomic percentages. It is therefore difficult to conclude from XPS whether the larger Raman enhancement on the spiky shell particles is due to increased surface area or increased electromagnetic enhancement caused by the spike shape.

Table 5.3: XPS-determined atomic percentages following coating procedures in different conditions

	Atomic Percentage			
	Si 2p	Au 4f	Ag 3d	(Au+Ag)/ (Au+Ag+Si)
EB-150-a, Spiky shell	15.6	8.0	1.6	0.38
EB-150-b, Bumpy shell	7.4	11.2	2.3	0.64
EB-150-c, NP spotted	10.6	0.9	0.2	0.09

5.4.4 Particle stability over time

Using the particles for detection applications requires that they are stable over a period of time. We synthesized spiky and bumpy particles and measured their absorbance (UV-Vis), change in morphology (TEM), and SERS enhancement (Raman spectroscopy) after

1 week and 1 month, stored in 10 mM CTAB at room temperature. Particles were washed three times in 10 mM CTAB before each measurement. The UV-Vis and TEM results are shown in Figure 5.16 and the Raman spectroscopy results in Figure 5.17.

The particles remained fairly stable after one week, although some morphological changes did occur. After one month, the UV-Vis absorbance of the particles decreases overall, but especially large decreases occur in the NIR range. We can observe a resemblance between these curves and those seen after short growth times (see section 5.4.3.1)—less complete shells show lower NIR absorbance because of decreased plasmon hybridization between the plasmons of individual gold nanostructures. The NIR absorbance decrease of the spiky particles is also likely due to the reduced aspect ratio of the gold nanostructures, as seen in TEM.

After one week, the bumpy particles remained stable while the spiky particles showed a change in SERS signal. Surprisingly, the SERS signals increased over time, with both spiky and bumpy particles showing the strongest signals after particles had been left for one month.

The morphological changes that occur over time are likely the result of Ostwald ripening, where the "spiky" areas with a small radius are less energetically stable and over time, the atoms will migrate to areas of a larger radius that are more energetically stable. Others looking at the long-term stability of CTAB-stabilized gold nanostars have observed this phenomenon.[290] A possible solution is to replace CTAB as a stabilizing group with a molecule that forms a monolayer through Au-S bonds; for example, by using 3-mercaptopropionic acid, researchers greatly improved the stability of high-aspect ratio nanostars.[291]

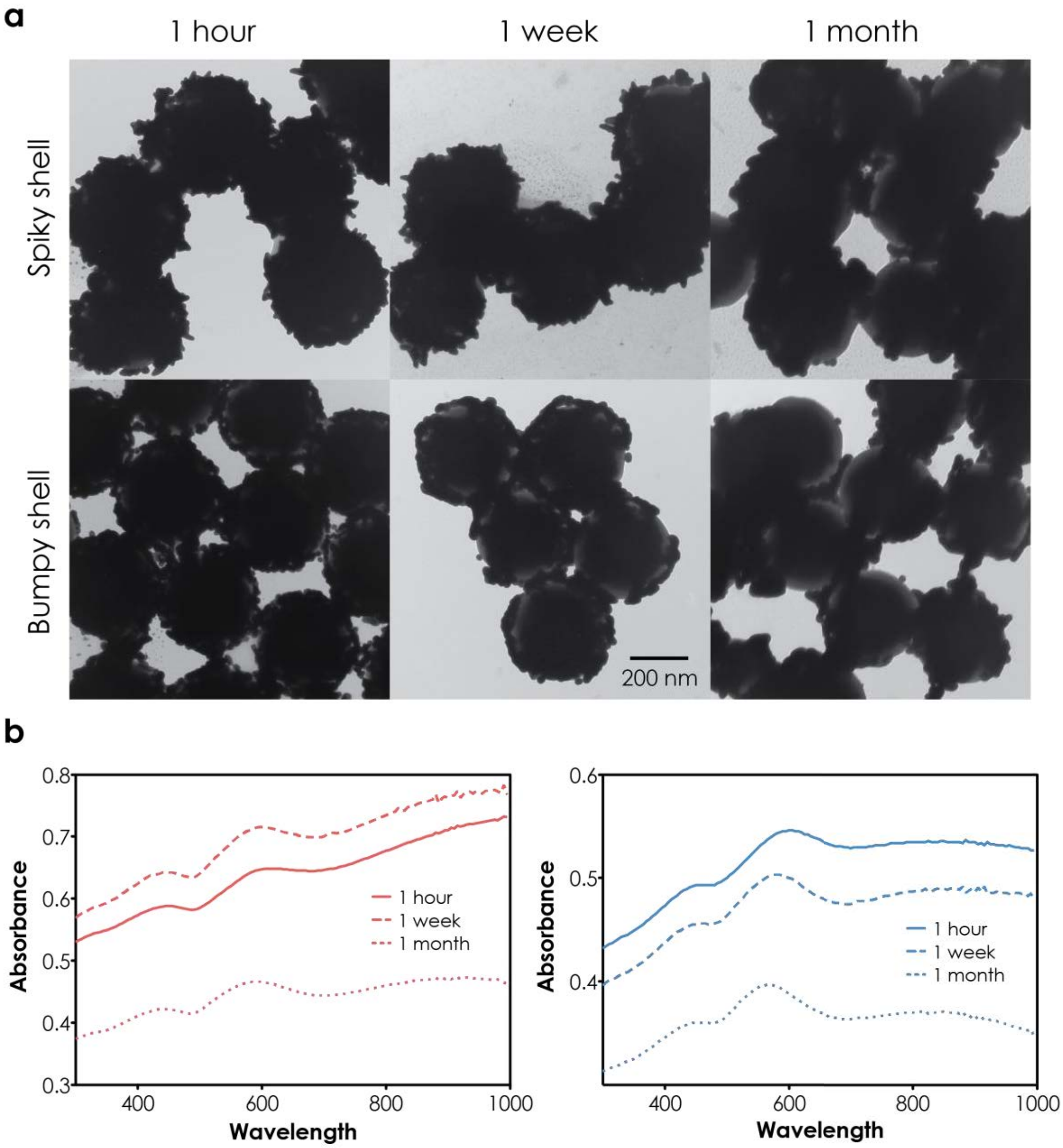

Figure 5.16: a) TEM images showing representative particles over time and b) corresponding UV-Vis extinction spectra for (left) spiky particles and (right) bumpy particles over time

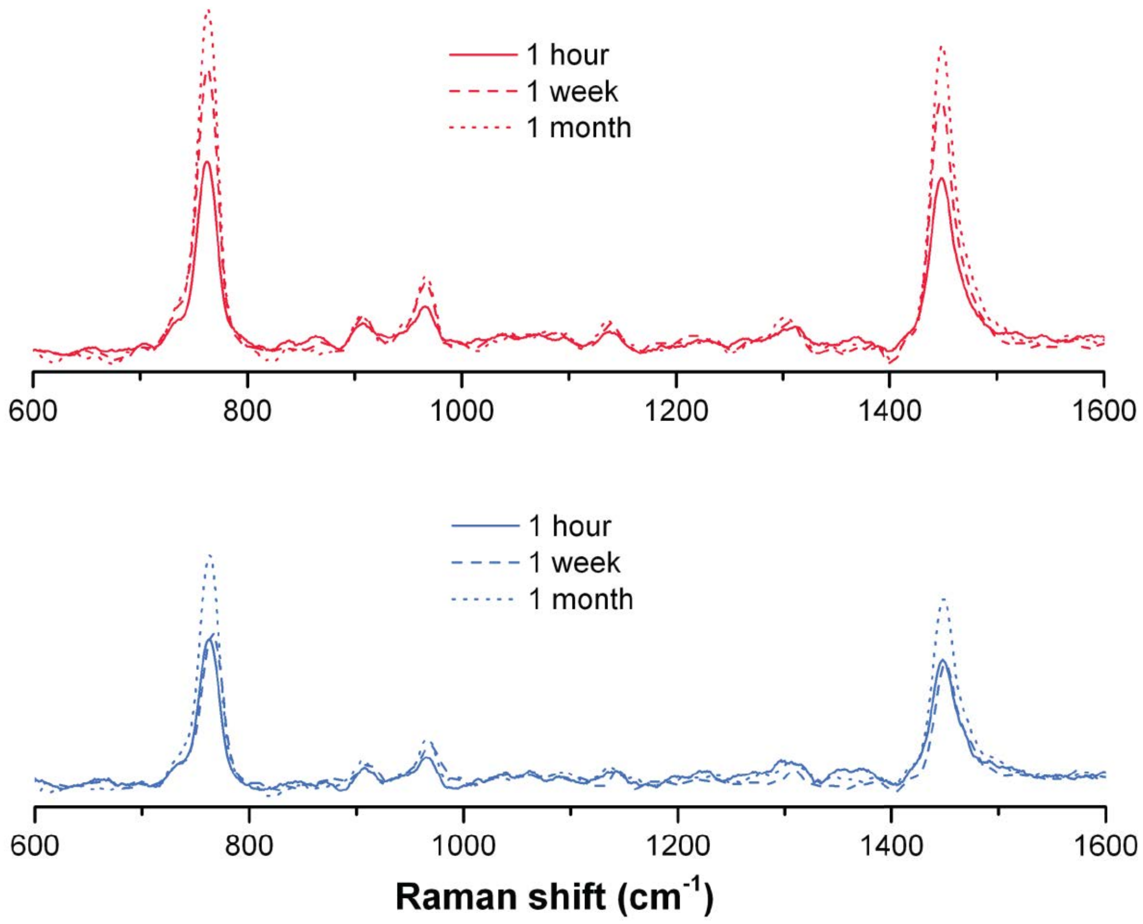

Figure 5.17: Raman spectra of (top) spiky and (bottom) bumpy particles in 167 μM CTAB

5.5 Conclusion

We synthesized spiky gold-coated superparamagnetic particles that are magnetically separable and can be used for surface enhanced Raman scattering (SERS) detection of a model molecule. This demonstrates a first step in the development of particles that can be used for combined separation and detection of biomolecules. The nanostructured gold shells enhance the SERS signal of an analyte bound to the surface and the signal increases with increased analyte binding. The morphology of the nanostructured shell plays a role in SERS enhancement—spiky shells lead to greater enhancement than bumpy shells—but the morphology also affects the stability of the particles over time—bumpy shells are more stable than spiky shells, showing fewer morphology changes and less change in SERS enhancement over time.

Chapter 6: Nanostructured gold shells on magnetic particles for oligonucleotide detection

6.1 Summary

Combined separation and detection of biomolecules has the potential to speed up and improve the sensitivity of disease detection, environmental testing, and biology laboratory experiments. In this chapter, we use the particles synthesized in Chapter 5 to magnetically separate out oligonucleotides and detect them using SERS. The particles were successfully used as SERS substrates to detect oligonucleotide binding without requiring particle aggregation. The distance dependence of the SERS signal was then harnessed to detect DNA hybridization using a Raman label bound to a hairpin probe. The distance of the Raman label from the surface increased upon complementary DNA hybridization, leading to a decrease in signal intensity.

6.2 Introduction

Methods to detect DNA sequences using base-pair recognition are often used in disease diagnosis and research.[69,292,293] Purifying out the DNA from the complex physiological fluid is a typical first step. One useful purification method is magnetic separation; the DNA is selectively bound to the surface of magnetic particles, which are then separated from the sample using a magnet.[19-21] For highly sequence selective purification, a probe oligonucleotide that is complementary to the DNA sequence of interest can be bound to the surface of the magnetic particles so that the target DNA will hybridize and can be separated.[22,23] In most cases, the purified DNA is then dissociated from the magnetic particles for subsequent analysis, but since the biomolecule is already pre-concentrated and specifically hybridized to the surface, an interesting possibility is to directly detect it while still bound. Surface-enhanced Raman spectroscopy (SERS) is an appealing method for this purpose. In SERS, the Raman scattering signal of molecules bound to a rough metallic surface is enhanced, meaning that fingerprint specificity of molecules bound to or near the surface is possible. In Chapter 5, we showed how particles of this type could be synthesized by forming a shell that acts as a SERS substrate on magnetic cores. Here, we look at binding oligonucleotide probes to the particles and using them to detect complementary sequences as a proof-of-concept of SERS detection of biomolecules using the nanostructured gold shell-coated magnetic particles.

Often, particle-based SERS methods involve adding salt to induce particle aggregation; this leads to greater enhancement by capturing the molecule of interest in nanogaps that greatly enhance the electromagnetic signal. While aggregation successfully enhances the signal, it presents issues regarding quantification, reproducibility and the ability to perform multiple analysis steps.[294-297] Aggregation-free methods are of interest as a way to overcome these challenges. Methods that rely on enhancement by individual particles include forming sharp tips on their surface, in the way of nanostars[103,147] or spiky particles [105,165,171,173,298], or by forming controlled nanogaps.[160] These methods have been discussed in detail in Chapter 2.

Another challenge in biomolecular detection using SERS is the sensitivity of the signal to multiple factors, including the molecule orientation, interaction with the surface, and distance from the surface, leading to problems with reproducibility and limiting the applications that may seem possible at first glance. The distance dependence of the signal is a crucial factor as signal intensity quickly decreases away from the surface, meaning that many biomolecules are larger than what can be fully detected—specifically, those that extend more than approximately 10 nm from the surface.[299-301] Signal intensity (I) due to electromagnetic enhancement in SERS has been shown to vary with distance (x) according to the following equation:[301-304]

$$I = \left(1 + \frac{x}{a}\right)^{-r}$$

The intensity fall-off with distance depends on characteristics of the substrate, including the effective radius of the metal structures (a) and other geometric factors that can lead to variation in the value of r. By modeling the surface as non-interacting ellipsoidal protrusions with a tip with a local radius of curvature a, the distance dependence of the SERS signal based on theory is proportional to $(x/a)^{-10}$.[302]

Label-free methods of detection using SERS are of interest because they can reduce the number of steps required for detection and because of the fingerprint specificity obtainable by SERS. Label-free detection of nucleic acids using SERS has been used to quantitatively analyze ssDNA,[305] identify single-base mismatches,[306,307] and to differentiate between ssDNA and dsDNA,[299,308,309]. This latter task can still be challenging, especially at the low concentrations seen with hybridization detection, since the same four bases are usually present in both probe and target. In addition, when this involves selective capture, a capture probe must first be bound to the surface, leading to an orientation-dependent signal[299,310] that can increase the challenge of hybridization detection.

Another approach is to harness the distance dependence of the signal by using a Raman tag bound to the probe; the probe is designed so that the proximity of the tag relative to the surface changes upon target binding, resulting in a signal change.[311-316] While this approach loses the direct correlation between the molecule and the signal (and thus potential information on the nature of the binding interaction), it still has the benefit of not requiring an extrinsic tag and has the potential for quantitative measurement of binding, both being beneficial features in a DNA detection method. It also offers the potential for multiplexed detection, as different tags providing different Raman signals can easily be used.[317,318]

In this chapter, we examine the specific characteristics of the nanostructured gold-coated magnetic particles as SERS substrates for oligonucleotide detection. We begin by demonstrating the ability of the particles to provide a SERS signal of oligonucleotide probes bound to the surface without requiring aggregation, then use this to study probe binding to the surface, as the nature of the probe binding is critical to obtaining efficient recognition of biomolecules. We then show initial results demonstrating the use of the particles in detecting specific sequences of DNA through hybridization.

6.3 Experimental Section

6.3.1 Materials

The materials used to synthesize to particles are given in Chapter 5. All oligonucleotides were purchased from IDT (Integrated DNA Technologies, Coralville, Iowa). DNA stock solutions were prepared in Millipore water then diluted in buffer (see below). For the micro-Raman experiments, the sequence used was an interferon-γ (IFN-γ) aptamer,[319-321] HS-$(CH_3)_6$-5′-GIG GTT GGT TGT GTT GGG TGT TGT GT-3′, purchased as a disulphide and reduced to a thiol using tris(2-carboxyethyl)phosphine (TCEP), purchased from Sigma Aldrich. For the oligonucleotide ruler experiment, the sequences used are listed in Table 6.2. For the hybridization experiments, the sequence used for the probe was Cy5-5′-TTTTTCGCTCCCTGGTGCCGTAGATGAGCGTTTTT-3′-$(CH_3)_3$-SH (also purchased as a disulphide), the complementary target sequence was 5′-ATCTACGGCACCAGG-3′, and the non-complementary target sequence was 5′-TCACACGGAGGCTAC-3′. Both 3-mercapto-1-propanol (MCP) and 6-mercapto-1-hexanol (MCH) were purchased from Sigma Aldrich.

6.3.2 Methods

6.3.2.1 *Particle synthesis and characterization*

Particles were synthesized using the procedure described in Chapter 5.

For the micro-Raman experiments, different morphologies were obtained by varying the amount of CTAB and the amount of time left in growth solution: super spiky particles were made using 100 mM CTAB and grown for 30 minutes, spiky particles were made using 100 mM CTAB and grown for 20 minutes, and bumpy particles were made using 10 mM CTAB and grown for 5 minutes.

For the oligonucleotide ruler and hybridization detection experiments, all particles used were spiky particles made using 100 mM CTAB and grown for 20 minutes.

Particles were characterized using TEM, UV-Vis, and Raman spectroscopy (see Chapter 5 for descriptions of methods) to confirm that results were consistent with previous work.

6.3.2.2 Oligonucleotide and mercapto-alcohol binding and characterization

Thiol-modified oligonucleotides were diluted to 100 μM and mixed with an equal volume of acetate buffer (500 mM, pH 5.2). To activate the thiol groups, TCEP was prepared at 10 mM and added at 5 μl for every 100 μl of above solution; this was left at room temperature for 1 hour.

For the micro-Raman experiments, 100 μl of gold-coated magnetic particles were used for each sample. Thiol-modified oligonucleotides with sequence 5′-GI GGTTGGTTGTGTTGGGTGTTGTGT-3′ were used. The particles in CTAB solution were added to microcentrifuge tubes (low DNA binding) and magnetically decanted; to the particles, 250 μl of Millipore water and 77.5 μl of the above oligonucleotide solution were added. A control sample was also made without particles, using 250 μl of Millipore water and 77.5 μl of the oligonucleotide solution.

For the oligonucleotide ruler and hybridization experiments, 50 μl of gold-coated magnetic particles were used for each sample. The particles in CTAB solution were magnetically decanted; to the particles, 100 μl of Millipore water with 0.1% Tween 20 and 52.5 μl of the above oligonucleotide solution were added for each of the different oligonucleotides.

MCP and MCH were diluted to 100 μM in 0.1% Tween 20. To activate the thiol groups, TCEP was prepared at 10 mM and added at 5 μl for every 100 μl of above solution; this was left at room temperature for 1 hour. Following this activation, 50 μl of gold-coated magnetic particles were magnetically decanted and redispersed in 50 μl of the MCP or MCH.

For all experiments, samples were mixed by pipetting. The microcentrifuge tubes were covered with aluminum foil and placed on a rotating mixer overnight. The next day, samples were magnetically decanted and washed three times in Millipore water or Millipore water with 0.1% Tween 20.

Oligonucleotide binding was confirmed by comparing the UV-Vis signal at 260 nm from the control sample with the supernatant removed after binding.

6.3.2.3 *Hybridization experiment oligonucleotide binding*

ssDNA and dsDNA binding

Thiol-functionalized probe oligonucleotides (100 μM) were combined with an equal concentration of either complementary oligonucleotides, non-complementary oligonucleotides, or water and diluted to 25 μM in 100 mM acetate buffer with 0.04% Tween 20. To activate the thiol groups, TCEP was prepared at 10 mM and added at 20 μl for every 100 μl of stock thiol-functionalized probes added. Hybridization was performed by heating the oligonucleotide mixtures in an oil bath at 94ºC for 2 minutes and then allowed to slowly cool in oil bath to room temperature for 3 hours.

Following the hybridization, 20 μl of gold-coated magnetic particles (1 mg/ml) were added to a microcentrifuge tube and magnetically decanted. The oligonucleotide mixtures were then added to the particles (100 μl) and the tubes were placed on a rotating mixer for 24 hours. The particles were washed in 20 μl of TE buffer (10 mM NaCl, 10 mM Tris, 1 mM EDTA, 0.1% Tween 20).

Hybridization detection

Particles were added to 1 mM MCH with 0.1% Tween 20 and left for 24 hours on a rotating mixer. Particles were then magnetically decanted and washed three times in TE buffer.

To bind the oligonucleotides, 50 µl of particles were magnetically decanted and 100 µl of Millipore water with 0.1% Tween 20 and 52.5 µl of the above oligonucleotide solution were added. The microcentrifuge tubes were covered with aluminum foil and placed on a rotating mixer for 2 hours. Samples were magnetically decanted and washed three times in Millipore water with 0.1% Tween 20.

Hybridization was performed by diluting the complementary or non-complementary oligonucleotides to 5 µM in PBS buffer (0.3 M, pH 7) with 3% dextran sulfate and adding 20 µl to 20 µl of particles (1 mg/ml) following magnetic decantation. Particles were placed in a 94ºC oil bath for 3 minutes, then placed on a rotating mixer in an oven held at 45ºC for 4 hours, then cooled to room temperature and left for 12 hours. Particles were washed three times in TE buffer.

6.3.2.4 *Micro-Raman study of individual particles and small clusters*

To prepare the particles for Raman spectroscopy measurement, the particles were first diluted by a factor of 200 then a 5 µl drop was placed on a cleaned silicon chip and evaporated. Raman scattering spectra of the particles were recorded in the 50–3500 cm^{-1} range on a modular Raman spectrometer (Kaiser Optical Systems, Inc., Model HL5R) equipped with a high-powered near-IR laser diode (785 nm). Before spectra acquisition, an optical microscope (Olympus; 100x objective) was used to focus the laser beam on areas containing only individual particles or small groups of particles (two to four). Focusing on areas that did not contain these particles was confirmed to give only the background silicon signal. Measurements were carried out using a 100x objective. The laser output power was 10 mW, which corresponds to ~1 mW on samples. For each spectrum, 15 acquisitions of 5 seconds each were recorded to improve the signal-to-noise ratio. To normalize the spectra to the number of particles imaged, ImageJ was used to count the particles in the focusing area according to microscope images.

6.3.2.5 *Raman study of oligonucleotide "rulers" and hybridization experiments*

A 20 μl drop of particles was placed on a glass slide with a hydrophobic coating. Raman scattering spectra of the particles were recorded in the 160-2400 cm^{-1} range on a Raman spectrometer (Tornado Spectral Systems) equipped with a near-IR laser diode (785 nm). The laser output power was 100 mW. For each spectrum, 15 acquisitions of 20 seconds each were recorded. Spectra were normalized using the peak height at 1089 cm^{-1}.

6.4 Results and Discussion

6.4.1 Oligonucleotide binding

Following the oligonucleotide binding procedure, the particles were visibly more stable in water or 0.1% Tween 20 solutions than before oligonucleotide binding. The amount of oligonucleotides bound to particles was estimated by measuring the UV-Vis absorbance at 260 nm of the supernatant compared with the initial oligonucleotide solution.

The oligonucleotides are received in disulphide form (Figure 6.1) so we first use TCEP to reduce them to their thiol form. Following TCEP reduction, there are two molecules that can bind to the surface: the thiolated oligonucleotide with an alkane chain as a linker and either 3-mercapto-1-propanol (MCP) or 6-mercapto-1-hexanol (MCH). For the DNA with a 3′ disulphide group, the linker was a three-carbon alkane chain and the corresponding thiol was MCP, while for the DNA with a 5′ disulphide group, the linker was a six-carbon alkane chain and the corresponding thiol was MCH.

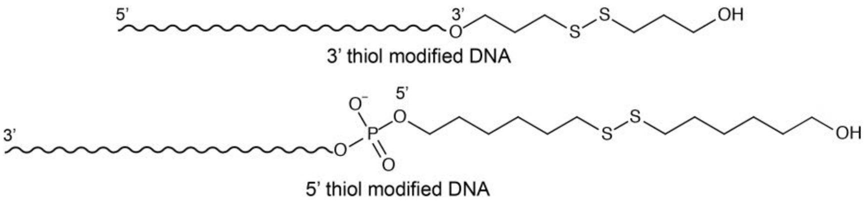

Figure 6.1: Oligonucleotides as received. TCEP is used to reduce them to thiol form.

To better understand what can be seen in the SERS spectra of thiolated oligonucleotides, we compared the spectra of MCP or MCH bound to the particles with the spectra of thiolated oligonucleotides combined with MCP or MCH bound to the particles (Figure 6.2). All spectra show peaks at 640 cm^{-1} and 705 cm^{-1}, which can be assigned to the C-S stretching vibrations (gauche and trans respectively).[225,322,323]

Both oligonucleotides feature the same sequence of bases: A_3C_{12}, where the AAA sequence is closest to the thiolated end. They differ in terms of which end is thiolated (3′ or 5′) and the length of the alkane chain spacer (three CH_2 groups or six CH_2 groups). These differences can be seen in the region from 1200 to 1550 cm^{-1}. When comparing MCP with the 3′ thiolated oligonucleotide + MCP (Figure 6.2a), the peaks at 1303 and 1425 cm^{-1}, assigned to the C-C twisting vibration/C-H deformation vibrations of the alkane groups, remain prominent peaks in the region. Similarly, when comparing MCH with the 5′ thiolated oligonucleotide + MCH (Figure 6.2b), the C-C twisting vibration/C-H deformation vibration peaks at 1303 and 1443 cm^{-1} (of higher intensity than those in MCP) remain prominent in the region.[225]

The influence of the chain length is seen when looking at the nucleotide base vibrations, which also contribute to peaks in the region. Cytosine has a prominent peak at 1300 cm^{-1} and adenosine has one at 1338 cm^{-1}, independent of oligonucleotide orientation.[324,325] Since SERS enhancement is distance dependent, we would expect that a longer linker between the Au-S bond and the nucleotide bases would result in a lower signal from the bases, as long as the chains were in any position but lying flat on the surface. This is what we observe—when a shorter spacer is used (three CH_2 groups), the spectrum features a large peak (relative to the peaks from the alkane spacer) from adenosine at 1338 cm^{-1}. When a longer spacer is used (six CH_2 groups), the same peak is much less prominent relative to the peaks from the spacer.

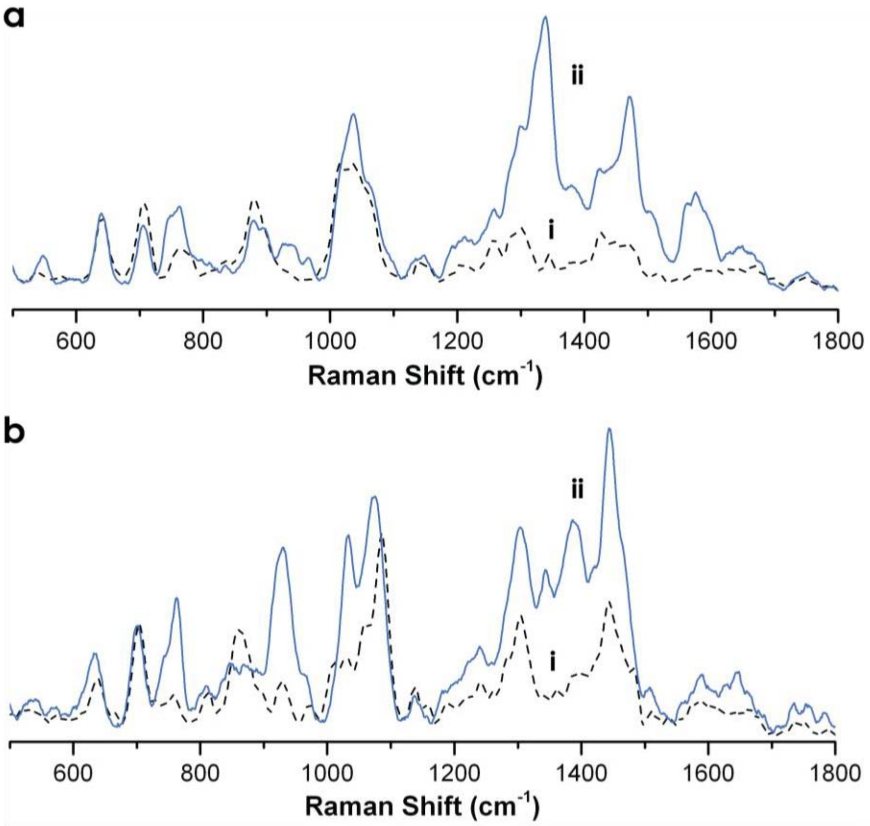

Figure 6.2: SERS spectra of spiky gold-coated magnetic particles functionalized with a) i) 3-mercapto-1-propanol, and ii) oligonucleotides with sequence 5′-$C_{12}A_3$-3′-$(CH_2)_3$-S-, b) i) 6-mercapto-1-hexanol, and ii) oligonucleotides with sequence -S-$(CH_2)_6$-5′-A_3C_{12}-3′

By varying the concentration of oligonucleotides in the binding solution, we can control the amount of oligonucleotides bound to the surface. Figure 6.3 shows the Raman spectra from these experiments, where the ratio of oligonucleotides to particles in the binding solution was varied, left for 24 hours, then washed several times in TE buffer. At lower concentrations, peaks from CTAB (756 and 1441 cm^{-1}) dominated the spectra, but these decreased as higher concentrations of oligonucleotides were used. When lower concentrations of oligonucleotides than shown were used, the particles became unstable and aggregated.

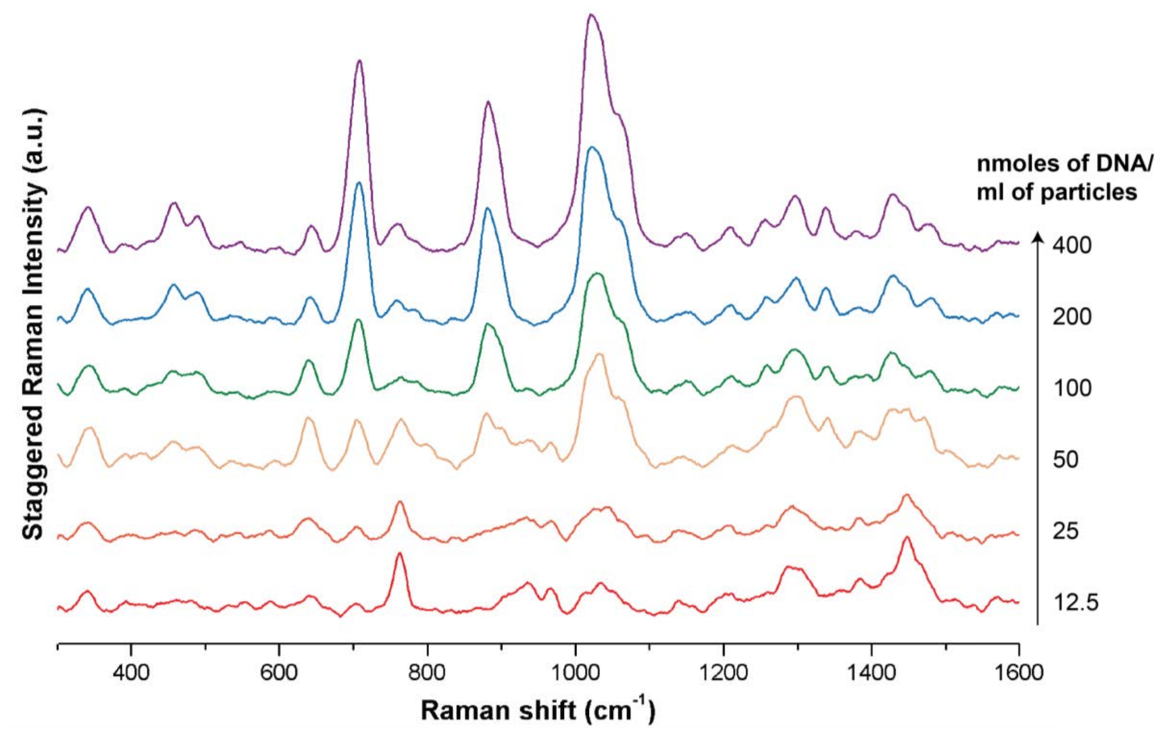

Figure 6.3: SERS spectra of oligonucleotides (5′-$C_8A_3C_4$-3′-S-) bound to particles using different binding concentrations

Using UV-Vis, we measured the concentration of oligonucleotides remaining in the supernatant following binding; due to subsequent washing that may remove non-specifically bound oligonucleotides, this value indicates a maximum amount of oligonucleotides bound, but low measured concentrations in the wash solutions and comparison with the intensity of the Raman peaks suggests that the measurement is accurate in a relative sense (Figure 6.4).

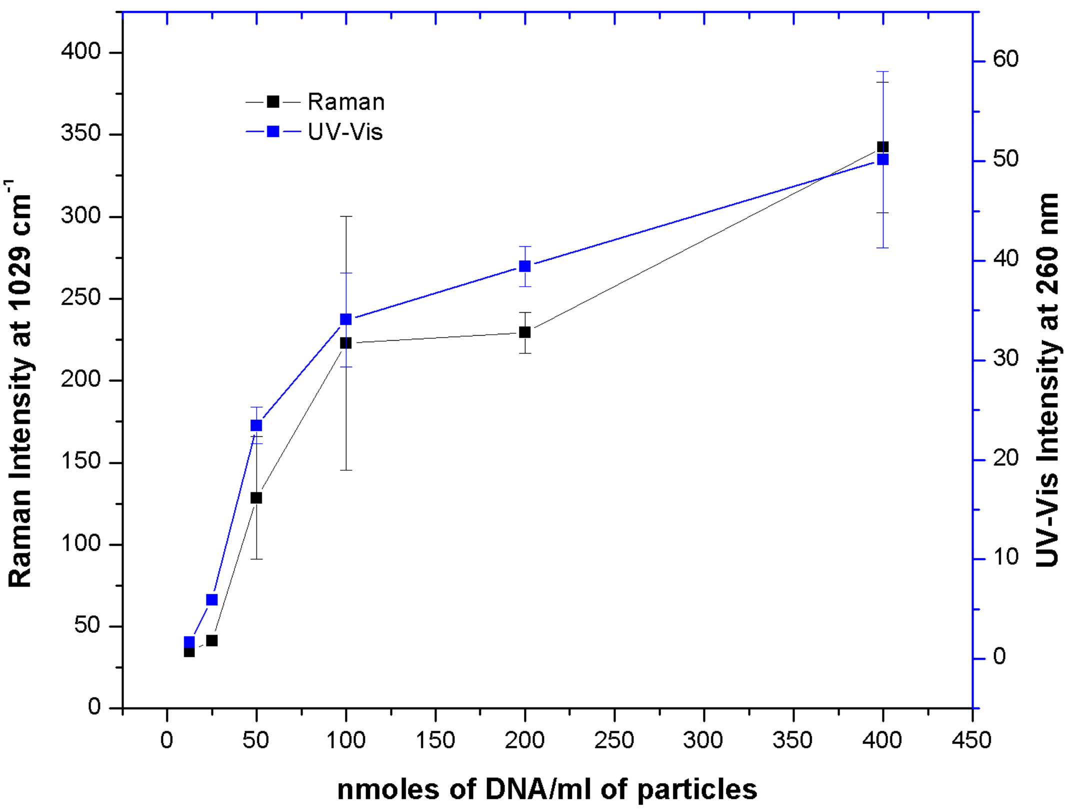

Figure 6.4: Comparison of measured Raman intensity of peak at 1029 cm^{-1} and UV-Vis intensity at 260 nm for oligonucleotides on particles using different binding concentrations

6.4.2 Micro-Raman study of individual particles and small clusters

When SERS measurements are taken using particles in solution, enhancement is often due to nanogaps formed in the space between particles. This led to a question of to what degree the enhancement seen with the nanostructured gold-coated magnetic particles was due to individual particles or to interactions between particles. To study this, we used micro-Raman to focus the laser on both individual particles and small clusters of particles (two to four) to compare the signals.

6.4.2.1 Oligonucleotide binding and Raman spectra

Three different particle morphologies were studied: "super spiky" shells, "spiky" shells, and "bumpy" shells, with the synthesis method described in Chapter 5 and the different synthesis parameters given in Table 6.1. The amount of oligonucleotides bound to each type of particle was measured using the UV-Vis procedure described above. All three particle morphologies showed similar amounts of binding (Table 6.1). The measured concentrations imply that a sub-attomole number of oligonucleotides (on the order of 10^5) are bound to each particle.

Table 6.1: Gold shell synthesis parameters and approximate concentration of oligonucleotides bound

	Particle morphology	CTAB concentration	Time in growth solution	Concentration of oligonucleotides bound
i	Super spiky	100 mM	30 minutes	3.6 µM ± 0.4 µM
ii	Spiky	100 mM	20 minutes	3.7 µM ± 0.4 µM
iii	Bumpy	10 mM	5 minutes	3.8 µM ± 0.3 µM

The spectra obtained in the micro-Raman experiments (Figure 6.5) showed variation between measurements, as would be expected; first, each measurement involves focusing on one to four individual particles so a small number of hot-spots would contribute strongly to the signal and thus vary between measurements, and second, the measurements were taken after drying the particles, so the oligonucleotides are unlikely to remain in a consistent orientation. Despite this, several peaks are consistently present in all measurements. In general, these correspond to alkane chain vibrations, from both the 6-mercapto-1-hexanol and the six carbon spacer group on the oligonucleotide, and appear clearly when the spectra are averaged (Figure 6.6b). The gauche and trans stretching vibrations of the C-S bond are at 625 cm^{-1} and 693 cm^{-1}. Peaks at 1086 cm^{-1}, 1300 cm^{-1}, and 1440 cm^{-1} are also seen in the spectrum for MCH (Figure 6.2) and correspond to C-C skeletal vibrations and C-H deformation vibrations.[225] Large peaks at 2850 cm^{-1} and 2915 cm^{-1} correspond to the alkane C-H asymmetric and symmetric stretching vibrations.[225] The large, broad peak at 940 cm^{-1} is from the silicon substrate. Variations between spectra in the region from 1200 to 1550 cm^{-1} are likely due to nucleic acid bases and would vary with oligonucleotide position and orientation near hot-spots.

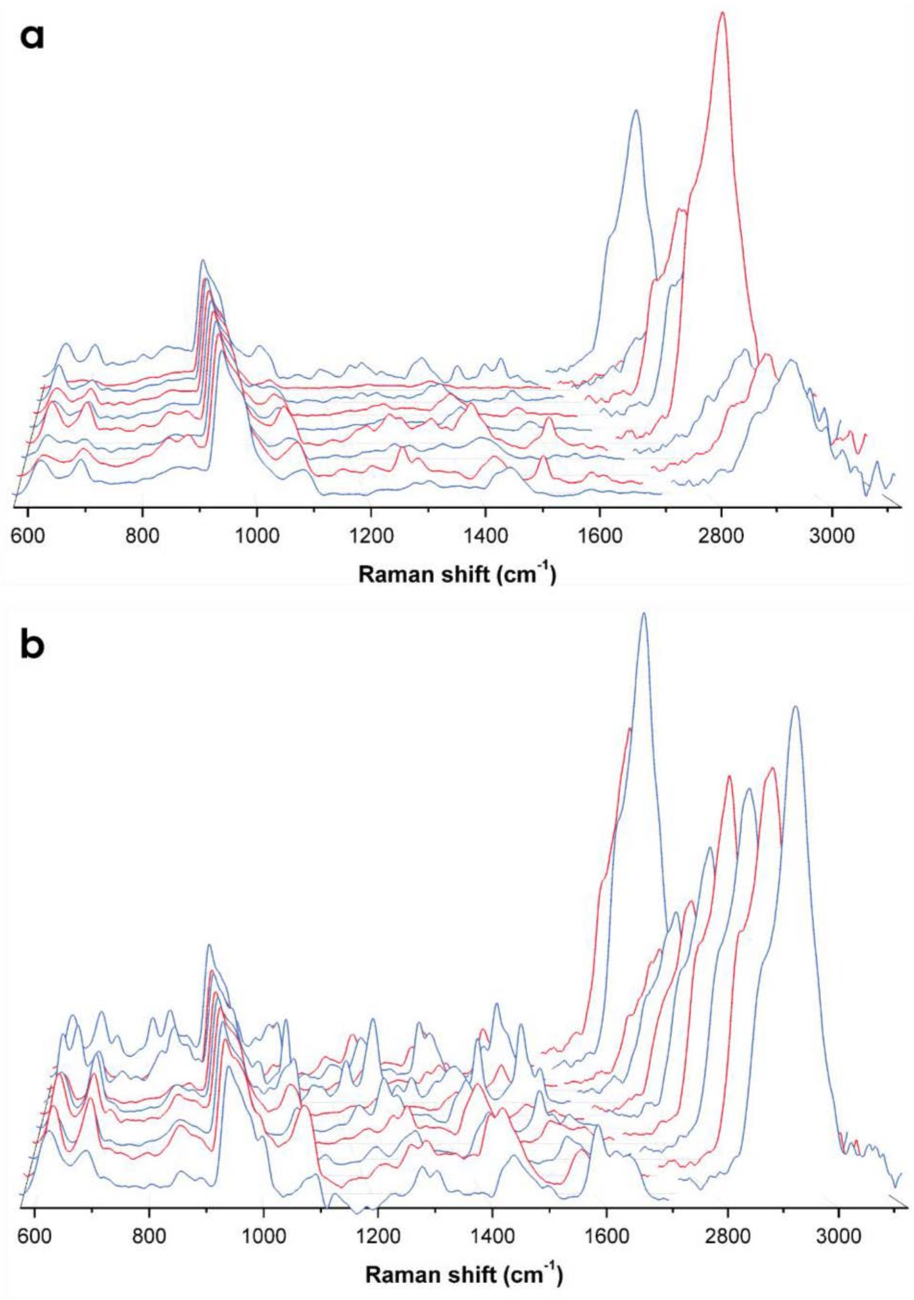

Figure 6.5: Micro-Raman (SERS) spectra of thiolated oligonucleotides bound to spiky gold-coated magnetic particles on silicon. Each spectrum represents a separate measurement focusing on a) individual particles and b) small groups of particles (2-4)

6.4.2.2 *SERS signal is due to nanostructures on individual particles*

To compare the signal from individual particles with the signal from small groups of particles, we used several different morphologies of particles (see Figure 6.6a) and averaged the signals from several different positions on the surface (seven to ten positions for each particle type) to obtain the spectra in Figure 6.6b. We used the background signal of the silicon substrate, specifically the peak at 939 cm^{-1}, to confirm that the signal variation was from the particles. The signals from the small groups of particles were larger than the signals from individual particles. Variations between the spectra were indicative of SERS hot-spots—certain features of each spectrum were similar, but others differed, likely due to different modes of the oligonucleotides being highlighted by different hot-spots. Once averaged, the features that become most clear corresponded to the parts of the molecule expected to be closest to the gold surface, specifically the thiol group and carbon linker chain, as discussed in (oligonucleotide binding section).

For further comparison, we determined the average number of particles in each small group of particles and normalized the average spectrum from small groups of particles using that value. The resulting spectrum is shown as the dotted red line in Figure 6.6b. Following the normalization, the difference between mean peak heights of the normalized spectra and the spectra of individual particles is not statistically significant. This suggests that the enhancement comes from the nanostructures on individual particles rather than nanogaps occurring between particles.

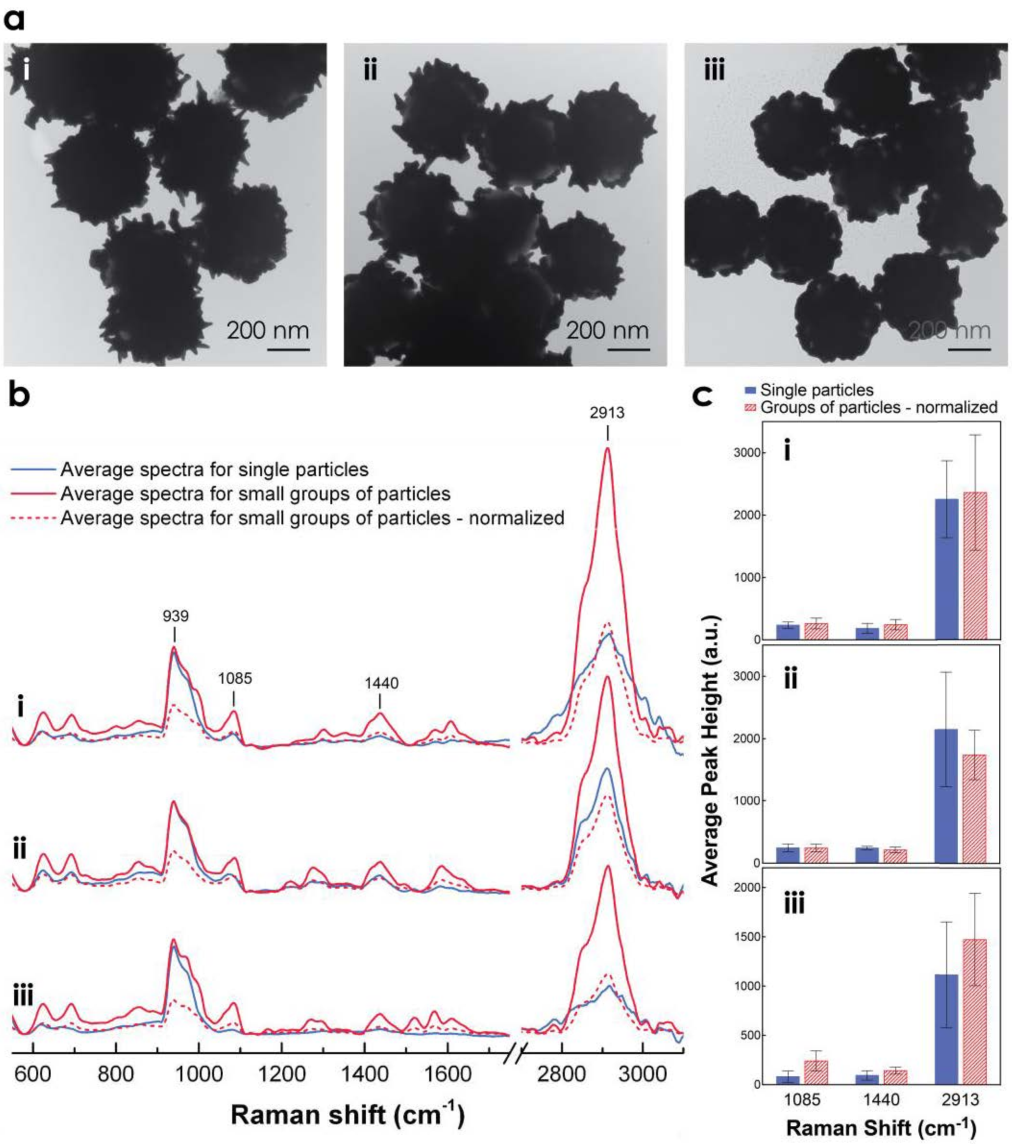

Figure 6.6: a) TEM images of particles with different gold shell morphologies: i) super spiky shells, ii) spiky shells, and iii) bumpy shells. b) Average micro-Raman (SERS) spectra of 7-10 measurements for (blue) individual particles, (solid red) small groups of particles, and (dashed red) small groups of particles normalized using the average number of particles in the measurements, which were i) 2.2, ii) 2.8, and iii) 2.4. c) Graphs highlighting average Raman spectra peak height similarity between signals from single particles and small groups of particles after adjusting for the average number of particles. No pairs of means show significant differences. Error bars indicate 95% confidence intervals.

6.4.2.3 *Particle morphology influences Raman signal of individual particles*

We also compared the Raman signal enhancement of different morphologies of particles. Three different morphologies were studied: "super spiky" shells, "spiky" shells, and "bumpy" shells. The different morphologies were synthesized by varying the growth parameters, as described in Chapter 5. All three particle types had similar amounts of oligonucleotide binding based on UV-Vis measurement (Table 6.1), so any differences between peak heights can most likely be attributed to differences in signal enhancement due to particle morphology.

We compared the peak heights of average spectra and found that the same trend occurred as seen when looking at the SERS signal from CTAB on particles in solution (Chapter 5); SERS enhancement was larger on spiky shells compared with bumpy shells. This was the case for both spiky shells and super spiky shells, but these two types showed no significant difference in enhancement.

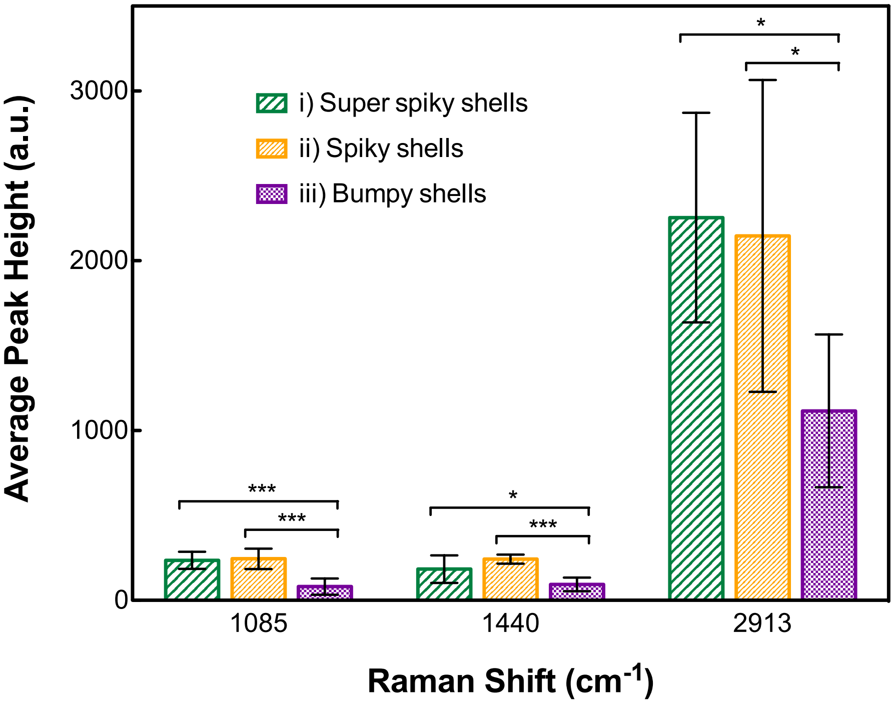

Figure 6.7: Graphs highlighting average micro-Raman (SERS) spectra peak height differences between signals from particles of different morphologies. Significant differences are indicated by asterisks: (*) indicates p ≤ 0.05 and (***) indicates p ≤ 0.001. Error bars indicate 95% confidence intervals.

6.4.3 Raman study of oligonucleotide "rulers"

The signal enhancement of SERS is a highly distance-dependent phenomenon.[299-304] To determine which future applications of the particles would be possible or ideal, it is important to characterize the distance dependence specific to the particles. Other researchers have used an oligonucleotide "ruler" approach to characterize the distance-dependence enhancement;[300,301,304] as the actual relationship between enhancement and distance from the surface varies by substrate,[302] oligonucleotide rulers were used to characterize the relationship for the spiky particle surfaces. We bound seven different thiolated oligonucleotides to the particles, each featuring three adenine bases at different positions within a series of cytosine bases (Table 6.2i-vii), as well as an all cytosine oligonucleotide for a baseline (Table 6.2viii).

Table 6.2: Oligonucleotide sequences used as "rulers"

	Position of AAA	Oligonucleotide Sequence
i	1	5'-CCCCCCCCCCCCAAA-3'-$(CH_3)_3$-S-
ii	2	5'-CCCCCCCCCCCAAAC-3'-$(CH_3)_3$-S-
iii	4	5'-CCCCCCCCCAAACCC-3'-$(CH_3)_3$-S-
iv	5	5'-CCCCCCCCAAACCCC-3'-$(CH_3)_3$-S-
v	7	5'-CCCCCCAAACCCCCC-3'-$(CH_3)_3$-S-
vi	10	5'-CCCAAACCCCCCCCC-3'-$(CH_3)_3$-S-
vii	13	5'-AAACCCCCCCCCCCC-3'-$(CH_3)_3$-S-
viii	-	5'-CCCCCCCCCCCCCCC-3'-$(CH_3)_3$-S-

The Raman spectra following oligonucleotide binding are shown in Figure 6.8. Spectra were normalized using the peak at 1035 cm^{-1}, which corresponds to a C-C stretching absorption (mostly due to the alkane spacer) and varies little between oligonucleotide sequences. Normalization was used because of bound concentration variations with oligonucleotide type. Two replicates were prepared for each oligonucleotide type and are shown overlaid; generally, there was high reproducibility between samples. The relative peak heights associated with adenine bases and cytosine bases vary with adenine position. Specifically, peaks that increase with the proximity of adenine to the surface are at 748 cm^{-1}, 1338 cm^{-1}, and 1472 cm^{-1}; peaks that increase with the proximity of cytosine to the surface are at 764 cm^{-1}, 1300 cm^{-1}, and 1645 cm^{-1}. Previous research has shown that non-thiolated oligonucleotides adsorbed non-specifically to SERS substrates have signals that vary significantly with adenine/cytosine content but do not vary significantly when adenine position is changed;[324] we thus conclude that the oligonucleotides are most likely, on average, oriented in a stretched, upright or slightly angled position with the sulfur group bound to the gold surface. Previous research also confirms that this is the most likely result.[299,301,326]

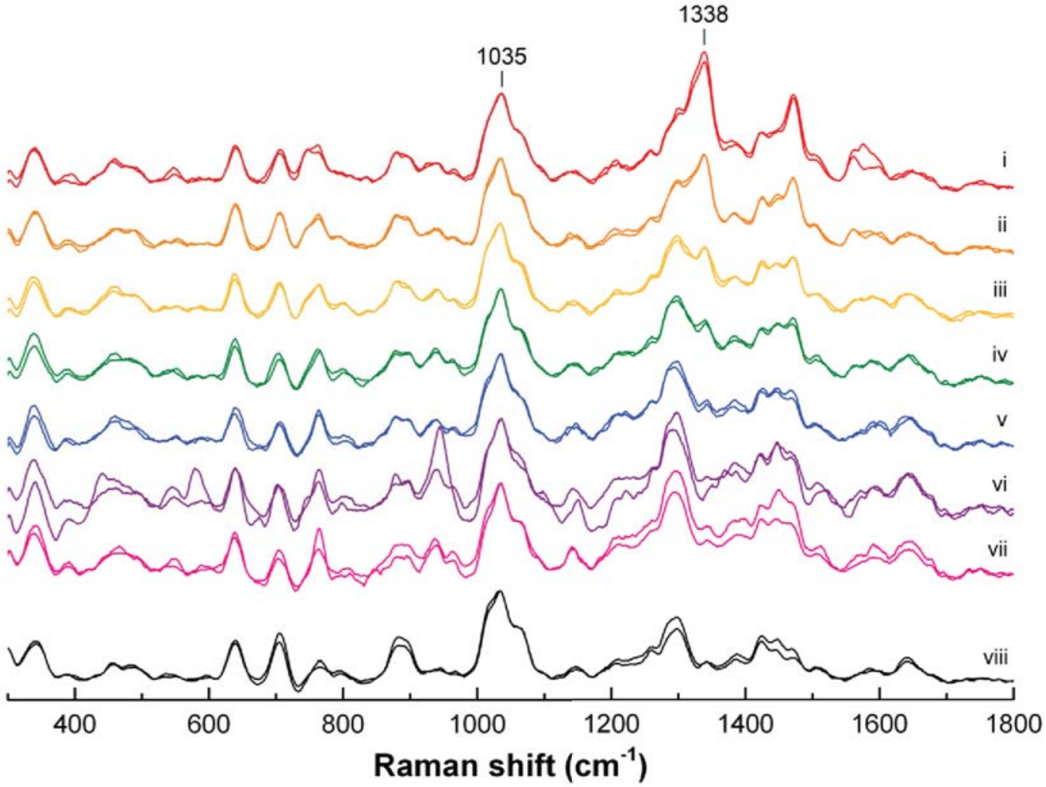

Figure 6.8: SERS spectra of oligonucleotide "rulers" bound to spiky gold-coated particles. The rulers (i-vii) correspond to those listed in Table 6.2. Two spectra are shown overlaid for each oligonucleotide.

To take this idea a step further, we fit the normalized intensity of the peak at 1338 cm^{-1} (adenosine ring stretching)[325] to a theoretical model that others have used to describe distance dependence, shown below.[301-304]

$$I = \left(1 + \frac{x}{a}\right)^{-10}$$

The model assumes a surface of electromagnetically isolated ellipsoidal protrusions of equal radius of curvature, *a*; since few real substrates fit this ideal model, the true distance dependence may not be x^{-10}, but this value is used for comparison with other work.

The length of the oligonucleotides includes the spacer group, bound to gold through the sulfur atom, and the chain of fifteen bases. The length of the spacer group can be estimated by looking at the length of similar groups (propanethiol and its derivatives) on gold. For 3-mercaptopropionic acid, the estimated layer thickness is 0.83 nm[227], which we use as an approximate value of the length of the spacer group bound to gold and to the oxygen of the first base. We use 0.7 nm as an upper-limit of the length per base of the single stranded oligonucleotides.[327,328] Again, as an upper-limit, we assume that the oligonucleotides are oriented normal to the surface. Thus, we estimate a maximum distance between each base and the gold surface, x, to be $0.83 + 0.7n$, where n is the position of the base in the chain.

The data was fit to the model by summing the calculated intensities of the three adenine bases and fitting it to the experimental intensities using a nonlinear least-squares fit. The solid red line in Figure 6.9 shows the values obtained by the model. The theoretical radius of curvature, a, was 23 nm, a value which is in the range of the substrate features observed by TEM if the theoretical model is taken to be suitable for the substrate.

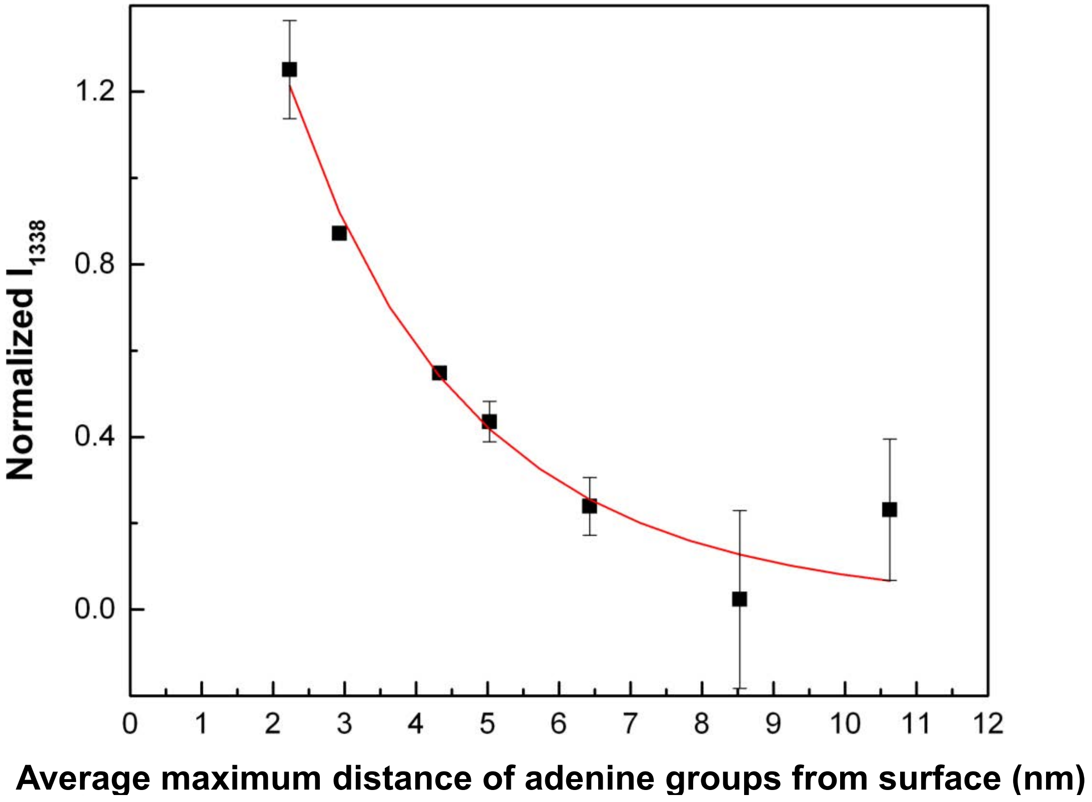

Figure 6.9: Normalized Raman peak intensity (I_{1338}) for oligonucleotides with different adenine group positions. The red line shows a fit to the data based on the distance dependence of the SERS signal. Error bars indicate a 95% confidence interval.

6.4.4 DNA hybridization detection

6.4.4.1 *Investigating signal differences between ssDNA and dsDNA*

Detecting DNA hybridization on the particles presents a challenge. Ideally, a label-free method would be used, where a change in signal occurs directly upon target binding to the probe. The above results, along with those seen in literature,[299,305-309] show that the Raman signal can vary with base composition, so it might be expected that DNA hybridization would present a different signal.

An alternative route to detect DNA hybridization that still does not require an extrinsic tag is to use a hairpin probe with a Raman tag attached to the end (Figure 6.10). This method takes advantage of the distance dependence of the SERS signal. Before adding a hybridizing target, the probe forms a hairpin structure that draws the Raman tag to the surface, so the signal from the Raman tag is high (closed position). When a target strand hybridizes with the probe, the hairpin will extend and bring the Raman tag away from the surface, so the signal from the Raman tag will decrease due to the distance dependence of the SERS enhancement (open position).

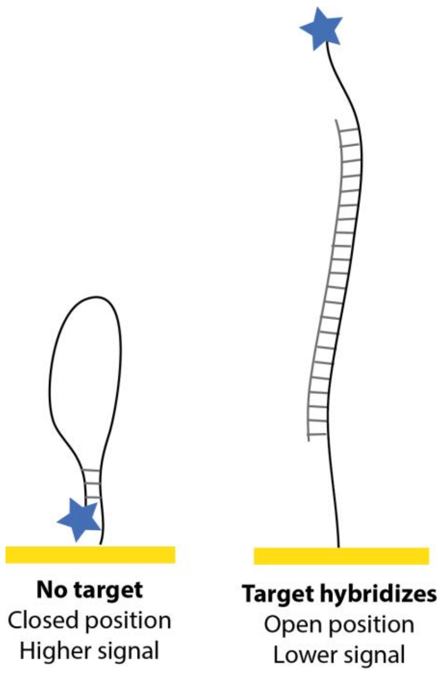

Figure 6.10: Scheme of hairpin probe with Raman tag, before and after hybridization to target strand

To test these two methods, we first tried performing the hybridization steps in solution using the thiolated probe DNA combined with complementary or non-complementary DNA, or without any additional DNA (binding probe ssDNA to the surface). Assuming that the complementary DNA fully hybridizes with the probe DNA, this gives a potential maximum signal change while avoiding the challenge of performing hybridization to a surface-bound probe.

The signals from the case of label-free, direct detection (where no Raman tag was used) are shown in Figure 6.11. No obvious changes could be observed between the case where dsDNA should have been binding compared with the case where ssDNA should have been binding. This is shown in Figure 6.11b, where the spectra from the dsDNA and ssDNA have been normalized by the peak at 1087 cm^{-1}, which corresponds to the alkane linker. In the case of non-complementary DNA combined with the probe DNA, there are additional peaks that are likely due to non-specific binding of the non-complementary oligonucleotide to the surface (Figure 6.11a).

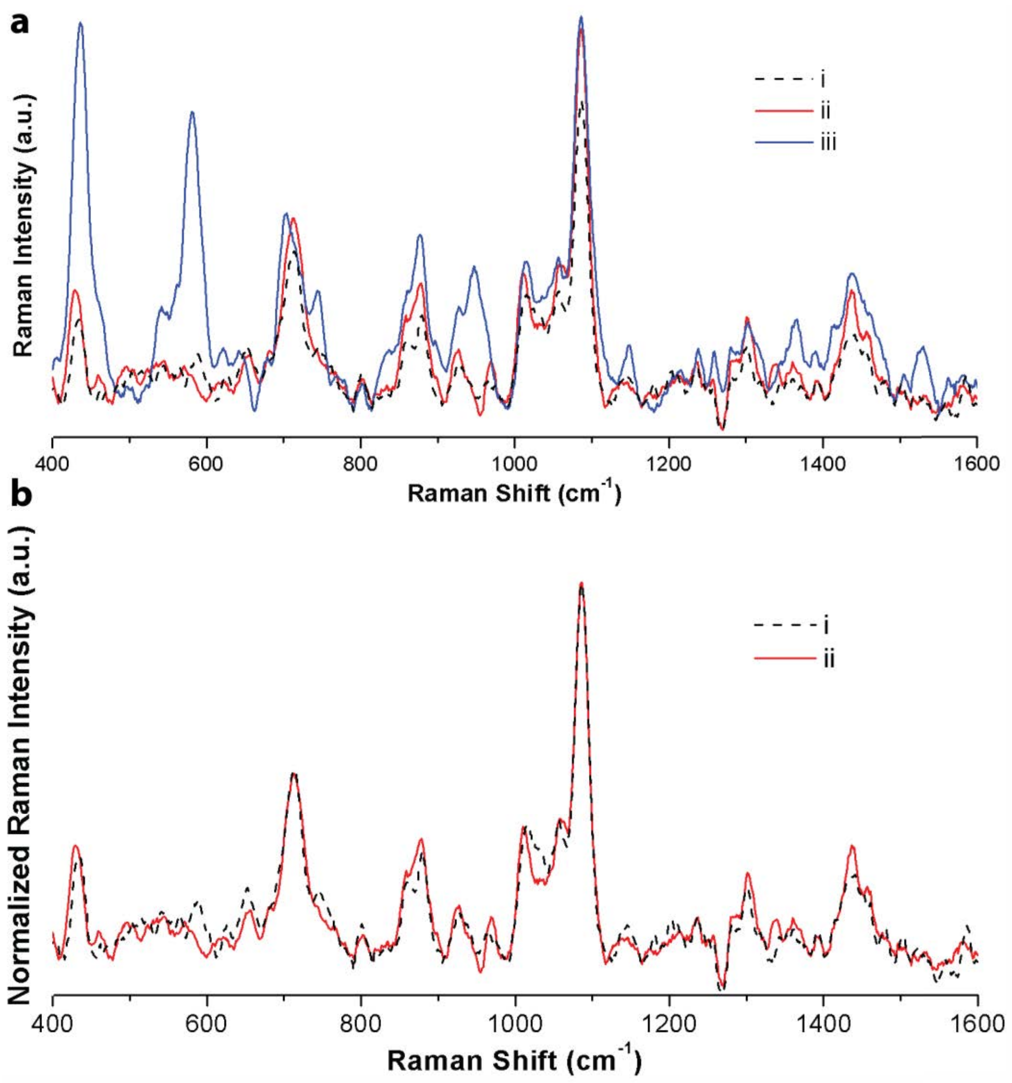

Figure 6.11: a) SERS spectra and b) normalized SERS spectra (using intensity at 1087 cm^{-1}) of i) oligonucleotide probes only, ii) oligonucleotide probes hybridized with complementary oligonucleotides, and iii) oligonucleotide probes hybridized with non-complementary oligonucleotides

We performed a similar experiment with the thiolated hairpin probe, using Cy5 as a Raman tag. In this case, the signal from the Cy5 tag should be lower in the case of dsDNA binding (probe and complementary oligonucleotides) compared with ssDNA binding (probe and non-complementary oligonucleotides or only probe). Figure 6.12

demonstrates that this is what is observed. In the case of complementary and non-complementary DNA, we observe similar peak intensities from the thiolated alkane chain linker (C-S bonds at 707 and 646 cm^{-1} and alkane chain at 1023 cm^{-1}), but lower peak intensities (50-60% of that from non-hybridized samples) from the Cy5 tag (558 cm^{-1}, many peaks in region from 1100-1600 cm^{-1} including 1189, 1363, and 1600 cm^{-1}).

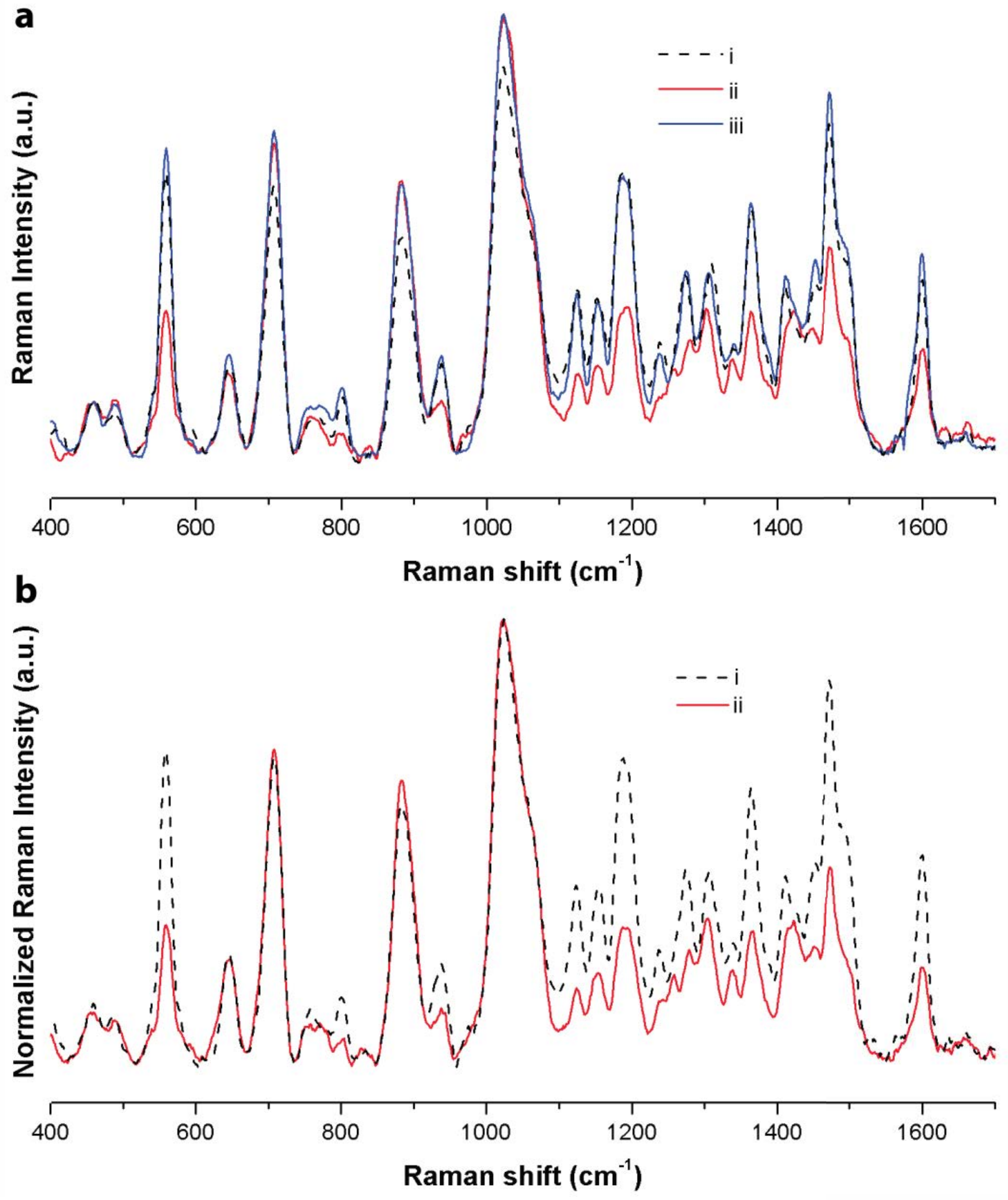

Figure 6.12: a) SERS spectra and b) normalized SERS spectra (using intensity at 1023 cm^{-1}) of i) Cy5-tagged oligonucleotide probes only, ii) Cy5-tagged oligonucleotide probes hybridized with complementary oligonucleotides, and iii) Cy5-tagged oligonucleotide probes hybridized with non-complementary oligonucleotides

Based on these results, the method using a hairpin probe with a Raman tag seemed more promising as it resulted in a larger signal change between ssDNA and dsDNA.

6.4.4.2 *Hybridization experiments*

The above experiments demonstrated that the signal changes when double-stranded versus single-stranded oligonucleotides are bound to the surface. A next step is to detect hybridization between target DNA and probe DNA bound to the surface. We bound the Cy5-tagged hairpin probe to the surface of the particles then compared the signal from hybridization with 5 μM of complementary and non-complementary targets to the probes. The high concentration of target oligonucleotides was used to ensure that binding was favoured in the equilibrium.

The obtained Raman signal from these samples was normalized using the intensity of the peak at 1087 cm^{-1} (corresponding to the alkane linker, thus normalizing based on the amount of probe DNA bound to the surface). The signal of Cy5 is lower when complementary DNA is used compared with non-complementary DNA, which is consistent with hybridization causing the hairpin probe to open and increase the distance of Cy5 from the surface (Figure 6.13). In Figure 6.13b, the difference is highlighted by the fact that the peak at 712 cm^{-1}, corresponding to the C-S bond of the thiol linker, is of similar intensity for all samples, while the peaks corresponding to Cy5 (558, 1189, 160 cm^{-1}) for the sample using complementary DNA are 60-70% of the intensity of peaks from the probe only or the sample using non-complementary DNA.

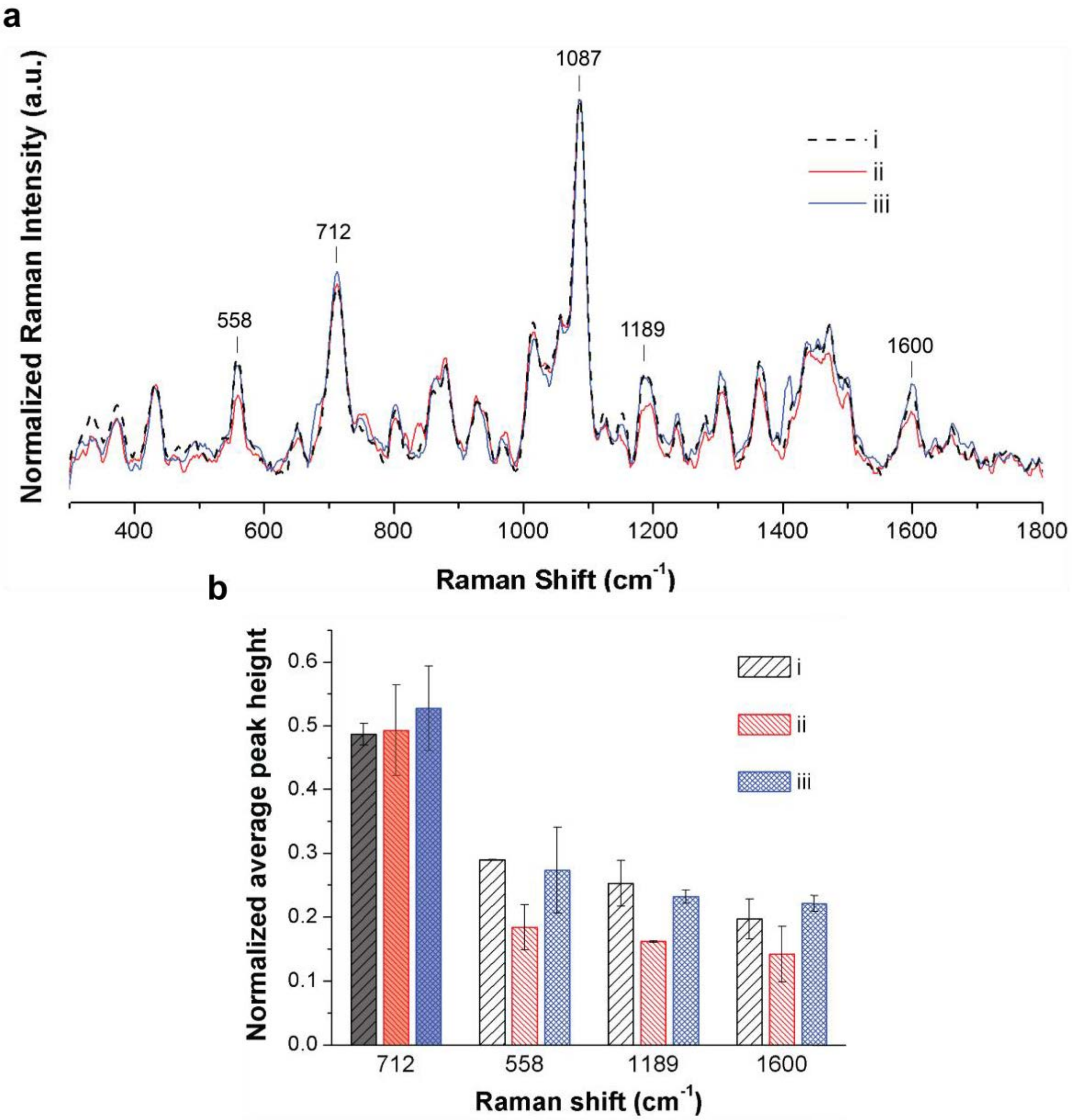

Figure 6.13: a) Normalized SERS spectra and b) average peak height of i) Cy5-tagged oligonucleotide hairpin probes, ii) hybridization with complementary oligonucleotides and iii) hybridization with non-complementary oligonucleotides. Error bars indicate 95% confidence intervals.

The hybridization conditions and/or the probe binding density appeared to be important with respect to the achievable hybridization efficiency, although these experiments did not investigate the relative importance. Probe binding density is known to play an important role in determining the hybridization efficiency to surface-bound probes.[4,6,329] Initial experiments used a backfilling method to prevent non-specific binding, where oligonucleotide probes were first bound to the surface then the particles were placed in 1 mM mercaptohexanol for 1 hour. We tried varying the DNA binding density by changing the amount of DNA in the initial solution (see Figure 6.3 for different densities); hybridization to probes bound to the particles with different binding densities using TE buffer (1 M NaCl, 10 mM Tris, 1 mM EDTA, 0.1% Tween 20) resulted in no significant differences in Raman intensity between complementary and non-complementary DNA. Lower binding densities could not be studied because the particles aggregated. Other buffers were also investigated, including TE buffer with different amounts of NaCl and HEPES buffer (30 mM HEPES, pH 7.5, 100 mM sodium acetate).

Hybridization was finally achieved by obtaining a lower DNA binding density by using an insertion method, where the particles were first functionalized with MCH, then DNA was inserted into the MCH layer[3] by immersing the particles in 50 μM of DNA probes for two hours. In addition, PBS buffer (0.01 M phosphate, 0.3 M NaCl) with 3% dextran sulfate was used, which has been shown to be effective in hybridizations where probes are bound to nanoparticles.[330] Dextran sulfate's improvement of hybridization efficiencies is attributed to macromolecular crowding, also known as the excluded volume effect, in which added macromolecules reduce the amount of accessible solvent, thus increasing the effective concentration of DNA.[331]

6.4.4.3 *Challenges in detection*

While a signal change occurred upon binding, sensitivity improvements would be required for use in practical applications. The sensitivity suffers from the fact that even when hybridization is assumed to be at a maximum, the open, or "off", signal is still fairly high (Figure 6.12). Whether or not this can be improved using the current system requires further work.

A challenge is found in negotiating the balance between efficient hybridization and obtaining a high SERS signal upon hybridization. Efficient hybridization requires a non-crowded layer of probes surrounded by blocking molecules preventing non-specific binding and bound with spacer groups of suitable length.[4,6,329,332,333] Contrarily, ideal conditions for a high SERS signal would be a large number of probe molecules relative to blocking molecules and spacer groups as short as possible to ensure that the molecule to be detected is as close as possible to the surface.

The methods used here present much room for optimization. Continuing optimization of the nanostructured gold coatings could result in surfaces with greater SERS enhancements. Further work looking at the hybridization conditions and optimization of probe density could also be beneficial. That the addition of dextran sulfate seemed to improve the hybridization efficiency is a good sign in terms of detection in more complex media, which would also increase macromolecular crowding. Only one type of Raman-tagged hairpin probe was investigated in these experiments, but varying the spacer lengths and sequence may result in greater sensitivities. Another potential improvement may be to use a Raman tag that is excited at the same wavelength of light used by the laser to make use of the surface enhanced resonance Raman scattering (SERRS) effect.

6.5 Conclusion

In these experiments, we showed that the nanostructured gold-coated magnetic particles could be used to study oligonucleotide probe binding on the surface and to detect oligonucleotide hybridization. The particles acted as SERS substrates by enhancing the signal of bound oligonucleotides without requiring particle aggregation, making it possible to easily wash them and to perform multiple binding steps using magnetic separation and to obtain a reproducible and quantitative signal. We showed that the distance dependence of the signal was comparable with other SERS substrates, with a limit of approximately 10 nm from the surface. Finally, we used the particles to detect oligonucleotide hybridization on their surface, based on the distance dependence of the signal and proximity to the surface of a Raman-tag on a hairpin probe.

Chapter 7: Conclusions and Perspectives

In the first part of this work, we furthered the understanding of the nature of self-assembled monolayer formation of short and long chain alkanethiols and their influence on protein binding. These experiments give some necessary insight into the processes underlying the use of SAMs in biosensing. We demonstrated how the atomic and molecular-level differences in the binding surface influence biomolecule adsorption and recognition. Surface science methods are useful tools in better understanding these surfaces, a requirement for achieving improved recognition efficiencies in a variety of methods of biomolecular detection.

Using PM-IRRAS, XPS, and DFT studies, we proposed a molecular picture of the thiol-gold interface to describe the differences observed between short and long chain alkanethiols. Less ordered short-chain alkanethiols (CEA) show an additional S2p peak in the XPS spectrum compared with more ordered long-chain alkanethiols (MUAM), meaning that the coordination of sulfur differs between the two cases. Using DFT models, we found that short chain alkanethiols bind more strongly to the surface and induce different gold surface restructuring compared with long chain alkanethiols, which leads to different binding environments of the sulfur groups. Binding of the short chain alkanethiols more closely resembles single-molecule adsorption than self-assembly. For applications of SAMs, these results have implications regarding the properties of the layer, which we explored in the subsequent chapter.

A main interest in studying alkanethiol formation is for applications in biosensing. We compared protein adsorption on amine-terminated SAMs—made from the same short (CEA) and long chain (MUAM) alkanethiols studied in the previous chapter. We covalently bound the proteins to the SAMs either by activating the carboxylic acid groups of the protein to bind to the amine groups of the SAM, or by using a cross-linking molecule (PDITC) to bind the amine groups of the protein to the surface. We then studied how well the proteins could be recognized by specific antibodies on the different surfaces. The SAM chain length influenced protein binding when the cross-linker was used—more protein binding occurred on short compared with long chains—but had little effect with the cross-linker. Recognition by specific antibodies was primarily dependent on the binding functions and not the SAM chain length; we therefore conclude that, in these experiments, the orientation of the protein was the primary factor in determining antibody recognition efficiencies.

In the second part of this work, we synthesized nanostructured gold-coated magnetic particles and, as a proof-of-concept, demonstrated their use as tools for DNA separation and SERS detection. The particles are magnetically separable, exhibiting superparamagnetic behavior. The nanostructured gold shells show a SERS signal that increases with analyte concentration in a predictable manner, as demonstrated with both 2-mercaptopyrimidine (MPym) and thiolated oligonucleotides. We explored how differences in morphology affected the degree of SERS enhancement and found that spiky shells gave a slightly larger signal compared with bumpy shells; this was observed when detecting both MPym and oligonucleotides. The distance dependence of the signal was harnessed to detect oligonucleotide hybridization. By using a hairpin probe with a Raman tag, we showed that binding a complementary strand to the probe resulted in the Raman tag moving further from the surface, thus showing a decreased intensity of the SERS signal.

This result is the first example, to our knowledge, of using nanostructured gold-coated magnetic particles to directly detect DNA hybridization using SERS. The method does not require the use of an extrinsic tag or a secondary hybridization step. Continued optimization of the method is required to achieve a greater sensitivity and limit of detection; we have shown that optimization may be effective at multiple steps in the process, from the initial nanostructured gold shell synthesis to probe binding, to the hybridization steps. The work presented here gives the first steps towards an advanced assay for biomolecule detection. A next step could involve using the particles in a microfluidic set-up, where additional control and separation is made possible using magnetic forces. Miniaturized Raman spectrometers are now commercially available, which could also be used in combination with the particles in a microfluidic system.

References

1. Cederquist, K. B. & Kelley, S. O. Nanostructured biomolecular detectors: pushing performance at the nanoscale. *Current Opinion in Chemical Biology* **16,** 415–421 (2012).
2. Castner, D. G. & Ratner, B. D. Biomedical surface science: Foundations to frontiers. *Surf. Sci.* **500,** 28–60 (2002).
3. Josephs, E. A. & Ye, T. Nanoscale Spatial Distribution of Thiolated DNA on Model Nucleic Acid Sensor Surfaces. *ACS Nano* **7,** 3653–3660 (2013).
4. Gong, P. & Levicky, R. DNA surface hybridization regimes. *Proceedings of the National Academy of Sciences* **105,** 5301–5306 (2008).
5. Irving, D., Gong, P. & Levicky, R. DNA Surface Hybridization: Comparison of Theory and Experiment. *J. Phys. Chem. B* **114,** 7631–7640 (2010).
6. Peterson, A. W. The effect of surface probe density on DNA hybridization. *Nucleic Acids Research* **29,** 5163–5168 (2001).
7. Boujday, S. *et al.* In-depth investigation of protein adsorption on gold surfaces: Correlating the structure and density to the efficiency of the sensing layer. *J. Phys. Chem. B* **112,** 6708–6715 (2008).
8. Reed, A. M. & Metallo, S. J. Oriented protein adsorption to gold nanoparticles through a genetically encodable binding motif. *Langmuir* **26,** 18945–18950 (2010).
9. Lu, B., Smyth, M. R. & O'Kennedy, R. Oriented immobilization of antibodies and its applications in immunoassays and immunosensors. *Analyst* **121,** R29–R32 (1996).
10. Tan, Y. H. *et al.* A nanoengineering approach for investigation and regulation of protein immobilization. *ACS Nano* **2,** 2374–2384 (2008).
11. Lebec, V. *et al.* Probing the Orientation of β-Lactoglobulin on Gold Surfaces Modified by Alkyl Thiol Self-Assembled Monolayers. *J. Phys. Chem. C* **117,** 11569–11577 (2013).
12. Dreaden, E. C., Alkilany, A. M., Huang, X., Murphy, C. J. & El-Sayed, M. A. The golden age: gold nanoparticles for biomedicine. *Chem. Soc. Rev.* **41,** 2740–2779 (2012).
13. Bedford, E. E., Spadavecchia, J., Pradier, C.-M. & Gu, F. X. Surface Plasmon Resonance Biosensors Incorporating Gold Nanoparticles. *Macromol. Biosci.* **12,** 724–739 (2012).
14. Bedford, E. E., Boujday, S., Pradier, C. M. & Gu, F. X. Nanostructured and spiky gold in biomolecule detection: improving binding efficiencies and enhancing optical signals. *RSC Adv.* **5,** 16461–16475 (2015).
15. Anker, J. N. *et al.* Biosensing with plasmonic nanosensors. *Nat Mater* **7,** 442–453 (2008).
16. Gordon, R., Sinton, D., Kavanagh, K. L. & Brolo, A. G. A New Generation of Sensors Based on Extraordinary Optical Transmission. *Acc. Chem. Res.* **41,** 1049–1057 (2008).
17. Stewart, M. E. *et al.* Nanostructured Plasmonic Sensors. *Chem. Rev.* **108,** 494–521 (2008).
18. Camden, J. P., Dieringer, J. A., Zhao, J. & Van Duyne, R. P. Controlled plasmonic nanostructures for surface-enhanced spectroscopy and sensing. *Acc. Chem. Res.* **41,** 1653–1661 (2008).
19. Rittich, B. & Španová, A. SPE and purification of DNA using magnetic particles. *Journal of Separation Science* **36,** 2472–2485 (2013).
20. Niemirowicz, K., Markiewicz, K. H., Wilczewska, A. Z. & Car, H. Magnetic nanoparticles as new diagnostic tools in medicine. *Advances in Medical Sciences* **57,** 196–207 (2012).
21. Shinkai, M. Functional magnetic particles for medical application. *Journal of Bioscience and Bioengineering* **94,** 606–613 (2002).
22. Paleček, E. & Fojta, M. Magnetic beads as versatile tools for electrochemical DNA and protein biosensing. *Talanta* **74,** 276–290 (2007).
23. Wang, J., Kawde, A.-N., Erdem, A. & Salazar, M. Magnetic bead-based label-free electrochemical detection of DNA hybridization. *Analyst* **126,** 2020–2024 (2001).
24. Nuzzo, R. G., Dubois, L. H. & Allara, D. L. Fundamental studies of microscopic wetting on organic surfaces. 1. Formation and structural characterization of a self-consistent series of polyfunctional organic monolayers. *J. Am. Chem. Soc.* **112,** 558–569 (1990).
25. Porter, M. D., Bright, T. B., Allara, D. L. & Chidsey, C. E. D. Spontaneously organized molecular

assemblies. 4. Structural characterization of n-alkyl thiol monolayers on gold by optical ellipsometry, infrared spectroscopy, and electrochemistry. *J. Am. Chem. Soc.* **109,** 3559–3568 (1987).

26. Fukushima, H. *et al.* Microstructure, Wettability, and Thermal Stability of Semifluorinated Self-Assembled Monolayers (SAMs) on Gold. *J. Phys. Chem. B* **104,** 7417–7423 (2000).
27. Ito, E. *et al.* Chain length dependence of adsorption structure of COOH-terminated alkanethiol SAMs on Au(111). *Applied Surface Science* **244,** 584–587 (2005).
28. Turner, A. P. F. Biosensors: sense and sensibility. *Chem. Soc. Rev.* **42,** 3184–3196 (2013).
29. Katz, E. & Willner, I. Integrated Nanoparticle-Biomolecule Hybrid Systems: Synthesis, Properties, and Applications. *Angew. Chem. Int. Ed.* **43,** 6042–6108 (2004).
30. Niemeyer, C. M. Nanoparticles, proteins, and nucleic acids: biotechnology meets materials science. *Angew. Chem. Int. Ed.* **40,** 4128–4158 (2001).
31. Eustis, S. & El-Sayed, M. A. Why Gold Nanoparticles Are More Precious than Pretty Gold: Noble Metal Surface Plasmon Resonance and Its Enhancement of the Radiative and Nonradiative Properties of Nanocrystals of Different Shapes. *ChemInform* **37,** (2006).
32. Garcia, M. A. Surface plasmons in metallic nanoparticles: fundamentals and applications. *Journal of Physics D: Applied Physics* **45,** 389501 (2011).
33. Lal, S. *et al.* Tailoring plasmonic substrates for surface enhanced spectroscopies. *Chem. Soc. Rev.* **37,** 898–911 (2008).
34. Sepúlveda, B., Angelomé, P. C., Lechuga, L. M. & Liz-Marzán, L. M. LSPR-based nanobiosensors. *Nano Today* **4,** 244–251 (2009).
35. Hrelescu, C., Sau, T. K., Rogach, A. L., Jäckel, F. & Feldmann, J. Single gold nanostars enhance Raman scattering. *Appl. Phys. Lett.* **94,** 153113 (2009).
36. Li, A. & Li, S. Large-volume hot spots in gold spiky nanoparticle dimers for high-performance surface-enhanced spectroscopy. *Nanoscale* **6,** 12921–12928 (2014).
37. Beeram, S. R. & Zamborini, F. P. Selective Attachment of Antibodies to the Edges of Gold Nanostructures for Enhanced Localized Surface Plasmon Resonance Biosensing. *J. Am. Chem. Soc.* **131,** 11689–11691 (2009).
38. Feuz, L., Jonsson, M. P. & Höök, F. Material-selective surface chemistry for nanoplasmonic sensors: optimizing sensitivity and controlling binding to local hot spots. *Nano Lett.* **12,** 873–879 (2012).
39. Jain, P. K., Huang, X., El-Sayed, I. H. & El-Sayed, M. A. Review of Some Interesting Surface Plasmon Resonance-enhanced Properties of Noble Metal Nanoparticles and Their Applications to Biosystems. *Plasmonics* **2,** 107–118 (2007).
40. Haes, A. J. & Van Duyne, R. P. A unified view of propagating and localized surface plasmon resonance biosensors. *Anal. Bioanal. Chem.* **379,** 920–930 (2004).
41. Cialla, D. *et al.* Surface-enhanced Raman spectroscopy (SERS): progress and trends. *Anal. Bioanal. Chem.* **403,** 27–54 (2012).
42. Osawa, M. in *Near-Field Optics and Surface Plasmon Polaritons* **81,** 163–187 (Springer Berlin Heidelberg, 2006).
43. Pradier, C. M., Salmain, M. & Boujday, S. in *Biointerface Characterization by Advanced IR Spectroscopy* 167–216 (Elsevier, 2011). doi:10.1016/B978-0-444-53558-0.00007-2
44. Darvill, D., Centeno, A. & Xie, F. Plasmonic fluorescence enhancement by metal nanostructures: shaping the future of bionanotechnology. *Phys. Chem. Chem. Phys.* **15,** 15709–15726 (2013).
45. Castelino, K., Kannan, B. & Majumdar, A. Characterization of Grafting Density and Binding Efficiency of DNA and Proteins on Gold Surfaces. *Langmuir* **21,** 1956–1961 (2005).
46. Kira, A., Kim, H. & Yasuda, K. Contribution of nanoscale curvature to number density of immobilized DNA on gold nanoparticles. *Langmuir* **25,** 1285–1288 (2009).
47. Hill, H. D., Millstone, J. E., Banholzer, M. J. & Mirkin, C. A. The Role Radius of Curvature Plays in Thiolated Oligonucleotide Loading on Gold Nanoparticles. *ACS Nano* **3,** 418–424 (2009).
48. Soleymani, L. *et al.* Nanostructuring of patterned microelectrodes to enhance the sensitivity of electrochemical nucleic acids detection. *Angewandte Chemie* **121,** 8609–8612 (2009).
49. Bin, X., Sargent, E. H. & Kelley, S. O. Nanostructuring of Sensors Determines the Efficiency of Biomolecular Capture. *Anal. Chem.* **82,** 5928–5931 (2010).

50. Soleymani, L., Fang, Z., Sargent, E. H. & Kelley, S. O. Programming the detection limits of biosensors through controlled nanostructuring. *Nature Nanotech* **4,** 844–848 (2009).
51. Ivanov, I. *et al.* Chip-Based Nanostructured Sensors Enable Accurate Identification and Classification of Circulating Tumor Cells in Prostate Cancer Patient Blood Samples. *Anal. Chem.* **85,** 398–403 (2013).
52. Vasilyeva, E. *et al.* Direct Genetic Analysis of Ten Cancer Cells: Tuning Sensor Structure and Molecular Probe Design for Efficient mRNA Capture. *Angew. Chem. Int. Ed.* **50,** 4137–4141 (2011).
53. Soleymani, L., Fang, Z., Lam, B., Bin, X. & Vasilyeva, E. Hierarchical nanotextured microelectrodes overcome the molecular transport barrier to achieve rapid, direct bacterial detection. *ACS Nano* **5,** 3360–3366 (2011).
54. Li, F., Han, X. & Liu, S. Development of an electrochemical DNA biosensor with a high sensitivity of fM by dendritic gold nanostructure modified electrode. *Biosens. Bioelectron.* **26,** 2619–2625 (2011).
55. Shi, L., Chu, Z., Liu, Y., Jin, W. & Chen, X. Facile synthesis of hierarchically aloe-like gold micro/nanostructures for ultrasensitive DNA recognition. *Biosens. Bioelectron.* **49,** 184–191 (2013).
56. Zanardi, C., Baldoli, C., Licandro, E., Terzi, F. & Seeber, R. Development of a gold-nanostructured surface for amperometric genosensors. *J. Nanopart. Res.* **14,** 1148 (2012).
57. Wang, L. *et al.* Electrochemical synthesis of gold nanostructure modified electrode and its development in electrochemical DNA biosensor. *Biosens. Bioelectron.* **30,** 151–157 (2011).
58. Kjällman, T. H. M., Peng, H., Soeller, C. & Travas-Sejdic, J. Effect of Probe Density and Hybridization Temperature on the Response of an Electrochemical Hairpin-DNA Sensor. *Anal. Chem.* **80,** 9460–9466 (2008).
59. Jung, Y., Jeong, J. Y. & Chung, B. H. Recent advances in immobilization methods of antibodies on solid supports. *Analyst* **133,** 697–701 (2008).
60. Sen, P., Yamaguchi, S. & Tahara, T. New insight into the surface denaturation of proteins: electronic sum frequency generation study of cytochrome c at water interfaces. *J. Phys. Chem. B* **112,** 13473–13475 (2008).
61. Lahari, C. *et al.* Adsorption induced enzyme denaturation: the role of polymer hydrophobicity in adsorption and denaturation of alpha-chymotrypsin on allyl glycidyl ether (AGE)-ethylene glycol dimethacrylate (EGDM) copolymers. *Langmuir* **26,** 1096–1106 (2010).
62. Makaraviciute, A. & Ramanaviciene, A. Site-directed antibody immobilization techniques for immunosensors. *Biosens. Bioelectron.* **50,** 460–471 (2013).
63. Briand, E. *et al.* Building of an immunosensor: How can the composition and structure of the thiol attachment layer affect the immunosensor efficiency? *Biosens. Bioelectron.* **22,** 440–448 (2006).
64. Ngunjiri, J. N., Stark, D. J., Tian, T., Briggman, K. A. & Garno, J. C. Immobilization of proteins on carboxylic acid functionalized nanopatterns. *Anal. Bioanal. Chem.* **405,** 1985–1993 (2013).
65. Tokuhisa, H. *et al.* Efficient Biosensor Interfaces Based on Space-Controlled Self-Assembled Monolayers. *Langmuir* **25,** 1633–1637 (2009).
66. Carbone, R. *et al.* Characterization of cluster-assembled nanostructured titanium oxide coatings as substrates for protein arrays. *Anal. Biochem.* **394,** 7–12 (2009).
67. Mani, V., Chikkaveeraiah, B. V., Patel, V., Gutkind, J. S. & Rusling, J. F. Ultrasensitive immunosensor for cancer biomarker proteins using gold nanoparticle film electrodes and multienzyme-particle amplification. *ACS Nano* **3,** 585–594 (2009).
68. Munge, B. S. *et al.* Nanostructured Immunosensor for Attomolar Detection of Cancer Biomarker Interleukin-8 Using Massively Labeled Superparamagnetic Particles. *Angew. Chem. Int. Ed.* **50,** 7915–7918 (2011).
69. Homola, J. Surface plasmon resonance sensors for detection of chemical and biological species. *Chem. Rev.* **108,** 462–493 (2008).
70. Estevez, M. C., Otte, M. A., Sepúlveda, B. & Lechuga, L. M. Trends and challenges of refractometric nanoplasmonic biosensors: A review. *Anal. Chim. Acta* **806,** 55–73 (2014).
71. Halas, N. J. *et al.* A Plethora of Plasmonics from the Laboratory for Nanophotonics at Rice University. *Adv. Mater.* **24,** 4842–4877 (2012).
72. Acuna, G. P. *et al.* Fluorescence enhancement at docking sites of DNA-directed self-assembled

nanoantennas. *Science* **338,** 506–510 (2012).

73. Hao, F., Nehl, C. L., Hafner, J. H. & Nordlander, P. Plasmon Resonances of a Gold Nanostar. *Nano Lett.* **7,** 729–732 (2007).
74. Kinkhabwala, A. *et al.* Large single-molecule fluorescence enhancements produced by a bowtie nanoantenna. *Nature Photonics* **3,** 654–657 (2009).
75. Mirkin, C. A., Letsinger, R. L., Mucic, R. C. & Storhoff, J. J. A DNA-based method for rationally assembling nanoparticles into macroscopic materials. *Nature* **382,** 607–609 (1996).
76. Aili, D., Selegård, R., Baltzer, L., Enander, K. & Liedberg, B. Colorimetric protein sensing by controlled assembly of gold nanoparticles functionalized with synthetic receptors. *Small* **5,** 2445–2452 (2009).
77. Liu, X. *et al.* Biofunctionalized Gold Nanoparticles for Colorimetric Sensing of Botulinum Neurotoxin A Light Chain. *Anal. Chem.* **86,** 2345–2352 (2014).
78. Lyon, L. A., Musick, M. D. & Natan, M. J. Colloidal Au-Enhanced Surface Plasmon Resonance Immunosensing. *Anal. Chem.* **70,** 5177–5183 (1998).
79. Hutter, E. *et al.* Role of Substrate Metal in Gold Nanoparticle Enhanced Surface Plasmon Resonance Imaging. *J. Phys. Chem. B* **105,** 8–12 (2001).
80. Yang, X., Wang, Q., Wang, K., Tan, W. & Li, H. Enhanced surface plasmon resonance with the modified catalytic growth of Au nanoparticles. *Biosens. Bioelectron.* **22,** 1106–1110 (2007).
81. Spadavecchia, J., Casale, S., Boujday, S. & Pradier, C.-M. Bioconjugated gold nanorods to enhance the sensitivity of FT-SPR-based biosensors. *Colloids and Surfaces B: Biointerfaces* **100,** 1–8 (2012).
82. Mitchell, J. S., Wu, Y., Cook, C. J. & Main, L. Sensitivity enhancement of surface plasmon resonance biosensing of small molecules. *Anal. Biochem.* **343,** 125–135 (2005).
83. Besselink, G. A. J., Kooyman, R. P. H., van Os, P. J. H. J., Engbers, G. H. M. & Schasfoort, R. B. M. Signal amplification on planar and gel-type sensor surfaces in surface plasmon resonance-based detection of prostate-specific antigen. *Anal. Biochem.* **333,** 165–173 (2004).
84. Wang, J. & Zhou, H. S. Aptamer-based Au nanoparticles-enhanced surface plasmon resonance detection of small molecules. *Anal. Chem.* **80,** 7174–7178 (2008).
85. Halpern, A. R., Wood, J. B., Wang, Y. & Corn, R. M. Single-nanoparticle near-infrared surface plasmon resonance microscopy for real-time measurements of DNA hybridization adsorption. *ACS Nano* **8,** 1022–1030 (2014).
86. Ko, S., Park, T. J., Kim, H.-S., Kim, J.-H. & Cho, Y.-J. Directed self-assembly of gold binding polypeptide-protein A fusion proteins for development of gold nanoparticle-based SPR immunosensors. *Biosens. Bioelectron.* **24,** 2592–2597 (2009).
87. Hutter, E., Fendler, J. H. & Roy, D. Surface Plasmon Resonance Studies of Gold and Silver Nanoparticles Linked to Gold and Silver Substrates by 2-Aminoethanethiol and 1,6-Hexanedithiol. *J. Phys. Chem. B* **105,** 11159–11168 (2001).
88. Jung, J., Na, K., Lee, J., Kim, K.-W. & Hyun, J. Enhanced surface plasmon resonance by Au nanoparticles immobilized on a dielectric SiO2 layer on a gold surface. *Anal. Chim. Acta* **651,** 91–97 (2009).
89. Gao, S. *et al.* Highly Stable Au Nanoparticles with Tunable Spacing and Their Potential Application in Surface Plasmon Resonance Biosensors. *Adv. Funct. Mater.* **20,** 78–86 (2010).
90. Hu, W. P. *et al.* A novel ultrahigh-resolution surface plasmon resonance biosensor with an Au nanocluster-embedded dielectric film. *Biosens. Bioelectron.* **19,** 1465–1471 (2004).
91. Kawaguchi, T. *et al.* Surface plasmon resonance immunosensor using Au nanoparticle for detection of TNT. *Sens. Actuator B-Chem.* **133,** 467–472 (2008).
92. Wang, Y., Yan, B. & Chen, L. SERS tags: novel optical nanoprobes for bioanalysis. *Chem. Rev.* **113,** 1391–1428 (2012).
93. Fleischmann, M., Hendra, P. J. & McQuillan, A. J. Raman spectra of pyridine adsorbed at a silver electrode. *Chemical Physics Letters* **26,** 163–166 (1974).
94. Ko, H., Singamaneni, S. & Tsukruk, V. V. Nanostructured surfaces and assemblies as SERS media. *Small* **4,** 1576–1599 (2008).
95. Moskovits, M. Surface-enhanced Raman spectroscopy: a brief retrospective. *J. Raman Spectrosc.* **36,** 485–496 (2005).

96. Schuck, P. J., Fromm, D. P., Sundaramurthy, A., Kino, G. S. & Moerner, W. E. Improving the mismatch between light and nanoscale objects with gold bowtie nanoantennas. *Phys. Rev. Lett.* **94,** 017402 (2005).
97. Gunnarsson, L. *et al.* Confined plasmons in nanofabricated single silver particle pairs: experimental observations of strong interparticle interactions. *J. Phys. Chem. B* **109,** 1079–1087 (2005).
98. Talley, C. E. *et al.* Surface-Enhanced Raman Scattering from Individual Au Nanoparticles and Nanoparticle Dimer Substrates. *Nano Lett.* **5,** 1569–1574 (2005).
99. Li, W., Camargo, P. H. C., Lu, X. & Xia, Y. Dimers of Silver Nanospheres: Facile Synthesis and Their Use as Hot Spots for Surface-Enhanced Raman Scattering. *Nano Lett.* **9,** 485–490 (2009).
100. Liao, P. F. & Wokaun, A. Lightning rod effect in surface enhanced Raman scattering. *J. Chem. Phys.* **76,** 751–752 (1982).
101. Hrelescu, C. *et al.* Selective excitation of individual plasmonic hotspots at the tips of single gold nanostars. *Nano Lett.* **11,** 402–407 (2011).
102. Barbosa, S. *et al.* Tuning size and sensing properties in colloidal gold nanostars. *Langmuir* **26,** 14943–14950 (2010).
103. Nalbant Esenturk, E. & Hight Walker, A. R. Surface-enhanced Raman scattering spectroscopy via gold nanostars. *J. Raman Spectrosc.* **40,** 86–91 (2009).
104. Lin, X.-M., Cui, Y., Xu, Y.-H., Ren, B. & Tian, Z.-Q. Surface-enhanced Raman spectroscopy: substrate-related issues. *Anal. Bioanal. Chem.* **394,** 1729–1745 (2009).
105. Aldeanueva-Potel, P. *et al.* Spiked Gold Beads as Substrates for Single-Particle SERS. *ChemPhysChem* **13,** 2561–2565 (2012).
106. Osinkina, L., Lohmüller, T., Jäckel, F. & Feldmann, J. Synthesis of Gold Nanostar Arrays as Reliable, Large-Scale, Homogeneous Substrates for Surface-Enhanced Raman Scattering Imaging and Spectroscopy. *J. Phys. Chem. C* **117,** 22198–22202 (2013).
107. Le, F. *et al.* Metallic nanoparticle arrays: a common substrate for both surface-enhanced Raman scattering and surface-enhanced infrared absorption. *ACS Nano* **2,** 707–718 (2008).
108. Aslan, K. *et al.* Metal-enhanced fluorescence: an emerging tool in biotechnology. *Current Opinion in Biotechnology* **16,** 55–62 (2005).
109. Luchowski, R. *et al.* Molecular Fluorescence Enhancement on Fractal-Like Structures. *Appl Spectrosc* **64,** 578–583 (2010).
110. Luchowski, R. *et al.* Single Molecule Immunoassay on Plasmonic Platforms. *Curr. Pharm. Biotech.* **11,** 96–102 (2010).
111. Aslan, K., Wu, M., Lakowicz, J. R. & Geddes, C. D. Fluorescent core-shell Ag@SiO2 nanocomposites for metal-enhanced fluorescence and single nanoparticle sensing platforms. *J. Am. Chem. Soc.* **129,** 1524–1525 (2007).
112. Love, J. C., Estroff, L. A., Kriebel, J. K., Nuzzo, R. G. & Whitesides, G. M. Self-Assembled Monolayers of Thiolates on Metals as a Form of Nanotechnology. *Chem. Rev.* **105,** 1103–1170 (2005).
113. Prime, K. L. & Whitesides, G. M. Self-Assembled Organic Monolayers: Model Systems for Studying Adsorption of Proteins at Surfaces. *Science* **252,** 1164–1167 (1991).
114. Wink, T., J van Zuilen, S., Bult, A. & P van Bennekom, W. Self-assembled Monolayers for Biosensors. *Analyst* **122,** 43R–50R (1997).
115. Boujday, S. *et al.* Detection of pathogenic Staphylococcus aureus bacteria by gold based immunosensors. *Microchimica Acta* **163,** 203–209 (2008).
116. Briand, E. *et al.* Functionalisation of gold surfaces with thiolate SAMs: Topography/bioactivity relationship - A combined FT-RAIRS, AFM and QCM investigation. *Surf. Sci.* **601,** 3850–3855 (2007).
117. Bedford, E. E., Boujday, S., Humblot, V., Gu, F. X. & Pradier, C.-M. Effect of SAM chain length and binding functions on protein adsorption: β-lactoglobulin and apo-transferrin on gold. *Colloids and Surfaces B: Biointerfaces* **116,** 489–496 (2014).
118. Vericat, C., Vela, M. E., Benitez, G., Carro, P. & Salvarezza, R. C. Self-assembled monolayers of thiols and dithiols on gold: new challenges for a well-known system. *Chem. Soc. Rev.* **39,** 1805–1834

(2010).
119. Smith, R. K., Lewis, P. A. & Weiss, P. S. Patterning self-assembled monolayers. *Prog. Surf. Sci.* **75,** 1–68 (2004).
120. Tamada, K., Hara, M., Sasabe, H. & Knoll, W. Surface Phase Behavior of n-Alkanethiol Self-Assembled Monolayers Adsorbed on Au(111): An Atomic Force Microscope Study. *Langmuir* **13,** 1558–1566 (1997).
121. Brewer, N. J. & Leggett, G. J. Chemical force microscopy of mixed self-assembled monolayers of alkanethiols on gold: evidence for phase separation. *Langmuir* **20,** 4109–4115 (2004).
122. Ostuni, E., Yan, L. & Whitesides, G. M. The interaction of proteins and cells with self-assembled monolayers of alkanethiolates on gold and silver. *Colloids and Surfaces B: Biointerfaces* **15,** 3–30 (1999).
123. Nelson, K. E. *et al.* Surface Characterization of Mixed Self-Assembled Monolayers Designed for Streptavidin Immobilization. *Langmuir* **17,** 2807–2816 (2001).
124. Samanta, D. & Sarkar, A. Immobilization of bio-macromolecules on self-assembled monolayers: methods and sensor applications. *Chem. Soc. Rev.* **40,** 2567–2592 (2011).
125. Josephs, E. A. & Ye, T. Nanoscale positioning of individual DNA molecules by an atomic force microscope. *J. Am. Chem. Soc.* **132,** 10236–10238 (2010).
126. Herne, T. M. & Tarlov, M. J. Characterization of DNA Probes Immobilized on Gold Surfaces. *J. Am. Chem. Soc.* **119,** 8916–8920 (1997).
127. Lee, C.-Y. *et al.* Surface coverage and structure of mixed DNA/alkylthiol monolayers on gold: characterization by XPS, NEXAFS, and fluorescence intensity measurements. *Anal. Chem.* **78,** 3316–3325 (2006).
128. Driskell, J. D., Lipert, R. J. & Porter, M. D. Labeled gold nanoparticles immobilized at smooth metallic substrates: systematic investigation of surface plasmon resonance and surface-enhanced Raman scattering. *J. Phys. Chem. B* **110,** 17444–17451 (2006).
129. Morel, A.-L. *et al.* Optimized immobilization of gold nanoparticles on planar surfaces through alkyldithiols and their use to build 3D biosensors. *Colloids and Surfaces B: Biointerfaces* **81,** 304–312 (2010).
130. Ben Haddada, M. *et al.* Optimizing the immobilization of gold nanoparticles on functionalized silicon surfaces: amine- vs thiol-terminated silane. *Gold Bull* **46,** 335–341 (2013).
131. Wei, A. Calixarene-encapsulated nanoparticles: self-assembly into functional nanomaterials. *Chem. Commun. (Camb.)* 1581–1591 (2006). doi:10.1039/b515806k
132. Eichler, M. *et al.* The impact of dendrimer-grafted modifications to model silicon surfaces on protein adsorption and bacterial adhesion. *Biomaterials* **32,** 9168–9179 (2011).
133. Mercier, D. *et al.* Bifunctional Polyoxometalates for Planar Gold Surface Nanostructuration and Protein Immobilization. *J. Phys. Chem. C* **116,** 13217–13224 (2012).
134. Yu, X., Munge, B., Patel, V. & Jensen, G. Carbon nanotube amplification strategies for highly sensitive immunodetection of cancer biomarkers. *J. Am. Chem. Soc.* **128,** 11199–11205 (2006).
135. Hulteen, J. C. & Van Duyne, R. P. Nanosphere lithography: A materials general fabrication process for periodic particle array surfaces. *Journal of Vacuum Science & Technology A: Vacuum, Surfaces, and Films* **13,** 1553–1558 (1995).
136. Haes, A. J., Chang, L., Klein, W. L. & Van Duyne, R. P. Detection of a Biomarker for Alzheimer's Disease from Synthetic and Clinical Samples Using a Nanoscale Optical Biosensor. *J. Am. Chem. Soc.* **127,** 2264–2271 (2005).
137. Haynes, C. L. & Van Duyne, R. P. Plasmon-Sampled Surface-Enhanced Raman Excitation Spectroscopy †. *J. Phys. Chem. B* **107,** 7426–7433 (2003).
138. Ye, W., Yan, J., Ye, Q. & Zhou, F. Template-Free and Direct Electrochemical Deposition of Hierarchical Dendritic Gold Microstructures: Growth and Their Multiple Applications. *J. Phys. Chem. C* **114,** 15617–15624 (2010).
139. Ye, W., Wang, D., Zhang, H., Zhou, F. & Liu, W. Electrochemical growth of flowerlike gold nanoparticles on polydopamine modified ITO glass for SERS application. *Electrochimica Acta* **55,** 2004–2009 (2010).
140. Wang, J. *et al.* An invisible template method toward gold regular arrays of nanoflowers by

electrodeposition. *Langmuir* **29,** 3512–3517 (2013).
141. Rosi, N. L. & Mirkin, C. A. Nanostructures in Biodiagnostics. *Chem. Rev.* **105,** 1547–1562 (2005).
142. Daniel, M.-C. & Astruc, D. Gold Nanoparticles: Assembly, Supramolecular Chemistry, Quantum-Size-Related Properties, and Applications toward Biology, Catalysis, and Nanotechnology. *Chem. Rev.* **104,** 293–346 (2004).
143. Zhao, P., Li, N. & Astruc, D. State of the art in gold nanoparticle synthesis. *Coordination Chemistry Reviews* **257,** 638–665 (2013).
144. Lohse, S. E. & Murphy, C. J. The Quest for Shape Control: A History of Gold Nanorod Synthesis. *Chem. Mater.* **25,** 1250–1261 (2013).
145. Murphy, C. J. *et al.* Anisotropic Metal Nanoparticles: Synthesis, Assembly, and Optical Applications. *J. Phys. Chem. B* **109,** 13857–13870 (2005).
146. Treguer-Delapierre, M., Majimel, J., Mornet, S., Duguet, E. & Ravaine, S. Synthesis of non-spherical gold nanoparticles. *Gold Bull* **41,** 195–207 (2008).
147. Guerrero-Martínez, A., Barbosa, S., Pastoriza-Santos, I. & Liz-Marzán, L. M. Nanostars shine bright for you. *Current Opinion in Colloid & Interface Science* **16,** 118–127 (2011).
148. Senthil Kumar, P., Pastoriza-Santos, I., Rodríguez-González, B., Javier García de Abajo, F. & Liz-Marzán, L. M. High-yield synthesis and optical response of gold nanostars. *Nanotechnology* **19,** 015606 (2008).
149. Maiorano, G. *et al.* Monodispersed and size-controlled multibranched gold nanoparticles with nanoscale tuning of surface morphology. *Nanoscale* **3,** 2227–2232 (2011).
150. Zhong, Z., Patskovskyy, S., Bouvrette, P., Luong, J. H. T. & Gedanken, A. The Surface Chemistry of Au Colloids and Their Interactions with Functional Amino Acids. *J. Phys. Chem. B* **108,** 4046–4052 (2004).
151. Nehl, C. L., Liao, H. & Hafner, J. H. Optical properties of star-shaped gold nanoparticles. *Nano Lett.* **6,** 683–688 (2006).
152. Hirsch, L. R. *et al.* Design and applications of gold nanoparticle conjugates by exploiting biomolecule–gold nanoparticle interactions. *Nanoscale* **5,** 2589–2599 (2013).
153. Zhou, H., Honma, I., Komiyama, H. & Haus, J. Controlled synthesis and quantum-size effect in gold-coated nanoparticles. *Phys. Rev. B* **50,** 12052–12056 (1994).
154. Oldenburg, S. J., Averitt, R. D., Westcott, S. L. & Halas, N. J. Nanoengineering of optical resonances. *Chemical Physics Letters* **288,** 243–247 (1998).
155. Sauerbeck, C. *et al.* Shedding light on the growth of gold nanoshells. *ACS Nano* **8,** 3088–3096 (2014).
156. Bigall, N. C., Parak, W. J. & Dorfs, D. Fluorescent, magnetic and plasmonic,ÄîHybrid multifunctional colloidal nano objects. *Nano Today* **7,** 282–296 (2012).
157. Levin, C. S. *et al.* Magnetic−Plasmonic Core−Shell Nanoparticles. *ACS Nano* **3,** 1379–1388 (2009).
158. Zhang, H., Harpster, M. H., Wilson, W. C. & Johnson, P. A. Surface-Enhanced Raman Scattering Detection of DNAs Derived from Virus Genomes Using Au-Coated Paramagnetic Nanoparticles. *Langmuir* **28,** 4030–4037 (2012).
159. Dunlop, D. J. Magnetite: Behavior near the single-domain threshold. *Science* **176,** 41–43 (1972).
160. Lim, D.-K. *et al.* Highly uniform and reproducible surface-enhanced Raman scattering from DNA-tailorable nanoparticles with 1-nm interior gap. *Nature Nanotech* **6,** 452–460 (2011).
161. Sau, T. K. & Murphy, C. J. Room temperature, high-yield synthesis of multiple shapes of gold nanoparticles in aqueous solution. *J. Am. Chem. Soc.* **126,** 8648–8649 (2004).
162. Wei, Q. *et al.* Gyromagnetic imaging: dynamic optical contrast using gold nanostars with magnetic cores. *J. Am. Chem. Soc.* **131,** 9728–9734 (2009).
163. Song, H.-M., Wei, Q., Ong, Q. K. & Wei, A. Plasmon-Resonant Nanoparticles and Nanostars with Magnetic Cores: Synthesis and Magnetomotive Imaging. *ACS Nano* **4,** 5163–5173 (2010).
164. Miao, X. *et al.* A facile synthetic route for the preparation of gold nanostars with magnetic cores and their reusable nanohybrid catalytic properties. *Nanoscale* **3,** 1189 (2011).
165. Sanchez-Gaytan, B. L. & Park, S.-J. Spiky Gold Nanoshells. *Langmuir* **26,** 19170–19174 (2010).
166. Sanchez-Gaytan, B. L. *et al.* Spiky Gold Nanoshells: Synthesis and Enhanced Scattering Properties. *J. Phys. Chem. C* **116,** 10318–10324 (2012).

167. Song, C. *et al.* Ultrasensitive detection of carcino-embryonic antigen by using novel flower-like gold nanoparticle SERS tags and SERS-active magnetic nanoparticles. *RSC Adv.* **4,** 41666–41669 (2014).
168. Pastoriza-Santos, I. & Liz-Marzán, L. M. N, N-Dimethylformamide as a Reaction Medium for Metal Nanoparticle Synthesis. *Adv. Funct. Mater.* **19,** 679–688 (2009).
169. Pazos-Pérez, N. *et al.* Growth of Sharp Tips on Gold Nanowires Leads to Increased Surface-Enhanced Raman Scattering Activity. *J. Phys. Chem. Lett.* **1,** 24–27 (2010).
170. Quaresma, P. *et al.* Star-shaped magnetite@gold nanoparticles for protein magnetic separation and SERS detection. *RSC Adv.* **4,** 3659 (2013).
171. Pedireddy, S. *et al.* Synthesis of Spiky Ag–Au Octahedral Nanoparticles and Their Tunable Optical Properties. *J. Phys. Chem. C* **117,** 16640–16649 (2013).
172. Li, J. *et al.* Controllable Synthesis of Stable Urchin-like Gold Nanoparticles Using Hydroquinone to Tune the Reactivity of Gold Chloride. *J. Phys. Chem. C* **115,** 3630–3637 (2011).
173. Zhou, H., Kim, J.-P., Bahng, J. H., Kotov, N. A. & Lee, J. Self-Assembly Mechanism of Spiky Magnetoplasmonic Supraparticles. *Adv. Funct. Mater.* **24,** 1439–1448 (2013).
174. Yuan, H. *et al.* Shape and SPR Evolution of Thorny Gold Nanoparticles Promoted by Silver Ions. *Chem. Mater.* **19,** 1592–1600 (2007).
175. Jiang, Y., Wu, X.-J., Li, Q., Li, J. & Xu, D. Facile synthesis of gold nanoflowers with high surface-enhanced Raman scattering activity. *Nanotechnology* **22,** 385601 (2011).
176. Xie, J., Zhang, Q., Lee, J. Y. & Wang, D. I. C. The Synthesis of SERS-Active Gold Nanoflower Tags for In VivoApplications. *ACS Nano* **2,** 2473–2480 (2008).
177. Ma, L. L. *et al.* Small Multifunctional Nanoclusters (Nanoroses) for Targeted Cellular Imaging and Therapy. *ACS Nano* **3,** 2686–2696 (2009).
178. Li, C. *et al.* Gold-Coated Fe_3O_4 Nanoroses with Five Unique Functions for Cancer Cell Targeting, Imaging, and Therapy. *Adv. Funct. Mater.* **24,** 1772–1780 (2013).
179. Ulman, A. Formation and Structure of Self-Assembled Monolayers. *Chem. Rev.* **96,** 1533–1554 (1996).
180. Ulman, A. *An Introduction to Ultrathin Organic Films*. (Academic Press, 1991).
181. Schreiber, F. Self-assembled monolayers: from 'simple' model systems to biofunctionalized interfaces. *J. Phys.: Condens. Matter* **16,** R881–R900 (2004).
182. Eck, W. in *Adsorbed Layers on Surfaces* **42A4,** 371–385 (Springer Berlin Heidelberg, 2005).
183. Laibinis, P. E. *et al.* Comparison of the structures and wetting properties of self-assembled monolayers of n-alkanethiols on the coinage metal surfaces, copper, silver, and gold. *J. Am. Chem. Soc.* **113,** 7152–7167 (1991).
184. Baralia, G. G., Pallandre, A., Nysten, B. & Jonas, A. M. Nanopatterned self-assembled monolayers. *Nanotechnology* **17,** 1160–1165 (2006).
185. Akkerman, H. B., Blom, P. W. M., de Leeuw, D. M. & de Boer, B. Towards molecular electronics with large-area molecular junctions. *Nature* **441,** 69–72 (2006).
186. Akkerman, H. B. *et al.* Self-Assembled-Monolayer Formation of Long Alkanedithiols in Molecular Junctions. *Small* **4,** 100–104 (2008).
187. Flood, A. H., Stoddart, J. F., Steuerman, D. W. & Heath, J. R. Whence Molecular Electronics? *Science* **306,** 2055–2056 (2004).
188. Woodruff, D. P. The interface structure of n-alkylthiolate self-assembled monolayers on coinage metal surfaces. *Phys. Chem. Chem. Phys.* **10,** 7211–7221 (2008).
189. Woodruff, D. P. The role of reconstruction in self-assembly of alkylthiolate monolayers on coinage metal surfaces. *Applied Surface Science* **254,** 76–81 (2007).
190. Maksymovych, P., Sorescu, D. C. & John T Yates, J. Gold-Adatom-Mediated Bonding in Self-Assembled Short-Chain Alkanethiolate Species on the Au(111) Surface. *Phys. Rev. Lett.* **97,** 146103 (2006).
191. Yu, M. *et al.* True Nature of an Archetypal Self-Assembly System: Mobile Au-Thiolate Species on Au(111). *Phys. Rev. Lett.* **97,** 166102 (2006).
192. Kankate, L., Turchanin, A. & Golzhauser, A. On the Release of Hydrogen from the S−H groups in the Formation of Self-Assembled Monolayers of Thiols. *Langmuir* **25,** 10435–10438 (2009).

193. Tielens, F. & Santos, E. AuS and SH Bond Formation/Breaking during the Formation of Alkanethiol SAMs on Au(111): A Theoretical Study. *J. Phys. Chem. C* **114,** 9444–9452 (2010).
194. Tielens, F., Humblot, V., Pradier, C.-M., Calatayud, M. & Illas, F. Stability of Binary SAMs Formed by ω-Acid and Alcohol Functionalized Thiol Mixtures. *Langmuir* **25,** 9980–9985 (2009).
195. Tielens, F., Humblot, V. & Pradier, C.-M. Exploring the reactivity of mixed ω-functionalized undecanethiol self-assembled monolayers—A DFT study. *International Journal of Quantum Chemistry* **108,** 1792–1795 (2008).
196. Tielens, F., Costa, D., Humblot, V. & Pradier, C.-M. Characterization of omega-functionalized undecanethiol mixed self-assembled monolayers on Au(111): A combined polarization modulation infrared reflection-absorption spectroscopy/X-ray photoelectron spectroscopy/periodic density functional theory study. *J. Phys. Chem. C* **112,** 182–190 (2008).
197. Luque, N. B., Santos, E., Andrés, J. & Tielens, F. Effect of Coverage and Defects on the Adsorption of Propanethiol on Au(111) Surface: A Theoretical Study. *Langmuir* **27,** 14514–14521 (2011).
198. Grönbeck, H. & Hakkinen, H. Polymerization at the Alkylthiolate−Au(111) Interface. *J. Phys. Chem. B* **111,** 3325–3327 (2007).
199. Grönbeck, H., Hakkinen, H. & Whetten, R. L. Gold−Thiolate Complexes Form a Unique c(4 × 2) Structure on Au(111). *J. Phys. Chem. C* **112,** 15940–15942 (2008).
200. Walter, M. *et al.* A unified view of ligand-protected gold clusters as superatom complexes. *Proc. Natl. Acad. Sci. U.S.A.* **105,** 9157–9162 (2008).
201. Grönbeck, H. Thiolate Induced Reconstruction of Au(111) and Cu(111) Investigated by Density Functional Theory Calculations †. *J. Phys. Chem. C* **114,** 15973–15978 (2010).
202. Grönbeck, H. & Odelius, M. Photoemission core-level shifts reveal the thiolate-Au(111) interface. *Phys. Rev. B* **82,** 085416 (2010).
203. Ferrighi, L., Pan, Y.-X., Grönbeck, H. & Hammer, B. Study of Alkylthiolate Self-assembled Monolayers on Au(111) Using a Semilocal meta-GGA Density Functional. *J. Phys. Chem. C* **116,** 7374–7379 (2012).
204. Grönbeck, H. The bonding in thiolate protected gold nanoparticles from Au4f photoemission core level shifts. *Nanoscale* **4,** 4178–4182 (2012).
205. Lustemberg, P. G., Martiarena, M. L., Martínez, A. E. & Busnengo, H. F. The Reaction Pathways for HSCH 3Adsorption on Au(111): A Density Functional Theory Study. *Langmuir* **24,** 3274–3279 (2008).
206. Wang, Y., Solano-Canchaya, J. G., Alcamí, M., Busnengo, H. F. & Martín, F. Commensurate Solid–Solid Phase Transitions in Self-Assembled Monolayers of Alkylthiolates Lying on Metal Surfaces. *J. Am. Chem. Soc.* **134,** 13224–13227 (2012).
207. Boujday, S., Méthivier, C., Beccard, B. & Pradier, C.-M. Innovative surface characterization techniques applied to immunosensor elaboration and test: comparing the efficiency of Fourier transform-surface plasmon resonance, quartz crystal microbalance with dissipation measurements, and polarization modulation-re. *Anal. Biochem.* **387,** 194–201 (2009).
208. Barner, B. J., Green, M. J., Saez, E. I. & Corn, R. M. Polarization modulation Fourier transform infrared reflectance measurements of thin films and monolayers at metal surfaces utilizing real-time sampling electronics. *Anal. Chem.* **63,** 55–60 (2002).
209. Buffeteau, T., Desbat, B. & Turlet, J. M. Polarization Modulation FT-IR Spectroscopy of Surfaces and Ultra-Thin Films: Experimental Procedure and Quantitative Analysis. *Appl Spectrosc* **45,** 380–389 (1991).
210. Scofield, J. H. Hartree-Slater subshell photoionization cross-sections at 1254 and 1487eV. *J. Electron Spectrosc. Relat. Phenom.* **8,** 129–137 (1976).
211. Kresse, G. & Hafner, J. *Ab initio* molecular dynamics for liquid metals. *Phys. Rev. B* **47,** 558–561 (1993).
212. Kresse, G. & Hafner, J. *Ab initio* molecular-dynamics simulation of the liquid-metal–amorphous-semiconductor transition in germanium. *Phys. Rev. B* **49,** 14251–14269 (1994).
213. Perdew, J. P., Burke, K. & Ernzerhof, M. Generalized Gradient Approximation Made Simple. *Phys. Rev. Lett.* **77,** 3865–3868 (1996).
214. Perdew, J. P., Burke, K. & Ernzerhof, M. Generalized Gradient Approximation Made Simple

[Phys. Rev. Lett. 77, 3865 (1996)]. *Phys. Rev. Lett.* **78,** 1396–1396 (1997).

215. Tielens, F., Gervais, C., Lambert, J.-F., Mauri, F. & Costa, D. Ab Initio Study of the Hydroxylated Surface of Amorphous Silica: A Representative Model. *Chem. Mater.* **20,** 3336–3344 (2008).
216. Calatayud, M., Tielens, F. & De Proft, F. Reactivity of gas-phase, crystal and supported V2O5 systems studied using density functional theory based reactivity indices. *Chemical Physics Letters* **456,** 59–63 (2008).
217. Visart de Bocarmé, T. *et al.* Oxygen adsorption on gold nanofacets and model clusters. *J. Chem. Phys.* **125,** 054703 (2006).
218. Tielens, F. & Andrés, J. Prediction of Gold Zigzag Nanotube-like Structure Based on Au 32Units: A Quantum Chemical Study. *J. Phys. Chem. C* **111,** 10342–10346 (2007).
219. Blöchl, P. E., Jepsen, O. & Andersen, O. K. Improved tetrahedron method for Brillouin-zone integrations. *Phys. Rev. B* **49,** 16223–16233 (1994).
220. Kresse, G. & Joubert, D. From ultrasoft pseudopotentials to the projector augmented-wave method. *Phys. Rev. B* **59,** 1758–1775 (1999).
221. Wu, X., Vargas, M. C., Nayak, S., Lotrich, V. & Scoles, G. Towards extending the applicability of density functional theory to weakly bound systems. *J. Chem. Phys.* **115,** 8748–8757 (2001).
222. Grimme, S. Semiempirical GGA-type density functional constructed with a long-range dispersion correction. *Journal of Computational Chemistry* **27,** 1787–1799 (2006).
223. Maeland, A. & Flanagan, T. B. Lattice spacings of gold–palladium alloys. *Canadian Journal of Physics* **42,** 2364–2366 (2011).
224. Vericat, C., Andreasen, G., Vela, M. E., Martin, H. & Salvarezza, R. C. Following transformation in self-assembled alkanethiol monolayers on Au(111) by in situ scanning tunneling microscopy. *J. Chem. Phys.* **115,** 6672 (2001).
225. Socrates, G. *Infrared characteristic group frequencies*. (Wiley, 1980).
226. Briand, E., Salmain, M., Compere, C. & Pradier, C. M. Immobilization of Protein A on SAMS for the elaboration of immunosensors. *Colloids and Surfaces B: Biointerfaces* **53,** 215–224 (2006).
227. Bain, C. D. *et al.* Formation of monolayer films by the spontaneous assembly of organic thiols from solution onto gold. *J. Am. Chem. Soc.* **111,** 321–335 (1989).
228. Wirde, M., Gelius, U. & Nyholm, L. Self-Assembled Monolayers of Cystamine and Cysteamine on Gold Studied by XPS and Voltammetry. *Langmuir* **15,** 6370–6378 (1999).
229. Castner, D. G., Hinds, K. & Grainger, D. W. X-ray Photoelectron Spectroscopy Sulfur 2p Study of Organic Thiol and Disulfide Binding Interactions with Gold Surfaces. *Langmuir* **12,** 5083–5086 (1996).
230. Nuzzo, R. G., Zegarski, B. R. & Dubois, L. H. Fundamental studies of the chemisorption of organosulfur compounds on Au(111) - implications for molecular self-assembly on gold surfaces. *J. Am. Chem. Soc.* **109,** 733–740 (1987).
231. Cavalleri, O. *et al.* High resolution XPS of the S 2p core level region of the L-cysteine/gold interface. *J. Phys.: Condens. Matter* **16,** S2477 (2004).
232. Gonella, G. *et al.* High resolution X-ray photoelectron spectroscopy of 3-mercaptopropionic acid self-assembled films. *Surf. Sci.* **566-568,** 638–643 (2004).
233. Ishida, T. *et al.* High Resolution X-ray Photoelectron Spectroscopy Measurements of Octadecanethiol Self-Assembled Monolayers on Au(111). *Langmuir* **14,** 2092–2096 (1998).
234. Mamun, A. H. A. & Hahn, J. R. Effects of Solvent on the Formation of Octanethiol Self-Assembled Monolayers on Au(111) at High Temperatures in a Closed Vessel: A Scanning Tunneling Microscopy and X-ray Photoelectron Spectroscopy Study. *J. Phys. Chem. C* **116,** 22441–22448 (2012).
235. Bensebaa, F., Zhou, Y., Deslandes, Y., Kruus, E. & Ellis, T. H. XPS study of metal–sulfur bonds in metal–alkanethiolate materials. *Surf. Sci.* **405,** L472–L476 (1998).
236. Cossaro, A. *et al.* Amine Functionalization of Gold Surfaces: Ultra High Vacuum Deposition of Cysteamine on Au(111). *J. Phys. Chem. C* **114,** 15011–15014 (2010).
237. Hayashi, T., Wakamatsu, K., Ito, E. & Hara, M. Effect of Steric Hindrance on Desorption Processes of Alkanethiols on Au (111). *J. Phys. Chem. C* **113,** 18795–18799 (2009).
238. Ishida, T. *et al.* High-resolution X-ray photoelectron spectra of organosulfur monolayers on Au (111): S (2p) spectral dependence on molecular species. *Langmuir* **15,** 6799–6806 (1999).

239. Lamp, B. D., Hobara, D., Porter, M. D., Niki, K. & Cotton, T. M. Correlation of the Structural Decomposition and Performance of Pyridinethiolate Surface Modifiers at Gold Electrodes for the Facilitation of Cytochrome *c* Heterogeneous Electron-Transfer Reactions. *Langmuir* **13,** 736–741 (1997).
240. Zhong, C.-J., Brush, R. C., Anderegg, J. & Porter, M. D. Organosulfur monolayers at gold surfaces: reexamination of the case for sulfide adsorption and implications to the formation of monolayers from thiols and disulfides. *Langmuir* **15,** 518–525 (1999).
241. Hakkinen, H. The gold-sulfur interface at the nanoscale. *Nat Chem* **4,** 443–455 (2012).
242. Di Felice, R. & Selloni, A. Adsorption modes of cysteine on Au(111): Thiolate, amino-thiolate, disulfide. *J. Chem. Phys.* **120,** 4906 (2004).
243. Laibinis, P. E., Nuzzo, R. G. & Whitesides, G. M. Structure of monolayers formed by coadsorption of two n-alkanethiols of different chain lengths on gold and its relation to wetting. *J. Phys. Chem.* **96,** 5097–5105 (1992).
244. Schreiber, F. Structure and growth of self-assembling monolayers. *Prog. Surf. Sci.* **65,** 151–256 (2000).
245. Prime, K. L. & Whitesides, G. M. Adsorption of proteins onto surfaces containing end-attached oligo(ethylene oxide): a model system using self-assembled monolayers. *J. Am. Chem. Soc.* **115,** 10714–10721 (1993).
246. Lahiri, J., Isaacs, L., Tien, J. & Whitesides, G. M. A strategy for the generation of surfaces presenting ligands for studies of binding based on an active ester as a common reactive intermediate: A surface plasmon resonance study. *Anal. Chem.* **71,** 777–790 (1999).
247. Eck, W. *et al.* Generation of Surface Amino Groups on Aromatic Self-Assembled Monolayers by Low Energy Electron Beams—A First Step Towards Chemical Lithography. *Adv. Mater.* **12,** 805–808 (2000).
248. Evans, S. D., Urankar, E., Ulman, A. & Ferris, N. Self-assembled monolayers of alkanethiols containing a polar aromatic group: effects of the dipole position on molecular packing, orientation, and surface wetting properties. *J. Am. Chem. Soc.* **113,** 4121–4131 (1991).
249. Frey, S. *et al.* Response of Biphenyl-Substituted Alkanethiol Self-Assembled Monolayers to Electron Irradiation: Damage Suppression and Odd−Even Effects. *Langmuir* **18,** 3142–3150 (2002).
250. Vallée, A., Humblot, V., Housseiny, Al, R., Boujday, S. & Pradier, C.-M. BSA adsorption on aliphatic and aromatic acid SAMs: investigating the effect of residual surface charge and sublayer nature. *Colloids and Surfaces B: Biointerfaces* **109,** 136–142 (2013).
251. Salmain, M., Ghasemi, M., Boujday, S. & Pradier, C.-M. Elaboration of a reusable immunosensor for the detection of staphylococcal enterotoxin A (SEA) in milk with a quartz crystal microbalance. *Sens. Actuator B-Chem.* **173,** 148–156 (2012).
252. Sawyer, L. & Kontopidis, G. The core lipocalin, bovine β-lactoglobulin. *Biochimica et Biophysica Acta* **1482,** 136–148 (2000).
253. Morgan, E. H. *Transferrin, Biochemistry, Physiology and Clinical Significance*. (Pergamon, 1981).
254. Arnold, R., Azzam, W., Terfort, A. & Woll, C. Preparation, modification, and crystallinity of aliphatic and aromatic carboxylic acid terminated self-assembled monolayers. *Langmuir* **18,** 3980–3992 (2002).
255. Himmel, H.-J., Terfort, A. & Wöll, C. Fabrication of a Carboxyl-Terminated Organic Surface with Self-Assembly of Functionalized Terphenylthiols: The Importance of Hydrogen Bond Formation. *J. Am. Chem. Soc.* **120,** 12069–12074 (1998).
256. Rao, C. N. R. & Venkataraghavan, R. The C=S stretching frequency and the '-N-C=S bands' in the infrared. *Spectrochimica Acta* **18,** 541–547 (1962).
257. Thébault, P., Boujday, S., Sénéchal, H. & Pradier, C.-M. Investigation of an Allergen Adsorption on Amine- and Acid-Terminated Thiol Layers: Influence on Their Affinity to Specific Antibodies. *J. Phys. Chem. B* **114,** 10612–10619 (2010).
258. Kelley, S. O. *et al.* Advancing the speed, sensitivity and accuracy of biomolecular detection using multi-length-scale engineering. *Nature Nanotechnology* **9,** 969–980 (2014).
259. Walt, D. R. Chemistry. Miniature analytical methods for medical diagnostics. *Science* **308,** 217–219 (2005).

260. Olsvik, O. *et al.* Magnetic separation techniques in diagnostic microbiology. *Clin. Microbiol. Rev.* **7,** 43–54 (1994).
261. Las Cuevas, De, G., Faraudo, J. & Camacho, J. Low-Gradient Magnetophoresis through Field-Induced Reversible Aggregation. *J. Phys. Chem. C* **112,** 945–950 (2008).
262. Lim, J. & Majetich, S. A. Composite magnetic–plasmonic nanoparticles for biomedicine: Manipulation and imaging. *Nano Today* **8,** 98–113 (2013).
263. Tartaj, P. Superparamagnetic Composites: Magnetism with No Memory. *European Journal of Inorganic Chemistry* **2009,** 333–343 (2009).
264. Teja, A. S. & Koh, P.-Y. Synthesis, properties, and applications of magnetic iron oxide nanoparticles. *Progress in Crystal Growth and Characterization of Materials* **55,** 22–45 (2009).
265. Benelmekki, M. *et al.* Horizontal low gradient magnetophoresis behaviour of iron oxide nanoclusters at the different steps of the synthesis route. *J. Nanopart. Res.* **13,** 3199–3206 (2011).
266. Lee, Y. *et al.* Large-Scale Synthesis of Uniform and Crystalline Magnetite Nanoparticles Using Reverse Micelles as Nanoreactors under Reflux Conditions. *Adv. Funct. Mater.* **15,** 503–509 (2005).
267. Leshuk, T. *et al.* Mesoporous Magnetically Recyclable Photocatalysts for Water Treatment. *J. Nanosci. Nanotechnol.* **13,** 3127–3132 (2013).
268. Couture, M., Zhao, S. S. & Masson, J.-F. Modern surface plasmon resonance for bioanalytics and biophysics. *Phys. Chem. Chem. Phys.* **15,** 11190–11216 (2013).
269. Wang *et al.* Monodispersed Core−Shell Fe 3O 4@Au Nanoparticles. *J. Phys. Chem. B* **109,** 21593–21601 (2005).
270. Xu, Z., Hou, Y. & Sun, S. Magnetic Core/Shell Fe_3O_4/Au and Fe_3O_4/Au/Ag Nanoparticles with Tunable Plasmonic Properties. *J. Am. Chem. Soc.* **129,** 8698–8699 (2007).
271. Crozier, K. B. *et al.* Plasmonics for surface enhanced raman scattering: Nanoantennas for single molecules. (2013).
272. Oh, Y., Lee, W., Kim, Y. & Kim, D. Self-aligned colocalization of 3D plasmonic nanogap arrays for ultra-sensitive surface plasmon resonance detection. *Biosens. Bioelectron.* **51,** 401–407 (2014).
273. Sanchez-Gaytan, B. L. *et al.* Controlling the Topography and Surface Plasmon Resonance of Gold Nanoshells by a Templated Surfactant-Assisted Seed Growth Method. *J. Phys. Chem. C* **117,** 8916–8923 (2013).
274. Cheng, W., Tang, K., Qi, Y., Sheng, J. & Liu, Z. One-step synthesis of superparamagnetic monodisperse porous Fe 3 O 4 hollow and core-shell spheres. *Journal of Materials Chemistry* **20,** 1799 (2010).
275. Wang, L., Li, J., Jiang, Q. & Zhao, L. Water-soluble Fe3O4 nanoparticles with high solubility for removal of heavy-metal ions from waste water. *Dalton Trans.* **41,** 4544–4551 (2012).
276. Lu, A.-H., Salabas, E. L. & Schüth, F. Magnetic nanoparticles: synthesis, protection, functionalization, and application. *Angew. Chem. Int. Ed.* **46,** 1222–1244 (2007).
277. Philipse, A. P., Van Bruggen, M. & Pathmamanoharan, C. Magnetic silica dispersions: preparation and stability of surface-modified silica particles with a magnetic core. *Langmuir* **10,** 92–99 (1994).
278. Faraudo, J. & Camacho, J. Cooperative magnetophoresis of superparamagnetic colloids: theoretical aspects. *Colloid Polym Sci* **288,** 207–215 (2010).
279. Haiss, W., Thanh, N. T. K., Aveyard, J. & Fernig, D. G. Determination of size and concentration of gold nanoparticles from UV-vis spectra. *Anal. Chem.* **79,** 4215–4221 (2007).
280. Amendola, V. & Meneghetti, M. Size Evaluation of Gold Nanoparticles by UV−vis Spectroscopy. *J. Phys. Chem. C* **113,** 4277–4285 (2009).
281. Torigoe, K. & Esumi, K. Preparation of colloidal gold by photoreduction of tetracyanoaurate (1-)-cationic surfactant complexes. *Langmuir* **8,** 59–63 (1992).
282. Pérez Juste, J., Liz Marzán, L. M., Carnie, S., Chan, D. Y. C. & Mulvaney, P. Electric-Field-Directed Growth of Gold Nanorods in Aqueous Surfactant Solutions. *Adv. Funct. Mater.* **14,** 571–579 (2004).
283. Le Ru, E. C., Blackie, E., Meyer, M. & Etchegoin, P. G. Surface enhanced Raman scattering enhancement factors: a comprehensive study. *J. Phys. Chem. C* **111,** 13794–13803 (2007).
284. Lee, S., Anderson, L. J. E., Payne, C. M. & Hafner, J. H. Structural Transition in the Surfactant Layer that Surrounds Gold Nanorods as Observed by Analytical Surface-Enhanced Raman Spectroscopy. *Langmuir* **27,** 14748–14756 (2011).

285. Rodríguez-Lorenzo, L., Romo-Herrera, J. M., Pérez-Juste, J., Alvarez-Puebla, R. A. & Liz-Marzán, L. M. Reshaping and LSPR tuning of Au nanostars in the presence of CTAB. *Journal of Materials Chemistry* **21,** 11544–11549 (2011).
286. Liu, M. & Guyot-Sionnest, P. Mechanism of Silver(I)-Assisted Growth of Gold Nanorods and Bipyramids. *J. Phys. Chem. B* **109,** 22192–22200 (2005).
287. Wu, H.-L., Chen, C.-H. & Huang, M. H. Seed-Mediated Synthesis of Branched Gold Nanocrystals Derived from the Side Growth of Pentagonal Bipyramids and the Formation of Gold Nanostars. *Chem. Mater.* **21,** 110–114 (2009).
288. Sanchez-Gaytan, B. L. Synthesis And Self-Assembly Of Nanoparticles And Amphiphilic Block Copolymers. (Publicly Accessible Penn Dissertations, 2012).
289. Khan, Z., Singh, T., Hussain, J. I. & Hashmi, A. A. Au(III)–CTAB reduction by ascorbic acid: Preparation and characterization of gold nanoparticles. *Colloids and Surfaces B: Biointerfaces* **104,** 11–17 (2013).
290. Trigari, S. *et al.* Synthesis and modelling of gold nanostars with tunable morphology and extinction spectrum. *Journal of Materials Chemistry* **21,** 6531–6540 (2011).
291. Vega, M. M. *et al.* Long-term stability of surfactant-free gold nanostars. *J. Nanopart. Res.* **16,** 1–6 (2014).
292. Sassolas, A., Leca-Bouvier, B. D. & Blum, L. J. DNA Biosensors and Microarrays. *Chem. Rev.* **108,** 109–139 (2008).
293. Paleček, E. & Bartošík, M. Electrochemistry of Nucleic Acids. *Chem. Rev.* **112,** 3427–3481 (2012).
294. Smith, W. E. Practical understanding and use of surface enhanced Raman scattering/surface enhanced resonance Raman scattering in chemical and biological analysis. *Chem. Soc. Rev.* **37,** 955–964 (2008).
295. Shkilnyy, A. *et al.* Poly(ethylene glycol)-stabilized silver nanoparticles for bioanalytical applications of SERS spectroscopy. *Analyst* **134,** 1868–1872 (2009).
296. Power, A. C., Betts, A. J. & Cassidy, J. F. Non aggregated colloidal silver nanoparticles for surface enhanced resonance Raman spectroscopy. *Analyst* **136,** 2794–2801 (2011).
297. Fazio, B. *et al.* SERS detection of Biomolecules at Physiological pH via aggregation of Gold Nanorods mediated by Optical Forces and Plasmonic Heating. *Sci. Rep.* **6,** 26952 (2016).
298. Guo, I. W., Pekcevik, I. C., Wang, M. C. P., Pilapil, B. K. & Gates, B. D. Colloidal core–shell materials with 'spiky' surfaces assembled from gold nanorods. *Chem. Commun.* **50,** 8157–8160 (2014).
299. Barhoumi, A., Zhang, D. & Tam, F. Surface-enhanced Raman spectroscopy of DNA. *J. Am. Chem. Soc.* (2008).
300. Lal, S., Grady, N. K., Goodrich, G. P. & Halas, N. J. Profiling the Near Field of a Plasmonic Nanoparticle with Raman-Based Molecular Rulers. *Nano Lett.* **6,** 2338–2343 (2006).
301. Marotta, N. E., Beavers, K. R. & Bottomley, L. A. Limitations of Surface Enhanced Raman Scattering in Sensing DNA Hybridization Demonstrated by Label-Free DNA Oligos as Molecular Rulers of Distance-Dependent Enhancement. *Anal. Chem.* **85,** 1440–1446 (2013).
302. Murray, C. A. in *Surface Enhanced Raman Scattering* 203–221 (Springer US, 1982). doi:10.1007/978-1-4615-9257-0_11
303. Kennedy, B. J., Spaeth, S., Dickey, M. & Carron, K. T. Determination of the Distance Dependence and Experimental Effects for Modified SERS Substrates Based on Self-Assembled Monolayers Formed Using Alkanethiols. *J. Phys. Chem. B* **103,** 3640–3646 (1999).
304. Liu, F. M., Köllensperger, P. A., Green, M. & Cass, A. A note on distance dependence in surface enhanced Raman spectroscopy. *Chemical Physics Letters* **430,** 173–176 (2006).
305. Prado, E., Daugey, N., Plumet, S., Servant, L. & Lecomte, S. Quantitative label-free RNA detection using surface-enhanced Raman spectroscopy. *Chem. Commun.* **47,** 7425–7427 (2011).
306. Guerrini, L., Krpetić, Ž., van Lierop, D., Alvarez-Puebla, R. A. & Graham, D. Direct Surface-Enhanced Raman Scattering Analysis of DNA Duplexes. *Angewandte Chemie* **127,** 1160–1164 (2015).
307. Papadopoulou, E. & Bell, S. E. J. Label-Free Detection of Single-Base Mismatches in DNA by Surface-Enhanced Raman Spectroscopy. *Angew. Chem. Int. Ed.* **50,** 9058–9061 (2011).
308. Abell, J. L., Garren, J. M., Driskell, J. D., Tripp, R. A. & Zhao, Y. Label-Free Detection of Micro-

RNA Hybridization Using Surface-Enhanced Raman Spectroscopy and Least-Squares Analysis. *J. Am. Chem. Soc.* **134,** 12889–12892 (2012).

309. Barhoumi, A. & Halas, N. J. Label-free detection of DNA hybridization using surface enhanced Raman spectroscopy. *J. Am. Chem. Soc.* **132,** 12792–12793 (2010).

310. Papadopoulou, E. & Bell, S. E. J. DNA reorientation on Au nanoparticles: label-free detection of hybridization by surface enhanced Raman spectroscopy. *Chem. Commun.* **47,** 10966–10968 (2011).

311. Ngo, H. T., Wang, H.-N., Fales, A. M. & Vo-Dinh, T. Label-Free DNA Biosensor Based on SERS Molecular Sentinel on Nanowave Chip. *Anal. Chem.* **85,** 6378–6383 (2013).

312. Ngo, H. T., Wang, H.-N., Burke, T., Ginsburg, G. S. & Vo-Dinh, T. Multiplex detection of disease biomarkers using SERS molecular sentinel-on-chip. *Anal. Bioanal. Chem.* **406,** 3335–3344 (2014).

313. Ngo, H. T., Wang, H.-N., Fales, A. M. & Vo-Dinh, T. Plasmonic SERS biosensing nanochips for DNA detection. *Anal. Bioanal. Chem.* **408,** 1773–1781 (2015).

314. Wabuyele, M. B. & Vo-Dinh, T. Detection of Human Immunodeficiency Virus Type 1 DNA Sequence Using Plasmonics Nanoprobes. *Anal. Chem.* **77,** 7810–7815 (2005).

315. Wang, H. *et al.* Hairpin DNA-Assisted Silicon/Silver-Based Surface-Enhanced Raman Scattering Sensing Platform for Ultrahighly Sensitive and Specific Discrimination of Deafness Mutations in a Real System. *Anal. Chem.* **86,** 7368–7376 (2014).

316. Chen, J. *et al.* A New Aptameric Biosensor for Cocaine Based on Surface-Enhanced Raman Scattering Spectroscopy. *Chemistry - A European Journal* **14,** 8374–8382 (2008).

317. Faulds, K., Smith, W. E. & Graham, D. Evaluation of Surface-Enhanced Resonance Raman Scattering for Quantitative DNA Analysis. *Anal. Chem.* **76,** 412–417 (2003).

318. Faulds, K., McKenzie, F., Smith, W. E. & Graham, D. Quantitative Simultaneous Multianalyte Detection of DNA by Dual-Wavelength Surface-Enhanced Resonance Raman Scattering. *Angewandte Chemie* **119,** 1861–1863 (2007).

319. Balasubramanian, V., Nguyen, L. T., Balasubramanian, S. V. & Ramanathan, M. Interferon-gamma-inhibitory oligodeoxynucleotides alter the conformation of interferon-gamma. *Mol. Pharmacol.* **53,** 926–932 (1998).

320. Liu, Y., Tuleouva, N., Ramanculov, E. & Revzin, A. Aptamer-Based Electrochemical Biosensor for Interferon Gamma Detection. *Anal. Chem.* **82,** 8131–8136 (2010).

321. Chang, C.-C. *et al.* Amplified surface plasmon resonance immunosensor for interferon-Gamma based on a streptavidin-incorporated aptamer. *Biosens. Bioelectron.* **37,** 68–74 (2012).

322. Bensebaa, F. *et al.* Raman characterization of metal-alkanethiolates. *Spectrochimica Acta Part A: Molecular and Biomolecular Spectroscopy* **55,** 1229–1236 (1999).

323. Rycenga, M., McLellan, J. M. & Xia, Y. A SERS study of the molecular structure of alkanethiol monolayers on Ag nanocubes in the presence of aqueous glucose. *Chemical Physics Letters* **463,** 166–171 (2009).

324. Papadopoulou, E. & Bell, S. E. J. Label-Free Detection of Nanomolar Unmodified Single- and Double-Stranded DNA by Using Surface-Enhanced Raman Spectroscopy on Ag and Au Colloids. *Chemistry - A European Journal* **18,** 5394–5400 (2012).

325. Bell, S. E. J. & Sirimuthu, N. M. S. Surface-enhanced Raman spectroscopy (SERS) for sub-micromolar detection of DNA/RNA mononucleotides. *J. Am. Chem. Soc.* **128,** 15580–15581 (2006).

326. Parak, W. J. *et al.* Conformation of Oligonucleotides Attached to Gold Nanocrystals Probed by Gel Electrophoresis. *Nano Lett.* **3,** 33–36 (2002).

327. Mills, J. B., Vacano, E. & Hagerman, P. J. Flexibility of single-stranded DNA: use of gapped duplex helices to determine the persistence lengths of Poly(dT) and Poly(dA). *Journal of Molecular Biology* **285,** 245–257 (1999).

328. Smith, S. B., Cui, Y. & Bustamante, C. Overstretching B-DNA: the elastic response of individual double-stranded and single-stranded DNA molecules. *Science* **271,** 795–799 (1996).

329. Wilkins Stevens, P., Henry, M. R. & Kelso, D. M. DNA hybridization on microparticles: determining capture-probe density and equilibrium dissociation constants. *Nucleic Acids Research* **27,** 1719–1727 (1999).

330. Donnelly, T., Faulds, K. & Graham, D. Investigation of Silver Nanoparticle Assembly Following Hybridization with Different Lengths of DNA. *Particle & Particle Systems Characterization* **33,** 404–

411 (2016).

331. Minton, A. P. The influence of macromolecular crowding and macromolecular confinement on biochemical reactions in physiological media. *J. Biol. Chem.* **276,** 10577–10580 (2001).

332. Peeters, S. *et al.* Impact of spacers on the hybridization efficiency of mixed self-assembled DNA/alkanethiol films. *Biosens. Bioelectron.* **24,** 72–77 (2008).

333. Milton, J. A. *et al.* Efficient self-assembly of DNA-functionalized fluorophores and gold nanoparticles with DNA functionalized silicon surfaces: the effect of oligomer spacers. *Nucleic Acids Research* **41,** e80 (2013).

334. Faraudo, J., Andreu, J. S. & Camacho, J. Understanding diluted dispersions of superparamagnetic particles under strong magnetic fields: a review of concepts, theory and simulations. *Soft Matter* **9,** 6654–6664 (2013).

335. Evans, D. F. & Wennerström, H. *The Colloidal Domain, where Physics, Chemistry, Biology and Technology Meet, 2nd Edition*. (Wiley-VCH, 1999). doi:10.5860/choice.37-0334

336. Thomas, D. N., Judd, S. J. & Fawcett, N. Flocculation modelling: a review. *Water Research* **33,** 1579–1592 (1999).

337. Li, D., Lam, C. N. & Biswal, S. L. Measuring short-range repulsive forces by imaging directed magnetic-particle assembly title. *Soft Matter* **6,** 239–242 (2010).

338. Milner, S. T., Witten, T. A. & Cates, M. E. Theory of the grafted polymer brush. *Macromolecules* **21,** 2610–2619 (1988).

339. Zhao, W., Chiuman, W., Brook, M. A. & Li, Y. Simple and Rapid Colorimetric Biosensors Based on DNA Aptamer and Noncrosslinking Gold Nanoparticle Aggregation. *ChemBioChem* **8,** 727–731 (2007).

340. Zhao, W. A., Lam, J. C. F., Chiuman, W., Brook, M. A. & Li, Y. F. Enzymatic cleavage of nucleic acids on gold nanoparticles: A generic platform for facile colorimetric biosensors. *Small* **4,** 810–816 (2008).

Appendix A: Apo-transferrin data

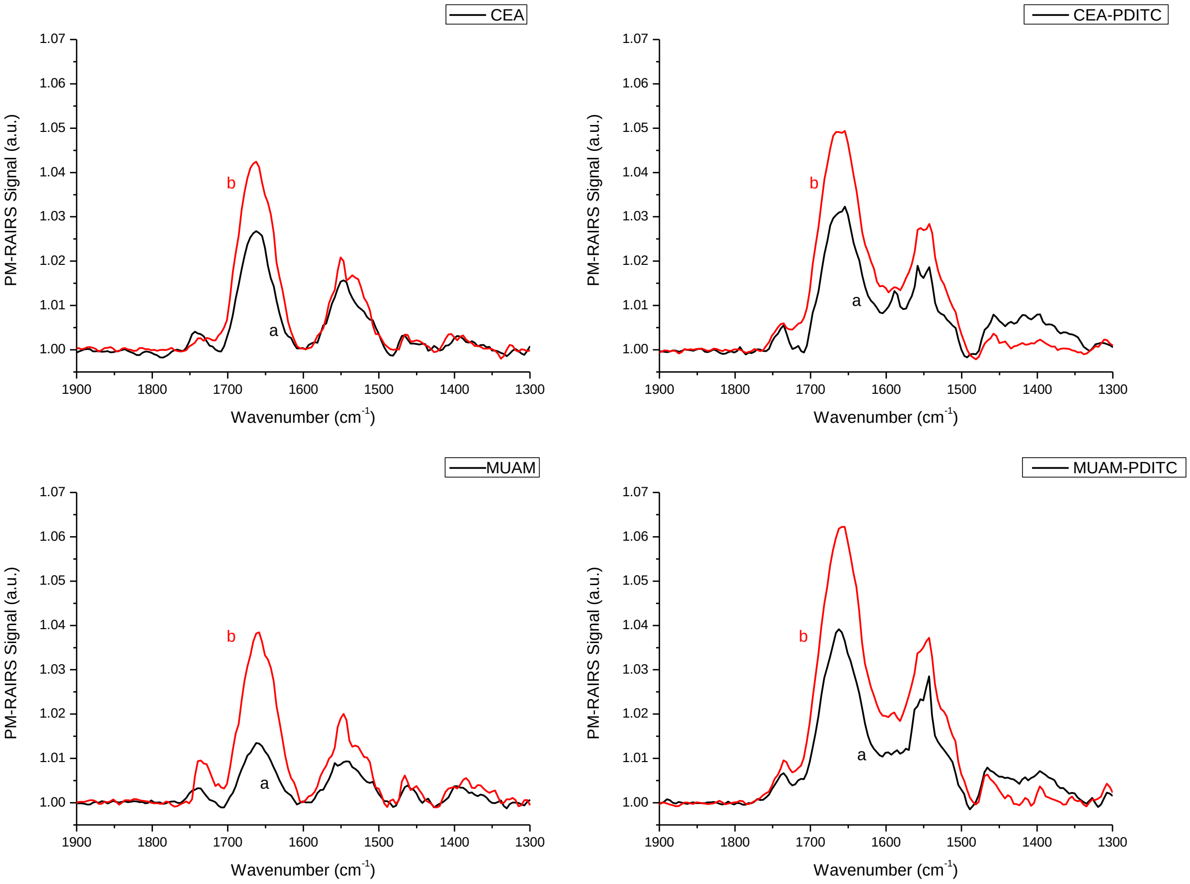

Figure A.1: PM-IRRAS spectra of apo-transferrin (a) and antibody recognition (b) on a) CEA, b) MUAM, c) PDITC/CEA and d) PDITC/MUAM.

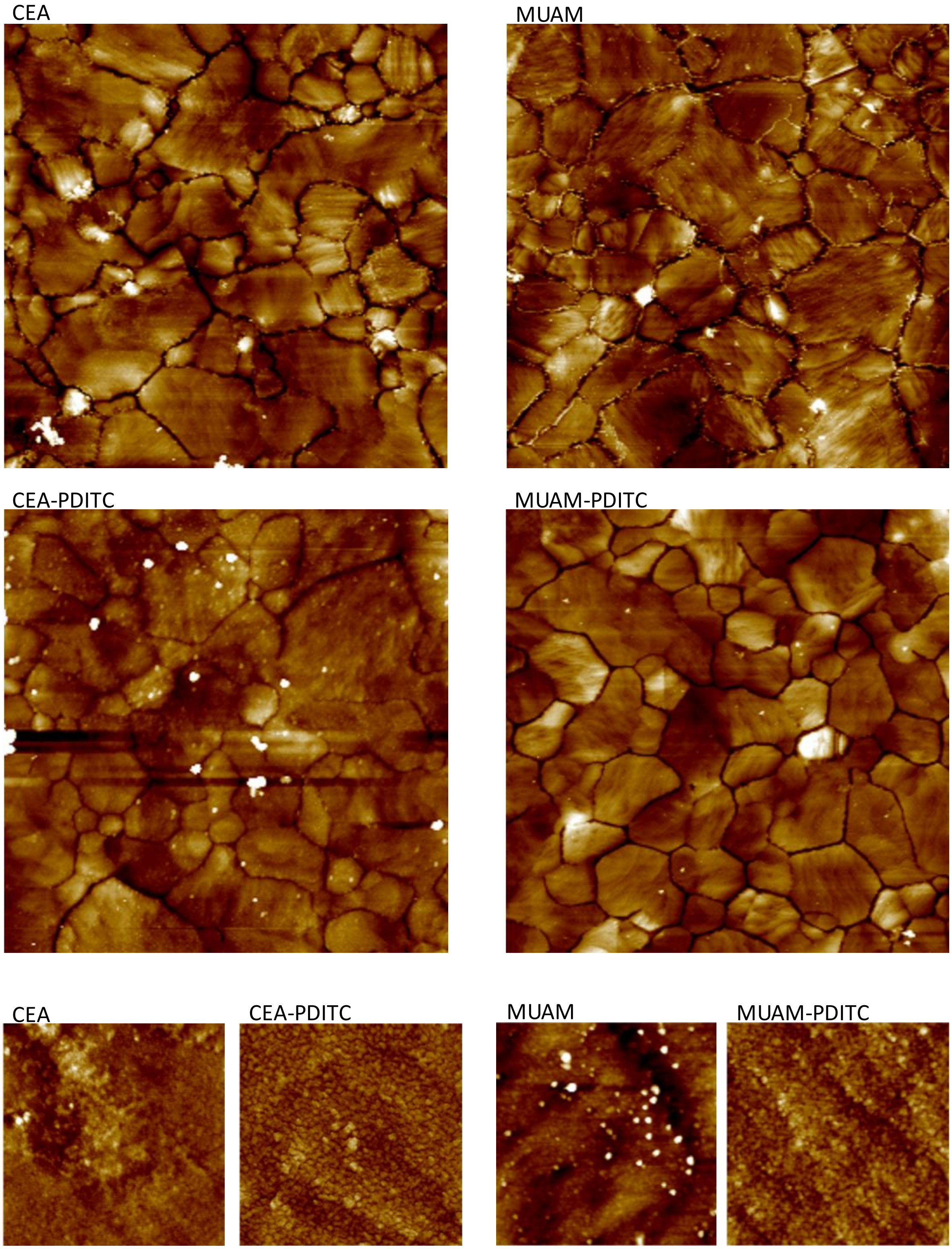

Figure A.2: AFM images of gold-coated substrates following SAM formation and apotransferrin binding. Upper images: Scan area: 10 μm x 10 μm, height scale: 40 nm. Lower images: Scan area: 1 μm x 1 μm, height scale: 10 nm.

Appendix B: Magnetic separation calculations

An expanded DLVO theory[278,334] was used to model the silica-coated magnetic particle interaction potentials. The following describes the theory used to produce the plots of Figure 5.5, as well as a brief discussion of particle stabilization when DNA is bound to the surface.

B.1 DLVO theory

The interactions between particles in solution can be described using DLVO theory (Derjaguin, Landau, Verwey, and Overbeek). The theory combines two competing forces—attractive Van der Waals forces and repulsive electrostatic forces—to describe the interaction between charged surfaces in a liquid medium.

The interaction potential, V, can be written in terms of the Van der Waals potential, V_{VdW}, and the double layer potential, V_{DL}:

$$V = V_{VdW} + V_{DL} \tag{1}$$

For two spherical particles of equivalent radii, R, the attractive Van der Waals potential depends on the particle radius, the distance between particle surfaces, D, and the Hamaker constant, H, a material property that depends on both the particle material and dispersion medium:

$$V_{VdW} \approx -\frac{H_{212}}{12}\frac{R}{D} \tag{2}$$

The equation uses the Derjaguin approximation to relate the force between two spheres to the interaction potential per unit area of two flat surfaces ($F(D) = \pi R W(D)$, for particles of equivalent radii).[278,335]

The double layer potential results from a layer of oppositely charged ions that form on the charged surfaces. When two similarly charged surfaces approach one another, differences in the ionic concentration between particles compared to that in bulk solution creates an osmotic pressure, which leads to a repulsive force between the surfaces. The Derjaguin approximation is again used to relate the force between spheres to the potential between flat surfaces. In a concentration, c_0, of 1:1 electrolyte (such as NaCl or KCl) the double layer potential can be written as:

$$V_{DL} \approx \frac{64k_BTc_0}{\kappa^2}\Gamma_0^2 e^{-D\kappa} \tag{3}$$

where k_B is the Boltzmann constant, T is temperature, κ^{-1} is the Debye screening length given by $\kappa^{-1} = (\varepsilon_0\varepsilon_r k_BT/2q_e^2c_0)^{1/2} = 0.304/\sqrt{c_0}$ nm, which is a function of constants (ε_0 is the vacuum permittivity, ε_r is the vacuum permittivity of the medium, and q_e is the elementary charge) and the ion concentration, c_0, and $\Gamma_0 = \tanh(\frac{q_e\Phi_0}{4k_BT})$, where Φ_0 is the surface potential of the particles.[278,335]

These competing forces give a potential curve as seen in Figure B.1. The curve features two minimums: a primary minimum at very small separations and a secondary minimum at larger separations. The particles are prevented from reaching the deep, primary minimum—resulting in particle coagulation—by an energy barrier created by electrostatic repulsion. A large enough energy barrier means that particles will be trapped in the secondary minimum where they can easily be redispersed with a small input of energy (shaking, for example).

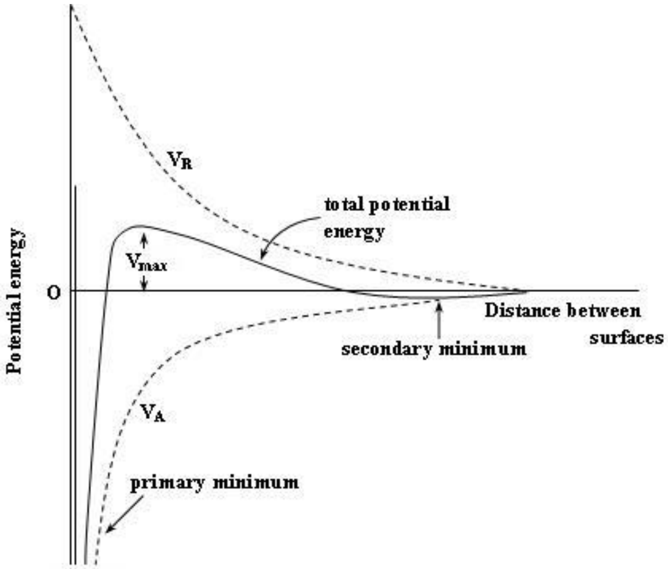

Figure B.1: Representation of DLVO theory[336]

B.2 Magnetic separation: expanded DLVO theory

When a magnetic field is applied to the colloidal dispersion, the theory needs to be expanded to include the magnetic dipole-dipole interaction. The interaction potential including the magnetic dipole-dipole interaction, V_{Mag}, of two superparamagnetic particles with dipole m becomes:

$$V = V_{VdW} + V_{DL} + V_{Mag} \tag{4}$$

where

$$V_{Mag} = \frac{\mu_0 m^2}{4\pi(D+2R)^3}\left[1 - 3\cos^2\theta\right] \tag{5}$$

where μ_0 is the magnetic permeability of free space and θ is the angle between the direction of the magnetic field and the line passing through the centers of the two particles.[334] The potential varies with the separation distance of the two particles, $D + 2R$.

For our purposes, the equation can be simplified to consider only the maximum attractive energy, occurring when $\theta = 0°$, and to consider that the particles are at saturation magnetization with dipoles m_s, a good assumption under most experimental conditions where fields are typically larger than 0.1 T.[278] The saturation magnetization can be given by $m_s = M_s \rho_p \left(\frac{4}{3}\right) \pi R^3$, where M_s is the saturation magnetization per unit mass of colloid (determined experimentally) and ρ_p is the density of a particle. This gives:

$$V_{Mag} = -\frac{\mu_0 m_s^2}{2\pi(D + 2R)^3} \tag{6}$$

Figure B.2 shows a plot of potential energy with distance based on equation 4 which looks extremely similar to Figure B.1, the case before a magnetic field is applied.

Superparamagnetic particles of this type have been shown to form linear chains aligned with the magnetic field. As long as the energy barrier between the primary and secondary minimums is large enough (i.e. electrostatic or steric repulsion is large enough to counteract the magnetic attraction), the particles stay in the "reversible chaining" regime. If the energy barrier is too low, the particles will enter into the primary minimum and irreversible aggregation will occur. This will prevent redispersion of the particles, thus preventing further work with the functionalized particles.

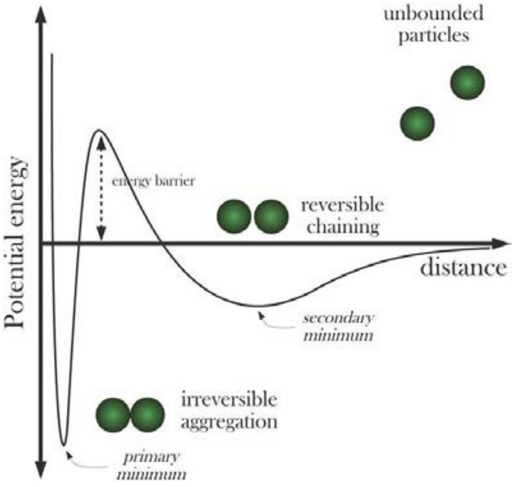

Figure B.2: Potential energy profile of interaction between two superparamagnetic particles in a strong magnetic field. The profile is based on a generalized DLVO theory that includes magnetic attraction and electrostatic repulsion[334]

B.3 Oligonucleotide probe coupled particle stabilization

When oligonucleotide probes are coupled to the carboxylated particles, the surface characteristics of the particles change, thus the forces governing colloidal stability also change. Research suggests that colloidal stability due to oligonucleotide binding results from both electrostatic and steric stabilization. DNA is negatively charged, thus double layer repulsion likely plays a role in colloidal stability, but in addition, interparticle interactions of DNA-functionalized particles have been shown to fit well with theories of steric stabilization; for example, AFM force measurements of the interaction between DNA functionalized magnetic particles[337] fit well with the theory of Milner *et al* discussing grafted polymer brushes.[338] The theory applies particularly well for longer oligonucleotides compared with shorter ones, suggesting that other forces may become more influential as steric stabilization becomes less significant.

Steric stabilization results from a difference in osmotic pressure between the space between particle surfaces and the bulk. As the two surfaces approach, the concentration of stabilizing polymer between the surfaces increases, thus increasing the difference in osmotic pressure.

One potential benefit of steric stabilization compared with electrostatic stabilization is that the addition of salt has less effect on the colloidal stability. For example, gold nanoparticles functionalized with DNA showed high colloidal stability even at relatively high salt concentrations.[339,340] This can be particularly useful in hybridization reactions that can require buffers with high salt concentrations.

With high enough steric repulsion, the theory predicts that no primary minimum will occur, thus particle interactions will always be repulsive. When the particles are used in magnetic separation, the presence of a magnetic field induces a small free energy minimum similar to the secondary minimum of Figure B.1.

B.4 MATLAB Code

```
% % Colloidal stability of superparamagnetic particles in
separation of biomolecules


% % Constants

H = 0.8e-20;
epsr = 78.5;
eps0 = 8.854e-12;
T = 298;
kb = 1.381e-23;
q = 1.602e-19;
NA = 6.022e23;
mu0 = 4*pi*1e-7; % Magnetic permeability of free space, in NA-2

% % Variables

D = 0:5e-11:20e-9;
R = 363e-9/2;
Ms_emu_g = [0,1,32]; % Saturation magnetization, in Am^2/kg=emu/g
rhop = 3420; % Particle density, in kg/m^3
Cs = 0.01; % Salt concentration, in mol/l
CB = (Cs*NA*1000); % Salt concentration, in molecules/m^3
phi0 = zeros(1,3);
Volp = 4/3*pi*R^3; % Volume of particles, m^3
Ms = Ms_emu_g*rhop; % Saturation magnetization, in
A/m=10^3emu/cm^3

% % DLVO equations

ms = Ms*4/3*pi*(224e-9/2)^3; % Magnetic dipole, determined using
iron oxide core volume

kappa = ((eps0*epsr*kb*T)./(2*q^2*CB)).^(-1/2); % Same as values
obtained using 0.304/sqrt(salt concentration)^-1

kappainv = kappa.^-1;

yB = q^2/(4*pi*eps0*epsr*kb*T);

yBm = (mu0*ms.^2./(2*pi*kb*T)).^(1/3);

syms p0

cd = -0.9*q; % Charge density, e/nm^2, use -0.9 to get
electrostatic potential of -73mv at 10mM NaCl

Q = cd*(1e9)^2*q*4*pi*(R*1e9)^2; % Total charge on surface of one
particle
```

```
phi0 = vpasolve(Q == q*2*R^2/yB/kappa^(-
1)*(sinh(q*p0/2/kb/T)+2*kappa^(-1)/R*tanh(q*p0/4/kb/T)),p0,0);

phi0 = double(phi0); % Electrostatic potential of particles

F = tanh(q.*phi0./4/kb/T);

Vvdw = -H./12.*R./D;

for i  = 1:3
    Vdl = 64*pi*kb*T*R*eps0*epsr*kb*T/q^2.*F.^2.*exp(-D.*kappa);
    Vmag(i,:) = -mu0.*ms(i).^2./(2*pi.*(D+2*R).^3);
    V(i,:) = Vvdw(1,:) + Vdl(1,:) + Vmag(i,:);
end

% Plots

figure

plot(D*1e9,V(1,:)/kb/T,'--b',D*1e9,V(2,:)/kb/T,'-r',
D*1e9,V(3,:)/kb/T,'-g',[0 max(D)*1e9],[0 0],'-k')

xlabel('Separation, D (nm)')

ylabel('V/kbT')

legend([num2str(Ms_emu_g(1)) ' emu/g'],[num2str(Ms_emu_g(2)) '
emu/g'],[num2str(Ms_emu_g(3)) ' emu/g'])

title('V')
```